Tracking Volatile Elements in Protoplanetary Disks and on Planetary Surfaces

Thesis by
Dana Eklund Anderson

In Partial Fulfillment of the Requirements for the
Degree of
Doctor of Philosophy

CALIFORNIA INSTITUTE OF TECHNOLOGY
Pasadena, California

2020
Defended August 12, 2019

Dana Eklund Anderson
ORCID: 0000-0002-8310-0554

ACKNOWLEDGEMENTS

This work was only made possible by the support of many individuals and I would like to offer them my deepest gratitude.

First and foremost, I am profoundly grateful to my thesis advisor, Geoff Blake, for his continuous support, patience, and guidance throughout this work. Geoff possesses a wealth of knowledge that crosses multiple disciplines and has taught me so much. He has given me invaluable advice and opportunities that will benefit my career for years to come. In addition, I would like to thank Bethany Ehlmann for her mentorship, for broadening my research focus, and for making me a part of the MSL Team. Furthermore, I want to thank my entire thesis committee—Bethany Ehlmann, Konstantin Batygin, Geoff Blake, and Heather Knutson—for providing encouragement and feedback that helped me to carry out this work. Many thanks also to all the faculty and staff who have supported my education and research efforts at Caltech.

A special thanks to all of my coauthors who have provided everything from general mentorship to teaching me specialized skills, many aspects of this work would not have been possible without them.

Thank you to all of the current and former members of the Blake group who have provided words of wisdom and shared their exciting (astro)chemistry research. In particular, thanks to fellow astrochemists Masha Kleshcheva, Cam Buzard, Olivia Wilkins, and Kayla Owens. I also want to give a very special thanks to my academic big sister Coco Zhang for her encouragement and numerous scientific discussions.

Many thanks to all of my students, especially the Cosmochemistry students of Fall 2017, who let me experiment in lecturing and activity-designing with them as a teaching assistant.

For getting me started in astrochemistry, from basic computer programming to H_2 formation on grains, I am eternally grateful to Ted Bergin and his entire group over the years including Nate Crockett, Justin Neill, Ruud Visser, Ilse Cleeves, Kamber Schwarz, and Fujun Du.

To the original crew, Christopher Spalding, Pushkar Kopparla, Ian Wong, Patrick Fischer, Abbey Nastan, and Peter Buhler, your friendship meant the

world to me throughout our first year and beyond. I also have to thank many more fellow graduate students who made my time and birthdays at Caltech special, including Peter Gao, Joe O'Rourke, Lulu Pan, Danielle Piskorz, Elizabeth Bailey, Ellen Leask, Nathan Stein, Nicole Wallack, and especially Henry Ngo and Mike Wong.

To Nancy Thomas and Dayne Privett, who took on too many roles and responsibilities to list, thank you for everything.

To my family—especially my parents—who have always been there for me, much love & thanks.

ABSTRACT

The formation of planets begins with collisions of tiny, micron-sized, dust grains. These grains reside in structures known as protoplanetary disks, rotating disks consisting of gas and dust that encircle young protostars as a natural outcome of star formation. Although the processes of planet formation and evolution take place over millions and billions of years, in our limited view we can only see snapshots of the different stages. Many of the formative processes are difficult, if not impossible, to observe directly. However, evidence of these events exists in the chemical composition of the bulk material and surfaces of planets themselves, the gas and solid components of protoplanetary disks, and planetary debris such as asteroids and comets. This thesis utilizes modeling and observations of the carbon and nitrogen content of protoplanetary disks to shed light on key factors that control the formation and chemical composition of planets. In addition, this thesis advances techniques for the elemental analysis of planetary surfaces facilitating the detection of salts on the surface of Mars.

Chapter 2 estimates the maximum potential destruction of solid, refractory carbon in protoplanetary disks in an effort to explain the lack of carbon found in meteorites and the bulk silicate Earth relative to the interstellar materials that seeded their formation. Oxidation and UV photolysis of refractory carbon grains and polycyclic aromatic hydrocarbons are modeled in a T-Tauri disk assuming uniform turbulence and passive heating from stellar photons. Under these conditions, destruction is limited to the warm, photochemically-active disk surface layers. The bulk refractory carbon reservoir is only affected when carbon remains in small grains, less than 10 microns in size, and grains are efficiently transported to the surface layers. Exploration of distinct disk environments, considering non-idealized mass transport or enhanced disk heating due to active stellar mass accretion, is needed to explain the widespread lack of carbon in rocky solar-system bodies.

Chapter 3 presents detections by the Atacama Large Millimeter/submillimeter Array (ALMA) of N_2H^+ in two mature, 5–11 Myr-old, protoplanetary disks in the Upper Scorpius region. Compared to a sample of gas-rich disks with a factor of 10 higher CO fluxes, these mature disks have significantly enhanced N_2H^+/CO flux ratios. The Upper Sco N_2H^+ and CO fluxes can only be repro-

duced by our thermo-chemical disk models using a typical gas-to-dust mass ratio of 100 and a significantly depleted CO/H_2 abundance of 10^{-6}. These results indicate diverging behavior of the key carbon and nitrogen species in the disk gas as disks evolve and that selective depletion of CO from the gas may cause disk gas masses to be underestimated if based on CO measurements alone. Accurate masses, particularly for older systems, are critical in determining the typical lifetime of gas and setting constraints on the timescale for gas-giant planet formation in protoplanetary disks. Chapter 4 describes a follow-up study to this work investigating the use of N_2H^+, HCO^+, and $C^{18}O$ observations together to better constrain disk masses and examines the interplay among disk mass, CO abundance, and ionization in determining line fluxes from the outer disk.

Chapter 5 seeks to explain the discrepancy between infrared observations of disks from Keck-NIRSPEC and the *Spitzer Space Telescope*, indicating that the innermost regions display signatures of CO- and water-rich gas, and submillimeter observations from ALMA revealing CO depletion in the outer disk. In the outer disk, CO may be chemically converted into less volatile species such as CO_2 and CH_3OH. Chemical models explore the fate of CO_2 and CH_3OH ices after being introduced to the hotter, denser inner regions of the disk. Carbon returns to CO in unshielded transparent regions of the inner disk surface, consistent with infrared observations, but carbon reservoirs in the disk midplane may be distinct depending on the efficiency of mass transport in the disk. These results have important implications for the distribution of volatile carbon in terrestrial-planet-forming regions of the disk and will inform upcoming observations with the *James Webb Space Telescope* (JWST).

Chapter 6 examines the abilities of the Laser-Induced Breakdown Spectroscopy (LIBS) instrument ChemCam on the Mars rover Curiosity in regards to the detection of salts. Sample pellets are prepared with decreasing concentrations of salt in a basaltic background, relevant to Mars surface compositions. Analysis of LIBS spectra from this sample set identifies elemental emission lines of Cl, C, and S that are sensitive to changes in chloride, carbonate, and sulfate salt concentrations, respectively, and provides detection limits for ChemCam measurements of these salts. These results are applicable to the study of past aqueous environments in Gale Crater, Mars through detection and identification of specific salts in the hundreds of thousands of spectra collected by

ChemCam.

The work presented in this thesis investigates the chemical reprocessing of refractory and volatile carbon in protoplanetary disks, reveals the need for multiple chemical tracers when predicting disk gas masses, and facilitates the quantification of salts on the surface Mars with ChemCam. Such chemical analyses probe unobservable environments, in the past or shielded from our view, providing valuable insight into the potential outcomes of planet formation and evolution.

PUBLISHED CONTENT AND CONTRIBUTIONS

Anderson, D. E., G. A. Blake, et al. (2019). "Probing the Gas Content of Late-stage Protoplanetary Disks with N_2H^+". In: *The Astrophysical Journal* 881, pp. 127–139. DOI: 10.3847/1538-4357/ab2cb5.
D.E.A. proposed for the observing time, imaged and analyzed the data, edited and ran the computational models, interpreted and visualized the model results, and wrote the manuscript.
Adapted for the contents of Chapter 3.

Anderson, D. E., E. A. Bergin, G. A. Blake, et al. (2017). "Destruction of Refractory Carbon in Protoplanetary Disks". In: *The Astrophysical Journal* 845, pp. 13–26. DOI: 10.3847/1538-4357/aa7da1.
D.E.A. edited and ran the computational models, interpreted and visualized the model results, and wrote the manuscript.
Adapted for the contents of Chapter 2.

Anderson, D. E., B. L. Ehlmann, et al. (2017). "Characterization of Laser-Induced Breakdown Spectroscopy (LIBS) emission lines for the identification of chlorides, carbonates, and sulfates in salt/basalt mixtures for the application to MSL ChemCam data". In: *Journal of Geophysical Research: Planets* 122, pp. 744–770. DOI: 10.1002/2016JE005164.
D.E.A. prepared and mixed sample powders, analyzed and interpreted the data, and wrote the manuscript.
Adapted for the contents of Chapter 6.

TABLE OF CONTENTS

LIST OF ILLUSTRATIONS

LIST OF TABLES

Chapter 1

INTRODUCTION

Planets around stars outside of our solar system are now known to be a common occurrence. Among the wide variety of discoveries are planets with radii similar to that of Earth and masses substantial enough to suggest Earth-like compositions of rock and iron (Howard et al. 2013; Pepe et al. 2013). Although this subset of extrasolar planets or *exoplanets* are rocky and Earth-sized, are they Earth-like in other ways? Are they made of the same materials? Did they form and evolve via comparable mechanisms? And, perhaps most interestingly, are they capable of hosting life similar to that on Earth?

To address the question of habitability, astronomers seek to determine which planets reside inside a region known as the *habitable zone* around their host star (e.g., Kasting et al. 1993). The habitable zone is typically determined based on the ability of a planetary surface to support the presence of liquid water. Although a valuable first approximation, this definition excludes other ingredients that are essential for life on Earth.

Carbon, hydrogen, nitrogen, oxygen, phosphorus, and sulfur are the six most common elements found in biological materials. The availability of these elements to or near the surfaces of rocky exoplanets (or large moons of gas giants) is largely unconstrained. Measurements of exoplanet compositions are limited to (1) spectroscopy of their upper atmospheres and (2) bulk density estimates based on their masses and radii. Rather than observing mature exoplanets, this thesis takes another approach and tracks elemental abundances throughout specific stages of planet formation and evolution. I seek to understand the dominant processes that affect the availability of life-enabling elements, in particular carbon and nitrogen, to planets via their formation in protoplanetary disks. In addition, I consider various bodies in our own solar system to provide additional compositional constraints regarding the possible outcomes of planet formation and evolution.

1.1 Chemistry in Protoplanetary Disks

Star formation occurs when the self-gravity of an interstellar molecular cloud core overwhelms any opposing forces including gas pressure, and thus initiates cloud collapse. A byproduct of star formation is the spreading of material into a disk encircling the growing protostar. In order to conserve angular momentum throughout the collapse, it is transferred away from the central stellar position to the outer gas. The increased angular momentum causes the gas to rotate faster and flatten into a disk. From this circumstellar disk, planets are made. Our own disk, out of which the Earth and our solar system formed, is often called the *solar nebula*. Because this disk disappeared over 4.5 billion years ago, we must study current planet-forming disks in order to infer the composition of the solar nebula and piece together the chemical history of the Earth from the initial formation of small rocky precursors known as planetesimals.

Planet-forming disks or *protoplanetary disks*, consist of gas and solid particles initially inherited from their parent molecular clouds in the interstellar medium. The extent to which these materials are reprocessed in the disk prior to and during planet formation is an active area of research (e.g., Cleeves et al. 2014; Pontoppidan and Blevins 2014; Eistrup et al. 2016). The composition of diffuse gas and sub-micron dust grains in the interstellar medium can be probed by ultraviolet to mm wavelengths, but extinction restricts denser regions to the longer wavelengths. At early stages of star formation, known as the Class 0 and Class I phases, protostars are embedded in envelopes made of the initial material from which they actively accrete (see Andre et al. 2000). The envelope material largely obscures their starlight and is difficult to disentangle emission originating in the forming disk from that originating in the envelope. Even in the later Class II phase, when the disk has formed and the star becomes visible, observation of the disk gas and dust composition is still not straightforward.

Different wavelength ranges probe different regions of the disk, dust grain sizes, and atomic and molecular transitions (see Andrews 2015; Bergin et al. 2007). Measurements from multiple instruments must therefore be combined in order to understand the chemical composition of the entire disk. Infrared telescopes, such as the *Spitzer Space Telescope* and the *James Webb Space Telescope* (JWST), detect hotter materials in the surface layers of the disk

and close to the central star. In addition, they are sensitive to scattered starlight off of micron-sized dust grains. Radio telescopes, such as the Atacama Large Millimeter/submillimeter Array (ALMA), probe the cooler, outer disk including rotational lines of molecules in addition to the thermal emission from larger, mm to cm-sized, dust (Dutrey et al. 2014). Denser regions of the inner disk midplane are hidden from view due to the optically-thick emission of the dust and some key molecular species.

Computational models are thus used, in part, to connect and interpret these observations that probe distinct regions of the protoplanetary disk. Given the dependence of chemistry on temperature, density, and radiation in the disk, both the physical conditions and chemical processes in the disk must be modeled to determine disk compositions (see Henning and Semenov 2013). Whereas early models of the solar nebula often relied on thermodynamic equilibrium and condensation sequences, chemical kinetics are primarily used in modern protoplanetary disks models. A numerical differential equation solver is used to estimate the evolution of chemical abundances based on a select set of chemical rate equations. Some of these rates are based on experimental data, but many must be extrapolated or approximated for the low density, low temperature environments (McElroy et al. 2013).

Together observations and computational modeling have allowed for the construction of volatile budgets in protoplanetary disks (Pontoppidan et al. 2014). In this context, *volatile* is used to refer to water and any substance that sublimates at lower temperatures than water. Observation-based estimates of the abundance of certain volatile elements in the gas phase may be low compared to expected cosmic abundance values. This is often attributed to the incorporation of these elements into solid dust grains and referred to as *depletion*. Depletion has been used to explain low H_2O and CO abundances observed in the outer disk gas (Du et al. 2017; Favre et al. 2013; McClure et al. 2016). However, these measurements have only been made for a small number of disks to date. Determining whether C and/or O depletion is common in protoplanetary disks will require observations of a larger and more diverse sample. The challenge for these analyses is that volatile element depletion is estimated relative to the H_2 content of the disk, but as a homonuclear diatomic molecule, H_2 is largely unobservable under most disk conditions. Given the uncertainties in total H_2 gas content, a variety of methods for estimating volatile depletion

are needed to approach this problem. Evaluating where volatile depletion occurs and what causes it will inform our understanding of the distribution of volatile elements such as carbon and nitrogen between gas- and solid-phase planet-forming materials throughout the disk.

1.2 The Composition of Solid Solar-System Bodies

The bodies present in our solar system serve as evidence of the initial materials present in the solar nebula. However, macroscopic bodies in disks are subjected to numerous environments and processes in the disk and during the accretion, alteration, and differentiation of planetary building-blocks that alter their volatile content (Marty 2012; Bergin et al. 2015). Final planet compositions are also affected by later gains and losses of volatiles through impacts on their surfaces. The best tracers of ancient solar system materials are primitive bodies including comets and certain classes of meteorites, carbonaceous chondrites in particular (see Sephton 2002). These bodies are thought to have undergone relatively little processing since their formation. Using a combination of remote observations, space missions, and laboratory analysis of samples that have arrived on Earth, the composition of a subset of these bodies, which serve as analogs of planetesimals and/or late-delivery volatile carriers, has been measured. When comparing available volatile element measurements of solid bodies throughout the solar system, two of the key trends that emerge are (1) rocky bodies in the inner solar system, namely the bulk silicate Earth and meteorites, lack carbon relative to the interstellar dust particles from which they formed (Lee et al. 2010), and (2) less of the total available nitrogen (based on solar abundances) is incorporated into solid bodies relative to carbon (Bergin et al. 2015). Identifying the planet/planetesimal-formation processes that are able to replicate these trends will constrain the possible formation pathways of the bodies in our solar system. The question of whether or not the composition of the Earth and our solar system is unique will depend on how common the necessary processes are in extrasolar systems. Moreover whether the dominant processes controlling solid body composition are general outcomes of planet formation in a disk or occur more stochastically and/or in localized environments will determine if these trends are universal.

Earth is currently the only planet known to host life. However, studies of ancient terrain on Mars suggest the presence of potentially habitable environments in the past (e.g., Grotzinger et al. 2014). Relative to Earth, Mars is

smaller, has a thinner atmosphere, and does not currently possess the conditions necessary for liquid water to flow in abundance on its surface. Mars represents a very different outcome of the terrestrial planet formation process. Ongoing missions, including the Mars Science Laboratory (MSL) Curiosity rover, are exploring the surface of Mars in search of biosignatures and indicators of past environmental conditions. One of the key science objectives of Curiosity's ChemCam instrument (Maurice et al. 2012) is to inventory volatile and life-enabling elements in the 3.6–3.8 billion year-old surfaces in Gale Crater (Thomson et al. 2011). ChemCam is also tracking the presence of salts, which trace aqueous chemistry and environmental conditions including acidity of past fluids and have been detected in martian basins (see Ehlmann and Edwards 2014). Investigating the evolution of Mars and determining whether habitable environments exist or ever existed on the planet will significantly contribute to our understanding of the range of outcomes of terrestrial planet formation (Ehlmann et al. 2016).

1.3 Thesis Chapter Summaries

In this thesis, I investigate elements that are essential for life on Earth and/or indicators of habitable environments. I use chemical modeling and ALMA observations to investigate the evolution of the bulk carbon and nitrogen reservoirs in circumstellar disks. In addition, I analyze laser-induced breakdown spectroscopy (LIBS) spectra to advance the tracking of salts on the surface of Mars via emission lines from carbon, sulfur, and chlorine.

Following the introduction, Chapter 2 seeks to explain the low carbon abundances observed in meteorites and the bulk silicate Earth relative to the interstellar dust that seeded their formation. Destruction of solid, refractory carbon grains in disks via oxidation and UV photolysis is modeled in a passively-heated and uniformly turbulent disk around a T-Tauri star. Grain growth is found to severely limit the release of carbon under these conditions. Distinct disk environments present earlier in the disk lifetime may be needed to enhance the loss of carbon from solid grains.

Chapter 3 investigates a nitrogen-based tracer, N_2H^+, as a supplement to CO in determining the gas masses of disks. For older sources in particular, accurate masses are crucial for characterizing the timescales of gas dissipation and gas accretion by growing giant planets. ALMA detections of N_2H^+ in two

5–11 Myr-old disks in the Upper Scorpius region indicate the presence of precursor ionized H_2 gas in these mature disks. Relative to previously-observed, gas-rich and CO-bright disks, the Upper Sco disks have enhanced N_2H^+/CO flux ratios. These N_2H^+ measurements provide additional constraints regarding the disk mass and CO abundance of the observed sources in Upper Sco. Based on a set of thermo-chemical disk models, the observed N_2H^+/CO flux ratios in Upper Sco can be explained by selective depletion of CO relative to N_2 and H_2 in the disk gas and are inconsistent with low (gas-to-dust mass ratios < 100) H_2 disk masses without CO depletion.

Chapter 4 furthers the analysis of one Upper Sco disk from Chapter 3. The potential to constrain the mass of this disk is explored using the following combination of strategically selected gas tracers: N_2H^+, HCO^+, and $C^{18}O$. A grid of models varying disk mass, CO abundance, and cosmic-ray ionization rates is used to determine how the emission of the selected gas tracers depends on these parameters. The ratio of optically thin $N_2H^+/C^{18}O$ emission constrains the CO abundance of the disk while the fluxes of individual species provide mass sensitivity. However, the ionization level of the disk cannot be uniquely constrained using this set of tracers and influences the CO abundance and disk mass determinations.

Chapter 5 explores the volatile carbon chemistry of the inner disk, including the terrestrial-planet-forming region in the disk midplane. In sources where the outer disk gas appears to be depleted in CO relative to total H_2, it has been suggested that CO could be converted into less volatile carbon carriers. After entering the hotter and denser inner disk, the fate of these carriers is modeled in Chapter 5, including the release of these carriers into the gas once vaporization conditions are reached and subsequent chemical processing. Carbon is rapidly transferred from the outer disk carriers to CO in optically thin disk regions near the disk surface, consistent with infrared observations. Inefficient vertical mixing could result in the preservation of compositions unique to each carrier in the disk midplane. However, the optical depth of the dust in these dense regions will likely inhibit direct observations of the volatile carbon reservoirs in the terrestrial-planet-forming region by JWST.

Chapter 6 evaluates the ability of the Laser-Induced Breakdown Spectroscopy (LIBS) instrument ChemCam on the Mars rover Curiosity to detect salts, which are indicators of past environmental conditions. LIBS analysis is per-

formed on a set of sample pellets created with decreasing concentrations of salt in a background of basalt in order to test for salt detections in materials with compositions relevant to the martian surface. Elemental emission lines of chlorine, carbon, and sulfur that respond to changes in chloride, carbonate, and sulfate salt concentrations, respectively, are identified. These select line are then used to determine ChemCam detection limits for these salts under Mars-like conditions. Chlorine lines are the most readily usable for quantification and detected in samples with $\gtrsim$5–10 wt.% chloride, whereas carbon and sulfur lines were more difficult to measure without interference and their detection often required higher salt concentrations. This work is applicable to future exploration of martian surfaces with ChemCam.

Chapter 7 provides concluding thoughts and future directions.

REFERENCES

P. Andre, D. Ward-Thompson, and M. Barsony. From Prestellar Cores to Protostars: the Initial Conditions of Star Formation. In V. Mannings, A. P. Boss, and S. S. Russell, editors, *Protostars and Planets IV*, page 59, May 2000.

Sean M. Andrews. Observations of Solids in Protoplanetary Disks. *Publications of the Astronomical Society of the Pacific*, 127(956):961, Oct 2015. doi: 10.1086/683178.

E. A. Bergin, Y. Aikawa, G. A. Blake, and E. F. van Dishoeck. The Chemical Evolution of Protoplanetary Disks. *Protostars and Planets V*, pages 751–766, 2007.

E. A. Bergin, G. A. Blake, F. Ciesla, M. M. Hirschmann, and J. Li. Tracing the ingredients for a habitable earth from interstellar space through planet formation. *Proceedings of the National Academy of Science*, 112:8965–8970, July 2015. doi: 10.1073/pnas.1500954112.

L. I. Cleeves, E. A. Bergin, C. M. O. '. Alexander, F. Du, D. Graninger, K. I. Öberg, and T. J. Harries. The ancient heritage of water ice in the solar system. *Science*, 345:1590–1593, September 2014. doi: 10.1126/science.1258055.

F. Du, E. A. Bergin, M. Hogerheijde, E. F. van Dishoeck, G. Blake, S. Bruderer, I. Cleeves, C. Dominik, D. Fedele, D. C. Lis, G. Melnick, D. Neufeld, J. Pearson, and U. Yıldız. Survey of Cold Water Lines in Protoplanetary Disks: Indications of Systematic Volatile Depletion. *ApJ*, 842:98, June 2017. doi: 10.3847/1538-4357/aa70ee.

A. Dutrey, D. Semenov, E. Chapillon, U. Gorti, S. Guilloteau, F. Hersant, M. Hogerheijde, M. Hughes, G. Meeus, H. Nomura, V. Piétu, C. Qi, and V. Wakelam. Physical and Chemical Structure of Planet-Forming Disks Probed by Millimeter Observations and Modeling. *Protostars and Planets VI*, pages 317–338, 2014. doi: 10.2458/azu_uapress_9780816531240-ch014.

B. L. Ehlmann and C. S. Edwards. Mineralogy of the Martian Surface. *Annual Review of Earth and Planetary Sciences*, 42:291–315, May 2014. doi: 10.1146/annurev-earth-060313-055024.

B. L. Ehlmann, F. S. Anderson, J. Andrews-Hanna, D. C. Catling, P. R. Christensen, B. A. Cohen, C. D. Dressing, C. S. Edwards, L. T. Elkins-Tanton, K. A. Farley, C. I. Fassett, W. W. Fischer, A. A. Fraeman, M. P. Golombek, V. E. Hamilton, A. G. Hayes, C. D. K. Herd, B. Horgan, R. Hu, B. M. Jakosky, J. R. Johnson, J. F. Kasting, L. Kerber, K. M. Kinch, E. S. Kite,

H. A. Knutson, J. I. Lunine, P. R. Mahaffy, N. Mangold, F. M. McCubbin, J. F. Mustard, P. B. Niles, C. Quantin-Nataf, M. S. Rice, K. M. Stack, D. J. Stevenson, S. T. Stewart, M. J. Toplis, T. Usui, B. P. Weiss, S. C. Werner, R. D. Wordsworth, J. J. Wray, R. A. Yingst, Y. L. Yung, and K. J. Zahnle. The sustainability of habitability on terrestrial planets: Insights, questions, and needed measurements from Mars for understanding the evolution of Earth-like worlds. *Journal of Geophysical Research (Planets)*, 121: 1927–1961, October 2016. doi: 10.1002/2016JE005134.

C. Eistrup, C. Walsh, and E. F. van Dishoeck. Setting the volatile composition of (exo)planet-building material. Does chemical evolution in disk midplanes matter? *A&A*, 595:A83, November 2016. doi: 10.1051/0004-6361/201628509.

C. Favre, L. I. Cleeves, E. A. Bergin, C. Qi, and G. A. Blake. A Significantly Low CO Abundance toward the TW Hya Protoplanetary Disk: A Path to Active Carbon Chemistry? *ApJ*, 776:L38, October 2013. doi: 10.1088/2041-8205/776/2/L38.

J. P. Grotzinger, D. Y. Sumner, L. C. Kah, K. Stack, S. Gupta, L. Edgar, D. Rubin, K. Lewis, J. Schieber, N. Mangold, and et al. A Habitable Fluvio-Lacustrine Environment at Yellowknife Bay, Gale Crater, Mars. *Science*, 343 (27):1242777, January 2014. doi: 10.1126/science.1242777.

T. Henning and D. Semenov. Chemistry in Protoplanetary Disks. *Chemical Reviews*, 113:9016–9042, December 2013. doi: 10.1021/cr400128p.

Andrew W. Howard, Roberto Sanchis-Ojeda, Geoffrey W. Marcy, John Asher Johnson, Joshua N. Winn, Howard Isaacson, Debra A. Fischer, Benjamin J. Fulton, Evan Sinukoff, and Jonathan J. Fortney. A rocky composition for an Earth-sized exoplanet. *Nature*, 503(7476):381–384, Nov 2013. doi: 10.1038/nature12767.

J. F. Kasting, D. P. Whitmire, and R. T. Reynolds. Habitable Zones around Main Sequence Stars. *Icarus*, 101:108–128, January 1993. doi: 10.1006/icar.1993.1010.

J.-E. Lee, E. A. Bergin, and H. Nomura. The Solar Nebula on Fire: A Solution to the Carbon Deficit in the Inner Solar System. *ApJ*, 710:L21–L25, February 2010. doi: 10.1088/2041-8205/710/1/L21.

B. Marty. The origins and concentrations of water, carbon, nitrogen and noble gases on Earth. *Earth and Planetary Science Letters*, 313:56–66, January 2012. doi: 10.1016/j.epsl.2011.10.040.

S. Maurice, R. C. Wiens, M. Saccoccio, B. Barraclough, O. Gasnault, O. Forni, N. Mangold, D. Baratoux, S. Bender, G. Berger, J. Bernardin, M. Berthé, N. Bridges, D. Blaney, M. Bouyé, P. Caïs, B. Clark, S. Clegg, A. Cousin,

D. Cremers, A. Cros, L. DeFlores, C. Derycke, B. Dingler, G. Dromart, B. Dubois, M. Dupieux, E. Durand, L. d'Uston, C. Fabre, B. Faure, A. Gaboriaud, T. Gharsa, K. Herkenhoff, E. Kan, L. Kirkland, D. Kouach, J.-L. Lacour, Y. Langevin, J. Lasue, S. Le Mouélic, M. Lescure, E. Lewin, D. Limonadi, G. Manhès, P. Mauchien, C. McKay, P.-Y. Meslin, Y. Michel, E. Miller, H. E. Newsom, G. Orttner, A. Paillet, L. Parès, Y. Parot, R. Pérez, P. Pinet, F. Poitrasson, B. Quertier, B. Sallé, C. Sotin, V. Sautter, H. Séran, J. J. Simmonds, J.-B. Sirven, R. Stiglich, N. Striebig, J.-J. Thocaven, M. J. Toplis, and D. Vaniman. The ChemCam Instrument Suite on the Mars Science Laboratory (MSL) Rover: Science Objectives and Mast Unit Description. *Space Science Reviews*, 170:95–166, September 2012. doi: 10.1007/s11214-012-9912-2.

M. K. McClure, E. A. Bergin, L. I. Cleeves, E. F. van Dishoeck, G. A. Blake, N. J. Evans, II, J. D. Green, T. Henning, K. I. Öberg, K. M. Pontoppidan, and C. Salyk. Mass Measurements in Protoplanetary Disks from Hydrogen Deuteride. *ApJ*, 831:167, November 2016. doi: 10.3847/0004-637X/831/2/167.

D. McElroy, C. Walsh, A. J. Markwick, M. A. Cordiner, K. Smith, and T. J. Millar. The UMIST database for astrochemistry 2012. *A&A*, 550:A36, February 2013. doi: 10.1051/0004-6361/201220465.

Francesco Pepe, Andrew Collier Cameron, David W. Latham, Emilio Molinari, Stéphane Udry, Aldo S. Bonomo, Lars A. Buchhave, David Charbonneau, Rosario Cosentino, Courtney D. Dressing, Xavier Dumusque, Pedro Figueira, Aldo F. M. Fiorenzano, Sara Gettel, Avet Harutyunyan, Raphaëlle D. Haywood, Keith Horne, Mercedes Lopez-Morales, Christophe Lovis, Luca Malavolta, Michel Mayor, Giusi Micela, Fatemeh Motalebi, Valerio Nascimbeni, David Phillips, Giampaolo Piotto, Don Pollacco, Didier Queloz, Ken Rice, Dimitar Sasselov, Damien Ségransan, Alessandro Sozzetti, Andrew Szentgyorgyi, and Christopher A. Watson. An Earth-sized planet with an Earth-like density. *Nature*, 503(7476):377–380, Nov 2013. doi: 10.1038/nature12768.

K. M. Pontoppidan and S. M. Blevins. The chemistry of planet-forming regions is not interstellar. *Faraday Discussions*, 169:49–60, May 2014. doi: 10.1039/C3FD00141E.

K. M. Pontoppidan, C. Salyk, E. A. Bergin, S. Brittain, B. Marty, O. Mousis, and K. I. Öberg. Volatiles in Protoplanetary Disks. *Protostars and Planets VI*, pages 363–385, 2014. doi: 10.2458/azu_uapress_9780816531240-ch016.

Mark A. Sephton. Organic compounds in carbonaceous meteorites. *Nat. Prod. Rep.*, 19:292–311, 2002. doi: 10.1039/B103775G. URL `http://dx.doi.org/10.1039/B103775G`.

B. J. Thomson, N. T. Bridges, R. Milliken, A. Baldridge, S. J. Hook, J. K. Crowley, G. M. Marion, C. R. de Souza Filho, A. J. Brown, and C. M. Weitz. Constraints on the origin and evolution of the layered mound in Gale Crater, Mars using Mars Reconnaissance Orbiter data. *Icarus*, 214: 413–432, August 2011. doi: 10.1016/j.icarus.2011.05.002.

Chapter 2

DESTRUCTION OF REFRACTORY CARBON IN PROTOPLANETARY DISKS

Dana E. Anderson[1], Edwin A. Bergin[2], Geoffrey A. Blake[1], Fred J. Ciesla[3], Ruud Visser[4] & Jeong-Eun Lee[5]

[1]Division of Geological and Planetary Sciences, California Institute of Technology, 1200 E. California Blvd., Pasadena, CA 91125, USA

[2]Department of Astronomy, University of Michigan, 1085 S. University, Ann Arbor, MI 48109-1107, USA

[3]Department of Geophysical Sciences, The University of Chicago, 5734 South Ellis Ave., Chicago, IL 60637, USA

[4]European Southern Observatory, Karl-Schwarzschild-Str. 2, D-85748, Garching, Germany

[5]School of Space Research, Kyung Hee University, 1732, Deogyeong-daero, Giheung-gu, Yongin-si, Gyeonggi-do 17104, Korea

Abstract The Earth and other rocky bodies in the inner solar system contain significantly less carbon than the primordial materials that seeded their formation. These carbon-poor objects include the parent bodies of primitive meteorites, suggesting that at least one process responsible for solid-phase carbon depletion was active prior to the early stages of planet formation. Potential mechanisms include the erosion of carbonaceous materials by photons or atomic oxygen in the surface layers of the protoplanetary disk. Under photochemically generated favorable conditions, these reactions can deplete the near-surface abundance of carbon grains and polycyclic aromatic hydrocarbons by several orders of magnitude on short timescales relative to the lifetime of the disk out to radii of ∼20–100+ au from the central star depending on the form of refractory carbon present. Due to the reliance of destruction mechanisms on a high influx of photons, the extent of refractory carbon depletion is quite sensitive to the disk's internal radiation field. Dust transport within the disk is required to affect the composition of the midplane. In our current model of a passive, constant-α disk, where $\alpha = 0.01$, carbon grains can be turbulently lofted into the destructive surface layers and depleted out to radii of ∼3–10 au

for 0.1-1 µm grains. Smaller grains can be cleared out of the planet-forming region completely. Destruction may be more effective in an actively accreting disk or when considering individual grain trajectories in non-idealized disks.

2.1 Introduction

The earliest stages of planet formation begin within a primordial disk of gas and submicron-sized dust grains surrounding a young star, formed due to the conservation of angular momentum through the collapse of a dense core in a molecular cloud. This material inherited from the interstellar medium (ISM) experiences a range of physical conditions and chemical environments. The dust grains within the disk concentrate toward the midplane due to the gravitational pull from the central star over time, increasing their likelihood of interaction. Dust grain aggregates are thought to grow through collisions, forming bodies that are orders of magnitude larger in size than typical interstellar dust as part of the planet formation process (e.g., Weidenschilling and Cuzzi 1993).

Provided that the original grains are of approximately interstellar composition, the amount of carbon available at the onset of planet formation can be roughly estimated. The carbon-to-silicon abundance ratio of the ISM is similar to that of the solar photosphere, C/Si$\sim$10 (Bergin et al. 2015, hereinafter B15; Grevesse et al. 2010). About 60% of carbon in the ISM is present in an unidentified solid, and thus potentially refractory, form (Savage and Sembach 1996). Suggested components include graphite, amorphous carbon or hydrocarbon grains with a combination of aliphatic-rich and aromatic-rich components (Chiar et al. 2013; Jones et al. 2013), large organics, and/or polycyclic aromatic hydrocarbons (PAHs). Once in the protoplanetary disk, carbon retained in the gas phase is subject to accretion by the central star or gas-giant planets or else to dissipation, ultimately being largely cleared from the disk. Any remaining volatile carbon species would likely be found in the form of ices in only the cold outer regions of the disk. In contrast, one would expect more-refractory carbon sources with vaporization temperatures of 425–626 K (Pollack et al. 1994; Lodders 2003) to be readily available and incorporated into solid planetary bodies, including planetesimals, throughout the entire disk except for the very innermost radii ($\lesssim$0.5 au from the central star, D'Alessio et al. 2005) and the directly irradiated surface. However, observations of rocky bodies in our solar system reveal a significant depletion in carbon compared to

the progenitorial interstellar dust (see Table 2.1; Geiss 1987; Lee et al. 2010; Pontoppidan et al. 2014; B15).

Table 2.1:
Bulk C/Si in Solar-system Bodies

Source	C/Si
ISM (dust)	6
Earth (BSE)	0.001
Meteorites (CI, CM)	0.4–0.7
Meteorites (CO, CV)	0.07–0.08
Comets (Halley, dust)	6
Comets (Halley, gas + dust)	8
Comets (Sun-grazing)	0.08–0.2
Interplanetary Dust Particles (IDPs)	2

Note.—See Bergin et al. (2015) and sources therein

The C/Si ratio of the bulk silicate Earth (BSE; the entire Earth, including the oceans and atmosphere, excluding the core) is about four orders of magnitude lower than that of the interstellar dust that seeded its formation (B15). This depletion of carbon could be the result of various events throughout Earth's formation and early stages, including devolatilization during processing of accreted material or impact events and sequestration of carbon via core formation (see B15 and references therein). However, carbonaceous chondrites, some of the most primitive materials known in our solar system, also exhibit carbon depletions (by one to two orders of magnitude; Wasson and Kallemeyn 1988) relative to the interstellar value. This suggests that a significant amount of the refractory carbon, which would have otherwise been incorporated into these solid bodies at a level of $\sim 6\times$ that of silicon, was destroyed early in the solar system's history and prior to the formation of rocky planets and differentiated planetesimals.

Not all solid bodies in our solar system are carbon poor. The dust of comet Halley has a C/Si ratio similar to that of the ISM (Pontoppidan et al. 2014; B15) and anhydrous interplanetary dust particles (IDPs), argued to be of cometary origin (Messenger et al. 2006), also have high carbon content. The

increased carbon retention by these outer-solar-system bodies cannot be explained by volatile ices alone; at least 50% of the carbon in comets is thought to be in refractory form (B15). Unlike Halley, the Sun-grazing comets resemble carbonaceous chondrites in terms of carbon abundance. These differences suggest that the mechanism responsible for refractory carbon destruction did not operate uniformly throughout the solar system and may have been less active in some comet-forming regions.

Evidence for carbon-deficient bodies is also found beyond our solar system. Spectra of polluted white dwarf atmospheres provide an opportunity to view the chemical composition of extrasolar planestimals. The strong gravitational forces of white dwarfs are expected to deplete heavier elements from their photospheres on relatively short timescales. Therefore, heavy elements observed in the atmospheres of white dwarfs are believed to have originated in rocky bodies that are destroyed near the tidal radius and accreted by the star (Zuckerman et al. 2007; Veras and Gänsicke 2015). Elemental measurements reveal these bodies to be carbon-poor with C/Fe ratios similar to those measured in chondritic meteorites in our own solar system (Jura and Young 2014; Farihi et al. 2016; Wilson et al. 2016).

Explaining the C/Si record of solid bodies in the solar system requires a mechanism that (1) selectively removes refractory carbon from the condensed phase while leaving silicates intact, (2) operates prior to the formation of the parent bodies of meteorites, (3) accounts for a range in carbon content among different solar-system bodies, and (4) may be a common process that is not unique to the specific conditions of our solar system. Once the disk enters the passive state, meaning that it is no longer accreting material from the interstellar cloud and is heated mainly by irradiation from the central star, vaporization of refractory carbon will be ineffective throughout most of the disk because the dust temperatures are too low (D'Alessio et al. 2005).

Alternative destruction mechanisms include those driven by energetic radiation. For example, photochemically activated oxidation of carbonaceous material via chemical reactions with O-bearing species, including OH and free atomic O, which can erode the surface of carbon grains releasing carbon into the gas phase (Bauer et al. 1997; Finocchi et al. 1997; Gail 2001, 2002). Lee et al. (2010) calculated that combustion through reactions with atomic O, which is abundant in the photochemically active surface layers of the disk,

can efficiently destroy carbon grains <10 µm in size and given sufficient vertical transport in the disk, potentially explain the observed carbon deficiencies of rocky bodies in our solar system. Direct photochemical destruction of refractory carbon sources, resulting in the ejection of small hydrocarbons, represents an additional destruction mechanism. Alata et al. (2014, 2015) experimentally investigated the rate of vacuum ultraviolet (VUV) photolysis for interstellar hydrogenated amorphous carbon (HAC) analogs; whereas the ability of large aromatic carbon species to survive photodissociation has been evaluated through modeling by Visser et al. (2007). Siebenmorgen and Krügel (2010) and Siebenmorgen and Heymann (2012) also explored the potential for PAH destruction via more energetic extreme ultraviolet (EUV) and X-ray photons.

Here we expand upon the work of Lee et al. (2010), exploring the possibility that refractory carbon sources in the disk can be depleted before grains grow to sufficient sizes and while most of the solid mass remains in 0.1–1 µm baseline seed particles. We use a full chemical disk model to explore the oxidation and photochemical destruction of two sources of refractory carbon: carbon grains and PAHs. With this model, we attempt to estimate the efficacy of these mechanisms throughout the disk and determine the radial distance to which carbon can be depleted for comparison with our own solar system. Section 2.2 describes the disk model used in our analysis, while Section 2.3 provides the results of the model and subsequent analysis of the capabilities of the proposed destruction mechanisms. A discussion of the results is presented in Section 2.4 followed by a final summary in Section 2.5.

2.2 Model

Here we model a static, passive protoplanetary disk around a T-Tauri star, a young, low-mass star thought to be similar to our early Sun. Chemistry within the disk is predicted by solving a set of ordinary differential equations describing the chemical reaction rates of the system. To the standard chemical model, we add a source of refractory carbon, either carbon grains or PAHs, and appropriate destruction mechanisms in order to track the abundance of these sources throughout the disk.

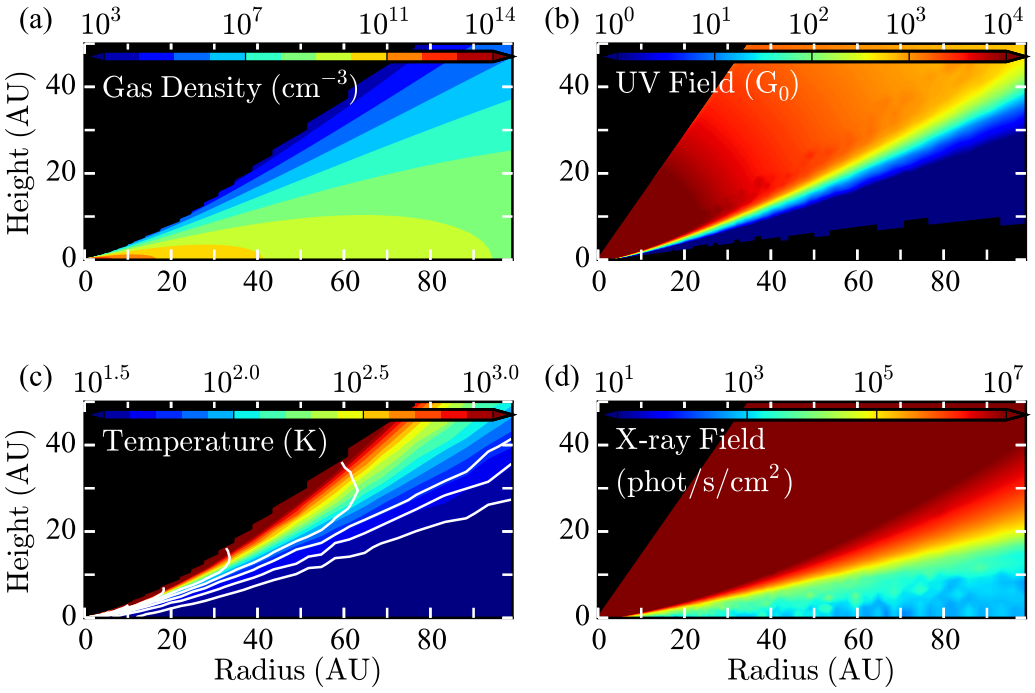

Figure 2.1: Physical conditions for our disk model: gas density (a), integrated UV flux, 930–2000 Å (b), gas temperature with dust temperature shown in white contours increasing in intervals of $10^{0.1}$K from $10^{1.5}$K in the midplane (c), and integrated X-ray flux, 1–20 keV (d) out to 100 au from the central star.

2.2.1 Physical Conditions

To provide the conditions representative of a disk surrounding a typical T-Tauri star, we use a physical disk model similar to that of Cleeves et al. (2013, 2015). The model is two-dimensional and azimuthally symmetric. To approximate the dust distribution of an early disk, prior to substantial grain growth and sequestration of mass in the midplane, we include a single population of small dust (radii $\leq$1–10 µm) that follows the distribution of the gas. The dust composition is 80% astronomical silicates (Draine and Lee 1984) and 20% graphite. Although ice coatings on the dust may affect the resulting opacity (Ossenkopf and Henning 1994), the model assumes the general approximation of bare grain surfaces. Given our static model, these grains are considered only for calculating the physical conditions of the disk and are not directly included in the chemical reactions. This dust distribution therefore remains unchanged as we destroy carbon-bearing grains. The gas and dust share a fixed radial surface density profile described by a power law with an exponential cutoff,

$\Sigma_{gas}(R) = \Sigma_c(R/R_c)^{-1}\exp[-(R/R_c)]$ where $\Sigma_c = 3.1$ g cm^{-2} and $R_c = 135$ au from Cleeves et al. (2013), and are related by assuming a vertically integrated gas-to-dust mass ratio of 100. The total mass of the disk gas is 0.039 $M_\odot$.

The UV field, including the propagation of Ly α photons, and the X-ray radiation field within the disk were generated using a Monte Carlo radiative transfer code as described by Bethell and Bergin (2011b,a). The input UV spectrum is taken to be that observed for TW Hya (Herczeg et al. 2002, 2004). The modeled X-ray spectrum has a total luminosity of $10^{29.5}$ erg s^{-1} between 1–20 keV, corresponding to that of a typical T-Tauri star. The gas temperature is estimated based on the computed UV field and gas density distributions using the thermochemical models of Bruderer (2013), as described in Cleeves et al. (2015). Figure 2.1 shows the final density, temperature, and radiation distributions provided to the chemical model.

2.2.2 Chemical Network

The disk chemistry model combines the higher-temperature ($\lesssim$800 K) gas-phase network of Harada et al. (2010) with the gas-grain network of Fogel et al. (2011). In total, over 600 chemical species and nearly 7000 reactions are specified, including gas-phase reactions among ions, neutrals, and electrons; photodissociation; X-ray and cosmic-ray ionization; gas-grain interactions (freeze-out, sublimation, photodesorption, and cosmic-ray-induced desorption); and formation of OH, H_2O, and H_2 on grains. The model is run for radii from 0.25 to 100 au from the central star, divided into a grid of 42 logarithmically spaced radii each containing 45 linearly spaced vertical zones. With the exception of H_2 and CO self-shielding, which are considered throughout the vertical column, chemistry within each grid space is modeled independently. The disk model is static, with no mixing between grid spaces. To this chemical network, we added sources of refractory carbon as described in the following sections.

2.2.3 Sources of Refractory Carbon

Carbon Grains

The first source of refractory carbon included in our model is solid grains. Different grain sizes are considered, with radii of 0.01–10 µm. Sizes are larger than the average interstellar values to account for growth within the disk. Large, ∼1–10 µm, silicate grains have been observed in emission at 10 and 18 µm originating from the irradiated layers. Modeling the grains as hav-

ing compact, spherical structures provides an upper limit on the destruction timescale. However, during growth due to collisions the aggregate structures can become open. Laboratory experiments using dust analogs find that initial growth through collisions resulting in the sticking and freezing together of individual particles leads to the formation of fractal structures (Blum and Wurm 2008). In addition, interplanetary dust particles collected from Earth's atmosphere are described as typically being porous aggregates composed of $\sim 10^6$ grains (Brownlee 1979). To account for porosity in our modeled carbon grains, volume-enlargement factors from the collisional evolution simulations of Ormel et al. (2007) are used. The resulting porosities are assumed to be 0% for the 0.01 and 0.1 µm grains, 88% for the 1 µm grains, and 96% for the 10 µm grains. The porosity (ϕ) represents the percentage of the grain volume that is unoccupied. Compared to a compact configuration of atoms, a porous grain of the same size will only contain (100-ϕ)% of the amount of carbon.

Oxidation of these carbon grains is modeled based on the approach of Lee et al. (2010). An oxygen atom that collides with a carbon grain removes a single C atom to form gaseous CO. Oxidation by OH is also possible (Bauer et al. 1997; Finocchi et al. 1997; Gail 2001, 2002), but O is more abundant in the photoactive surface layers of the disk. The reaction occurs at a rate of $R_{ox} = n_{cgr} n_o \sigma v_o Y$, where n_{cgr} is the number density of carbon grains, n_o is the number density of oxygen atoms, σ is the cross-section of a carbon grain, v_o is the thermal velocity of an oxygen atom, and Y is the yield of the reaction (Draine 1979, $Y = 170 \exp[-4430/T_{gas}]$ if $T_{gas} > 440\,\mathrm{K}$ and $Y = 2.30 \exp[-2580/T_{gas}]$ if $T_{gas} \leq 440\,\mathrm{K}$). The abundance of carbon grains is determined by taking the initial abundance of refractory carbon and dividing it by the number of carbon atoms per grain, equal to $[\rho_{cgr} \frac{4}{3} \pi r^3 (100\% - \phi)]/m_c$ where ρ_{cgr} is taken to be the density of graphite, 2.24 g cm^{-3}; r is the grain radius; ϕ is the porosity; and m_c is the mass of a carbon atom.

Photolysis rates for carbon grains of amorphous structure are taken from Alata et al. (2014, 2015), who measured the production rates of hydrogen and small hydrocarbons released from a plasma-produced HAC surface irradiated by VUV photons. Methane was the C-bearing product of highest yield and is the sole product considered here. The rate is $R_{UV} = n_{cgr} \sigma Y_{CH_4} (\Phi_{ISRF}^{FUV}/1.69) F_{UV}$, where n_{cgr} and σ are the same as above, Y_{CH_4} is the photo-production yield of CH_4 per incoming photon ($\sim 8 \times 10^{-4}$), Φ_{ISRF}^{FUV} is the far ultraviolet (FUV) flux

of the interstellar radiation field divided by 1.69 to convert from the Draine to Habing values, and F_{UV} is the FUV flux relative to the interstellar value from the disk model. Here the term "photolysis" is used to refer to the photon-induced release of small hydrocarbons from the surface of a grain containing $\sim 10^6$ or more C atoms, distinct from the photodissociation of the PAHs, where the structure of a $\lesssim$100 C atom molecule is broken resulting in the loss of small hydrocarbons.

Small grains are also subject to destruction by higher energy, X-ray photons through heating to the point of sublimation or grain charging increasing electrostatic stress to the point of shattering. The conditions under which X-ray radiation will lead to grain destruction have been estimated by Fruchter et al. (2001) for emission from γ-ray bursts. X-ray emission from T-Tauri stars is dominated by 1–2 keV photons. The energy deposited by these photons will be insufficient to heat 0.01–10 µm grains above the sublimation temperature of refractory carbon throughout most of the disk (Najita et al. 2001). Shattering due to the buildup of electrostatic charge relies on successive interactions with X-ray photons. However, in the protoplanetary disk, grains will cycle between the surface and the midplane. Whereas X-ray ionization rates may dominate at the disk surface, in denser gas toward the midplane recombination with free electrons will be a competitive process potentially preventing the buildup of charge on grains. Cosmic rays and high-energy X-rays, if present in these dense layers, will be key sources of ionization in the inner disk resulting in the production of free electrons (Igea and Glassgold 1999; Cleeves et al. 2015). The susceptibility of silicate grains to shattering is slightly greater than that of carbonaceous grains Fruchter et al. (2001). Therefore, this mechanism would not selectively destroy carbonaceous grains and efficient reformation of silicate grains would be required to explain the observed composition of solar-system bodies. Further modeling is required to understand the effectiveness of X-rays in reducing refractory carbon abundances.

PAHs

PAHs represent the second source of refractory carbon included in our model. Refractory carbon is introduced initially as large, 50 C atom PAHs representative of interstellar species. For comparison of destruction rates versus PAH size, additional models start with 20 C atom PAHs to demonstrate the

breakdown of smaller PAHs after some initial destruction in the disk. As time progresses in the model, reactions with O, H, and OH dismantle the initial PAHs removing fragments containing ∼2 C atoms per reaction. Rates involving small PAHs from pyrene (16 C atoms) down to a single aromatic ring are from Wang and Frenklach (1997). Where necessary, reverse-reaction rate coefficients are calculated using the thermodynamic data they provided.[1] For larger PAHs, rates are taken as those of the analogous reaction (O, H, or OH) with benzene as is the case for pyrene, phenanthrene, and naphthalene in Wang and Frenklach (1997). Given that the specific structure of PAHs in astrophysical environments is largely unknown, the molecular structure of the large PAHs was not strictly considered aside from ensuring conservation of mass within the reaction network.

Visser et al. (2007) provide UV photodissociation rates resulting in the loss of two C atoms for PAHs of different sizes based on theoretical calculations. These rates incorporate the modulated UV field, specifically the FUV field, at each grid location in the disk. C_2H is successively removed to break down the larger PAHs and reaction products from the photodissociation of PAHs smaller than pyrene were selected to mimic the oxidation reaction pathways where appropriate.

The rate of photodissociation by X-ray photons follows Siebenmorgen and Krügel (2010) using the cross-section for PAHs from Siebenmorgen et al. (2004), $N_C \times C^{abs}$ where N_C is the number of carbon atoms per PAH and $C^{abs} \simeq 10^{-17} \times 20E^{2.2}$ cm^2 is the cross-section per carbon atom for photon energies (E) greater than 20 eV. The energy-dependent cross section is multiplied by the X-ray flux distribution at E integrated over E = 1–20 keV. X-ray photons carry enough energy such that a single interaction can dismantle an entire 50 C PAH. In this case, we assumed the products of the reaction to be small hydrocarbons in our reaction network containing four or fewer C atoms. However, the photodestruction of large PAHs via X-rays has not been characterized through laboratory experiments and the dispersion of energy from X-ray photons among different molecular processes is not well known. Given

[1]We derive the reverse-reaction rate coefficient from $k_r = k_f/K$, where the forward reaction rate coefficient provided is $k_f = AT^n \exp(-E/RT)$, and A, n, and the activation energy E are given by Wang and Frenklach (1997), R is the gas constant, and T is the gas temperature. The equilibrium constant is given by $K = \exp(-\Delta G/RT) = \exp(-\Delta H/RT + \Delta S/R)$ where ΔG, ΔH and ΔS are the change in the standard Gibbs free energy, enthalpy, and entropy of the reaction.

the uncertainty in how to define an X-ray photodissociation rate for large PAHs (Voit 1992; Micelotta et al. 2010), we also tested models where X-ray absorption resulted in the removal of C_2H (analogous to the network used for UV photodissociation of PAHs above) for reaction yields of 0.5 and 1.0.

The breakdown of PAHs with more than 60 C atoms may result in the production of fullerenes, such as C_{60}, that are highly stable and resistant to destruction. Berné et al. (2015) suggest that $\lesssim$1% of the instellar PAH abudance may be in the form of C_{60}. PAHs in the surface layers will likely have predominately neutral charge. Abundant PAH cations are not produced by the radiation field of T-Tauri stars (Visser et al. 2007) and PAH anions will only be present in denser regions of the disk toward the midplane. The inclusion of PAH formation reactions is not important since we found the formation of benzene (as a proxy) to be inefficient in comparison to the rate of PAH destruction under the conditions in our disk model.

Model Setup

At the onset of the model, carbon is divided between the refractory and volatile phases. Several iterations of the model were run with different initial forms for the refractory carbon. This phase is represented by either carbon grains of a single size and porosity (six different cases: R = 0.01, 0.1, 1, or 10 µm, and for the larger two sizes: porous or non-porous structures) or PAHs (two cases: initial PAHs of 50 or 20 C atoms in size). For the carbon grain scenarios, the total abundance of carbon ($\sim 2 \times 10^{-4}$ relative to H, about the solar value; Grevesse et al. 2010) is divided equally between the grains and the volatile phase. In the case of the PAHs, an abundance of 1.5×10^{-5} C relative to H, approximately the abundance observed in the ISM (Tielens 2005), is distributed among the 50 or 20 C molecules. Volatile species are set to 1×10^{-4} relative to H. Nearly all the volatile carbon is initially stored in CO (with minor amounts in CN, C, HCN, C^+, HCO^+, H_2CO, and C_2H). All chemical species are spread uniformly in abundance relative to H over the entire grid of the disk at the beginning of the model run. Radial and vertical mixing within the disk are not considered here.

2.3 Results

A chemical model of an irradiated (passive) protoplanetary disk is used to identify the regions where destruction of refractory carbon sources occurs. Further analysis of the timescales of grain transport and the distribution of grains within the disk allow for the estimation of the radial extent of refractory carbon depletion due to the mechanisms described here.

2.3.1 Regions of Active Refractory Carbon Destruction

The model described in Section 2.2 is used to identify the locations in the disk where oxidation and photochemical destruction could cause significant depletion of refractory carbon sources. Figures 2.2 and 2.3 show the abundance of refractory carbon remaining after running the model for 10^6 years, on the order of the lifetime of a protoplanetary disk. Each panel illustrates a vertical cross-section of the disk above the midplane with contours representing the level of depletion of a particular refractory carbon source (with an abundance relative to H of 10^{-4} representing zero depletion for the carbon grains and 1.5×10^{-5} likewise for the PAHs). Here the PAH abundance is considered to be the total abundance of all aromatic components larger than benzene in our model. As demonstrated in these panels, oxidation and photochemical destruction are only operative near the disk surface. Whereas oxidation is restricted to within a radius that depends fairly weakly on the size and nature of the refractory carbon sources, photochemical destruction can be unlimited in the radial direction out to at least 100 au.

Photochemical Destruction vs. Oxidation

In a passive disk, irradiation from the central star and the ISM produces environmental conditions—temperatures of at least a few 100 K and high atomic oxygen abundances—in the surface layers that allow oxidation to proceed at an appreciable rate. The exponential dependence of the chemical kinetics on the gas temperature is the main limiting factor toward the disk midplane. Additionally, the dominant carriers of oxygen vary within the vertical column at each radius. Atomic O is most abundant above the cool middle layers that are protected from stellar photons, where H_2O ice and other molecular forms dominate, and below the surface of the disk where at radii $\lesssim$10 au ionized O^+ begins to form. Radially, at a certain distance from the star the sufficiently dense layers of the disk no longer reach the required temperatures and atomic

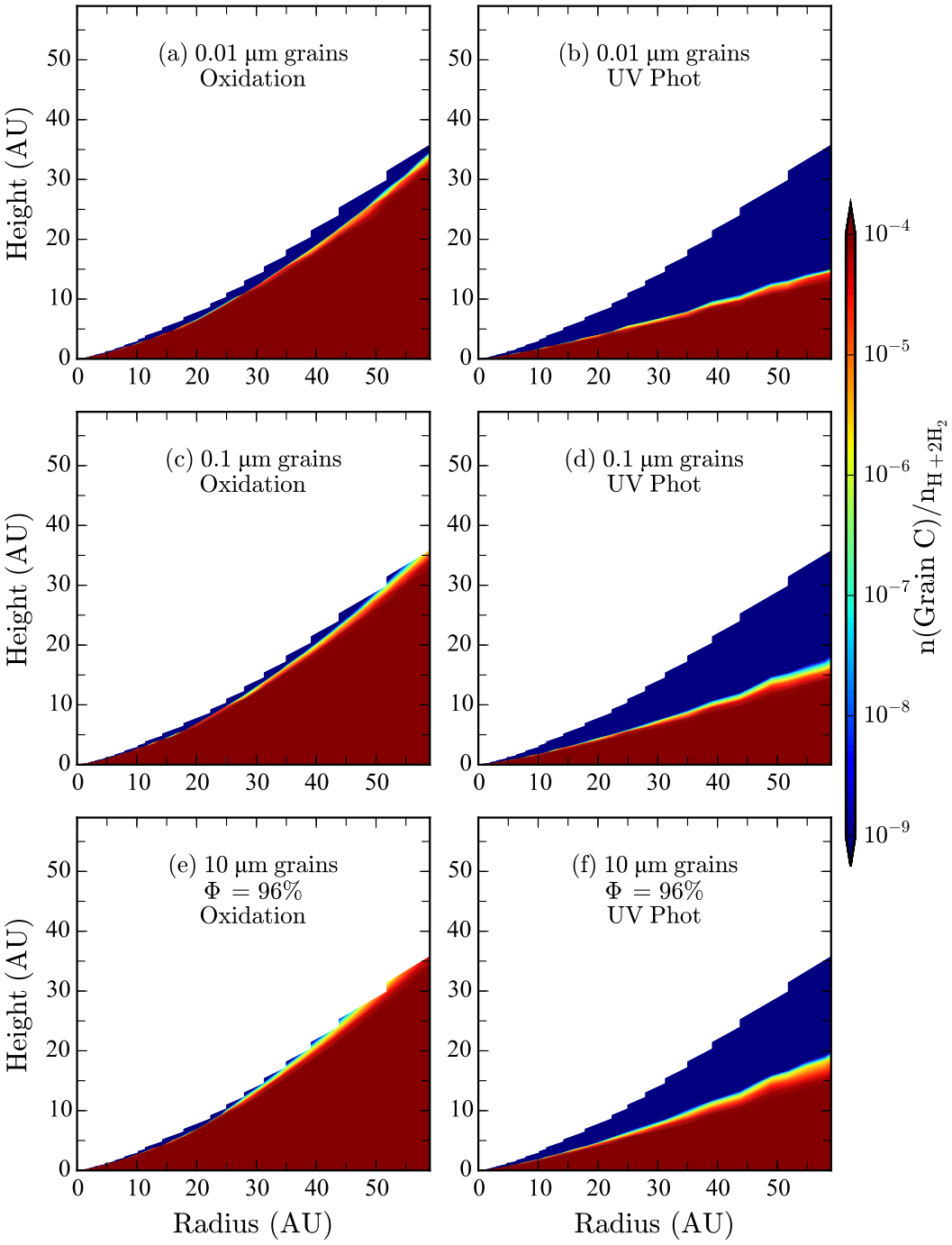

Figure 2.2: Vertical cross-sections of the protoplanetary disk above the mid-plane demonstrating the refractory carbon abundance relative to total hydrogen at 10^6 years for carbon grains with grain radii equal to 0.01 µm (a,b), 0.1 µm (c,d), and 10 µm with 96% porosity (e,f) including oxidation (a,c,e) and UV photolysis (b,d,f).

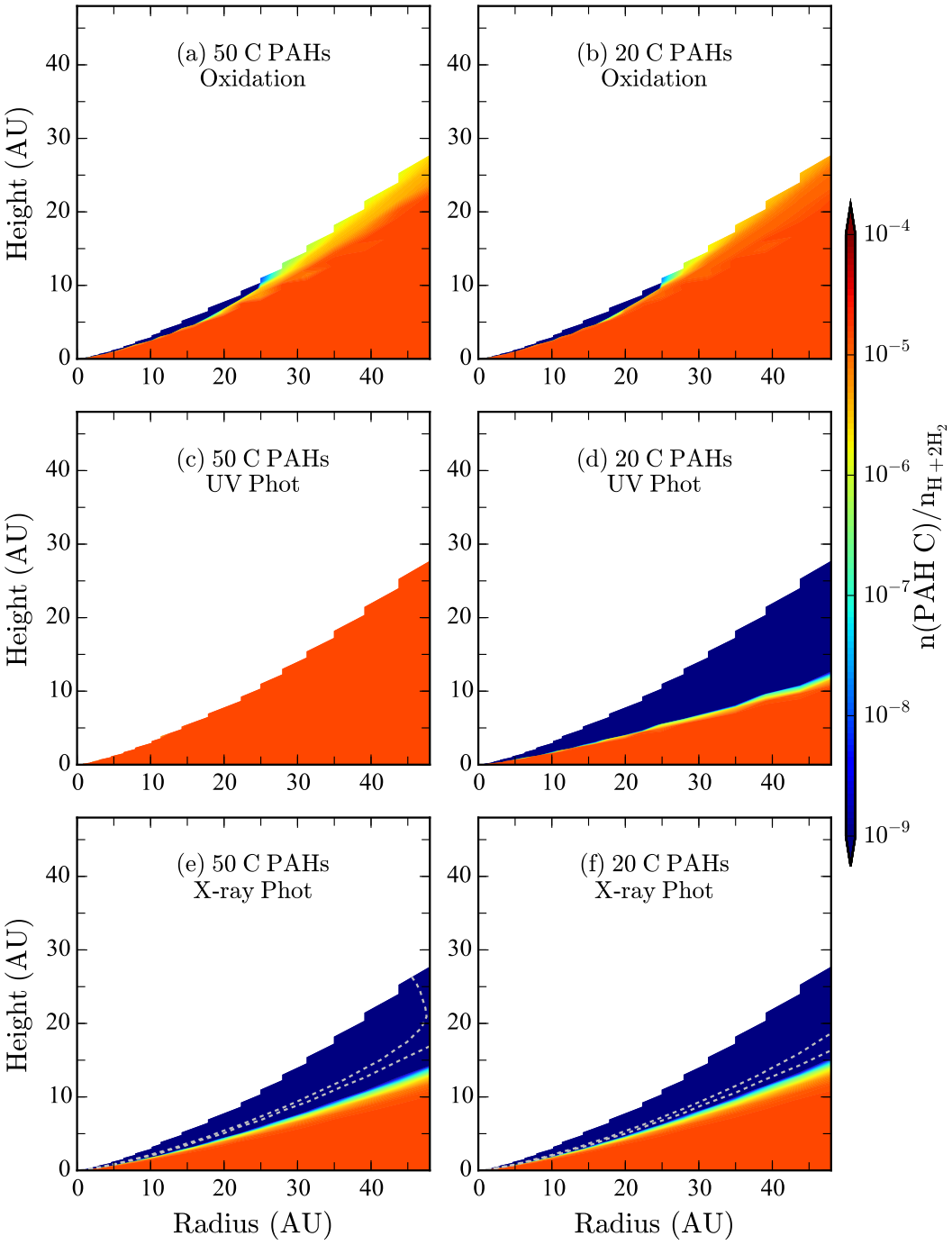

Figure 2.3: Vertical cross-sections of the protoplanetary disk above the midplane demonstrating the refractory carbon abundance relative to total hydrogen at 10^6 years for PAHs containing 50 C atoms (a,c,e) and 20 C atoms (b,d,f) including oxidation (a,b), UV photodissociation using the rates of Visser et al. (2007, c, d), and X-ray photodissociation using the rates of Siebenmorgen and Krügel (2010, e, f). Dashed contours indicate the abundances of 10^{-6} and 10^{-9} for successive removal of C_2H by X-ray photodissociation of 50 C PAHs (e).

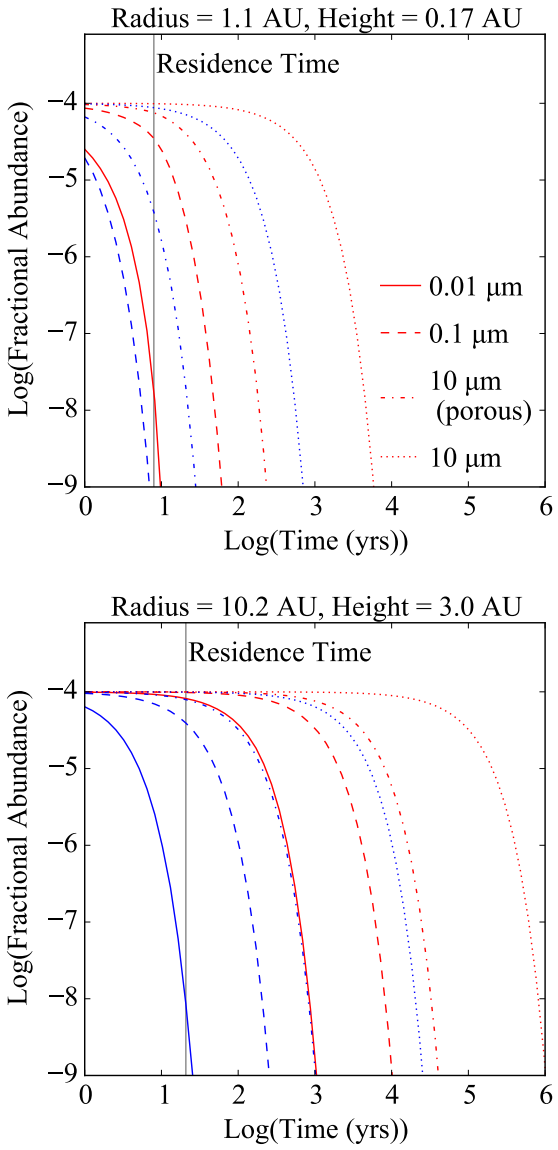

Figure 2.4: Abundance of refractory carbon in grains over time in the middle of the destructive regions at radii of 1 au (upper plot) and 10 au (lower plot) including destruction by oxidation (red) and photolysis (blue). For comparison, the vertical line denotes the amount of time grains spend exposed to these conditions throughout the disk lifetime. At 1.1 au, the 0.01 µm grains are depleted within the first time step due to UV photolysis.

oxygen abundances to activate oxidation and the reaction shuts off. This radial cutoff occurs at ∼20–65 au depending on the refractory carbon source.

Photolysis occurs over a larger region of the disk due to the lack of temperature dependence in the reaction rate. The layer to which UV photons reach extends below the hot region where oxidation can occur and to larger radii in the disk. However, the reaction is limited by the modulation of the UV field by disk material, leaving the midplane of the disk shielded. UV photolysis of HAC grains occurs down to interstellar UV levels, implying the need for reformation of carbonaceous grains in the ISM (e.g., Jones and Nuth 2011), if they are

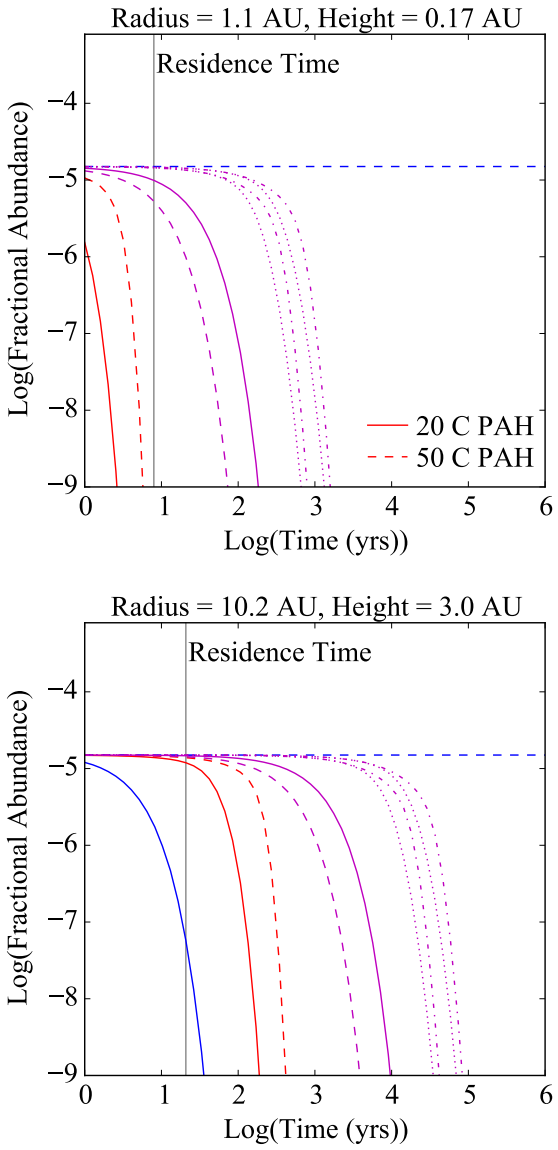

Figure 2.5: Abundance of refractory carbon in PAHs over time in the middle of the destructive regions at radii of 1 au (upper plot) and 10 au (lower plot) including destruction by oxidation (red), UV photodissociation (blue), and X-ray photodissociation (magenta). For comparison, the vertical line denotes the amount of time grains spend exposed to these conditions throughout the disk lifetime. At 1.1 au, the 20 C PAHs are depleted within the first time step due to UV photodissociation. Rates of X-ray photodissociation are shown for entire PAH destruction by individual X-rays (solid lines for 20 C PAHs, dashed lines for 50 C PAHs) and successive removal of C_2H by X-rays with a yield of 1.0 and 0.5 (dotted lines for 20 C PAHs, dash-dotted lines for 50 C PAHs).

indeed of HAC composition as predicted by current interstellar grain models (Chiar et al. 2013; Jones et al. 2013). UV photodissociation is only efficient for small PAHs, occurring within the disk lifetime for sizes $\lesssim$24 C atoms and FUV photons as shown by Visser et al. (2007). Significant depletion, by four orders of magnitude or greater in total refractory C abundance, occurs deeper in the disk for UV photodissociation on these small PAHs than for oxidation or X-ray photodissociation. However, the vertical cutoff for photodissociation of PAHs by X-rays is not as sharply defined as that in the UV. Minor amounts of depletion, less than 0.01% of the total refractory C abundance, continue

deeper into the disk approaching the midplane.

The timescales for UV photochemical destruction are faster than those of oxidation for all carbon grain sizes and for small PAHs (Figures 2.4 and 2.5). In the case of the PAHs, UV photodissociation will accelerate the depletion of small PAHs following the destruction of 50 C PAHs via oxidation or X-ray photodissociation. In comparison to X-ray photodissociation, oxidation of PAHs occurs over a smaller region of the disk, but at a faster rate.

Carbon Grain and PAH Sizes

The extent of refractory carbon depletion has some dependence on the size and structure of the carbon sources. Fig. 2.4 shows the abundance of the different carbon grains over time at radii of 1 and 10 au in the surface layers where rapid oxidation and photolysis are occurring. Larger and less porous grains are destroyed more slowly because they have a smaller [cross-section]/[occupied volume] ratio reducing the frequency of their interaction with O atoms and UV photons. For the smaller or more porous grains, faster destruction rates facilitate depletion over a larger range of vertical heights and, in the case of oxidation, radii. The cutoff in disk radius for oxidation of different grain sizes decreases from ∼65 au to ∼45 au for grain radii from 0.01 to 10 (porous) µm in panels (a), (c), and (e) of Fig. 2.2 and down to ∼20 au for 10 µm compact grains. There is no such radial cutoff within 100 au for photolysis until grain sizes of 10 µm are reached, where depletion by a factor of 100 occurs beyond 100 au but depletion by 10^4 only occurs out to 80 au. In addition, the vertical extent of depletion is slightly less for larger grains at large radii. At distances of 10s of au, depletion occurs down to ∼4 scale heights above the midplane for 0.01 µm grains vs. just above 5 scale heights for porous 10 µm grains.

Within 10^6 years, oxidation depletes abundances of the initial 20 or 50 C PAHs by several orders of magnitude at radii out to 100 au in the surface layers of the disk. However, this is only the first step. Breakdown of the subsequent PAH products depends on the reaction rates of each of the following steps in the network. PAH depletion occurs rapidly in the inner few au for all species. Further out in the disk where conditions become less ideal for oxidation, the results will be more dependent on the chemical pathways included in the model. For the network selected here, in 10^6 years, all PAH species are cleared from the surface layers as shown in Fig. 2.3 for radii $\lesssim$30 au regardless of initial

size. However, where oxidation operates, the total abundance of C in PAHs is lower when the PAHs start out in 50 C molecules as can be observed by comparing the surface layers of the disk in panels (a) and (b) of Fig. 2.3. Since the rate-limiting steps in the breakdown process are the destruction of the smaller, 2- or 3-ring-containing species, the refractory carbon piles up in these small PAHs. In breaking down the larger 50 C PAHs, a larger portion of the total carbon has been removed in the form of small fragments before reaching these bottleneck species. Starting with larger PAHs does slow down the rate of carbon depletion by oxidation, as shown in Fig. 2.5.

UV photodissociation here only affects small PAHs. Large PAHs (greater than 24 carbon atoms, Visser et al. 2007) cannot be photodissociated by FUV radiation within the disk lifetime and therefore can only be broken down by oxidation or more energetic photons. The inclusion of EUV photons would result in the break down of 50 C PAHs in addition to faster depletion of 20 C PAHs in the uppermost layers of the disk, about 1–2 scale heights above the current vertical cutoff for FUV photodissociation (Siebenmorgen and Krügel 2010). X-ray photodissociation rates are slower than those for FUV photons. In the case of the complete dissociation of a PAH molecule by a single X-ray photon, destruction occurs faster (Fig. 2.5) for the larger PAHs due to the dependence of the absorption cross-section on the number of carbon atoms. PAH destruction rates are decreased by an order of magnitude when considering the successive removal of C_2H compared to complete dissociation of the PAH molecule (Fig. 2.5), which also limits the radial and vertical extent of PAH depletion (Fig. 2.3).

Chemical Modeling Summary

Figures 2.4 and 2.5 demonstrate that under favorable conditions present in the surface layers of the disk, depletion of refractory carbon sources occurs very rapidly compared to the disk lifetime. In terms of the chemistry, the amount of refractory carbon destroyed in these regions can exceed that required to explain the disparity among carbonaceous chondrites and the Earth relative to the interstellar dust (1–2 and $\sim$4 orders of magnitude, respectively). As shown in Fig. 2.2 and 2.3, these carbon-deficient regions in the surface layers reach out beyond the terrestrial-planet- and asteroid-forming regimes of the disk. However, material in the midplane remains largely unaffected by oxidation

and photochemical destruction in the static chemical model.

2.3.2 Radial Extent of Refractory Carbon Depletion

The conditions required for oxidation and photochemical destruction become less attainable (higher up in the disk) at larger distances from the central star suggesting that there may be a radial cutoff beyond which the mechanism is ineffective and refractory carbon will remain in the condensed phase at abundances similar to the interstellar value. In contrast to snow lines, this boundary, akin to the "soot line" described by Kress et al. (2010) for the abundance of PAHs, would mark the location of an irreversible transition. Once carbon in the inner disk enters the gas phase it will likely remain volatile given the limited mechanisms available to return it to a more-refractory state. The high abundance of refractory carbon in the ISM will cause a potentially drastic change in the carbon chemistry from one side of the transition region, where nearly all the cosmically available carbon would be in volatile form and—in the warm inner disk—largely removed from the planetesimal formation process, to the other, where about half of this carbon would exist in a more-refractory phase and be available to be incorporated into forming planetesimals. Therefore, estimating the radial extent of carbon depletion mechanisms such as oxidation and photochemical destruction may allow us to relate the chemistry of the disk to the carbon content of solar-system bodies.

As shown in Section 2.3, active oxidation and photochemical destruction of refractory carbon is limited to the photochemically active surface layers. However, the majority of the disk material is concentrated in the midplane and it is in this region that planet formation occurs. As suggested by Lee et al. (2010), mixing within the disk could introduce dust from these deeper layers into the destructive regions causing depletion throughout the vertical column. Turbulent motion is thought to counteract dust grain settling, continually stirring up disk material and maintaining the presence of grains in layers high above the midplane (Weidenschilling and Cuzzi 1993; Dullemond and Dominik 2004; Ciesla 2010). Fully assessing the extent to which destruction in the surface layers could affect material in the midplane requires a treatment of dust evolution and transport including processes such as growth, settling, fragmentation, and radial drift. The extent will further depend upon the underlying mechanism driving disk accretion and causing the turbulent motions throughout the disk. The dominant radial flow in the disk midplane is inward, but there is

also evidence for outward transport in the solar nebula (e.g., crystalline silicates found in the comet Wild 2 by the NASA Stardust mission, Brownlee et al. 2006) that could carry carbon-depleted materials from close to the Sun to larger radii. Given these complexities, here we start by only considering the limit where vertical motion is more rapid than this radial transport and where the turbulence in the disk is characterized by a constant value of the Shakura & Sunyaev α parameter ranging from 10^{-4} to 10^{-2} (Hartmann et al. 1998; Mulders and Dominik 2012).

The vertical height to which grains can be suspended due to turbulent motion is estimated by comparing the timescale of grain stirring to that of grain settling throughout the disk as described by Dullemond and Dominik (2004) and used by Lee et al. (2010). The stirring timescale ($t_{stir} = \mathrm{Sc}(z)z^2/[\alpha c_s H]$) describes the amount of time required for grains to diffuse to a height z above the midplane, effectively describing the time required for components within a vertical column between the midplane and z to become well-mixed. The Schmidt number, Scz, is assumed to equal one such that the small particles considered here are perfectly coupled to the turbulence. This number can greatly exceed one in the low-density, upper layers of the disk making the stirring timescale used here a lower limit. In addition to the height above the midplane, t_{stir} depends on the level of turbulence parameterized by α (a more turbulent disk has shorter stirring timescales) and the temperature structure of the disk, which affects the sound speed $c_s(z)$ and disk scale height $H = c_s(0)\ /\ \mathbf{\Omega}_K$, where $\mathbf{\Omega}_K$ is the Keplerian rotation rate at radius R. The settling timescale ($t_{sett} = [4\sigma c_s(z)\rho_{gas}(z)]/[3m\mathbf{\Omega}_K^2]$) is shorter for larger and more compact grains due to its dependence on the cross-section/mass ratio [$\sigma/m = 3/\ (4\rho_{cgr}(100\% - \phi)\ r)$] of the grains but is also affected by the disk temperature and density [$\rho_{gas}(z)$] structure. Grains can be lofted up to a maximum height, where $t_{stir} = 100 \times t_{sett}$, above which the downward gravitational force sufficiently overcomes the turbulent motion causing grains to be completely settled out.

Figure 2.6 shows the maximum height reached by grains of sizes 0.01–10 µm within the disk lifetime given the conditions in our physical disk model. Due to their longer settling times, smaller and more porous grains can reach heights closer to the disk surface. Excluding the larger (1–10 µm) compact grains, all other grains can be lofted into the photo-destructive layer shown in Fig. 2.2

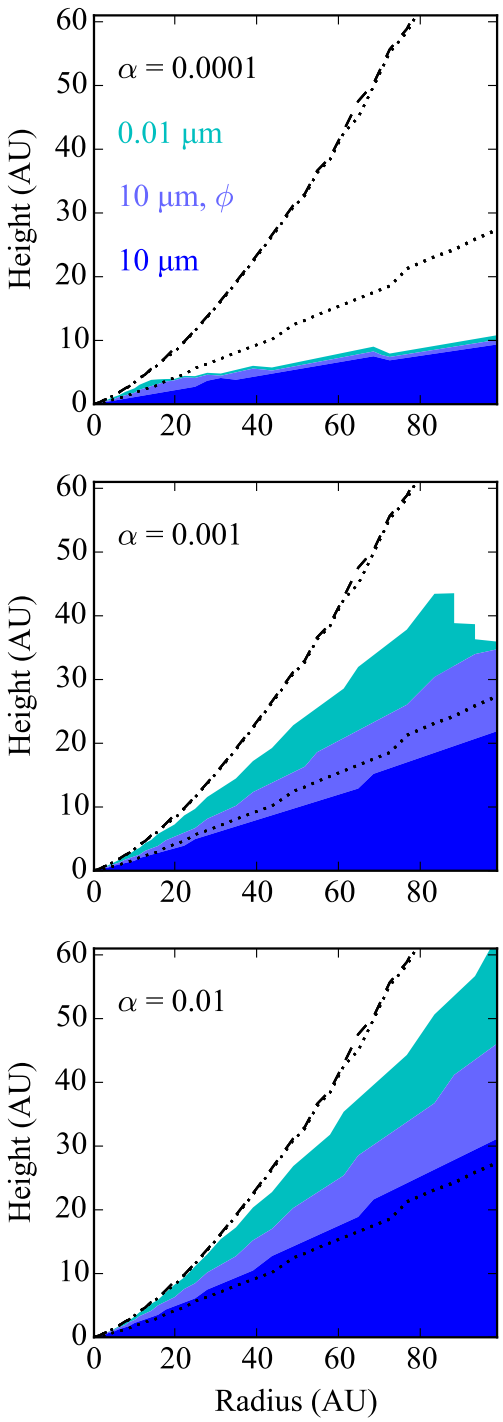

Figure 2.6: Maximum height to which carbon grains of sizes 0.01 and 10 µm, porous (ϕ) and compact, can be lofted for different levels of disk turbulence parameterized by $\alpha = 10^{-4}$–10^{-2}. For reference, the height of the UV destructive layer for 0.01 µm carbon grains is indicated by the dotted line and the disk surface by the dash-dotted line.

out to radii of nearly 100 or more au for sufficiently turbulent disks ($\alpha = 10^{-3}$–10^{-2}). This distance is only ∼10–100+ au for compact 1 µm grains and 0–2 au for compact 10 µm grains for the same range in α. At low α, t_{stir} approaches the disk lifetime of several million years and therefore restricts the

upward mobility of grains of all sizes. For $\alpha = 10^{-4}$, only grains smaller or more porous than compact 1 µm grains can be lofted into the photo-destructive layers and within a limited distance from the star of ∼15 au.

PAHs in the gas phase would remain coupled to the gas, similar to the small carbon grains, and are not subject to settling. However, given that hydrocarbons have a sublimation temperature of ∼400 K (B15), in dense regions of the disk where the chance of interaction with grains is high, PAHs will likely freeze out and remain on grain surfaces. We would expect these PAHs to attach mainly to the smallest grains because they represent the largest surface area. Therefore, in the limit where all of the PAHs are frozen out, the results would be similar to those of the 0.01 µm grains. PAHs that evade interaction with grains would be destroyed at the rates presented in Section 2.2.3 at the disk surface where conditions are appropriate for oxidation, but would remain largely unaffected in deeper layers of the disk.

Even if grains are able to reach the heights where destruction occurs within the disk, the amount of time grains spend at those heights is equally important to ensure their destruction. Where the stirring timescale is short compared to the disk lifetime, grains will cycle through the vertical column multiple times. In lower α disks with longer stirring timescales, grains tend to experience longer excursions through a smaller number of different environments. Alternatively, in higher α disks with shorter stirring timescales, grains rapidly change environments spending brief intervals of time in each one (Ciesla 2010). The average time spent in a particular region over multiple stirring cycles ends up being only weakly dependent on α, however, and related primarily to the density structure of the disk. Here the fraction of the disk lifetime that an average grain spends above a height z is taken to be approximately the ratio of the integrated gas density above height z to the total gas density of the vertical column above the midplane.

Figure 2.7 compares the time spent at heights above the midplane for a disk lifetime on the order of 10^6 years to the time required to deplete the 0.1 µm grains by one order of magnitude. Although carbon grain destruction occurs rapidly, grains would only be exposed to destructive conditions several scale heights above the midplane for ∼1–10 years for oxidation or ∼100–1000 years for photolysis. Where the depletion timescale, represented by the filled contours in Fig. 2.7, is longer than the exposure timescale and therefore a

filled contour crosses over solid contour lines corresponding to comparable or shorter amounts of time, depletion of refractory carbon in 0.1 µm grains can occur within the disk lifetime. For UV photolysis in panel (a), the crossover occurs around 10 au, where the depletion and exposure times are on the order of 10 years. In comparison, this crossover occurs at ∼0.5 au for oxidation. These numbers represent upper estimates because they assume that the particles spend all of their time behaving aerodynamically as small monomers. This may be true in very turbulent cases, where collisions become destructive and prohibit growth or if grains are part of very porous aggregates. Growth to large or more compact aggregates may limit the time spent at these higher altitudes (Krijt and Ciesla 2016).

In the exposure time, refractory carbon abundances can be depleted to the levels observed in solar-system bodies out to maximum radii shown in Figure 2.8. For 0.01 µm grains, the maximum is about 3–5 au for depletion levels similar to the carbonaceous chondrites via oxidation. However, UV photolysis will clear out these grains throughout the planet-forming region. Larger, from compact 0.1 to porous 1 µm, grains are depleted out to less than 1 au via oxidation but 3–10 au via photolysis. Once carbon has been incorporated into grains of 10 µm or larger (or compact 1 µm grains), it will likely survive these processes and remain in refractory form with the exception of porous grains in very turbulent disks within 1 au. For a constant-α disk, depletion requires sufficient turbulence to allow for lofting of the grains into the surface layers within the disk lifetime. Values of $\alpha \sim 10^{-2}$ are needed to deplete carbon from 1 µm grains out to even a few au. For lower turbulence disks, depletion is limited to submicron grain sizes out to a few au (α=10^{-3}) or 0.01 µm grains out to ∼10 au (α=10^{-4}).

The sizes of the depleted regions in the surface layers of the disk from Fig. 2.2 represent the upper limit for the radial extent of carbon depletion assuming perfectly efficient transfer of material from the midplane to the surface and sufficient exposure times to destruction mechanisms. The actual extent of depletion in the midplane will almost certainly be less and highly dependent on the transport processes, grain evolution, and the temperature and density structure within the disk. In the simplest case of a constant-α model with our physical disk structure, depletion of submicron to micron-sized carbon grains can occur within $\lesssim$3–10 au in turbulent disks and average interstellar-sized

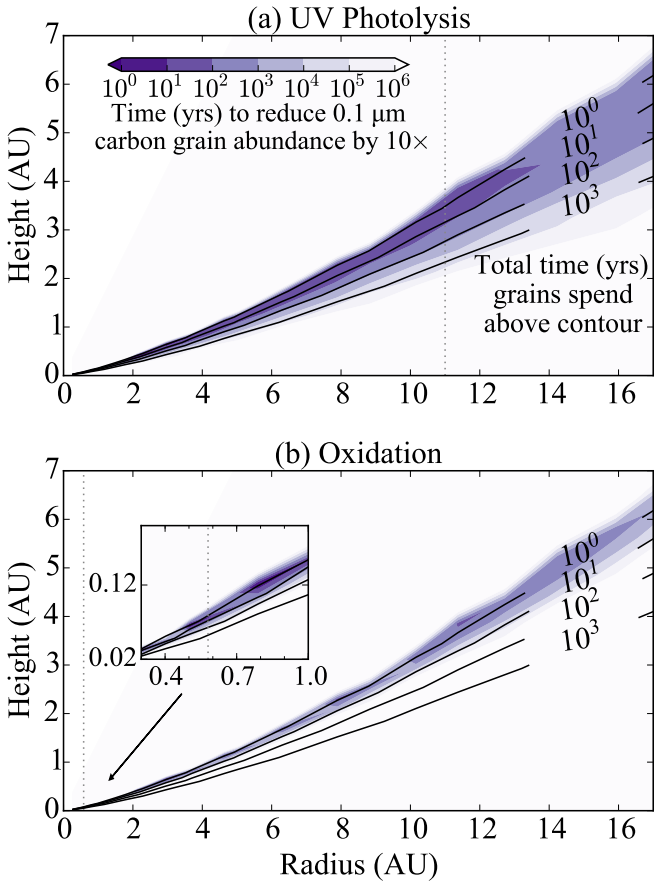

Figure 2.7: Comparison of the time grains are exposed to the conditions above heights outlined in contours to the time required to deplete the abundance of 0.1 µm carbon grains by an order of magnitude via UV photolysis (a) and oxidation (b) represented by the filled contours. The dotted line represents the radius beyond which the depletion time is less than the exposure time and the 0.1 µm carbon grains will mostly survive. As discussed in the text, the exposure time does not strongly depend on the choice of α regarding the disk turbulence.

carbon grains can be cleared out of the planet-forming region.

2.4 Discussion

The analysis of the potential refractory carbon depletion due to oxidation and photochemical destruction depends on several unconstrained factors. The extent to which grains can be destroyed depends on their growth rate. Smaller grains are destroyed faster and can be lofted higher allowing them to reach the surface layers more easily. Larger grains are more likely to survive destruction. Therefore, the effectiveness of this destruction mechanism depends on the

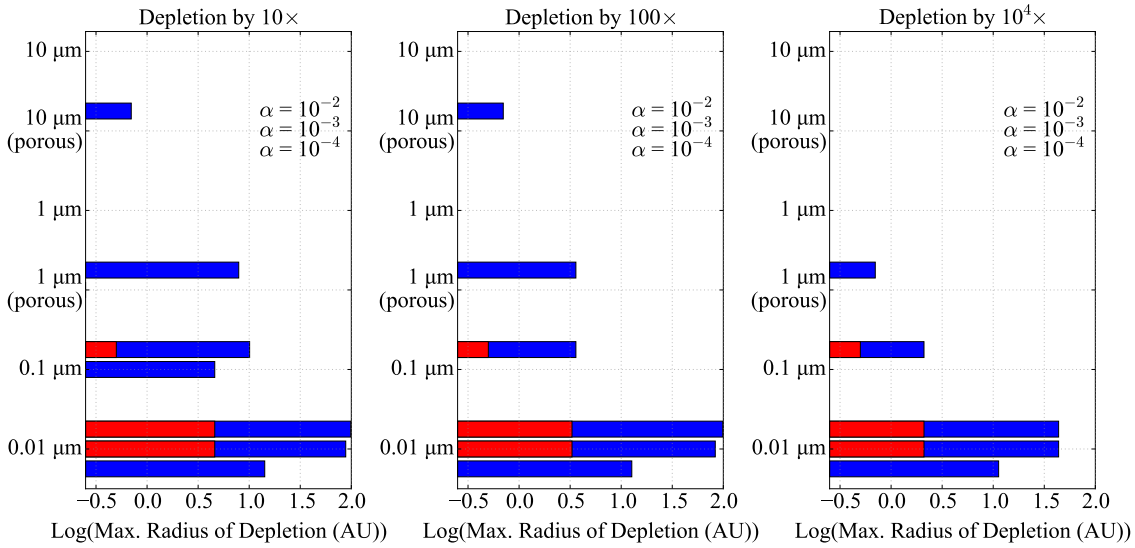

Figure 2.8: Maximum radii where depletion in the midplane can occur—where grains can be turbulently lofted to a height multiple times within the disk lifetime and the time to deplete the carbon grain population is shorter than the total fraction of the disk lifetime that grains spend at that height—for different grain sizes, levels of turbulence, and levels of carbon abundance depletion including oxidation (red) and photolysis (blue).

timescale and efficiency of grain growth. When growth is accompanied by collisional erosion and fragmentation, maintaining a constant supply of small grains in the disk, photochemical destruction and combustion remain effective. However, the formation of sufficiently large bodies that sweep up small dust grains prevents the small grains from traveling efficiently from the midplane to the surface (Krijt and Ciesla 2016) and therefore hinders the destruction of refractory carbon.

The locations where the tested destruction mechanisms occur at an appreciable rate depend on the radiation field and temperature structure (for oxidation) within the disk. In order to have sufficient UV photons for photochemical destruction of refractory carbon in disks around low-mass stars where the UV field is dominated by accretion luminosity, the star must be accreting. The current analysis is based on an approximately solar-mass star. Increasing the stellar mass and therefore its luminosity would result in a warmer disk and potentially extend the distances out to which destruction can occur. However, changing the stellar mass would alter the input stellar irradiation field as well, which is a topic to be explored in future work. The assumed disk properties are

also important. Younger disks may be more massive, preventing radiation from penetrating as deeply into the disk affecting both the temperature structure and atomic O abundances, causing the photoactive and oxidative regions to be higher above the midplane away from the majority of the disk material. An active disk undergoing accretion and potentially subject to large bursts of episodic accretion similar to those of FU Orionis objects will have a vastly different temperature profile than the passive disk modeled here. Warming dense regions of the disk may increase the effectiveness of oxidation throughout the disk.

Furthermore, this analysis depends on the composition, optical properties, and distribution of materials within the disk. Dust grains may not have pure carbon surfaces and in cooler regions of the disk may be coated in volatile ice. This would reduce the efficiency of destruction mechanisms tested here. The change in opacity due to icy mantles could also alter the modeled temperature distribution in the disk. However, evidence suggests that ice coatings may not be a concern for this analysis. Observed water emission due to UV desorption of water ice from grains in the outer disk is relatively weak. This may be the result of differential settling where larger, ice-coated grains typically reside below the UV-irradiated layers and the small grains above have bare surfaces (Hogerheijde et al. 2011). Additional settling of dust grains, approximated by increasing the fraction of the dust mass in larger grains and restricting the large grain population to lower scale heights, has little effect on the location of the high temperature ($>100\,\mathrm{K}$) gas in our model.

Mass transport within the disk is required in order for this mechanism to reproduce the observed carbon deficit in solar-system bodies relative to interstellar dust. In the constant-α model, sufficiently turbulent disks are able to loft grains above the midplane. However, increasing the amount of time grains spend exposed to destructive conditions requires some asymmetry in their vertical motion that would cause them to spend additional time in the upper layers of the disk. Consideration of different angular momentum transport processes may be important for this analysis. For example, a disk model including wind-driven accretion, where Bai and Stone (2013) found that at 1 au the accretion flow occurs in a thin layer offset from the midplane by multiple scale heights, may alter the patterns of dust migration relative to the destructive regions. To further explore grain motion, a numerical (i.e.,

non-ideal) turbulent disk model could be employed, coupling dust evolution to the physical and chemical state of the disk and allowing timescales and lofting heights to be determined by averaging over the trajectories and lifetimes of individual grains in the simulation (Ciesla 2010, 2011). Ultimately, such models could be combined with dust coagulation and planetesimal formation scenarios to provide a quantitative assessment of the refractory carbon distribution in the disk prior to and through the formation of planetesimals.

2.5 Conclusion

We ran a chemistry model for an irradiated, passive disk, including destruction mechanisms for solid carbon grains and PAHs – two potential sources of refractory carbon that could have been inherited from the ISM and present in the protoplanetary disk. Oxidation and photochemical destruction rapidly deplete refractory carbon but are limited to the photochemically active surface layers of the disk. Oxidation and photolysis of large grains are further limited within a particular radial distance depending on the size and structure of the refractory carbon source. The maximum radial distance to which refractory carbon can be oxidized at the surface is ∼20–65 au after 10^6 years for the 0.01–10 µm grains and ∼30 au for PAHs whereas photochemical destruction can extend out to 100+ au.

Motion of grains within the disk is required to deplete refractory carbon at the midplane to the levels observed in solar-system bodies. This motion is difficult to model analytically. Approximations for the timescales of the average motion of dust grains are used to constrain the extent to which refractory carbon can become depleted at the midplane. For our model of a passive, constant-α disk with high turbulence, carbon grains smaller or more porous than compact 10 µm grains (and PAHs frozen to their surfaces) can be lofted into the destructive regions within 10–100+ au from the central star but their depletion is limited by the amount of time they are exposed to the destructive conditions. UV photolysis has proved to be an important mechanism in depleting refractory carbon. The fast reaction rates allow for destruction of grains in the surface layers of the disk even if they spend very little time there and the lack of temperature dependence extends the destructive region to any surface layers with sufficient UV radiation.

Early on in planet formation, cm-sized and larger “pebbles” are built up

through the interaction of smaller grains starting with interstellar sizes and compositions. These initial small grains will be subjected to physical and chemistry processes in the protoplanetary disk. While these grains remain small, photolysis (and to a lesser extent oxidation) can selectively erode the refractory carbon component of the population releasing it into the volatile phase in the inner portions of the disk. Photolysis can destroy the 0.01 µm carbon grains throughout the planet-forming region of the disk assuming sufficient turbulence. However, the 0.1–1 µm grains may be a more significant source of material for planetesimals. If the primordial grain size distribution is similar to that of the ISM, small grains will represent most of the surface area but the bulk of the mass will be in the 0.1–1 µm grains. Once grains reach 10 µm in size they will be largely unaffected by oxidation and photochemical destruction unless they are broken down and rebuilt from smaller grains. Therefore, in order to be effective, destruction of refractory carbon grains will need to occur early in the lifetime of the disk prior to significant grain growth and the building of planetesimals.

Based on our model, submicron to micron-sized carbon grain abundances can be depleted down to the levels of the carbonaceous chondrites and planetesimals sampled in the atmospheres of polluted white dwarfs out to a few to 10 au in sufficiently turbulent disks. Interstellar-sized grains can be cleared out of the planet-forming region of the disk in such turbulent disks and up to ∼10 au even in disks with lower turbulence. However, this analysis depends on several unconstrained parameters in the disk including the temperature and density structure, the amount of turbulence present, and the nature of the carbon sources. Further exploration of refractory carbon depletion in protoplanetary disks may therefore require consideration of alternative disk structures, dust transport, and/or accretion mechanisms. Ultimately, estimating the efficacy and radial cutoff of refractory carbon destruction mechanisms within the protoplanetary disk, including oxidation and photochemical destruction, may provide an explanation for the carbon content of planetary bodies in our solar system and how it relates to their place of origin.

2.6 Acknowledgments

The authors thank the anonymous reviewer whose comments and suggestions improved this work. This material is based upon work supported by the National Science Foundation, via the Graduate Research Fellowship Program un-

der Grant No. DGE-1144469 and the Astronomy and Astrophysics Research Grants Program under Grant No. AST-1514918.

2.7 Appendix

Regions of the disk where active depletion of refractory carbon occurs are determined by the physical conditions present. Figure 2.A1 aids in the direct comparison of the abundance of refractory carbon after 10^6 years for models shown in Figures 2.2 and 2.3 to the gas temperature and radiation fields from Figure 2.1 for select radii.

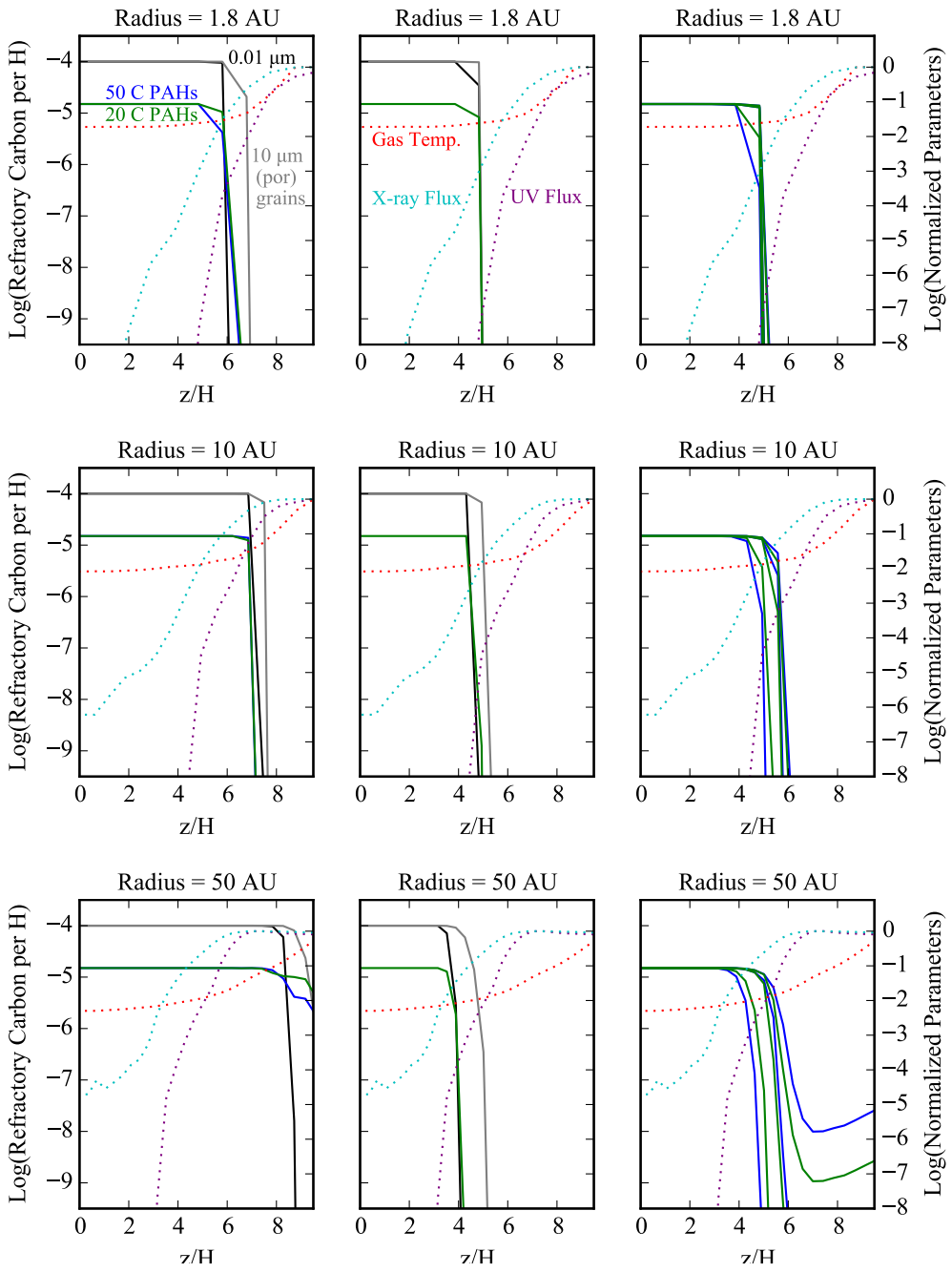

Figure 2.A1: Vertical profiles relative to the disk scale height (H) of refractory carbon abundance (solid lines) after 10^6 years on the left axis and gas temperature (red dotted line), integrated UV flux (purple dotted line), and integrated X-ray flux (cyan dotted line) normalized to the maximum value for each radius on the right axis. Models of oxidation, UV and X-ray photodissociation of 0.01 and porous 10 µm carbon grains (black and gray solid lines, respectively) and 50 and 20 C PAHs (blue and green solid lines, respectively) are shown. See Section 2.2.3 for further description of these models. Maximum values used for normalization are 4200 K, 2.9×10^6 G_0, and 4.8×10^9 photons cm^{-2} s^{-1} at 1.8 au; 4200 K, 6.6×10^4 G_0, and 1.4×10^9 photons cm^{-2} s^{-1} at 10 au; and 4200 K, 2.5×10^3 G_0, and 4.9×10^7 photons cm^{-2} s^{-1} at 50 au.

REFERENCES

I. Alata, G. A. Cruz-Diaz, G. M. Muñoz Caro, and E. Dartois. Vacuum ultraviolet photolysis of hydrogenated amorphous carbons . I. Interstellar H_2 and CH_4 formation rates. *A&A*, 569:A119, September 2014. doi: 10.1051/0004-6361/201323118.

I. Alata, A. Jallat, L. Gavilan, M. Chabot, G. A. Cruz-Diaz, G. M. Munoz Caro, K. Béroff, and E. Dartois. Vacuum ultraviolet of hydrogenated amorphous carbons. II. Small hydrocarbons production in Photon Dominated Regions. *A&A*, 584:A123, December 2015. doi: 10.1051/0004-6361/201526368.

X.-N. Bai and J. M. Stone. Wind-driven Accretion in Protoplanetary Disks. I. Suppression of the Magnetorotational Instability and Launching of the Magnetocentrifugal Wind. *ApJ*, 769:76, May 2013. doi: 10.1088/0004-637X/769/1/76.

I. Bauer, F. Finocchi, W. J. Duschl, H.-P. Gail, and J. P. Schloeder. Simulation of chemical reactions and dust destruction in protoplanetary accretion disks. *A&A*, 317:273–289, January 1997.

E. A. Bergin, G. A. Blake, F. Ciesla, M. M. Hirschmann, and J. Li. Tracing the ingredients for a habitable earth from interstellar space through planet formation. *Proceedings of the National Academy of Science*, 112:8965–8970, July 2015. doi: 10.1073/pnas.1500954112.

O. Berné, J. Montillaud, and C. Joblin. Top-down formation of fullerenes in the interstellar medium. *A&A*, 577:A133, May 2015. doi: 10.1051/0004-6361/201425338.

T. J. Bethell and E. A. Bergin. The Propagation of Lyα in Evolving Protoplanetary Disks. *ApJ*, 739:78, October 2011a. doi: 10.1088/0004-637X/739/2/78.

T. J. Bethell and E. A. Bergin. Photoelectric Cross-sections of Gas and Dust in Protoplanetary Disks. *ApJ*, 740:7, October 2011b. doi: 10.1088/0004-637X/740/1/7.

J. Blum and G. Wurm. The Growth Mechanisms of Macroscopic Bodies in Protoplanetary Disks. *ARA&A*, 46:21–56, September 2008. doi: 10.1146/annurev.astro.46.060407.145152.

D. Brownlee, P. Tsou, J. Aléon, C. M. O. '. Alexander, T. Araki, S. Bajt, G. A. Baratta, R. Bastien, P. Bland, P. Bleuet, J. Borg, J. P. Bradley, A. Brearley, F. Brenker, S. Brennan, J. C. Bridges, N. D. Browning, J. R. Brucato, E. Bullock, M. J. Burchell, H. Busemann, A. Butterworth, M. Chaussidon,

A. Cheuvront, M. Chi, M. J. Cintala, B. C. Clark, S. J. Clemett, G. Cody, L. Colangeli, G. Cooper, P. Cordier, C. Daghlian, Z. Dai, L. D'Hendecourt, Z. Djouadi, G. Dominguez, T. Duxbury, J. P. Dworkin, D. S. Ebel, T. E. Economou, S. Fakra, S. A. J. Fairey, S. Fallon, G. Ferrini, T. Ferroir, H. Fleckenstein, C. Floss, G. Flynn, I. A. Franchi, M. Fries, Z. Gainsforth, J.-P. Gallien, M. Genge, M. K. Gilles, P. Gillet, J. Gilmour, D. P. Glavin, M. Gounelle, M. M. Grady, G. A. Graham, P. G. Grant, S. F. Green, F. Grossemy, L. Grossman, J. N. Grossman, Y. Guan, K. Hagiya, R. Harvey, P. Heck, G. F. Herzog, P. Hoppe, F. Hörz, J. Huth, I. D. Hutcheon, K. Ignatyev, H. Ishii, M. Ito, D. Jacob, C. Jacobsen, S. Jacobsen, S. Jones, D. Joswiak, A. Jurewicz, A. T. Kearsley, L. P. Keller, H. Khodja, A. L. D. Kilcoyne, J. Kissel, A. Krot, F. Langenhorst, A. Lanzirotti, L. Le, L. A. Leshin, J. Leitner, L. Lemelle, H. Leroux, M.-C. Liu, K. Luening, I. Lyon, G. MacPherson, M. A. Marcus, K. Marhas, B. Marty, G. Matrajt, K. McKeegan, A. Meibom, V. Mennella, K. Messenger, S. Messenger, T. Mikouchi, S. Mostefaoui, T. Nakamura, T. Nakano, M. Newville, L. R. Nittler, I. Ohnishi, K. Ohsumi, K. Okudaira, D. A. Papanastassiou, R. Palma, M. E. Palumbo, R. O. Pepin, D. Perkins, M. Perronnet, P. Pianetta, W. Rao, F. J. M. Rietmeijer, F. Robert, D. Rost, A. Rotundi, R. Ryan, S. A. Sandford, C. S. Schwandt, T. H. See, D. Schlutter, J. Sheffield-Parker, A. Simionovici, S. Simon, I. Sitnitsky, C. J. Snead, M. K. Spencer, F. J. Stadermann, A. Steele, T. Stephan, R. Stroud, J. Susini, S. R. Sutton, Y. Suzuki, M. Taheri, S. Taylor, N. Teslich, K. Tomeoka, N. Tomioka, A. Toppani, J. M. Trigo-Rodríguez, D. Troadec, A. Tsuchiyama, A. J. Tuzzolino, T. Tyliszczak, K. Uesugi, M. Velbel, J. Vellenga, E. Vicenzi, L. Vincze, J. Warren, I. Weber, M. Weisberg, A. J. Westphal, S. Wirick, D. Wooden, B. Wopenka, P. Wozniakiewicz, I. Wright, H. Yabuta, H. Yano, E. D. Young, R. N. Zare, T. Zega, K. Ziegler, L. Zimmerman, E. Zinner, and M. Zolensky. Comet 81P/Wild 2 Under a Microscope. *Science*, 314: 1711, December 2006. doi: 10.1126/science.1135840.

D. E. Brownlee. Interplanetary dust. *Reviews of Geophysics and Space Physics*, 17:1735–1743, October 1979. doi: 10.1029/RG017i007p01735.

S. Bruderer. Survival of molecular gas in cavities of transition disks. I. CO. *A&A*, 559:A46, November 2013. doi: 10.1051/0004-6361/201321171.

J. E. Chiar, A. G. G. M. Tielens, A. J. Adamson, and A. Ricca. The Structure, Origin, and Evolution of Interstellar Hydrocarbon Grains. *ApJ*, 770:78, June 2013. doi: 10.1088/0004-637X/770/1/78.

F. J. Ciesla. Residence Times of Particles in Diffusive Protoplanetary Disk Environments. I. Vertical Motions. *ApJ*, 723:514–529, November 2010. doi: 10.1088/0004-637X/723/1/514.

F. J. Ciesla. Residence Times of Particles in Diffusive Protoplanetary Disk Environments. II. Radial Motions and Applications to Dust Annealing. *ApJ*, 740:9, October 2011. doi: 10.1088/0004-637X/740/1/9.

L. I. Cleeves, F. C. Adams, and E. A. Bergin. Exclusion of Cosmic Rays in Protoplanetary Disks: Stellar and Magnetic Effects. *ApJ*, 772:5, July 2013. doi: 10.1088/0004-637X/772/1/5.

L. I. Cleeves, E. A. Bergin, C. Qi, F. C. Adams, and K. I. Öberg. Constraining the X-Ray and Cosmic-Ray Ionization Chemistry of the TW Hya Protoplanetary Disk: Evidence for a Sub-interstellar Cosmic-Ray Rate. *ApJ*, 799:204, February 2015. doi: 10.1088/0004-637X/799/2/204.

P. D'Alessio, N. Calvet, and D. S. Woolum. Thermal Structure of Protoplanetary Disks. In A. N. Krot, E. R. D. Scott, and B. Reipurth, editors, *Chondrites and the Protoplanetary Disk*, volume 341 of *Astronomical Society of the Pacific Conference Series*, page 353, December 2005.

B. T. Draine. On the chemisputtering of interstellar graphite grains. *ApJ*, 230: 106–115, May 1979. doi: 10.1086/157066.

B. T. Draine and H. M. Lee. Optical properties of interstellar graphite and silicate grains. *ApJ*, 285:89–108, October 1984. doi: 10.1086/162480.

C. P. Dullemond and C. Dominik. The effect of dust settling on the appearance of protoplanetary disks. *A&A*, 421:1075–1086, July 2004. doi: 10.1051/0004-6361:20040284.

J. Farihi, D. Koester, B. Zuckerman, L. Vican, B. T. Gänsicke, N. Smith, G. Walth, and E. Breedt. Solar abundances of rock-forming elements, extreme oxygen and hydrogen in a young polluted white dwarf. *MNRAS*, 463: 3186–3192, December 2016. doi: 10.1093/mnras/stw2182.

F. Finocchi, H.-P. Gail, and W. J. Duschl. Chemical reactions in protoplanetary accretion disks. II. Carbon dust oxidation. *A&A*, 325:1264–1279, September 1997.

J. K. J. Fogel, T. J. Bethell, E. A. Bergin, N. Calvet, and D. Semenov. Chemistry of a Protoplanetary Disk with Grain Settling and Lyα Radiation. *ApJ*, 726:29, January 2011. doi: 10.1088/0004-637X/726/1/29.

A. Fruchter, J. H. Krolik, and J. E. Rhoads. X-Ray Destruction of Dust along the Line of Sight to γ-Ray Bursts. *ApJ*, 563:597–610, December 2001. doi: 10.1086/323520.

H.-P. Gail. Radial mixing in protoplanetary accretion disks. I. Stationary disc models with annealing and carbon combustion. *A&A*, 378:192–213, October 2001. doi: 10.1051/0004-6361:20011130.

H.-P. Gail. Radial mixing in protoplanetary accretion disks. III. Carbon dust oxidation and abundance of hydrocarbons in comets. *A&A*, 390:253–265, July 2002. doi: 10.1051/0004-6361:20020614.

J. Geiss. Composition measurements and the history of cometary matter. *A&A*, 187:859–866, November 1987.

N. Grevesse, M. Asplund, A. J. Sauval, and P. Scott. The chemical composition of the Sun. *Astrophysics and Space Science*, 328:179–183, July 2010. doi: 10.1007/s10509-010-0288-z.

N. Harada, E. Herbst, and V. Wakelam. A New Network for Higher-temperature Gas-phase Chemistry. I. A Preliminary Study of Accretion Disks in Active Galactic Nuclei. *ApJ*, 721:1570, October 2010. doi: 10.1088/0004-637X/721/2/1570.

L. Hartmann, N. Calvet, E. Gullbring, and P. D'Alessio. Accretion and the Evolution of T Tauri Disks. *ApJ*, 495:385–400, March 1998. doi: 10.1086/305277.

G. J. Herczeg, J. L. Linsky, J. A. Valenti, C. M. Johns-Krull, and B. E. Wood. The Far-Ultraviolet Spectrum of TW Hydrae. I. Observations of H_2 Fluorescence. *ApJ*, 572:310–325, June 2002. doi: 10.1086/339731.

G. J. Herczeg, B. E. Wood, J. L. Linsky, J. A. Valenti, and C. M. Johns-Krull. The Far-Ultraviolet Spectra of TW Hydrae. II. Models of H_2 Fluorescence in a Disk. *ApJ*, 607:369–383, May 2004. doi: 10.1086/383340.

M. R. Hogerheijde, E. A. Bergin, C. Brinch, L. I. Cleeves, J. K. J. Fogel, G. A. Blake, C. Dominik, D. C. Lis, G. Melnick, D. Neufeld, O. Panić, J. C. Pearson, L. Kristensen, U. A. Yıldız, and E. F. van Dishoeck. Detection of the Water Reservoir in a Forming Planetary System. *Science*, 334:338, October 2011. doi: 10.1126/science.1208931.

J. Igea and A. E. Glassgold. X-Ray Ionization of the Disks of Young Stellar Objects. *ApJ*, 518:848–858, June 1999. doi: 10.1086/307302.

A. P. Jones and J. A. Nuth. Dust destruction in the ISM: a re-evaluation of dust lifetimes. *A&A*, 530:A44, June 2011. doi: 10.1051/0004-6361/201014440.

A. P. Jones, L. Fanciullo, M. Köhler, L. Verstraete, V. Guillet, M. Bocchio, and N. Ysard. The evolution of amorphous hydrocarbons in the ISM: dust modelling from a new vantage point. *A&A*, 558:A62, October 2013. doi: 10.1051/0004-6361/201321686.

M. Jura and E. D. Young. Extrasolar Cosmochemistry. *Annual Review of Earth and Planetary Sciences*, 42:45–67, May 2014. doi: 10.1146/annurev-earth-060313-054740.

M. E. Kress, A. G. G. M. Tielens, and M. Frenklach. The soot line: Destruction of presolar polycyclic aromatic hydrocarbons in the terrestrial planet-forming region of disks. *Advances in Space Research*, 46:44–49, July 2010. doi: 10.1016/j.asr.2010.02.004.

S. Krijt and F. J. Ciesla. Dust Diffusion and Settling in the Presence of Collisions: Trapping (sub)micron Grains in the Midplane. *ApJ*, 822:111, May 2016. doi: 10.3847/0004-637X/822/2/111.

J.-E. Lee, E. A. Bergin, and H. Nomura. The Solar Nebula on Fire: A Solution to the Carbon Deficit in the Inner Solar System. *ApJ*, 710:L21–L25, February 2010. doi: 10.1088/2041-8205/710/1/L21.

K. Lodders. Solar System Abundances and Condensation Temperatures of the Elements. *ApJ*, 591:1220–1247, July 2003. doi: 10.1086/375492.

S. Messenger, S. Sandford, and D. Brownlee. *The Population of Starting Materials Available for Solar System Construction*, pages 187–208. 2006.

E. R. Micelotta, A. P. Jones, and A. G. G. M. Tielens. Polycyclic aromatic hydrocarbon processing in a hot gas. *A&A*, 510:A37, February 2010. doi: 10.1051/0004-6361/200911683.

G. D. Mulders and C. Dominik. Probing the turbulent mixing strength in protoplanetary disks across the stellar mass range: no significant variations. *A&A*, 539:A9, March 2012. doi: 10.1051/0004-6361/201118127.

J. Najita, E. A. Bergin, and J. N. Ullom. X-Ray Desorption of Molecules from Grains in Protoplanetary Disks. *ApJ*, 561:880–889, November 2001. doi: 10.1086/323320.

C. W. Ormel, M. Spaans, and A. G. G. M. Tielens. Dust coagulation in protoplanetary disks: porosity matters. *A&A*, 461:215–232, January 2007. doi: 10.1051/0004-6361:20065949.

V. Ossenkopf and T. Henning. Dust opacities for protostellar cores. *A&A*, 291:943–959, November 1994.

J. B. Pollack, D. Hollenbach, S. Beckwith, D. P. Simonelli, T. Roush, and W. Fong. Composition and radiative properties of grains in molecular clouds and accretion disks. *ApJ*, 421:615–639, February 1994. doi: 10.1086/173677.

K. M. Pontoppidan, C. Salyk, E. A. Bergin, S. Brittain, B. Marty, O. Mousis, and K. I. Öberg. Volatiles in Protoplanetary Disks. *Protostars and Planets VI*, pages 363–385, 2014. doi: 10.2458/azu_uapress_9780816531240-ch016.

B. D. Savage and K. R. Sembach. Interstellar Abundances from Absorption-Line Observations with the Hubble Space Telescope. *ARA&A*, 34:279–330, 1996. doi: 10.1146/annurev.astro.34.1.279.

R. Siebenmorgen and F. Heymann. Polycyclic aromatic hydrocarbons in protoplanetary disks: emission and X-ray destruction. *A&A*, 543:A25, July 2012. doi: 10.1051/0004-6361/201219039.

R. Siebenmorgen and E. Krügel. The destruction and survival of polycyclic aromatic hydrocarbons in the disks of T Tauri stars. *A&A*, 511:A6, February 2010. doi: 10.1051/0004-6361/200912035.

R. Siebenmorgen, E. Krügel, and H. W. W. Spoon. Mid-infrared emission of galactic nuclei. TIMMI2 versus ISO observations and models. *A&A*, 414: 123–139, January 2004. doi: 10.1051/0004-6361:20031633.

A. G. G. M. Tielens. *The Physics and Chemistry of the Interstellar Medium*. August 2005.

D. Veras and B. T. Gänsicke. Detectable close-in planets around white dwarfs through late unpacking. *MNRAS*, 447:1049–1058, February 2015. doi: 10.1093/mnras/stu2475.

R. Visser, V. C. Geers, C. P. Dullemond, J.-C. Augereau, K. M. Pontoppidan, and E. F. van Dishoeck. PAH chemistry and IR emission from circumstellar disks. *A&A*, 466:229–241, April 2007. doi: 10.1051/0004-6361:20066829.

G. M. Voit. Destruction and survival of polycyclic aromatic hydrocarbons in active galaxies. *MNRAS*, 258:841–848, October 1992. doi: 10.1093/mnras/258.4.841.

H. Wang and M. Frenklach. A detailed kinetic modeling study of aromatics formation in laminar premixed acetylene and ethylene flames. *Combustion and Flame*, 110:173–221, July 1997. doi: 10.1016/S0010-2180(97)00068-0.

J. T. Wasson and G. W. Kallemeyn. Compositions of chondrites. *Royal Society of London Philosophical Transactions Series A*, 325:535–544, July 1988. doi: 10.1098/rsta.1988.0066.

S. J. Weidenschilling and J. N. Cuzzi. Formation of planetesimals in the solar nebula. In E. H. Levy and J. I. Lunine, editors, *Protostars and Planets III*, pages 1031–1060, 1993.

D. J. Wilson, B. T. Gänsicke, J. Farihi, and D. Koester. Carbon to oxygen ratios in extrasolar planetesimals. *MNRAS*, 459:3282–3286, July 2016. doi: 10.1093/mnras/stw844.

B. Zuckerman, D. Koester, C. Melis, B. M. Hansen, and M. Jura. The Chemical Composition of an Extrasolar Minor Planet. *ApJ*, 671:872–877, December 2007. doi: 10.1086/522223.

Chapter 3

PROBING THE GAS CONTENT OF LATE-STAGE PROTOPLANETARY DISKS WITH N_2H^+

Dana E. Anderson[1], Geoffrey A. Blake[1], Edwin A. Bergin[2], Ke Zhang[2,3], John M. Carpenter[4], Kamber R. Schwarz[2], Jane Huang[5] & Karin I. Öberg[5]

[1]Division of Geological and Planetary Sciences, California Institute of Technology, 1200 E. California Blvd., Pasadena, CA 91125, USA

[2]Department of Astronomy, University of Michigan, 1085 South University Ave., Ann Arbor, MI 48109, USA

[3]Hubble Fellow

[4]Joint ALMA Observatory, Av. Alonso de Córdova 3107, Vitacura, Santiago, Chile

[5]Harvard-Smithsonian Center for Astrophysics, 60 Garden Street, Cambridge, MA 02138, USA

Abstract The lifetime of gas in circumstellar disks is a fundamental quantity that informs our understanding of planet formation. Studying disk gas evolution requires measurements of disk masses around stars of various ages. Because H_2 gas is unobservable under most disk conditions, total disk masses are based on indirect tracers such as sub-mm dust and CO emission. The uncertainty in the relation between these tracers and the disk mass increases as the disk evolves. In a few well-studied disks, CO exhibits depletions of up to 100× below the assumed interstellar value. Thus, additional tracers are required to accurately determine the total gas mass. The relative lack of nitrogen found in solid solar system bodies may indicate that it persists in volatile form, making nitrogen-bearing species more robust tracers of gas in more evolved disks. Here we present Atacama Large Millimeter/submillimeter Array (ALMA) detections of N_2H^+ in two mature, ∼5–11 Myr-old disks in the Upper Scorpius OB Association. Such detections imply the presence of H_2-rich gas and sources of ionization, both required for N_2H^+ formation. The Upper Sco disks also show elevated N_2H^+/CO flux ratios when compared to previously observed disks with $\gtrsim$10× higher CO fluxes. Based on line ratio predictions from a grid of thermochemical disk models, a significantly reduced CO/H_2

abundance of $<10^{-6}$ for a gas-to-dust ratio of $\gtrsim$100 is required to produce the observed N_2H^+ fluxes. These systems appear to maintain H_2 gas reservoirs and indicate that carbon- and nitrogen-bearing species follow distinct physical or chemical pathways as disks evolve.

3.1 Introduction

The formation of planets in a circumstellar disk is enabled and controlled by the quantity of gas present. Interactions between the gaseous and solid components of the disk play a crucial role in disk dynamics and the initial stages of planet formation (e.g., Weidenschilling and Cuzzi 1993). Following coagulation of micron-sized dust grains into larger particles, the efficiency of further planetesimal growth through streaming instabilities depends on the ratio of gas to solids in the disk (Youdin and Goodman 2005). Gas giant planets are generally thought to form through runaway accretion of disk gas onto sufficiently large planetary cores. The timescales for both the formation and migration of these planets in the disk are limited by the eventual dissipation of disk gas. Furthermore, the exact timing of gas dissipation may determine whether forming-planets become rocky super-Earths or gas giants (e.g., Pollack et al. 1996; Ansdell et al. 2016; Lee and Chiang 2016). The lifetime of disk gas therefore affects both the likelihood of forming of planetary systems and their final architectures. Key components of our theoretical understanding of planet formation depend on estimations of the total disk gas mass over time. Nevertheless, observationally characterizing the gas content of disks of different ages is challenging.

The bulk of disk gas present is expected to be primordial throughout the disk lifetime, inherited from the parent molecular cloud. This gas is removed from the disk as it evolves, first mainly via viscous accretion. Photoevaporation dominates dispersal for the outer radii and for the disk overall at later evolutionary stages, progressing rapidly outward once the inner disk is depleted (Alexander et al. 2014). In this scenario, we would expect to find the last remaining primordial gas in outer regions of the disk. However, the mechanisms for gas dissipation are still largely unconstrained. In particular, the effects of photoevaporation depend on the relative flux of FUV, EUV, and X-ray photons attenuated by disk material (Gorti et al. 2009).

Although gas dissipation itself can be observed directly for the hot disk surface

through ion emission (e.g., Pascucci et al. 2011), the evolution of the bulk gas disk must be estimated through measurements of disk masses for systems of different ages. H_2 is the main component of the primordial gas, but does not emit strongly under most disk conditions, resulting in the need for indirect tracers of disk mass. Tracers of inner disk gas include UV continuum excess and H recombination lines, which measure accretion rates; H_2 electronic transitions; and, for radii out to 50 AU, *Spitzer* observations of cooling lines at infrared wavelengths (Alexander et al. 2014). Hydrogen deuteride (HD) has also been used as a gas tracer for a small number of disks through *Herschel* measurements (Bergin et al. 2013; McClure et al. 2016), but further use of this tracer is limited by the current lack of instrumentation capable of making these measurements. For older disks and the determination of bulk disk masses, observations of the outer, optically thin regions of the disk are required. Conventional, indirect tracers of the outer disk include (sub-)mm dust continuum and CO isotopologue emission. Estimating the total gas mass of the disk based on these tracers relies on several assumptions, and the validity of these assumptions becomes increasingly questionable with the age of the system as grain growth, gas dispersal, and CO depletion invalidate the use of canonical CO/H_2 and dust/H_2 ratios.

Observations of sub-mm continuum from optically thin dust reveal the total disk dust mass in grains of cm size or less. Larger solid bodies are undetectable. Furthermore, dust masses depend on assumptions regarding the dust properties including the opacity. After measuring the dust mass, an assumed gas-to-dust mass ratio is required to estimate the gas mass of the disk. Even if the assumed interstellar value of 100 is valid for disks shortly after formation, this value becomes highly uncertain after several million years of gas and dust evolution. In particular, growth and inward migration of dust may deplete the outer disk of dust particles. Observations of several disks find that the outer edge of the dust disk is interior to that of CO emission, potentially providing evidence of inward radial drift of solid particles (e.g., Andrews et al. 2012; Zhang et al. 2014).

CO has many advantages as a bulk gas tracer because it is an abundant component of the gas, emissive, and resistant to freezeout (having a condensation temperature of $\sim$20 K). However, the spatial and temporal behavior of the CO/H_2 abundance ratio in the disk is not well understood. A combination

of Atacama Large Millimeter/submillimeter Array (ALMA) CO isotopologue and *Herschel* HD measurements reveal CO/H_2 ratios of up to 5–100× below the canonical interstellar value for the three protoplanetary disks with HD detections by *Herschel* (Favre et al. 2013; McClure et al. 2016). Resolved CO isotopologue emission shows depletion of CO even interior to the CO snowline (Schwarz et al. 2016; Zhang et al. 2017). Surveys of nearby star-forming regions also observe lower-than-expected emission from CO isotopologues, indicative of low gas-to-dust ratios and/or widespread CO depletion (Ansdell et al. 2016; Long et al. 2017; Ansdell et al. 2017). Given the young age of some of these regions, this could indicate that significant CO depletion occurs within 1–3 Myr. Chemical reactions can cause removal of CO from the gas (e.g., Bergin et al. 2014; Reboussin et al. 2015; Yu et al. 2016), but only result in the loss of up to an order of magnitude of CO from the warm molecular layer under the right disk conditions (Schwarz et al. 2018). Physical disk processes are therefore needed to explain further depletion (e.g., Krijt et al. 2018). Without proper evaluation of the CO/H_2 abundance ratio, disk gas masses may be severely underestimated.

Addressing this problem requires additional tracers of the disk gas. Here we investigate another abundant element, nitrogen. Relative to carbon, a smaller fraction of the total available nitrogen abundance (based on the solar value) is found in meteorites and comets (Bergin et al. 2015). The Rosetta mission has revealed a lack of nitrogen in both the volatile ice and refractory phases of comet 67P/Churyumov-Gerasimenko (Rubin et al. 2015; Fray et al. 2017). In fact, comets with high N_2/CO abundance ratios, similar to the estimated value for the solar nebula, are rarely observed (Biver et al. 2018). This may indicate that CO, and perhaps carbon in general, is better captured and/or retained in solid bodies than volatile nitrogen. If not efficiently locked into solid bodies via the planetesimal formation process, the remaining volatile nitrogen may have lingered in the gas phase. Under such conditions, nitrogen-bearing species would be more robust tracers of gas in older, more evolved disks than CO. We aim to investigate this hypothesis.

Nitrogen in the disk is thought to mainly reside in the form of N_2 (Schwarz and Bergin 2014), which has similar volatility to CO (Bisschop et al. 2006; Fayolle et al. 2016), but unfortunately is not emissive under typical disk conditions. However, N_2H^+, a product of N_2 and ionized H_2, is observed in a large number

of disks (e.g., Öberg et al. 2010, 2011). Because H_2 is a required precursor and the chemical lifetime of N_2H^+ is relatively short, N_2H^+ detections also indicate the presence of H_2-rich, primordial gas. N_2 has a higher proton affinity than H_2, promoting the generation of N_2H^+ from H_3^+ in ionized H_2 gas. In contrast, abundant N_2H^+ is not expected in gas generated from the destruction of volatile-rich solid bodies because the proton affinity of N_2 is lower than that of H_2O, the major volatile component of comets. This is supported by analysis of the ion chemistry of comet 67P, which reveals that the dominant ion species generated are produced from neutral species with proton affinities higher than that of H_2O (Heritier et al. 2017).

Furthermore, the proton affinity of N_2 relative to that of CO results in the abundances of N_2H^+ and CO being interdependent. In addition to recombination with electrons, proton transfer to CO represents one of the main destruction pathways of N_2H^+, whose abundances and fluxes are therefore sensitive to changes in CO abundance. For this reason, N_2H^+ has been used as a tracer of the CO snowline in protoplanetary disks (e.g., Qi et al. 2013b). Physical/chemical disk models find that both the N_2H^+ column density and emission tend to peak beyond the CO snowline, but the exact location where they peak depends on disk conditions (Aikawa et al. 2015; van 't Hoff et al. 2017). van 't Hoff et al. (2017) identified two regions in the disk where N_2H^+ appears: a layer extending from the midplane beyond the CO snowline and a layer near the disk surface. The surface layer results from N_2 having a slightly lower photodissociation rate than CO when self-shielding by both species is taken into account, and is present when the N_2/CO abundance ratio exceeds 0.2. It appears that both the absolute CO abundance and the N_2/CO ratio are key parameters in determining the N_2H^+ abundance.

Here we use ALMA to search for N_2H^+ emission in two disks in the Upper Scorpious OB Association in order to investigate the use of N_2H^+ as an indicator of disk composition and mass. Disks in Upper Sco are estimated to be $\sim$5–11 Myr old (Preibisch et al. 2002; Pecaut et al. 2012), probing the end of primordial disk evolution and ages around the typical timescale for gas dissipation. Section 3.2 describes our observations and results including comparison to previous studies. Our grid of thermochemical disk models is introduced and used to interpret our observations in §3.3 and our results are discussed in §3.4. We present our conclusions in §3.5.

Table 3.1: Source Properties.

Source	Stellar Properties			
	SpT	$\log(M_*/M_\odot)$	$\log(L_*/L_\odot)$	$\log(T_*/K)$
J160900-190852	K9	-0.19(-0.05, +0.05)	-0.45 ± 0.15	3.59 ± 0.01
J160823-193001	K9	-0.18(-0.04, +0.05)	-0.59 ± 0.15	3.59 ± 0.01
	Disk Properties			
	Geometry		Dust Mass ($M_\oplus$)[a]	
J160900-190852	Full		13.50 ± 3.34	
J160823-193001	Full		13.94 ± 3.45	

[a]Barenfeld et al. (2016)

3.2 Observations

3.2.1 ALMA Cycle 3 Observations

The two disks, J160900-190852 and J160823-193001, were selected based on previous ALMA continuum and CO J=3–2 observations from a Cycle 0 survey of Upper Sco by Carpenter et al. (2014). The disks chosen have readily detectable CO rotational emission, indicating the presence of molecular gas. Both stars are of spectral type K9 and their disks have similar dust masses of 13–14 $M_\oplus$ (Barenfeld et al. 2016). Table 3.1 describes properties of our selected sources.

ALMA Band 7 observations (PI: Anderson,
2015.1.01199.S) were taken with the 12 m array during Cycle 3 in 2016 March. Baselines ranged from 15.1 to 460.0 m using 38–41 antennas. The on-source integration time was ∼1.8 hr per source. The desired target was the N_2H^+ J=3–2 line at 279.511 GHz. Five spectral windows were used to capture emission lines each with a bandwidth of 117.19 MHz. These windows were centered at 279.533 GHz for N_2H^+ and 281.549, 282.403, 282.942, and 293.935 GHz for potential additional tracers: H_2CO 4(1,4)–3(1,3), C_3H_2, $D^{13}CO^+$ 4–3, and CS 6–5, respectively. Finally, a window centered at 293.900 GHz with a bandwidth of 1875 MHz was dedicated to the collection of continuum emission.

These measurements are compared with Cycle 3 ALMA observations of J160900-190852 in 2016 June and July (PI: Öberg, 2015.1.00964.S). These data were also collected with the 12 m array, with baselines from 15.1 to 641.5 m in June and to 704.1 m in July. The total time on source was ∼0.3 hr. Spectral windows, each with a total bandwith of 117.19 MHz, were centered at

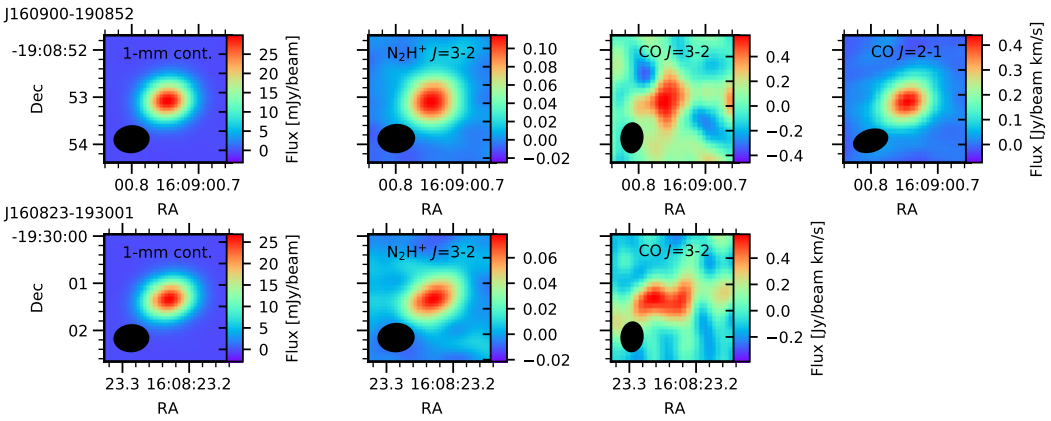

Figure 3.1: 1.04-mm continuum emission and moment 0 maps of N_2H^+ and CO emission from the Upper Sco disks J160900-190852 (top row) and J160823-193001 (bottom row). Maximum continuum flux values are 26.8 and 29.9 mJy per beam, respectively. The synthesized beam size is indicated in the lower left corner of each subplot.

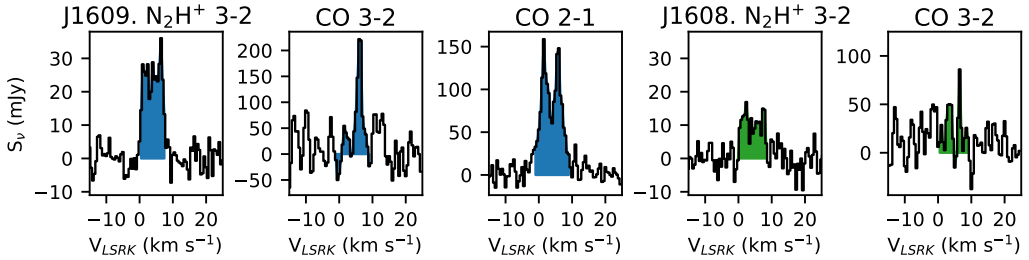

Figure 3.2: Spectra of N_2H^+ and CO emission from the J160900-190852 (shown in blue) and J160823-193001 (shown in green) disks.

230.524–230.530, 220.385–220.391, and 219.547–219.553 GHz to capture CO, ^{13}CO, and C^{18}O emission, respectively.

Data calibration was performed using the Common Astronomy Software Applications (CASA) package (McMullin et al. 2007) version 5.1.2. Atmospheric calibration, bandpass calibration, flux calibration, and phase calibration were applied by the ALMA project. Calibrations were based on observations of J1517-2422 for the bandpass, Titan for the flux, and J1626-2951 and J1553-2422 for the phase for 2015.1.01199.S; and J1517-2422 for the bandpass, J1517-2422 in June and Titan in July for the flux, and J1625-2527 for the phase for 2015.1.00964.S. Flux calibration uncertainty is assumed to be 10%. Continuum emission was estimated from line-free channels of all windows and self-

Table 3.2: Observed Line Fluxes.

Continuum	Line Flux (mJy km s^{-1})			
1.04-mm	N_2H^+	CO	CO	$C^{18}O$
(mJy)	J=3–2	3–2	2–1	2–1
J160900-190852				
36.4 ± 0.3	183 ± 8	460 ± 68	860 ± 21	43 ± 17
J160823-193001				
32.4 ± 0.4	90 ± 7	222 ± 39	...	...

calibration was used to produce images using the *clean* algorithm. Spectral line windows were continuum subtracted using *uvcontsub*, then deconvolved using the *tclean* algorithm. We used Briggs weighting with a robust parameter of 1.8, channel widths of 0.5 km s^{-1}, and the "auto-thresh" automasking algorithm with a mask resolution of 0.25 arcsec and mask threshold of 3.0σ. Small mask components identified far from the source location were removed. The resulting mask components were summed over the entire spectral range and the flux within this total masked region was collected for each channel to produce a spectrum. Flux uncertainties listed are based on the rms noise. The rms noise was computed from the standard deviation of the flux measured in 24 different masked regions offset from the source emission combined over all channels containing spectral line emission. The synthesized beam size was approximately $0.8''$ by $0.6''$ with a position angle of -86° for images from 2015.1.01199.S and $0.8''$ by $0.5''$ with a position angle of -73° for 2015.1.00964.S.

3.2.2 Spectral Line Observations

Images and spectra are provided in Figures 3.1, 3.2, and 3.A1. Continuum flux densities are derived from the images generated using continuum (line-free) channels with an average frequency of 287.106 GHz (Fig. 3.1). Using the method from Barenfeld et al. (2016), we derived dust masses of 14–15 $M_\oplus$, which are consistent with their values from the 0.88 mm continuum.

Spectra were produced as described in Section 3.2.1 (Fig. 3.2). Summing over the velocity channels containing line emission gave the line fluxes in Table 3.2. The velocity ranges are 0–7.5 km s^{-1} for N_2H^+ and -1.0–9.0 km s^{-1} for CO J = 2–1 in J160900-190852. The CO J = 2–1 velocity range is adopted for the CO J = 3–2 and $C^{18}O$ J = 2–1 emission. These ranges are 0–8.5 km s^{-1}

for N_2H^+ and 0.0–9.0 km s^{-1} for CO J = 3–2 in J160823-193001. The CO J = 3–2 fluxes measured using our method are about 90% of the values found by Barenfeld et al. (2016), 246 ± 42 mJy km s^{-1} J160823-193001 and 815 ± 64 mJy km s^{-1} for J160900-190852, when a similar velocity range is used (in this case, 1.0–13.5 km s^{-1} for J160900-190852 rather than our narrower range based on the CO J = 2–1 emission). Our methods differ in the selection of the aperture, velocity range, and image components used for computing CO fluxes based on the goals of each study. In our further analysis, we elected to use the values derived here using the same method as that for our N_2H^+ measurements to provide an appropriate comparison.

3.2.3 Comparison to Disks with Strong CO Emission

Figure 3.3 compares the fluxes observed in our two sources in Upper Sco to observations of other disks where comparable data are available. N_2H^+ has been observed in several bright, gas-rich disks as part of the Disk Imaging Survey of Chemistry with SMA (DISCS) survey with the Submillimeter Array (Öberg et al. 2010, 2011), along with the CO J=2–1 transition. The CO J = 3–2 emission from J160823-193001 was scaled using the flux ratio from J160900-190852 (CO J=2–1 / CO J=3–2 flux ∼1.9) to produce the CO J=2–1 estimate used in Fig. 3.3. This scaling ratio could be the result of low excitation temperatures similar to those derived for Taurus disks (e.g., Guilloteau et al. 2016) and would be lower, ∼0.3, for the case of optically thin gas in local thermal equilibrium (LTE) at 20 K. Additional disks have been observed by the SMA and/or ALMA including TW Hya, HD 163296, and V4046 Sgr (Rosenfeld et al. 2012, 2013; Qi et al. 2013a, 2015; Kastner et al. 2018). In comparison to the Upper Sco disks, the other disks have CO fluxes typically 1–2 orders of magnitude higher (Fig. 3.3, top panel). However, the N_2H^+ J=3–2 fluxes, some of which are upper limits, are at most an order of magnitude higher than the Upper Sco values. This results in relatively high N_2H^+/CO flux ratios in Upper Sco compared to the other disks (Fig. 3.3, middle panel).

$C^{18}O$ J=2–1 data are available for a selection of the sources including the Upper Sco disk J160900-190852 (PI: Öberg, 2015.1.00964.S). $C^{18}O$ is a more accurate tracer of the disk material given that it has relatively optically thin emission as compared to the more abundant and optically thick $^{12}C^{16}O$ parent isotopologue. The $N_2H^+/C^{18}O$ flux ratio therefore provides a closer approximation of the relative abundances. $C^{18}O$ fluxes are taken from the literature

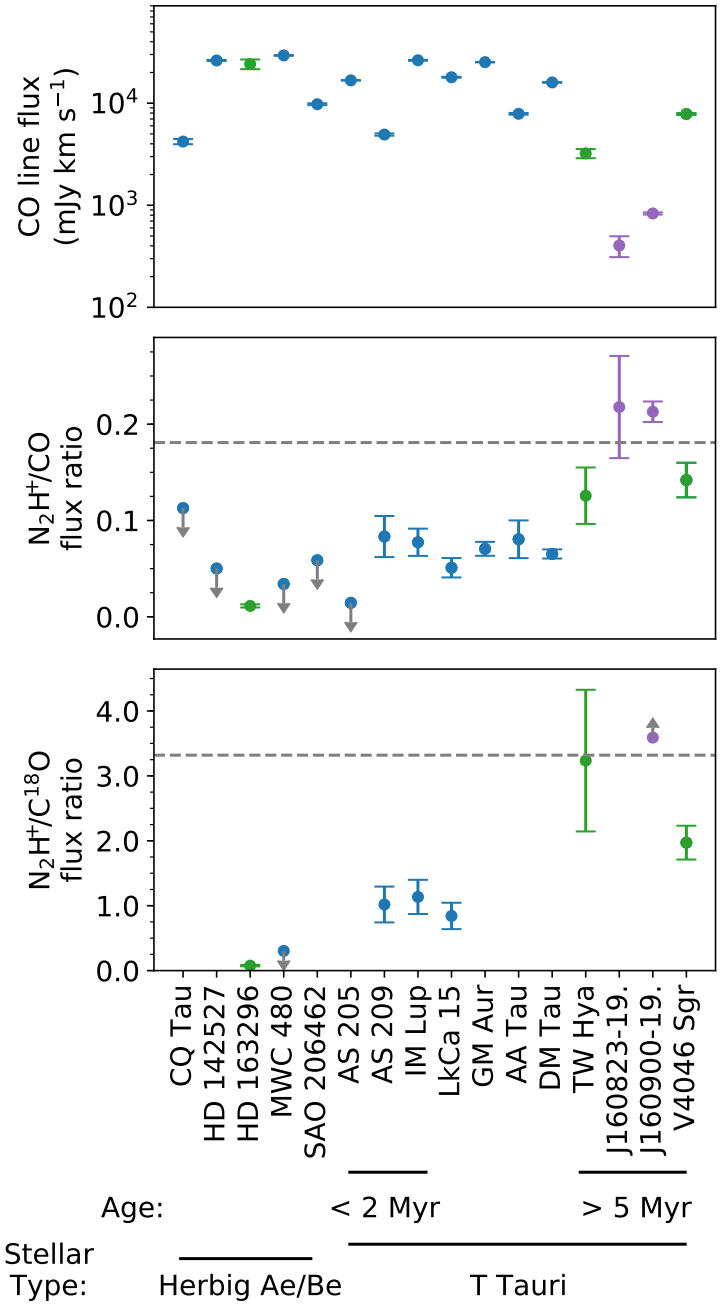

Figure 3.3: Comparison of CO $J = 2$–1 line fluxes (scaled to a distance of 140 pc based on Gaia Collaboration et al. (2018), top panel), N_2H^+ $J = 3$–2/CO $J = 2$–1 flux ratios (middle panel), and N_2H^+ $J = 3$–2/$C^{18}O$ $J = 2$–1 flux ratios (bottom panel) among disks where data were obtained. This includes 11 disks from the DISCS survey with the Submillimeter Array (Öberg et al. 2010, 2011, indicated in blue), V4046 Sgr (Kastner et al. 2018) and HD 163296 (Rosenfeld et al. 2013; Qi et al. 2015) from ALMA (indicated in green), TW Hya (Rosenfeld et al. 2012; Qi et al. 2013a) from the SMA and ALMA (also indicated in green), and 2 disks in Upper Sco from ALMA (this work, indicated in violet). The dashed line indicates 3 standard deviations above the mean for all sources excluding Upper Sco. Arrows indicate upper or lower limits. $C^{18}O$ values are included when available (PI: Öberg, 2013.1.00226.S & 2015.1.00964.S; Qi et al. 2013b, 2015; Cleeves et al. 2016; Huang et al. 2016; Kastner et al. 2018). The 3σ upper limit of the $C^{18}O$ $J = 2$–1 flux is used to derive the J160900-190852 $N_2H^+/C^{18}O$ limit.

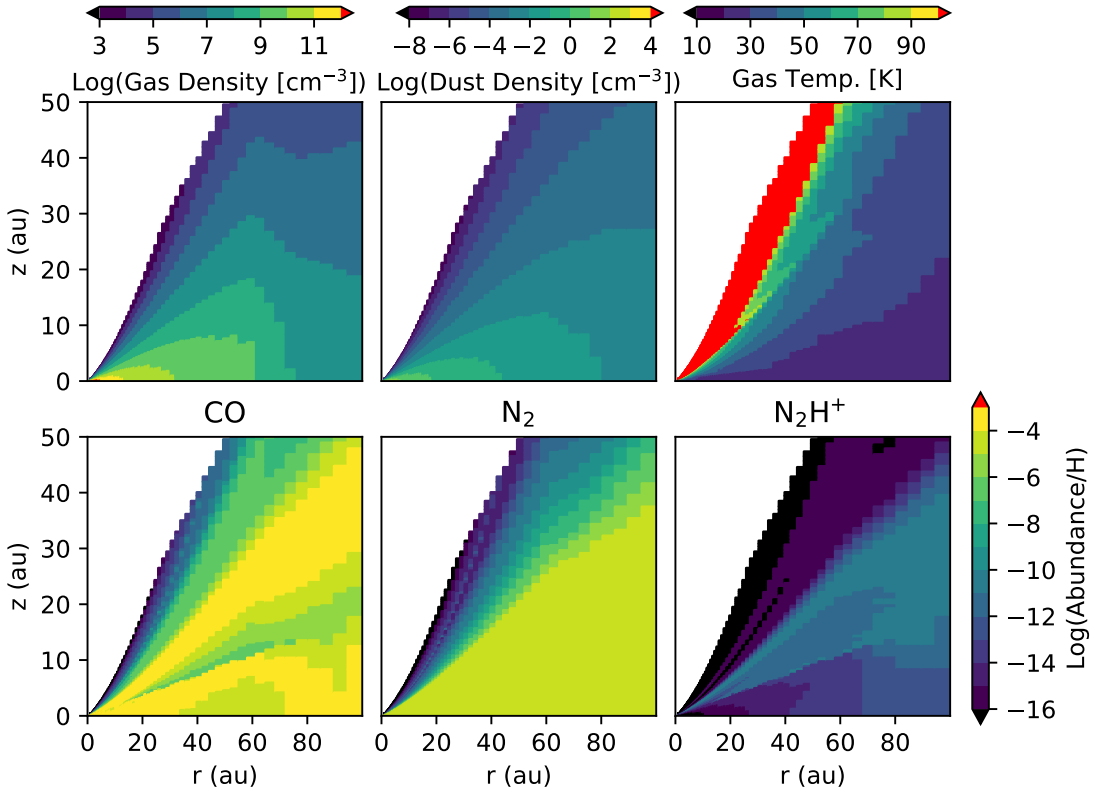

Figure 3.4: Disk gas density, dust density, gas temperature, and abundances of CO, N_2, and N_2H^+ after 1 Myr in our fiducial model.

for TW Hya (Qi et al. 2013b), HD 163296 (Qi et al. 2015), IM Lup (Cleeves et al. 2016), AS 209 (Huang et al. 2016), and V4046 Sgr (Kastner et al. 2018). The values for LkCa 15 and MWC 480 were estimated from moment 0 maps prepared as part of the study by Huang et al. (2017). An upper limit of the $C^{18}O$ flux in J160900-190852 is estimated as 3× the rms flux collected using the CO J=2–1 masked region and velocity range (described in Sections 3.2.1–3.2.2). This upper limit on $C^{18}O$ provides a lower limit for the $N_2H^+/C^{18}O$ ratio, which is above the values for the other observed disks (Fig. 3.3, bottom panel). This reinforces the trend seen in the N_2H^+/CO values.

3.3 Modeling

3.3.1 Thermo-chemical Disk Models

In the following sections, we aim to explore the general trends in N_2H^+ and CO fluxes for disks of varying gas mass and composition. The thermochemical and radiative transfer code of Du and Bergin (2014) is used to run a set of disk

Table 3.3: Fiducial Model Input Parameters.

Stellar Properties:	
M_*	0.65 $M_\odot$
R_*	1.25 $R_\odot$
T_*	3890 K
Source of stellar spectrum	TW Hya
L_{X-ray}	1.6(30) erg s^{-1}
Disk Properties:	
Disk gas mass	4(-3) $M_\odot$
Disk dust mass	4(-5) $M_\odot$
Inner radius	1 au
Outer radius	100 au
Scale height at radius of 80 au	10 au
Power index: surface density vs. radius	1.0
Power index: scale height vs. radius	1.0
Total run time	10^6 yrs
Turbulent viscosity	$\alpha = 0.01$
H_2 cosmic-ray ionization rate	1.36(-17) s^{-1}
Initial abundances: (Relative to total H)	
H_2	5.0(-1)
He	9.0(-2)
CO	1.4(-4)
N	7.5(-5)
H_2O ice	1.8(-4)
S	8.0(-8)
Si^+	8.0(-9)
Na^+	2.0(-8)
Mg^+	7.0(-9)
Fe^+	3.0(-9)
P^+	3.0(-9)
F^+	2.0(-8)
Cl^+	4.0(-9)

Note: a(b) indicates a$\times 10^b$

models in order to estimate spectral line ratios for the various cases. Initial parameters for the fiducial model are included in Table 3.3. The parameters describing the central star are set based on Barenfeld et al. (2016) for the two Upper Sco sources observed here and the stellar spectrum of the well-studied T Tauri star TW Hya is used. The disk outer radius is set at 100 au (the effects

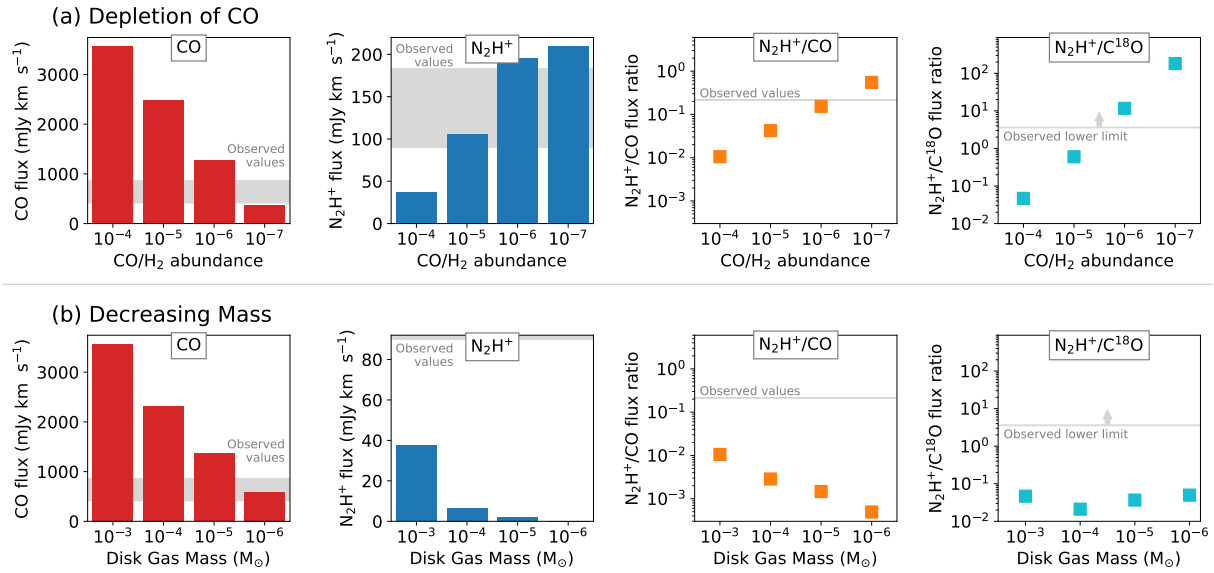

Figure 3.5: Calculated fluxes for our set of disk models. From left to right, the CO J=2–1 flux, N_2H^+ J=3–2 flux, ratio of the N_2H^+ J=3–2 to CO J=2–1 flux, and ratio of the N_2H^+ J=3–2 to $C^{18}O$ J=2–1 flux are plotted. Values are shown for the fiducial model and additional models where the CO/H_2 abundance ratio is lowered by factors of 10–1000× (a) and for the fiducial model and additional models where the disk gas mass is lowered by factors of 10–1000× (b). The range of observed values for the Upper Sco sources are show for comparison in gray.

of this choice are explored in Section 3.3.3). Gas and dust components share a mass surface density profile with an exponent of 1.0 and an initial scale height of 10 au at a radius of 80 au. Vertical structure is determined using hydrostatic equilibrium over multiple iterations of the dust temperature calculation with a Monte Carlo radiative transfer model. The dust contains two components with sizes following a Mathis-Rumpl-Nordsieck (MRN) distribution: 90% of the dust mass is in large dust grains, up to 1 mm in radius, and the remaining in small dust, up to 1 micron in radius. The surface density of the large dust is tapered in the outer disk beyond 60 au as follows: $\Sigma' r = \Sigma r \exp r - r_{out} r_s$, if $r > r_{out}$, where r_{out} is 60 au and r_s is 5 au. The mass of the gas disk for the fiducial model is $4{\times}10^{-3}$ $M_\odot$, based on a total dust mass of $4{\times}10^{-5}$ $M_\odot$ or 13–14 $M_\oplus$ from Barenfeld et al. (2016) and a gas-to-dust mass ratio of 100. The chemistry and disk temperature are evolved for 10^6 years.

The initial composition of the gas is based on interstellar values. All volatile carbon is assumed to be in the form of gas-phase CO at an abundance of

1.4×10^{-4} relative to total H. Nitrogen starts in the form of gas-phase N at an abundance of 7.5×10^{-5}. The binding energies assumed for pure ices of CO and N_2 are 855 and 800 K, respectively (Bisschop et al. 2006). CO self-shielding is included in the model and we added self-shielding of N_2. N_2 shielding as a function of H, H_2, and N_2 column densities is determined by Heays et al. (2014).

We test the effects of two types of changes to the disk gas: (1) selective depletion of the initial CO gas abundance, and (2) a decrease in the total gas abundance where the relative abundances of chemical species remain at their initial interstellar values. We therefore run seven models including the fiducial model; models with initial CO abundances reduced by factors of 10×, 100×, and 1000×; and with total gas masses reduced by factors of 10×, 100×, and 1000×. In the models with initial CO depletion, the N and all other initial abundances are held constant at the fiducial levels. When the gas mass is reduced, the dust-to-gas mass ratio in the model is increased proportionally. Additional modeling described in Section 3.3.3 explores the effects of varying the disk temperature, nitrogen content, ionization, size, dust scale height, and lifetime. For a full list of models tested see Table 3.4.

3.3.2 Modeling of Line Ratios

As described in Section 3.3.1, the thermochemical disk models (Du and Bergin 2014) simulate a low mass, 13 $M_\oplus$, dust disk around a star similar to our Upper Sco sources for various disk gas masses and CO/H_2 abundance ratios. Figure 3.4 shows the disk gas and dust densities and resulting temperature and abundance distributions for CO, N_2, and N_2H^+ after 10^6 years for the fiducial model.

The model setup assumes an outer disk radius of 100 au and an inclination of 45° at a distance of 140 pc. Figure 3.5 shows the calculated line fluxes for CO J = 2–1 and N_2H^+ J = 3–2 in addition to ratios of the N_2H^+/CO and $N_2H^+/C^{18}O$ fluxes for various disk models in comparison to the observed values. $C^{18}O$ abundances are based on an assumed interstellar $^{18}O/^{16}O$ ratio of 0.002 relative to CO. Actual values may be up to 10× lower than simulated due to isotopic processes in the disk that were not included in our model (Visser et al. 2009; Miotello et al. 2014) producing lower $C^{18}O$ fluxes.

Our thermochemical models reveal distinct trends in spectral line ratios. CO

and $C^{18}O$ fluxes decrease with both the CO/H_2 abundance ratio (Fig. 3.5a, CO shown in red bars) and disk gas mass (Fig. 3.5b). However, whereas N_2H^+ fluxes also decrease with decreasing disk gas mass (Fig. 3.5b, shown in blue bars), they display the opposite behavior with regard to CO depletion (Fig. 3.5a). As the CO/H_2 ratio decreases, the N_2H^+/CO flux ratio increases significantly (Fig. 3.5a, shown in orange points). The increase in N_2H^+/CO is expected based on theoretical predictions of chemistry in such environments. It is not only due to the increase in relative N_2/CO abundances but also because when CO is abundant, it actively destroys N_2H^+ (Qi et al. 2013b, see Section 3.1). The $N_2H^+/C^{18}O$ flux ratios reinforce the trend with CO abundance (Fig. 3.5a, shown in light blue points). In comparison, decreasing the disk mass causes the N_2H^+/CO flux ratio to decrease to levels well below the observed values (Fig. 3.5b, shown in orange points). Rather than decreasing, the $N_2H^+/C^{18}O$ flux ratios appear to remain roughly constant with decreasing disk mass (Fig. 3.5b, shown in light blue points). This difference is caused by the relative optical depth of the species' emission. Modeled outer disk column densities of N_2H^+ and $C^{18}O$ indicate that the emission from these species is optically thin (or close to optically thin in the case of $C^{18}O$ for CO at interstellar abundances) and therefore traces the disk mass. When CO is abundant, its emission is optically thick, limiting its response to the decreasing disk mass.

Low CO fluxes can be achieved by either low CO abundances or low disk gas masses, but recreating the observed N_2H^+/CO values in Upper Sco requires sufficient H_2 gas in combination with CO depletion. According to the model grid shown in Fig. 3.5, CO depletion by 100–1000$\times$ relative to the interstellar abundance is required to reproduce the N_2H^+/CO flux ratios seen in J160823-193001 and J160900-190852. Similar CO depletion is also needed to exceed the lower limit of the $N_2H^+/C^{18}O$ flux ratio estimated for J160900-190852.

3.3.3 Alternative Scenarios

The N_2H^+/CO flux ratio will be sensitive to various physical and chemical parameters. The disk temperature structure, for example, will affect the location of CO and N_2 snowlines and determine the emitting regions of each species, while the initial abundances of N and C further set the observed flux ratios. The formation of N_2H^+ is also affected by the level of ionization in the disk. In this section, we aim to test whether or not these and other factors

Table 3.4: Model Variations.

Model	Varied parameters	Values
Fiducial with CO depletion	Initial CO abundance	1.4(-5),1.4(-6),1.4(-7) per total H
Fiducial with low mass	Disk mass	4(-4), 4(-5), 4(-6) $M_\odot$
	Gas-to-dust mass ratio	10, 1, 0.1
Low mass disk with high N	Initial N abundance	7.5(-4), 7.5(-2) per total H
	Disk mass	4(-6) $M_\odot$
	Gas-to-dust mass ratio	0.1
Low mass disk with high ionization	Cosmic-ray ionization rate	3(-16), 3(-14) s^{-1}
	Disk mass	4(-6) $M_\odot$
	Gas-to-dust mass ratio	0.1
Low mass disk with high stellar ionization	Stellar X-ray luminosity	1.6(32) s^{-1}
	Disk mass	4(-6) $M_\odot$
	Gas-to-dust mass ratio	0.1
Fiducial with low ionization	Cosmic-ray ionization rate	3(-19) s^{-1}
Smaller fiducial	Outer radius	50 au
Larger fiducial	Outer radius	200 au
Larger fiducial with high mass	Outer radius	200 au
	Disk mass	5(-2) $M_\odot$
	Gas-to-dust mass ratio	100
Cold disk	Scale height of large and small grain populations at r = 80 au	5 au
	Determination of vertical disk structure	Fixed
	*All variations above were also tested with this disk structure	Also included: Disk mass of 4(-2)$M_\odot$ Gas-to-dust = 1000
Settled disk (large dust)	Scale height of large grain population at r = 80 au	1, 2, 5, 10 au
	Determination of vertical disk structure	Fixed

Note: a(b) indicates a$\times 10^b$

alter our main result that, given our disk model, gas-rich disks with CO/H_2 substantially below the interstellar value are needed to explain high N_2H^+/CO flux ratios, such as those observed in the Upper Sco disks. First, we compare two different sets of physical disk models, the fiducial setup presented in the

previous section and a colder disk model, produced by enhanced grain settling. Next we evaluate two other possible explanations of the observed N_2H^+/CO flux ratios: enhanced N/C elemental abundances and enhanced disk ionization rates. Then we discuss the effects of disk size, the degree of dust settling, and the disk lifetime.

Spatial Origin of N_2H^+ Emission

The cold models differ from the previous model set by using a fixed vertical disk structure with the scale height of both the large and small dust set to 5 au at a radius of 80 au, rather than the hydrostatically supported disk. Compared to the fiducial model, which overproduces continuum emission in the far infrared, the cold disk better approximates the observed spectral energy distributions (SEDs; Figure 3.6). Reducing the vertical extent of the small dust population together with the large dust prevents mid-infrared fluxes from exceeding those observed. The cold disk structure and relevant chemical abundances are shown in Figure 3.7.

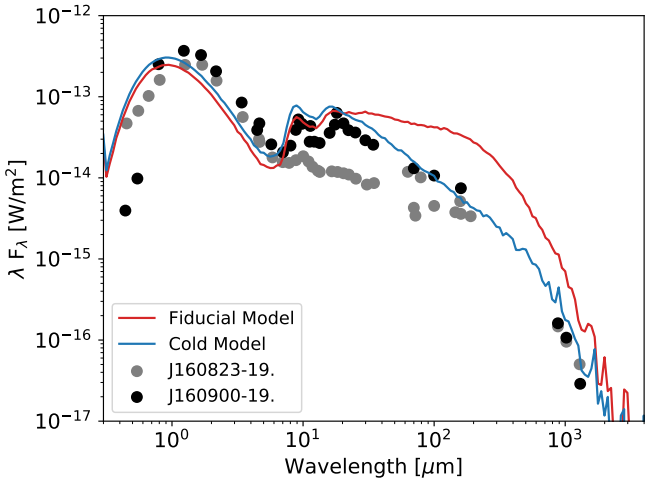

Figure 3.6: Modeled SEDs for fiducial (red line) and cold disk (blue line) models used in this work. SED data points are taken from the literature (Mathews et al. 2013, and data within).

In a sufficiently cold disk, CO freezeout allows N_2H^+ to form in abundance beyond the CO snowline as long as sufficient N_2 is present. N_2H^+ also originates from the surface layers, sensitive to the N_2/CO ratio as a result of self-shielding by both molecular species and the fact that N_2 has a slightly lower photodissociation rate (van 't Hoff et al. 2017). This N_2H^+ surface layer

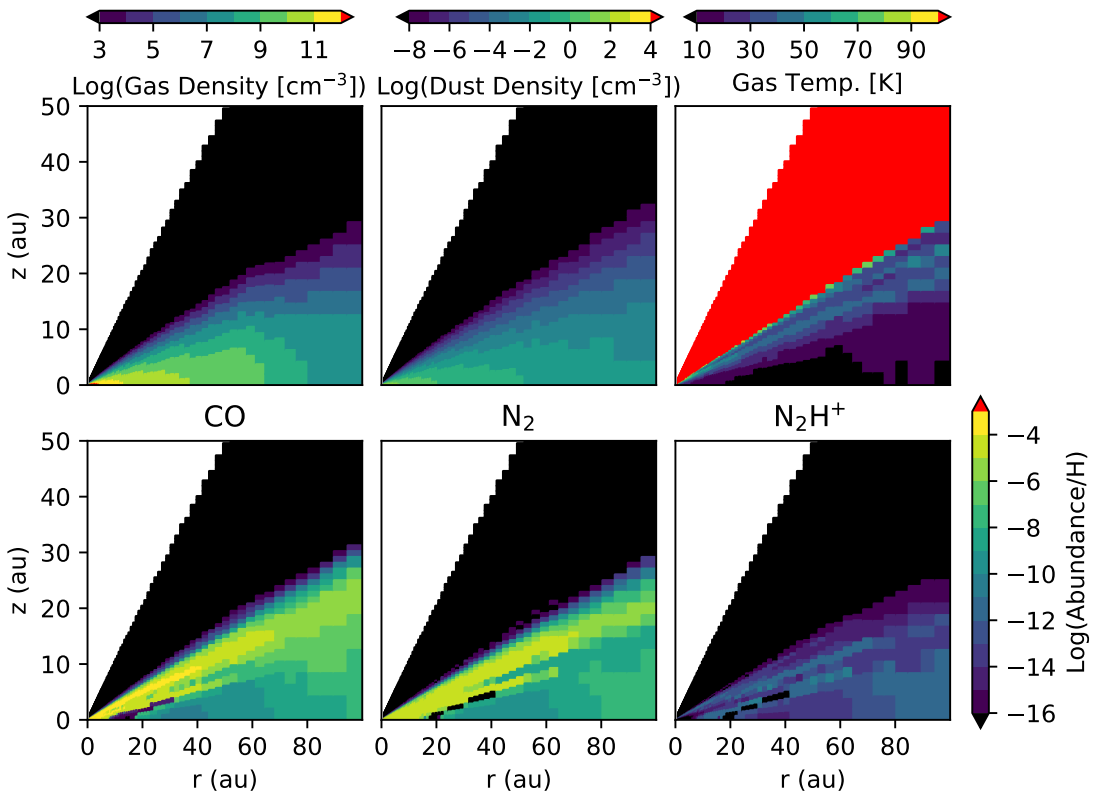

Figure 3.7: Disk gas density, dust density, gas temperature, and abundances of CO, N_2, and N_2H^+ after 1 Myr in our cold disk model.

exists for the less-settled fiducial disk models producing N_2H^+ emission even when the disk is too warm to have a CO snowline. The degree of settling in the cold disk models causes this surface layer to largely disappear. However, the temperatures in the cold disk model are also low enough to produce a CO snowline. These regions are consistent with the emerging interpretation of radial patterns of CO and N_2H^+ in disks (van 't Hoff et al. 2017). The location of the CO snow surface relative to the distribution of N_2H^+ in a selection of our models is shown in Figure 3.8. Ultimately, our model comparison shows that regardless of whether N_2H^+ originates from a limited region beyond the CO snowline (in the cold disk) or the surface layers of the disk (in the fiducial disk), the trends in the N_2H^+/CO and $N_2H^+/C^{18}O$ flux ratios are the same (Figures 3.5 and 3.9). These ratios increase as CO is selectively depleted and remain roughly constant or decrease with decreasing total gas content.

Whereas the cold models better approximate the SEDs, the models based on the fiducial setup provide higher line fluxes, which are needed to reproduce

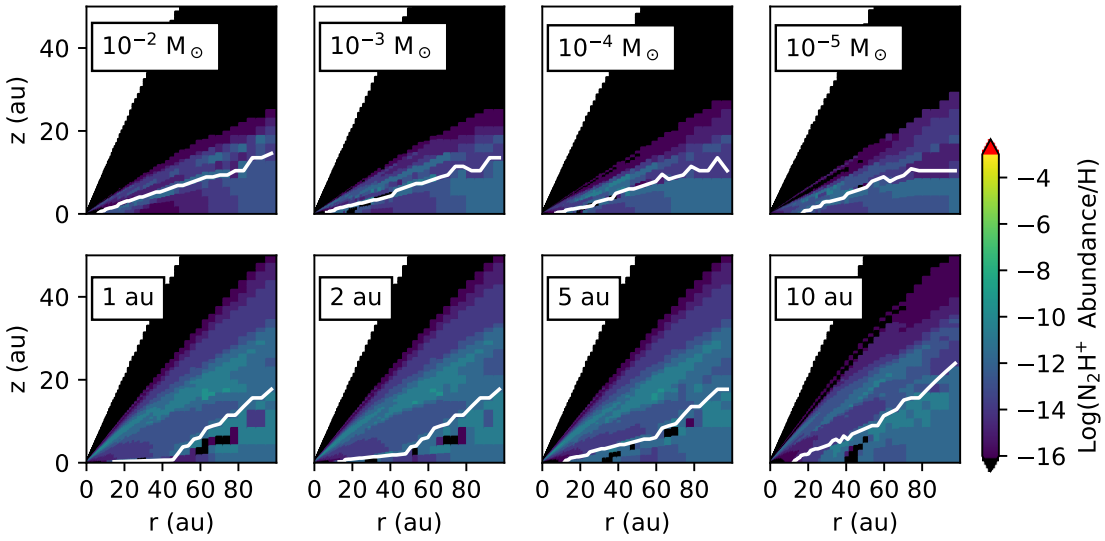

Figure 3.8: Location of the CO snow surface (indicated by the solid white line) plotted on top of the N_2H^+ abundance distribution in a subset of the disk models. The unsettled models based on the fiducial disk setup are too warm for a CO snowline to be present within 100 au with the exception of the high mass (10^{-2} M$_\odot$) disk models. This set of models is therefore not plotted. The CO snow surface location changes with the disk mass in the cold disk models (upper row). Furthermore, the degree of settling of the large dust relative to the fiducial model also affects the CO snow surface location (lower row). Panels are labeled in the top lefthand corner with the disk mass (upper row) or the scale height of the large dust at 80 au (lower row).

the N_2H^+ observations in the Upper Sco disks. Assuming a gas-to-dust mass ratio of 100, CO/H_2 depletion by 100-1000× is required to reach the observed N_2H^+/CO flux ratios. However, the absolute N_2H^+ and CO fluxes are underproduced for the cold disk conditions. Even after increasing the disk H_2 mass by a factor of 10, the predicted N_2H^+ flux is only 63 mJy km s^{-1} and CO is 260 mJy km s^{-1} for a CO/H_2 abundance of 10^{-7}. These values could further increase if the elemental N/C ratio and/or ionization rates in the disk are enhanced relative to our model assumptions. A complete exploration of this parameter space will be performed in future work.

Enhanced N/C and Disk Ionization

Without any CO depletion, achieving CO fluxes below 1000 mJy km s^{-1} requires gas-to-dust mass ratios 1000× below interstellar. We therefore ran test

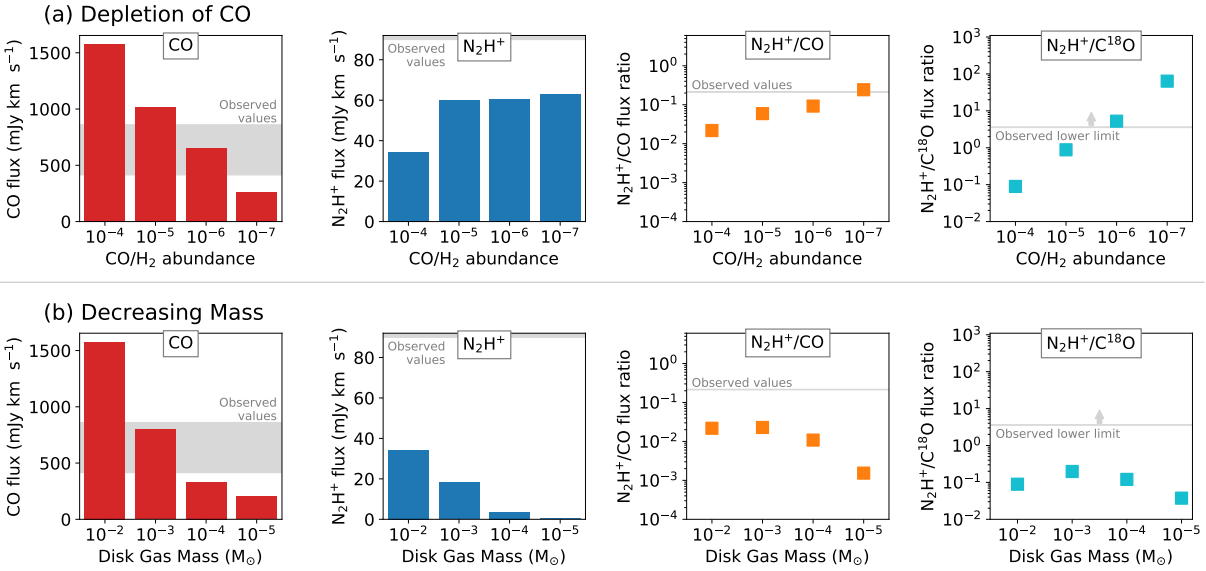

Figure 3.9: Calculated fluxes for our set of cold disk models. From left to right, the CO J=2–1 flux, N_2H^+ J=3–2 flux, ratio of the N_2H^+ J=3–2 to CO J=2–1 flux, and ratio of the N_2H^+ J=3–2 to $C^{18}O$ J=2–1 flux are plotted. Values are shown for the cold disk model with the gas mass increased by a factor of 10 (gas-to-dust mass ratio of 0.001) and additional models with this gas mass where the CO/H_2 abundance ratio is lowered by factors of 10–1000× (a) and for the high mass model and additional models where the disk gas mass is lowered by factors of 10–1000× (b). The range of observed values for the Upper Sco sources are show for comparison in gray.

models with a gas-to-dust ratio of 0.1 (gas mass of 4×10^{-6} $M_\odot$) to approximate the low CO flux observed in the Upper Sco disks for three additional scenarios: (1) increased initial N abundances of 7.5×10^{-4}–7.5×10^{-2} relative to H, 10–1000x× higher than the original model, (2) an increased cosmic-ray ionization rate of 3×10^{-16} s^{-1}–3×10^{-14} s^{-1}, 1–3 orders of magnitude above the interstellar value used in the original model, and (3) a stellar X-ray luminosity of 1.6×10^{32} erg s^{-1}, the maximum value associated with T Tauri stars (see Table 3.4). All three sets of changes produced higher N_2H^+ fluxes. Increasing the nitrogen content of the disk increased the N_2H^+ flux by a factor of ∼4 for N/H = 7.5×10^{-4} and ∼6 for N/H = 7.5×10^{-2} relative to the original 0.1 gas-to-dust ratio model. However, the N_2H^+/CO flux ratios of 0.002–0.003 and $N_2H^+/C^{18}O$ flux ratios of 0.17–0.25 remain too low to reproduce the observed Upper Sco values even when considering rather extreme nitrogen abundances. The same is true for the cold disk models with gas-to-dust ratios of 10–100.

Increasing the comic-ray ionization rates had a greater effect on the targeted flux ratios by enhancing the N_2H^+ flux while simultaneously decreasing the CO and $C^{18}O$ fluxes. N_2H^+/CO flux ratios increased to 0.01 for an ionization rate of 3×10^{-16} s^{-1} and 0.2 for 3×10^{-14} s^{-1} relative to the fiducial model. This is approaching the observed values in Upper Sco. The $N_2H^+/C^{18}O$ flux ratios were much greater, with values of 5–90. The cold disk models saw similar increases with a maximum of 0.08 and 13 for N_2H^+/CO and $N_2H^+/C^{18}O$, respectively, for an ionization rate of 3×10^{-14} s^{-1}. Nevertheless, the individual fluxes of N_2H^+ and CO were lower than in the previous gas-rich models with similar flux ratios. For the model with 1000× the interstellar cosmic-ray ionization rate and an N_2H^+/CO flux ratio at the lower end of the observed Upper Sco values, the N_2H^+ and CO fluxes were at least a factor of ∼3 below those observed in the weaker of the two Upper Sco disks. The cosmic-ray ionization rate is not well constrained in disks, but current observations of TW Hya suggest that the rate in this disk is low, less than 10^{-19} s^{-1} (Cleeves et al. 2015). Rates this low produce fluxes of $N_2H^+/C^{18}O = 0.02$ and N_2H^+/CO = 0.007 given our fiducial model setup.

Ionization from the central star could also affect the target flux ratios. Increasing the stellar X-ray luminosity to 1.6×10^{32} erg s^{-1} had little effect on the flux ratios relative to the fiducial model. However, it did increase the N_2H^+/CO flux ratio to 0.04–1.8 and $N_2H^+/C^{18}O$ flux ratio to 1–800 in the cold disk model for gas-to-dust ratios of 10–100. Although the upper end of these ratios exceeds the observed values, the absolute fluxes are too low to be consistent with observations (factor of 3–20× lower). Therefore, enhanced disk ionization alone is not enough to explain the high N_2H^+/CO flux ratios in the observed Upper Sco disks.

Disk Size

These model results depend on the assumed disk structure including the radial extent of gas and dust. Additional versions of the fiducial model were run with outer disk radii of 50 and 200 au (Table 3.4). The resulting N_2H^+/CO flux ratios were 0.01 and 0.005 for the 50 and 200 au cases, respectively. This compares to 0.01 for the fiducial model with an outer disk radius of 100 au and remains far below the observed values of 0.21–0.35 in Upper Sco. $N_2H^+/C^{18}O$ flux ratios remained at about 0.04–0.05 in the models of all three sizes. N_2H^+

and CO fluxes scaled roughly with the disk size, with the exception of the $C^{18}O$ and N_2H^+ fluxes being comparable for the 100 and 200 au disks. An additional model of a more massive disk with a total gas mass of 5×10^{-2} $M_\odot$ and an outer radius of 200 au was also run. The $N_2H^+/C^{18}O$ flux ratio for the massive disk was 0.15 and N_2H^+/CO was 0.02, which are still 10× lower than the observed values. Similarly minimal changes were seen in the flux ratios for the cold disk model in these cases. Altering the disk size does not appear to significantly alter the N_2H^+/CO flux ratio in the manner necessary to explain the observations.

Effects of Dust Settling

The median SED for disks in Upper Sco shows that on average these older disks are more settled than a typical disk from the Taurus region (Mathews et al. 2013). To approximate increased dust settling in the models, the large dust population was constrained to a lower scale height than the small dust. The small dust was set to have a scale height of 10 au at a radius of 80 au. Values of 1, 2, 5, and 10 au were used for the scale height of the large dust to test a range relative to the extent of the small dust and illustrate the effects of large dust settling on the target flux ratios. The resulting N_2H^+/CO and $N_2H^+/C^{18}O$ flux ratios varied from each other by a factor of $\lesssim$2 and were no greater than 5× the values from the fiducial model. Although the degree of large dust settling may alter the flux ratios, changes due to this factor alone are not enough to reproduce the observed flux ratios with our models.

Disk Lifetime

The models presented so far were run for 1 Myr as a representative timescale. However, at longer timescales of 1–10 Myr, additional chemical reactions become important, especially the conversion of CO and N_2 into less volatile species through destruction in the gas-phase by He^+ and/or reactions with H and OH on grain surfaces. The depletion of gas-phase CO through these reactions has been studied under a wide range of physical parameters in the disk (Bosman et al. 2018; Schwarz et al. 2018). The effectiveness of these reactions depends on the disk conditions, including the level of ionization in the disk. It is possible that this chemical depletion of CO may result in the low CO abundances needed to explain the observed fluxes in the Upper Sco disks, if

N_2 is impacted relatively less.

The relative depletion that occurs in the time period from 1 to 10 Myr of CO vs. N_2 differs between our fiducial and cold disk models. Adopting a timescale of 10 Myr results in higher N_2H^+ and lower CO and $C^{18}O$ fluxes in the fiducial model and lower fluxes for all three in the cold disk model. The flux values and the flux ratios of interest are changed by less than a factor of 10. Given the dependency of the late-stage chemical depletion of CO on disk conditions, a more comprehensive comparison of the relative depletion of CO and N_2 and how this alters the N_2H^+/CO and $N_2H^+/C^{18}O$ flux ratios is recommended for future work.

3.4 Discussion

3.4.1 Disk Comparison

The DISCS program probed the chemical composition of a diverse set of protoplanetary disks with a series of observations by the Sumbmilliter Array in 2009–2010. The observations targeted 10 different chemical species in six Taurus sources (DM Tau, AA Tau, LkCa 15, GM Aur, CQ Tau, and MWC 480) and six Southern sky sources (IM Lup, SAO 206462, HD 142527, AS 209, AS 205, and V4046 Sgr). The DISCS sample focuses on only large, CO-bright disks, such that they would be resolvable at a few hundred au by the SMA in the compact configuration. In addition, the chosen sources could be mapped in CO and disks with contaminating emission from the parent cloud were excluded based on previous observations. A range in spectral types and bolometric luminosities, accretion rates, X-ray luminosities, and disk geometries (disks with gaps or holes vs. full disks) are represented in the DISCS sample. The observed Upper Sco disks show distinct behavior in their relative N_2H^+ and CO fluxes from the entire sample, despite its diversity.

Acknowledging the uncertainties in stellar age, the majority of the sources targeted in the DISCS survey are similar or younger in age than the Upper Sco disks, which are estimated to be in the range of 5–11 Myr old (Preibisch et al. 2002; Pecaut et al. 2012). A portion of the DISCS disks are considered (pre-)transitional and show evidence of disk clearing via gaps or inner holes in their structures. J160823-193001 and J160900-190852 are not known to be transitional disks. Even so, the low dust masses and weak CO emission seen in the Upper Sco population are taken to be signs of disk evolution indicating

a progression toward transitional or debris-disk stages relative to disks from younger star-forming regions (Ansdell et al. 2017). A rough age comparison is shown for T Tauri sources in Fig. 3.3 based on values from the following sources: Kraus and Hillenbrand (2009); Andrews et al. (2010); Mawet et al. (2012); Miret-Roig et al. (2018); Sokal et al. (2018).

Because CO depletion has been proposed to be a time-dependent process (e.g., Favre et al. 2013), if N_2H^+/CO flux ratios are tracking CO depletion as predicted, and CO depletion increases over time, we would expect to see larger N_2H^+/CO flux ratios for older sources. In the middle panel of Fig. 3.3, we do not see a clear trend in the N_2H^+/CO flux ratios with stellar age. In particular, V4046 Sgr is part of the β Pictoris moving group with an estimated age of 13^{+7}_{-0} Myr (Miret-Roig et al. 2018) and therefore older than our Upper Sco targets, but has a lower value. However, this may be an effect caused by optically thick $^{12}C^{16}O$ emission and the circumbinary nature of the disk. In fact, the $N_2H^+/C^{18}O$ flux ratios do hint at a trend with age where the older disks (V4046 Sgr, TW Hya, and J160900-190852) have higher values than the younger disks (Fig. 3.3, bottom panel).

HD 163296 and MWC 480 do not fit within this trend, but they are also the only disks around Herbig Ae/Be stars in the sample with $C^{18}O$ measurements. We can therefore conclude that some environmental factors, such as the spectral type of the central star and its impact on the disk thermal structure, are likely important for determining the observed flux ratios and that further measurements are needed to investigate these potential trends with source parameters. Ultimately, given that the disks in Upper Sco differ in multiple ways from the other observed disks, having fainter CO and continuum fluxes and perhaps smaller sizes as well as advanced age, the primary cause of the differences in flux ratios is not yet clear.

Based on HD measurements, TW Hya, GM Aur, and DM Tau are found to have CO/H_2 ratios lower than interstellar by up to 5–100$\times$ (Bergin et al. 2013; McClure et al. 2016). Despite the observed CO depletion, these disks do not show enhanced N_2H^+/CO fluxes relative to the other DISCS sample targets. This again may be a result of the likely optically thick $^{12}C^{16}O$ emission in these large disks, preventing accurate comparisons of the N_2H^+/CO column densities based on flux. For TW Hya, where $C^{18}O$ emission is available, the $N_2H^+/C^{18}O$ flux does appear relatively high compared to other sources, the

younger sources in particular (Fig. 3.3).

3.4.2 Connections to Solar-System N & C Elemental Ratios

Bergin et al. (2015) highlights the low nitrogen-to-carbon ratios of bodies in our solar system. In the case of the Earth, complex processes occurring at various stages of planet formation including differentiation, metamorphism, atmospheric loss, and late delivery of materials can affect the final composition. However, the amount of processing is more limited for primitive meteorites and comets, placing a larger emphasis on accretion of materials and processing occurring within the protoplanetary disk. Observations of comets have found N_2/CO ratios below the solar nebula value of 0.15, ranging from a comparable value of N_2/CO$\sim$0.08 for comet C/2016 R2 to the highly depleted value of $<6\times10^{-5}$ in Hale-Bopp (Cochran et al. 2000; Biver et al. 2018). An in situ measurement by ROSINA, the mass spectrometer on board the *Rosetta* spacecraft, determined a N_2/CO ratio of 5.7×10^{-3} for comet 67P/Churyumov-Gerasimenko (Rubin et al. 2015). This is $\sim$25$\times$ below the estimated value for the solar nebula.

Photodesorption of mixed layered ices can result in the enhanced release of some chemical species relative to others. Bertin et al. (2013) consider the scenario where N_2 condenses at a slightly lower temperature (2 K less) than CO and deposits as a thin layer of N_2 on top of an existing CO-rich ice. This results in decreased CO and increased N_2 photodesorption rates according to their laboratory experiments. They propose this scenario as an explanation for nitrogen-enriched gas in dense cores where N_2 depletion onto grains appears to occur at higher densities than for CO (Bergin et al. 2002; Pagani et al. 2005, 2012). Such a mechanism could release enhanced levels of nitrogen into the gas while CO remains frozen onto grain surfaces and becomes incorporated into forming planestimals with a greater efficiency. Such a scenario is consistent with both the low nitrogen content relative to carbon in primitive solar system bodies in addition to the high N_2H^+/CO fluxes observed in the Upper Sco disks. This correlation may indicate that similar chemical evolution of the gas occurred in the solar nebula and the Upper Sco disks.

3.5 Conclusion

Here we present the detection of N_2H^+ J=3–2 emission in two disks in the Upper Scorpius region. Ionized H_2 gas is necessary for the main N_2H^+ pro-

duction reaction, therefore revealing these disks to still be rich in primordial gas at their age of ∼5–11 Myr. Previous ALMA observations found the disks in Upper Sco to have weaker CO and continuum emission relative to younger star-forming regions, presumably as a result of disk evolution (Barenfeld et al. 2016, 2017; Ansdell et al. 2017). The two disks observed here have higher N_2H^+/CO flux ratios than previously observed CO-bright disks. This may be the result of disk evolution, indicating different chemical and/or physical pathways for nitrogen- and carbon-bearing species. Line fluxes predicted by the thermochemical model show that enhanced N_2H^+/CO emission can by explained by selective CO depletion relative to H_2. The resulting high nitrogen-to-carbon content in the gas would correspond to low nitrogen-to-carbon ratios in solids forming in the disk, consistent with trends in elemental abundances of meteorites and comets in our solar system compared to the Sun (Bergin et al. 2015). This connection may hint at similar evolutionary pathways existing in the Upper Sco disks and the solar nebula.

Our basic set of thermochemical disk models show that low CO fluxes can be achieved via total gas depletion or selective depletion of CO, but the N_2H^+ fluxes of the observed Upper Sco disks can only be explained by relatively high disk gas masses in combination with removal of CO. Without the additional constraints provided by N_2H^+, the disk gas mass would be severely underpredicted in the case of CO depletion. However, time-dependent loss of CO via disk evolution similar to that proposed in TW Hya may not be the only explanation for the enhanced N_2H^+/CO flux ratios. Individual disk environments including initial gas composition, ionization, temperature structure, and timescales of disk evolution may also influence these flux ratios. Further study of a larger sample of disks is required to constrain the effects of these additional parameters. Disks that are suspected to be CO-depleted based on comparisons of CO measurements to other indicators of the total disk mass may be particularly interesting targets for N_2H^+ follow-up observations. Regardless, the N_2H^+ observations here indicate that the bright protoplanetary disks often targeted for observational studies are not fully representative of the ∼5–11 Myr old, weak-CO-emitting disks in Upper Sco. The gas chemistry (and/or physical structure) of these Upper Sco disks differs in an observable way due to their disk conditions and/or evolutionary stage.

The investigation of volatile species beyond CO is crucial for understanding

how disks evolve chemically and physically. This is particularly true if CO depletion is a widespread phenomenon among disk populations even at young ages. N_2H^+ provides additional information regarding the disk composition and/or physical structure and warrants further investigation.

3.6 Acknowledgments

This material is based upon work supported by the National Science Foundation Graduate Research Fellowship under Grant No. DGE-1144469 and funding from NSF grants AST-1514670 and AST-1344133 (INSPIRE) as well as NASA NNX16AB48G. J.C. acknowledge support from the National Aeronautics and Space Administration under grant No. 15XRP15_20140 issued through the Exoplanets Research Program. K.Z. acknowledges the support of NASA through Hubble Fellowship grant HST-HF2-51401.001-A. J.H. acknowledges support from the National Science Foundation Graduate Research Fellowship under Grant No. DGE-1144152. This work makes use of the following ALMA data:
ADS/JAO.ALMA#2015.1.01199.S,
ADS/JAO.ALMA#2011.0.00526.S, and
ADS/JAO.ALMA#2015.1.00964.S,
ADS/JAO.ALMA#2013.1.00226.S. ALMA is a partnership of ESO (representing its member states), NSF (USA) and NINS (Japan), together with NRC (Canada), MOST and ASIAA (Taiwan), and KASI (Republic of Korea), in cooperation with the Republic of Chile. The Joint ALMA Observatory is operated by ESO, AUI/NRAO and NAOJ. The National Radio Astronomy Observatory is a facility of the National Science Foundation operated under cooperative agreement by Associated Universities, Inc. We thank NRAO for assistance with data reduction and the anonymous reviewer for critically reading the manuscript and providing insightful feedback.

3.7 Appendix

Figure 3.A1 shows the moment 1 maps of N_2H^+ and CO emission from the observed Upper Sco disks.

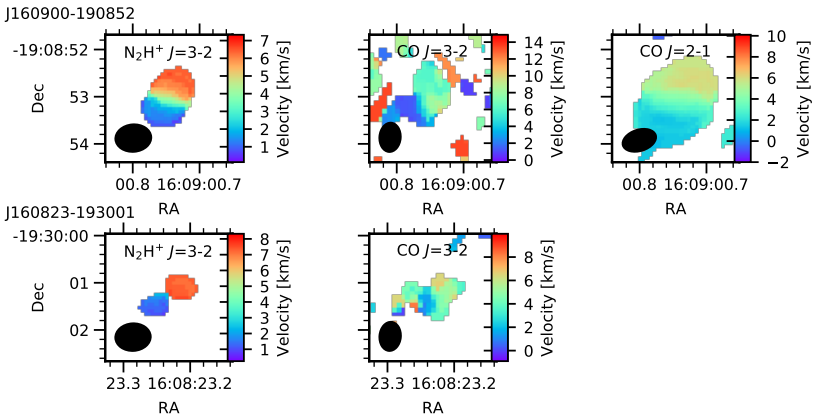

Figure 3.A1: Moment 1 maps of N_2H^+ and CO emission from the Upper Sco disks J160900-190852 (top row) and J160823-193001 (bottom row).

REFERENCES

Y. Aikawa, K. Furuya, H. Nomura, and C. Qi. Analytical Formulae of Molecular Ion Abundances and the N_2H^+ Ring in Protoplanetary Disks. *ApJ*, 807: 120, July 2015. doi: 10.1088/0004-637X/807/2/120.

R. Alexander, I. Pascucci, S. Andrews, P. Armitage, and L. Cieza. The Dispersal of Protoplanetary Disks. *Protostars and Planets VI*, pages 475–496, 2014. doi: 10.2458/azu_uapress_9780816531240-ch021.

S. M. Andrews, D. J. Wilner, A. M. Hughes, C. Qi, and C. P. Dullemond. Protoplanetary Disk Structures in Ophiuchus. II. Extension to Fainter Sources. *ApJ*, 723:1241–1254, November 2010. doi: 10.1088/0004-637X/723/2/1241.

S. M. Andrews, D. J. Wilner, A. M. Hughes, C. Qi, K. A. Rosenfeld, K. I. Öberg, T. Birnstiel, C. Espaillat, L. A. Cieza, J. P. Williams, S.-Y. Lin, and P. T. P. Ho. The TW Hya Disk at 870 μm: Comparison of CO and Dust Radial Structures. *ApJ*, 744:162, January 2012. doi: 10.1088/0004-637X/744/2/162.

M. Ansdell, J. P. Williams, N. van der Marel, J. M. Carpenter, G. Guidi, M. Hogerheijde, G. S. Mathews, C. F. Manara, A. Miotello, A. Natta, I. Oliveira, M. Tazzari, L. Testi, E. F. van Dishoeck, and S. E. van Terwisga. ALMA Survey of Lupus Protoplanetary Disks. I. Dust and Gas Masses. *ApJ*, 828:46, September 2016. doi: 10.3847/0004-637X/828/1/46.

M. Ansdell, J. P. Williams, C. F. Manara, A. Miotello, S. Facchini, N. van der Marel, L. Testi, and E. F. van Dishoeck. An ALMA Survey of Protoplanetary Disks in the σ Orionis Cluster. *AJ*, 153:240, May 2017. doi: 10.3847/1538-3881/aa69c0.

S. A. Barenfeld, J. M. Carpenter, L. Ricci, and A. Isella. ALMA Observations of Circumstellar Disks in the Upper Scorpius OB Association. *ApJ*, 827:142, August 2016. doi: 10.3847/0004-637X/827/2/142.

S. A. Barenfeld, J. M. Carpenter, A. I. Sargent, A. Isella, and L. Ricci. Measurement of Circumstellar Disk Sizes in the Upper Scorpius OB Association with ALMA. *ApJ*, 851:85, December 2017. doi: 10.3847/1538-4357/aa989d.

E. A. Bergin, J. Alves, T. Huard, and C. J. Lada. N_2H^+ and $C^{18}O$ Depletion in a Cold Dark Cloud. *ApJ*, 570:L101–L104, May 2002. doi: 10.1086/340950.

E. A. Bergin, L. I. Cleeves, U. Gorti, K. Zhang, G. A. Blake, J. D. Green, S. M. Andrews, N. J. Evans, II, T. Henning, K. Öberg, K. Pontoppidan, C. Qi, C. Salyk, and E. F. van Dishoeck. An old disk still capable of forming a planetary system. *Nature*, 493:644–646, January 2013. doi: 10.1038/nature11805.

E. A. Bergin, L. I. Cleeves, N. Crockett, and G. A. Blake. Exploring the Origins of Carbon in Terrestrial Worlds. *Faraday Discussions*, 168, February 2014. doi: 10.1039/C4FD00003J.

E. A. Bergin, G. A. Blake, F. Ciesla, M. M. Hirschmann, and J. Li. Tracing the ingredients for a habitable earth from interstellar space through planet formation. *Proceedings of the National Academy of Science*, 112:8965–8970, July 2015. doi: 10.1073/pnas.1500954112.

M. Bertin, E. C. Fayolle, C. Romanzin, H. A. M. Poderoso, X. Michaut, L. Philippe, P. Jeseck, K. I. Öberg, H. Linnartz, and J.-H. Fillion. Indirect Ultraviolet Photodesorption from CO:N_2 Binary Ices — an Efficient Grain-gas Process. *ApJ*, 779:120, December 2013. doi: 10.1088/0004-637X/779/2/120.

S. E. Bisschop, H. J. Fraser, K. I. Öberg, E. F. van Dishoeck, and S. Schlemmer. Desorption rates and sticking coefficients for CO and N_2 interstellar ices. *A&A*, 449:1297–1309, April 2006. doi: 10.1051/0004-6361:20054051.

N. Biver, D. Bockelée-Morvan, G. Paubert, R. Moreno, J. Crovisier, J. Boissier, E. Bertrand, H. Boussier, F. Kugel, A. McKay, N. Dello Russo, and M. A. DiSanti. The extraordinary composition of the blue comet C/2016 R2 (PanSTARRS). *A&A*, 619:A127, November 2018. doi: 10.1051/0004-6361/201833449.

A. D. Bosman, C. Walsh, and E. F. van Dishoeck. CO destruction in protoplanetary disk midplanes: Inside versus outside the CO snow surface. *A&A*, 618:A182, October 2018. doi: 10.1051/0004-6361/201833497.

J. M. Carpenter, L. Ricci, and A. Isella. An ALMA Continuum Survey of Circumstellar Disks in the Upper Scorpius OB Association. *ApJ*, 787:42, May 2014. doi: 10.1088/0004-637X/787/1/42.

L. I. Cleeves, E. A. Bergin, C. Qi, F. C. Adams, and K. I. Öberg. Constraining the X-Ray and Cosmic-Ray Ionization Chemistry of the TW Hya Protoplanetary Disk: Evidence for a Sub-interstellar Cosmic-Ray Rate. *ApJ*, 799:204, February 2015. doi: 10.1088/0004-637X/799/2/204.

L. I. Cleeves, K. I. Öberg, D. J. Wilner, J. Huang, R. A. Loomis, S. M. Andrews, and I. Czekala. The Coupled Physical Structure of Gas and Dust in the IM Lup Protoplanetary Disk. *ApJ*, 832:110, December 2016. doi: 10.3847/0004-637X/832/2/110.

A. L. Cochran, W. D. Cochran, and E. S. Barker. N^+_2 and CO^+ in Comets 122P/1995 S1 (deVico) and C/1995 O1 (Hale-Bopp). *Icarus*, 146:583–593, August 2000. doi: 10.1006/icar.2000.6413.

F. Du and E. A. Bergin. Water Vapor Distribution in Protoplanetary Disks. *ApJ*, 792:2, September 2014. doi: 10.1088/0004-637X/792/1/2.

C. Favre, L. I. Cleeves, E. A. Bergin, C. Qi, and G. A. Blake. A Significantly Low CO Abundance toward the TW Hya Protoplanetary Disk: A Path to Active Carbon Chemistry? *ApJ*, 776:L38, October 2013. doi: 10.1088/2041-8205/776/2/L38.

E. C. Fayolle, J. Balfe, R. Loomis, J. Bergner, D. Graninger, M. Rajappan, and K. I. Öberg. N_2 and CO Desorption Energies from Water Ice. *ApJ*, 816: L28, January 2016. doi: 10.3847/2041-8205/816/2/L28.

N. Fray, A. Bardyn, H. Cottin, D. Baklouti, C. Briois, C. Engrand, H. Fischer, K. Hornung, R. Isnard, Y. Langevin, H. Lehto, L. Le Roy, E. M. Mellado, S. Merouane, P. Modica, F.-R. Orthous-Daunay, J. Paquette, J. Rynö, R. Schulz, J. Silén, S. Siljeström, O. Stenzel, L. Thirkell, K. Varmuza, B. Zaprudin, J. Kissel, and M. Hilchenbach. Nitrogen-to-carbon atomic ratio measured by COSIMA in the particles of comet 67P/Churyumov-Gerasimenko. *MNRAS*, 469:S506–S516, July 2017. doi: 10.1093/mnras/stx2002.

Gaia Collaboration, A. G. A. Brown, A. Vallenari, T. Prusti, J. H. J. de Bruijne, C. Babusiaux, C. A. L. Bailer-Jones, M. Biermann, D. W. Evans, L. Eyer, and et al. Gaia Data Release 2. Summary of the contents and survey properties. *A&A*, 616:A1, August 2018. doi: 10.1051/0004-6361/201833051.

U. Gorti, C. P. Dullemond, and D. Hollenbach. Time Evolution of Viscous Circumstellar Disks due to Photoevaporation by Far-Ultraviolet, Extreme-Ultraviolet, and X-ray Radiation from the Central Star. *ApJ*, 705:1237–1251, November 2009. doi: 10.1088/0004-637X/705/2/1237.

S. Guilloteau, L. Reboussin, A. Dutrey, E. Chapillon, V. Wakelam, V. Piétu, E. Di Folco, D. Semenov, and T. Henning. Chemistry in disks. X. The molecular content of protoplanetary disks in Taurus. *A&A*, 592:A124, August 2016. doi: 10.1051/0004-6361/201527088.

A. N. Heays, R. Visser, R. Gredel, W. Ubachs, B. R. Lewis, S. T. Gibson, and E. F. van Dishoeck. Isotope selective photodissociation of N_2 by the interstellar radiation field and cosmic rays. *A&A*, 562:A61, February 2014. doi: 10.1051/0004-6361/201322832.

K. L. Heritier, K. Altwegg, H. Balsiger, J.-J. Berthelier, A. Beth, A. Bieler, N. Biver, U. Calmonte, M. R. Combi, J. De Keyser, A. I. Eriksson, B. Fiethe, N. Fougere, S. A. Fuselier, M. Galand, S. Gasc, T. I. Gombosi, K. C. Hansen, M. Hassig, E. Kopp, E. Odelstad, M. Rubin, C.-Y. Tzou, E. Vigren, and V. Vuitton. Ion composition at comet 67P near perihelion: Rosetta observations and model-based interpretation. *MNRAS*, 469:S427–S442, July 2017. doi: 10.1093/mnras/stx1912.

J. Huang, K. I. Öberg, and S. M. Andrews. Evidence for a CO Desorption Front in the Outer AS 209 Disk. *ApJ*, 823:L18, May 2016. doi: 10.3847/2041-8205/823/1/L18.

J. Huang, K. I. Öberg, C. Qi, Y. Aikawa, S. M. Andrews, K. Furuya, V. V. Guzmán, R. A. Loomis, E. F. van Dishoeck, and D. J. Wilner. An ALMA Survey of DCN/$H^{13}CN$ and $DCO^+/H^{13}CO^+$ in Protoplanetary Disks. *ApJ*, 835:231, February 2017. doi: 10.3847/1538-4357/835/2/231.

J. H. Kastner, C. Qi, D. A. Dickson-Vandervelde, P. Hily-Blant, T. Forveille, S. Andrews, U. Gorti, K. Öberg, and D. Wilner. A Subarcsecond ALMA Molecular Line Imaging Survey of the Circumbinary, Protoplanetary Disk Orbiting V4046 Sgr. *ApJ*, 863:106, August 2018. doi: 10.3847/1538-4357/aacff7.

A. L. Kraus and L. A. Hillenbrand. The Coevality of Young Binary Systems. *ApJ*, 704:531–547, October 2009. doi: 10.1088/0004-637X/704/1/531.

S. Krijt, K. R. Schwarz, E. A. Bergin, and F. J. Ciesla. Transport of CO in Protoplanetary Disks: Consequences of Pebble Formation, Settling, and Radial Drift. *ApJ*, 864:78, September 2018. doi: 10.3847/1538-4357/aad69b.

E. J. Lee and E. Chiang. Breeding Super-Earths and Birthing Super-puffs in Transitional Disks. *ApJ*, 817:90, February 2016. doi: 10.3847/0004-637X/817/2/90.

F. Long, G. J. Herczeg, I. Pascucci, E. Drabek-Maunder, S. Mohanty, L. Testi, D. Apai, N. Hendler, T. Henning, C. F. Manara, and G. D. Mulders. An ALMA Survey of CO Isotopologue Emission from Protoplanetary Disks in Chamaeleon I. *ApJ*, 844:99, August 2017. doi: 10.3847/1538-4357/aa78fc.

G. S. Mathews, C. Pinte, G. Duchêne, J. P. Williams, and F. Ménard. A Herschel PACS survey of the dust and gas in Upper Scorpius disks. *A&A*, 558:A66, October 2013. doi: 10.1051/0004-6361/201321228.

D. Mawet, O. Absil, G. Montagnier, P. Riaud, J. Surdej, C. Ducourant, J.-C. Augereau, S. Röttinger, J. Girard, J. Krist, and K. Stapelfeldt. Direct imaging of extra-solar planets in star forming regions. Lessons learned from a false positive around IM Lupi. *A&A*, 544:A131, August 2012. doi: 10.1051/0004-6361/201219662.

M. K. McClure, E. A. Bergin, L. I. Cleeves, E. F. van Dishoeck, G. A. Blake, N. J. Evans, II, J. D. Green, T. Henning, K. I. Öberg, K. M. Pontoppidan, and C. Salyk. Mass Measurements in Protoplanetary Disks from Hydrogen Deuteride. *ApJ*, 831:167, November 2016. doi: 10.3847/0004-637X/831/2/167.

J. P. McMullin, B. Waters, D. Schiebel, W. Young, and K. Golap. CASA Architecture and Applications. In R. A. Shaw, F. Hill, and D. J. Bell, editors, *Astronomical Data Analysis Software and Systems XVI*, volume 376 of *Astronomical Society of the Pacific Conference Series*, page 127, October 2007.

A. Miotello, S. Bruderer, and E. F. van Dishoeck. Protoplanetary disk masses from CO isotopologue line emission. *A&A*, 572:A96, December 2014. doi: 10.1051/0004-6361/201424712.

N. Miret-Roig, T. Antoja, M. Romero-Gómez, and F. Figueras. Dynamical ages of the young local associations with Gaia. *A&A*, 615:A51, July 2018. doi: 10.1051/0004-6361/201731976.

K. I. Öberg, C. Qi, J. K. J. Fogel, E. A. Bergin, S. M. Andrews, C. Espaillat, T. A. van Kempen, D. J. Wilner, and I. Pascucci. The Disk Imaging Survey of Chemistry with SMA. I. Taurus Protoplanetary Disk Data. *ApJ*, 720: 480–493, September 2010. doi: 10.1088/0004-637X/720/1/480.

K. I. Öberg, C. Qi, J. K. J. Fogel, E. A. Bergin, S. M. Andrews, C. Espaillat, D. J. Wilner, I. Pascucci, and J. H. Kastner. Disk Imaging Survey of Chemistry with SMA. II. Southern Sky Protoplanetary Disk Data and Full Sample Statistics. *ApJ*, 734:98, June 2011. doi: 10.1088/0004-637X/734/2/98.

L. Pagani, J.-R. Pardo, A. J. Apponi, A. Bacmann, and S. Cabrit. L183 (L134N) revisited. III. The gas depletion. *A&A*, 429:181–192, January 2005. doi: 10.1051/0004-6361:20041044.

L. Pagani, A. Bourgoin, and F. Lique. A method to measure CO and N_2 depletion profiles inside prestellar cores. *A&A*, 548:L4, December 2012. doi: 10.1051/0004-6361/201220137.

I. Pascucci, M. Sterzik, R. D. Alexander, S. H. P. Alencar, U. Gorti, D. Hollenbach, J. Owen, B. Ercolano, and S. Edwards. The Photoevaporative Wind from the Disk of TW Hya. *ApJ*, 736:13, July 2011. doi: 10.1088/0004-637X/736/1/13.

M. J. Pecaut, E. E. Mamajek, and E. J. Bubar. A Revised Age for Upper Scorpius and the Star Formation History among the F-type Members of the Scorpius-Centaurus OB Association. *ApJ*, 746:154, February 2012. doi: 10.1088/0004-637X/746/2/154.

J. B. Pollack, O. Hubickyj, P. Bodenheimer, J. J. Lissauer, M. Podolak, and Y. Greenzweig. Formation of the Giant Planets by Concurrent Accretion of Solids and Gas. *Icarus*, 124:62–85, November 1996. doi: 10.1006/icar.1996.0190.

T. Preibisch, A. G. A. Brown, T. Bridges, E. Guenther, and H. Zinnecker. Exploring the Full Stellar Population of the Upper Scorpius OB Association. *AJ*, 124:404–416, July 2002. doi: 10.1086/341174.

C. Qi, K. I. Öberg, and D. J. Wilner. H_2CO and N_2H^+ in Protoplanetary Disks: Evidence for a CO-ice Regulated Chemistry. *ApJ*, 765:34, March 2013a. doi: 10.1088/0004-637X/765/1/34.

C. Qi, K. I. Öberg, D. J. Wilner, P. D'Alessio, E. Bergin, S. M. Andrews, G. A. Blake, M. R. Hogerheijde, and E. F. van Dishoeck. Imaging of the CO Snow Line in a Solar Nebula Analog. *Science*, 341:630–632, August 2013b. doi: 10.1126/science.1239560.

C. Qi, K. I. Öberg, S. M. Andrews, D. J. Wilner, E. A. Bergin, A. M. Hughes, M. Hogherheijde, and P. D'Alessio. Chemical Imaging of the CO Snow Line in the HD 163296 Disk. *ApJ*, 813:128, November 2015. doi: 10.1088/0004-637X/813/2/128.

L. Reboussin, V. Wakelam, S. Guilloteau, F. Hersant, and A. Dutrey. Chemistry in protoplanetary disks: the gas-phase CO/H_2 ratio and the carbon reservoir. *A&A*, 579:A82, July 2015. doi: 10.1051/0004-6361/201525885.

K. A. Rosenfeld, C. Qi, S. M. Andrews, D. J. Wilner, S. A. Corder, C. P. Dullemond, S.-Y. Lin, A. M. Hughes, P. D'Alessio, and P. T. P. Ho. Kinematics of the CO Gas in the Inner Regions of the TW Hya Disk. *ApJ*, 757: 129, October 2012. doi: 10.1088/0004-637X/757/2/129.

K. A. Rosenfeld, S. M. Andrews, A. M. Hughes, D. J. Wilner, and C. Qi. A Spatially Resolved Vertical Temperature Gradient in the HD 163296 Disk. *ApJ*, 774:16, September 2013. doi: 10.1088/0004-637X/774/1/16.

M. Rubin, K. Altwegg, H. Balsiger, A. Bar-Nun, J.-J. Berthelier, A. Bieler, P. Bochsler, C. Briois, U. Calmonte, M. Combi, J. De Keyser, F. Dhooghe, P. Eberhardt, B. Fiethe, S. A. Fuselier, S. Gasc, T. I. Gombosi, K. C. Hansen, M. Hässig, A. Jäckel, E. Kopp, A. Korth, L. Le Roy, U. Mall, B. Marty, O. Mousis, T. Owen, H. Rème, T. Sémon, C.-Y. Tzou, J. H. Waite, and P. Wurz. Molecular nitrogen in comet 67P/Churyumov-Gerasimenko indicates a low formation temperature. *Science*, 348:232–235, April 2015. doi: 10.1126/science.aaa6100.

K. R. Schwarz and E. A. Bergin. The Effects of Initial Abundances on Nitrogen in Protoplanetary Disks. *ApJ*, 797:113, December 2014. doi: 10.1088/0004-637X/797/2/113.

K. R. Schwarz, E. A. Bergin, L. I. Cleeves, G. A. Blake, K. Zhang, K. I. Öberg, E. F. van Dishoeck, and C. Qi. The Radial Distribution of H_2 and CO in TW Hya as Revealed by Resolved ALMA Observations of CO Isotopologues. *ApJ*, 823:91, June 2016. doi: 10.3847/0004-637X/823/2/91.

K. R. Schwarz, E. A. Bergin, L. I. Cleeves, K. Zhang, K. I. Öberg, G. A. Blake, and D. Anderson. Unlocking CO Depletion in Protoplanetary Disks. I. The Warm Molecular Layer. *ApJ*, 856:85, March 2018. doi: 10.3847/1538-4357/aaae08.

K. R. Sokal, C. P. Deen, G. N. Mace, J.-J. Lee, H. Oh, H. Kim, B. T. Kidder, and D. T. Jaffe. Characterizing TW Hydra. *ApJ*, 853:120, February 2018. doi: 10.3847/1538-4357/aaa1e4.

M. L. R. van 't Hoff, C. Walsh, M. Kama, S. Facchini, and E. F. van Dishoeck. Robustness of N_2H^+ as tracer of the CO snowline. *A&A*, 599:A101, March 2017. doi: 10.1051/0004-6361/201629452.

R. Visser, E. F. van Dishoeck, and J. H. Black. The photodissociation and chemistry of CO isotopologues: applications to interstellar clouds and circumstellar disks. *A&A*, 503:323–343, August 2009. doi: 10.1051/0004-6361/200912129.

S. J. Weidenschilling and J. N. Cuzzi. Formation of planetesimals in the solar nebula. In E. H. Levy and J. I. Lunine, editors, *Protostars and Planets III*, pages 1031–1060, 1993.

A. N. Youdin and J. Goodman. Streaming Instabilities in Protoplanetary Disks. *ApJ*, 620:459–469, February 2005. doi: 10.1086/426895.

M. Yu, K. Willacy, S. E. Dodson-Robinson, N. J. Turner, and N. J. Evans, II. Probing Planet Forming Zones with Rare CO Isotopologues. *ApJ*, 822:53, May 2016. doi: 10.3847/0004-637X/822/1/53.

K. Zhang, A. Isella, J. M. Carpenter, and G. A. Blake. Comparison of the Dust and Gas Radial Structure in the Transition Disk [PZ99] J160421.7-213028. *ApJ*, 791:42, August 2014. doi: 10.1088/0004-637X/791/1/42.

K. Zhang, E. A. Bergin, G. A. Blake, L. I. Cleeves, and K. R. Schwarz. Mass inventory of the giant-planet formation zone in a solar nebula analogue. *Nature Astronomy*, 1:0130, June 2017. doi: 10.1038/s41550-017-0130.

Chapter 4

CONSTRAINING GAS MASSES OF CO-DEPLETED DISKS WITH MULTIPLE TRACERS

Dana E. Anderson[1], Geoffrey A. Blake[1], Ke Zhang[2,3] & Edwin A. Bergin[2]

[1]Division of Geological and Planetary Sciences, California Institute of Technology, 1200 E. California Blvd., Pasadena, CA 91125, USA
[2]Department of Astronomy, University of Michigan, 1085 S. University, Ann Arbor, MI 48109, USA
[3]Hubble Fellow

Abstract Accurate measurement of disk masses is crucial for determining when and where various stages of planet formation can occur. The relation between canonical gas tracers, including rotational line emission from CO isotopologues, and the total amount of H_2 may vary with time, location in the disk, and among different sources. In particular, measured CO/H_2 ratios in disks are up to two orders of magnitude below the interstellar value of 10^{-4}. Estimating disk masses based on CO and its derivatives results in a range of possible values because of the uncertainty in CO abundance. Additional tracers that do not strictly follow the behavior of CO are needed to break this degeneracy. N_2H^+ is one potential candidate from a limited number of non-carbon-bearing chemical species detected in protoplanetary disks. We model emission of N_2H^+, HCO^+, and $C^{18}O$ from disks of various masses, CO abundances, and cosmic-ray ionizations rates. Whereas $C^{18}O$ and HCO^+ fluxes can be matched by multiple combinations of mass and CO abundance, N_2H^+ provides additional constraints. Furthermore, the ratio of optically thin $N_2H^+/C^{18}O$ emission is relatively stable with disk mass but sensitive to the CO abundance. Combining these tracers provides one potential way of correcting for CO depletion in mass estimates for disks where nitrogen-bearing species are not (as) depleted. However, ionization remains a confounding factor. Further characterization of the behavior of N_2H^+ in a wide variety of sources is needed to determine the accuracy and applicability of this method.

4.1 Introduction

The lifetime of primordial gas in circumstellar disks provides constraints on timescales relevant to the formation of our solar system and planets overall. According to the core accretion theory of planet formation, gas-giants such as Jupiter and Saturn must grow sufficiently massive cores in order to enter the runaway accretion phase prior to the dissipation of the disk's gas (e.g., Pollack et al. 1996). Migration of these giant planets, which is often cited as a potential explanation of observed planetary system architectures, also requires the presence of gas. The timing of gas dissipation may be key to preventing Neptune-sized planets from becoming Jupiter-sized giants and it has been suggested that rapidly dissipated disks may explain the prevalence of super-Earths (e.g., Ansdell et al. 2016; Lee and Chiang 2016). Therefore, the gas lifetime may ultimately determine the type and arrangement of planets in a given system.

In addition to connecting distinct primordial disk environments and evolutionary paths to the wide range of exoplanetary systems observed, constraining disk dissipation timescales can inform studies of our own solar system. The lifetime of gas in the solar nebula may have played a key role in developing the Earth and its planetary environment. Our gas-giant planets, which required the presence of gas over a sufficiently long time to form, shaped the architecture of our solar system through gravitational interactions. Furthermore, the isotopic composition of deep mantle plumes suggests that nebular gas coexisted and interacted with an early magma ocean of the Earth (Williams and Mukhopadhyay 2019). Paleomagnetism studies of meteorites have found very weak remnant magnetism in angrites suggesting dissipation of nebular gas by 3.8 Myr after the formation of CAIs (Wang et al. 2017). Context can be provided for this value via statistical studies of solar nebula analogs.

Protoplanetary disk lifetimes are observationally determined by comparing the prevalence of disk tracers throughout stellar clusters of different ages. In one key analysis summarizing *Spitzer* findings, Mamajek (2009) fit an exponential function to the disk fraction over stellar cluster age and find a characteristic timescale of 2.5 Myr. This value ranges from 1.2–3 Myr depending on the stellar mass and environment. These estimates are based on Hα emission from accretion of material onto the central star or excess infrared emission from small dust grains in the inner disk observed in the spectral energy distributions

(SEDs) of sources aged 0.3–16 Myr. Surveys of gas signatures from the outer regions of disks beyond a few au are less complete statistically but suggest that in general gas does not last longer than 10–20 Myr (Dent et al. 2013; Pascucci et al. 2006). Evaluating the potential for planet formation, however, requires knowledge of the masses of these disks over time. Understanding the rate of gas dissipation is crucial, including to what extent disk populations dissipate at a consistent rate and extremely massive outliers at relatively advanced ages exist. Perhaps the formation of distinct planetary systems can be tied to the lifetime of the gas.

Disk masses are crucial to our understanding of disk evolution and planet formation, but difficult to determine. The dominant gas species, H_2, is unobservable under most disk conditions therefore we rely on indirect tracers to determine the bulk H_2 mass. CO is a commonly used disk gas tracer but its relation to H_2 may vary radially, temporally, and among different systems including depletion of up to two orders of magnitude below the typically-assumed interstellar value (e.g., McClure et al. 2016, , Zhang et al., in prep). As an isotopologue of H_2, HD may be the most appropriate tracer and has been detected in a few disks using *Herschel* (Bergin et al. 2013; McClure et al. 2016). However, further observations are limited by the availability of instrumentation capable of making such measurements. Here we explore our ability to constrain the mass of the disk of J160900-190852 in Upper Scorpius using only measurements from the Atacama Large Millimeter/submillimeter Array (ALMA) of widely observable gas tracers. This disk was selected for its advanced age of 5–11 Myr (e.g, Preibisch et al. 2002; Pecaut et al. 2012) and its high N_2H^+/CO flux ratio relative to previously observed protoplanetary disks with $\sim$10$\times$ higher CO fluxes (Anderson et al. 2019). In combination with our chemical model, we will use observations of N_2H^+ and HCO^+ in addition to the canonical gas tracer CO to constrain the total gas mass of J160900-190852.

4.2 Observations

Multiple gas tracers have been observed for Upper Sco disk J160900-190852. CO J = 3–2 emission was collected in a snapshot survey of Upper Sco in ALMA Cycle 0 by Carpenter et al. (2014). N_2H^+ J = 3–2 and CO and $C^{18}O$ J = 2–1 observations were carried out in ALMA Cycle 3, details are provided by Anderson et al. (2019). Here we add ALMA Cycle 6 observations of HCO^+ J = 3–2 and $C^{18}O$ J = 3–2 using the 12 m array including baselines

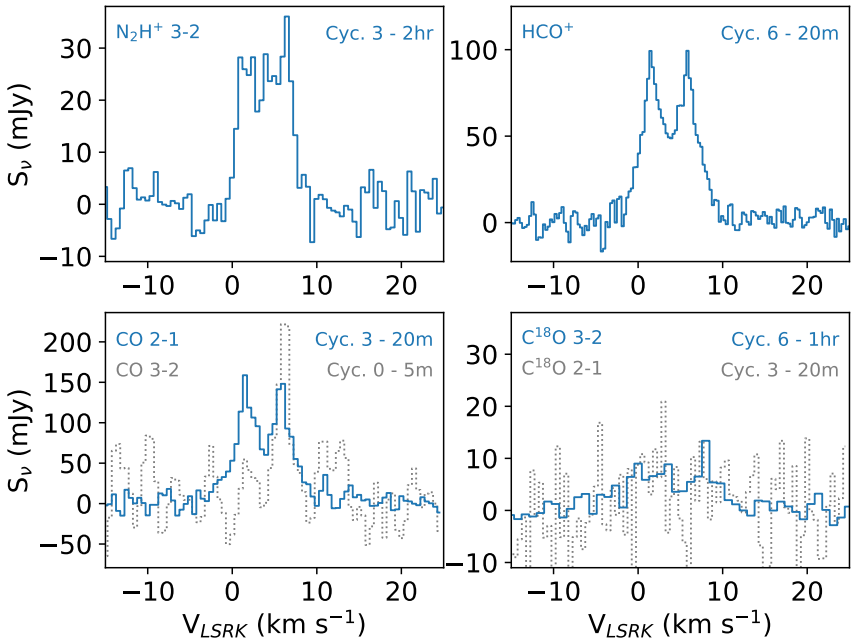

Figure 4.1: Spectra of N_2H^+, HCO^+, CO and $C^{18}O$ emission from J160900-190852 plotted as flux density vs. radial velocity. See Section 4.2 for details on observations.

Table 4.1: Observed Line Fluxes.

Spectral Line		Flux (mJy km s^{-1})	Velocity Range (km s^{-1})
N_2H^+	J=3–2	183 ± 8	0.0–7.5
HCO^+	J=3–2	440 ± 4	-1.0–10.0
CO	J=2–1	860 ± 21	-1.0–9.0
$C^{18}O$	J=3–2	96 ± 8	-1.0–10.0
$C^{18}O$	J=2–1	43 ± 17	-1.0–9.0

from 15.1 to 783.5 m and 43 antennas for Band 6 and baselines from 15.1 to 360.6 m and 44–47 antennas for Band 7 (PI: Anderson, 2018.1.01623.S). Band 6 observations in December 2018 included three spectral windows each with a bandwidth of 234.38 MHz centered at 267.557 GHz for HCO^+ J = 3–2 and additional tracers: HCN J = 3–2 at 265.886 GHz and $HC^{18}O^+$ J = 3–2 at 255.479 GHz. Two additional windows were centered at 269.500 and 251.800 GHz with a bandwidth of 1875 MHz for the collection of continuum emission. The on-source integration time was ∼23 minutes per source. Band 7 observations in March 2019 included two spectral windows each with a bandwidth of

234.38 MHz centered at 329.331 GHz for $C^{18}O$ and 330.588 GHz for ^{13}CO and one spectral window with a bandwidth of 468.75 MHz centered at 340.248 GHz for CN. The on-source integration time was ∼1 hr per source. Additional windows were centered at 329.331 and 341.500 GHz with a bandwidth of 1875 MHz for the collection of continuum emission.

The Common Astronomy Software Applications (CASA) package (McMullin et al. 2007) version 5.1.2 was used for data processing. Atmospheric calibration, bandpass calibration, flux calibration and phase calibration were applied by the ALMA project. Calibrations were based on observations of J1427-4206 for the bandpass and flux and J1625-2527 for the phase for Band 6 and J1517-2422 for the bandpass and flux and J1625-2527 for the phase for Band 7. The synthesized beam size was approximately 0.45″ by 0.40″ with a position angle of -85° for Band 6 images and 0.82″ by 0.57″ with a position angle of -90° for Band 7 images. A summary of flux values is provided in Table 4.1 and spectra in Figure 4.1.

4.3 Constraining the Gas Mass of J160900-190852

We carry out a computational study of the sensitivity of disk gas tracers N_2H^+, HCO^+, and $C^{18}O$ to changes in the total disk gas mass, CO/H_2 abundance, and cosmic-ray ionization rate. We aim to determine what constraints can be placed on the H_2 gas mass of J160900-190852 based on this set of tracers. A 2-D thermo-chemical disk model is used based on the framework of Du and Bergin (2014) and setup of Anderson et al. (2019). Initial disk parameters are listed in Table 4.2 and initial abundances are those from Anderson et al. (2019) with the exception of CO. The total disk gas mass, CO abundance, and H_2 cosmic-ray ionization rate are varied in order of magnitude steps over the ranges provided in Table 4.2. The dust mass in unaltered, resulting in gas-to-dust ratios of 0.1–100 for the gas masses tested. CO abundances start at the interstellar level of $\sim 10^{-4}$ and decrease by factors of up to 1000×. Current observations of protoplanetary disks suggest that CO abundances may be up to 100× below interstellar (Favre et al. 2013; McClure et al. 2016). The range of H_2 cosmic-ray ionization rates corresponds to one order of magnitude above the interstellar level down to two orders of magnitude below, which is the upper limit estimated based on molecular ion observations for TW Hya (Cleeves et al. 2016). Variations in modeled fluxes over the tested parameter ranges are shown in Figure 4.2.

Table 4.2: Fiducial Model Input Parameters.

Fixed Parameters	
Stellar Properties:	
M_*	0.65 $M_\odot$
R_*	1.25 $R_\odot$
T_*	3890 K
Source of stellar spectrum	TW Hya
L_{X-ray}	1.6(30) erg s^{-1}
Disk Properties:	
Disk dust mass	4(-5) $M_\odot$
Inner radius	1 au
Outer radius	100 au
Scale height at radius of 80 au	10 au
Power index: surface density	1.0
Power index: scale height vs. radius	1.0
Total run time	10^6 yrs
Turbulent viscosity	$\alpha = 0.01$
Varied Parameters	
Disk gas mass	4(-6)–4(-3) $M_\odot$
Initial CO abundance (per H)	1.4(-7)–1.4(-4)
H_2 cosmic-ray ionization rate	1.36(-17) s^{-1}
—	1.36(-14) & 1.36(-19) s^{-1}

Note: a(b) indicates a$\times 10^b$

CO is expected to be the dominant carbon carrier throughout most of the disk. Emission from the dominant isotopologue often becomes optically thick in disks because of the high abundance of CO combined with its self-shielding properties. Consequently, observations of less abundant CO isotopologues, such as $C^{18}O$, are used to probe deeper regions of the disk gas and provide flux measurements that are more reflective of the total CO gas column. As a result, $C^{18}O$ emission is dependent on both the CO/H_2 abundance in the disk as well as the H_2 gas mass. Decreasing either will cause a reduction in the observed $C^{18}O$ flux as seen in Fig. 4.2.

HCO^+ is formed mainly through the protonation of CO via H_3^+, which is prevalent in ionized H_2 gas. The amount of HCO^+ will therefore be largely tied to the CO abundance of the disk in addition to the bulk H_2 mass and the H_2 ionization rate. As expected, modeled HCO^+ fluxes follow similar trends as

$C^{18}O$ with decreasing CO abundance and H_2 mass (Fig. 4.2).

Analogous to HCO^+, N_2H^+ is formed mainly through the protonation of N_2 via H_3^+. N_2 is expected to be the dominant nitrogen carrier throughout most of the disk and has similar volatility to CO. As a non-carbon-bearing species, the formation of N_2H^+ tracks N_2 content and is independent of the amount of CO in the disk. However, the N_2H^+ abundance is still related to the CO abundance. CO has a higher proton affinity than N_2 resulting in destruction of N_2H^+ forming HCO^+ where CO is abundant. The relationship between N_2H^+ and CO may result in emission originating in distinct regions of the disk for these species depending on the disk structure (Aikawa et al. 2015; van 't Hoff et al. 2017). This could complicate estimates of N_2/CO ratios for specific disk locations based on this analysis where the the emission is not spatially resolved. However, the modeled fluxes do indicate that the total fluxes derived from the disk for N_2H^+ and $C^{18}O$ remain sensitive to the bulk properties of the disk. Because high CO abundances result in the destruction of N_2H^+, the modeled N_2H^+ fluxes increase with decreasing CO abundance (Fig. 4.2). This represents a distinct trend relative to the $C^{18}O$ and HCO^+ tracers, providing additional information that may break the degeneracy between CO abundance and H_2 mass.

Comparing two optically thin gas tracers provides a flux ratio that is not very sensitive to the disk mass. This is the case for the $N_2H^+/C^{18}O$ flux ratio, which is strongly dependent on the CO abundance but relatively less sensitive to the disk gas mass (Fig. 4.2). The N_2H^+/HCO^+ flux ratio shows some sensitivity to both parameters suggesting that HCO^+ fluxes respond less to changes in the disk mass and may be more optically thick than the other two tracers. Perhaps the use of HCO^+ isotopologues, such as DCO^+, would be more appropriate for CO abundance estimates.

The $N_2H^+/C^{18}O$ and $HCO^+/C^{18}O$ flux ratios depend on the level of ionization in the disk. As cosmic-ray ionization rates increase the fluxes of molecular ions N_2H^+ and HCO^+ increase as well, whereas $C^{18}O$ fluxes decrease (Fig. 4.2). The N_2H^+/HCO^+ flux ratio should have a lower dependence on the level of ionization in the disk because both species are molecular ions. However, the model results show that N_2H^+ fluxes are more sensitive to changes in the cosmic-ray ionization rate than HCO^+ fluxes creating a similar dependence on the ionization level. This also means that the $HCO^+/C^{18}O$ flux ratio is only

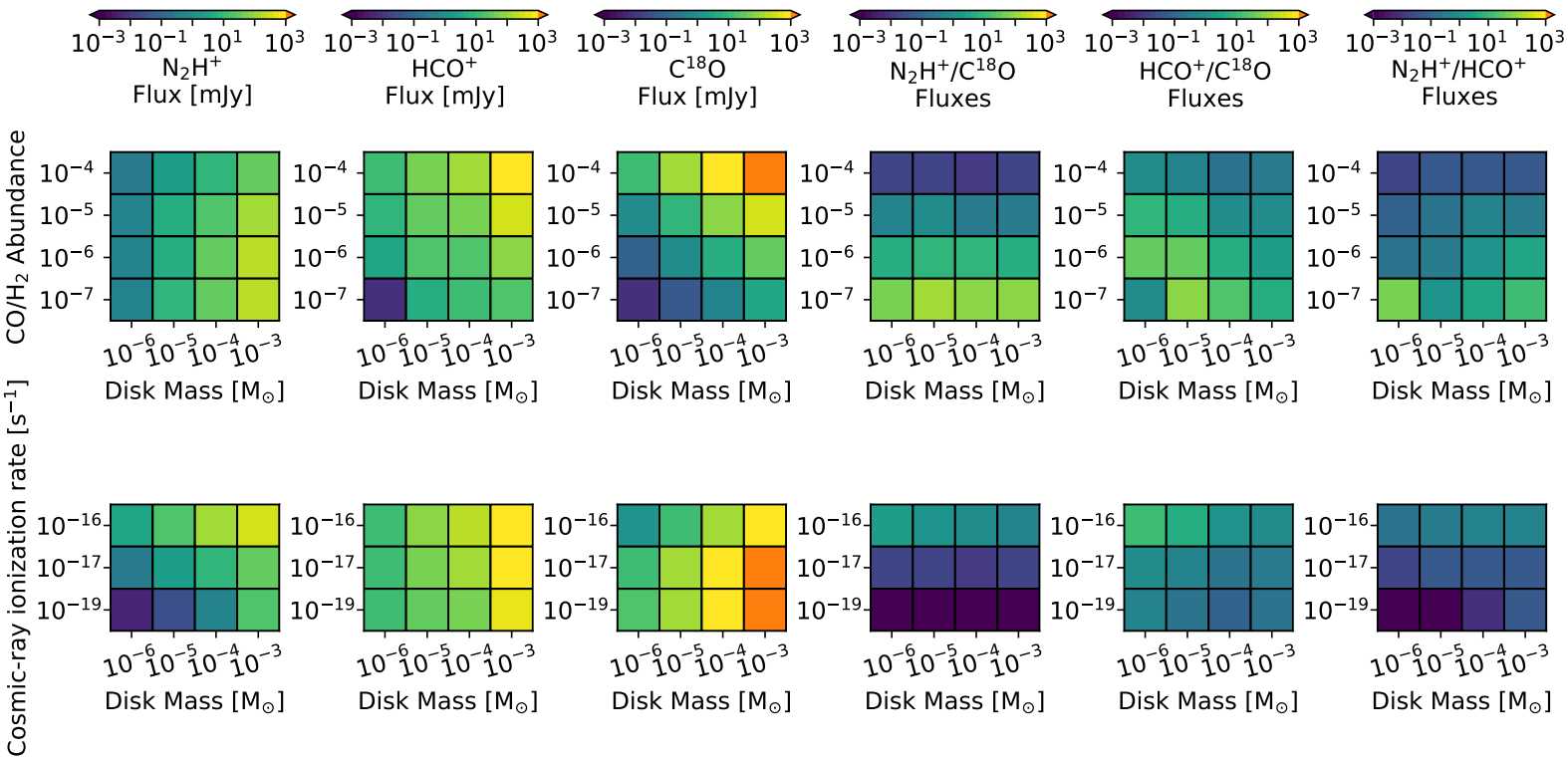

Figure 4.2: Modeled N_2H^+, HCO^+, and $C^{18}O$ fluxes in addition to $N_2H^+/C^{18}O$, $HCO^+/C^{18}O$, and N_2H^+/HCO^+ flux ratios. Variations in model parameters span CO abundances from the interstellar value to 1000× below and gas-to-dust mass ratios of 0.1 to 100 for an interstellar H_2 cosmic-ray ionization rate of 3×10^{-17} s^{-1}(top panels) and H_2 cosmic-ray ionization rates from 3×10^{-19}–3×10^{-16} s^{-1} for an interstellar CO/H_2 abundance of $\sim10^{-4}$ (bottom panels). Modeled fluxes and flux ratios are to be compared with observations in order to constrain the underlying disk parameters, namely CO abundance, cosmic-ray ionization rate, and total gas mass.

weakly dependent on the cosmic-ray ionization rate relative to the $N_2H^+/C^{18}O$ flux ratio. Therefore, disk ionization remains a confounding factor for the flux ratios in this analysis. Further investigations into additional sources of ionization are also needed. For example, Cleeves et al. (2015) find that a hardened stellar X-ray spectrum is a key component of their best-fit model to the N_2H^+ and HCO^+ observations of TW Hya.

From this analysis, we can use the $N_2H^+/C^{18}O$ flux ratio to constrain the CO abundance for a given cosmic-ray ionization rate (Fig. 4.2). For an interstellar ionization rate, CO depletion by two orders of magnitude is required to reproduce the observed $N_2H^+/C^{18}O$ flux ratio of 1.9. The level of CO depletion required decreases with increasing disk ionization and vice versa. Combining this information with the individual gas tracer fluxes, we can attempt to place some constraints on the total disk gas mass. The current model does not provide a satisfactory fit to the fluxes of all three tracers in J160900-190852 and requires further testing of potential sources of ionization and the parameters describing the disk structure in this model. However, certain patterns do emerge from the current model grid. The observed $C^{18}O$ flux can be reproduced by CO abundances 10–100× below the interstellar value or gas-to-dust ratios of 0.1–10 depending on the cosmic-ray ionization rate. The observed HCO^+ flux requires a high mass and high CO abundance to be reproduced by this model grid. In the case of N_2H^+, low masses are unable to reproduce the observed flux. The N_2H^+ observations require a disk gas mass of $\gtrsim 4\times10^{-3}$ M$\odot$ and CO depletion of $\lesssim$100× below interstellar for an interstellar ionization rate. For a 10× higher ionization rate, the N_2H^+ observations require a disk mass of $\gtrsim 4\times10^{-4}$ M$\odot$ for a similar level of CO depletion or $\gtrsim 4\times10^{-3}$ M$\odot$ for interstellar CO abundances. The low ionization rate of 3×10^{-19} s^{-1} is incapable of reproducing the molecular ion fluxes. Overall, at least interstellar levels of disk ionization and gas-to-dust ratios of 10–100 are needed to explain the observed N_2H^+ and HCO^+ fluxes.

4.4 Discussion

Characterization of gas masses for disks of various ages is required to understand disk evolution and constrain timescales for planet formation. The observations of J160900-190852 provide evidence of gas-rich disks extending to ages of $\gtrsim$5 Myr. At $\gtrsim$0.004 $M_\odot$ or about 4.2 $M_{Jupiter}$, this disk would still contain sufficient mass to form giant planets. Additional estimations of the gas mass

of disks around other $\gtrsim$5 Myr sources will characterize the potential for planet formation at these later timescales and aid in determining the environmental conditions needed to support such potential for late-stage planet formation. Multiple examples of early planet formation have been recently observed including the direct detection of planets in PDS 70 and indirect detection via velocity deviations in molecular emission lines of HD 163296 (Keppler et al. 2018; Pinte et al. 2018; Teague et al. 2018, 2019). Whether or not significant formation of giant planets is still occurring at $\gtrsim$5 Myr and the role of these late-stage massive gas disks has yet to be determined.

The use of indirect tracers to estimate the H_2 mass of the disk requires making various assumptions about the disk structure. For example, using HD as mass tracer requires knowledge or prediction of the temperature structure of the disk (Bergin et al. 2013). In the case of this analysis, the relative distributions of N_2H^+, HCO^+, and CO depend on the temperature structure, including the vertical temperature gradient due to the degree of dust settling (Qi et al. 2019), and the level and distribution of ionization in the disk. Further calibration of the physical disk structure and how it affects these tracers is needed. Whereas fully spatially resolved images of N_2H^+ in J160900-190852 are likely unfeasible because of the time required, comparison with the resolved subset of closer and more massive disks may provide key insight. N_2H^+ emission has been spatially resolved by ALMA in several disks (Qi et al. 2019). In depth analyses of a few disks have also constrained key physical and chemical parameters for well-studied sources. Estimates for the cosmic-ray ionization rate for TW Hya (Cleeves et al. 2015) and physical structure and C/N/O abundances for IM Lup (Cleeves et al. 2016, 2018) have been made. Further observation and characterization of a diverse sample of sources is necessary to determine how applicable these cases of nearby, well-studied disks will be to the disks in Upper Sco.

The investigation of non-carbon-based volatiles will be critical for the development of future observations aimed at identifying gas-rich disks in large surveys. Such species are needed to break the degeneracy between CO abundance and disk mass when reproducing observed fluxes. This is particularly pertinent if CO-depletion is a widespread phenomenon among disk populations even at young ages, as current data may suggest (Ansdell et al. 2016; Long et al. 2017). Chemical species detected in the outer disk gas that do not contain

carbon are limited to H_2O, SO, and N_2H^+. Sub-mm emission from H_2O has been observed in a few disks and is found to be underabundant by *Herschel* likely due to sequestration of volatiles into solids (Du et al. 2017). Observations of H_2O may increase in the coming years with ALMA Band 5 recently coming online. Detections of SO in mm emission are also currently limited to a few disks and suggest that this emission originates from the outflow rather than the disk itself (Guilloteau et al. 2013). N_2H^+ is one of a limited number of non-carbon-bearing species observed in the outer regions of protoplanetary disks and could provide valuable additional constraints on the disk mass, given further investigation of how this tracer is affected by the disk structure in a diverse sample of disks.

4.5 Acknowledgments

This material is based upon work supported by the National Science Foundation via the Graduate Research Fellowship Program under Grant No. DGE-1144469 and the Astronomy and Astrophysics Research Grants Program under Grant No. AST-1514918. This work makes use of the following ALMA data:
ADS/JAO.ALMA#2018.1.01623.S,
ADS/JAO.ALMA#2015.1.01199.S,
ADS/JAO.ALMA#2015.1.00964.S, and
ADS/JAO.ALMA#2011.0.00526.S. ALMA is a partnership of ESO (representing its member states), NSF (USA) and NINS (Japan), together with NRC (Canada), MOST and ASIAA (Taiwan), and KASI (Republic of Korea), in cooperation with the Republic of Chile. The Joint ALMA Observatory is operated by ESO, AUI/NRAO and NAOJ. The National Radio Astronomy Observatory is a facility of the National Science Foundation operated under cooperative agreement by Associated Universities, Inc.

REFERENCES

Y. Aikawa, K. Furuya, H. Nomura, and C. Qi. Analytical Formulae of Molecular Ion Abundances and the N_2H^+ Ring in Protoplanetary Disks. *ApJ*, 807: 120, July 2015. doi: 10.1088/0004-637X/807/2/120.

D. E. Anderson, G. A. Blake, E. A. Bergin, K. Zhang, J. M. Carpenter, K. R. Schwarz, J. Huang, and K. I. Öberg. Probing the Gas Content of Late-stage Protoplanetary Disks with N_2H^+. *ApJ*, 881:127, August 2019. doi: 10.3847/1538-4357/ab2cb5.

M. Ansdell, J. P. Williams, N. van der Marel, J. M. Carpenter, G. Guidi, M. Hogerheijde, G. S. Mathews, C. F. Manara, A. Miotello, A. Natta, I. Oliveira, M. Tazzari, L. Testi, E. F. van Dishoeck, and S. E. van Terwisga. ALMA Survey of Lupus Protoplanetary Disks. I. Dust and Gas Masses. *ApJ*, 828:46, September 2016. doi: 10.3847/0004-637X/828/1/46.

E. A. Bergin, L. I. Cleeves, U. Gorti, K. Zhang, G. A. Blake, J. D. Green, S. M. Andrews, N. J. Evans, II, T. Henning, K. Öberg, K. Pontoppidan, C. Qi, C. Salyk, and E. F. van Dishoeck. An old disk still capable of forming a planetary system. *Nature*, 493:644–646, January 2013. doi: 10.1038/nature11805.

J. M. Carpenter, L. Ricci, and A. Isella. An ALMA Continuum Survey of Circumstellar Disks in the Upper Scorpius OB Association. *ApJ*, 787:42, May 2014. doi: 10.1088/0004-637X/787/1/42.

L. I. Cleeves, E. A. Bergin, C. Qi, F. C. Adams, and K. I. Öberg. Constraining the X-Ray and Cosmic-Ray Ionization Chemistry of the TW Hya Protoplanetary Disk: Evidence for a Sub-interstellar Cosmic-Ray Rate. *ApJ*, 799:204, February 2015. doi: 10.1088/0004-637X/799/2/204.

L. I. Cleeves, K. I. Öberg, D. J. Wilner, J. Huang, R. A. Loomis, S. M. Andrews, and I. Czekala. The Coupled Physical Structure of Gas and Dust in the IM Lup Protoplanetary Disk. *ApJ*, 832:110, December 2016. doi: 10.3847/0004-637X/832/2/110.

L. I. Cleeves, K. I. Öberg, D. J. Wilner, J. Huang, R. A. Loomis, S. M. Andrews, and V. V. Guzman. Constraining Gas-phase Carbon, Oxygen, and Nitrogen in the IM Lup Protoplanetary Disk. *ApJ*, 865:155, October 2018. doi: 10.3847/1538-4357/aade96.

W. R. F. Dent, W. F. Thi, I. Kamp, J. P. Williams, F. Menard, S. Andrews, D. Ardila, G. Aresu, J.-C. Augereau, D. Barrado y Navascues, S. Brittain, A. Carmona, D. Ciardi, W. Danchi, J. Donaldson, G. Duchene, C. Eiroa, D. Fedele, C. Grady, I. de Gregorio-Molsalvo, C. Howard, N. Huélamo,

A. Krivov, J. Lebreton, R. Liseau, C. Martin-Zaidi, G. Mathews, G. Meeus, I. Mendigutía, B. Montesinos, M. Morales-Calderon, A. Mora, H. Nomura, E. Pantin, I. Pascucci, N. Phillips, C. Pinte, L. Podio, S. K. Ramsay, B. Riaz, P. Riviere-Marichalar, A. Roberge, G. Sandell, E. Solano, I. Tilling, J. M. Torrelles, B. Vandenbusche, S. Vicente, G. J. White, and P. Woitke. GASPS—A Herschel Survey of Gas and Dust in Protoplanetary Disks: Summary and Initial Statistics. *Publications of the Astronomical Society of the Pacific*, 125:477–505, May 2013. doi: 10.1086/670826.

F. Du and E. A. Bergin. Water Vapor Distribution in Protoplanetary Disks. *ApJ*, 792:2, September 2014. doi: 10.1088/0004-637X/792/1/2.

F. Du, E. A. Bergin, M. Hogerheijde, E. F. van Dishoeck, G. Blake, S. Bruderer, I. Cleeves, C. Dominik, D. Fedele, D. C. Lis, G. Melnick, D. Neufeld, J. Pearson, and U. Yıldız. Survey of Cold Water Lines in Protoplanetary Disks: Indications of Systematic Volatile Depletion. *ApJ*, 842:98, June 2017. doi: 10.3847/1538-4357/aa70ee.

C. Favre, L. I. Cleeves, E. A. Bergin, C. Qi, and G. A. Blake. A Significantly Low CO Abundance toward the TW Hya Protoplanetary Disk: A Path to Active Carbon Chemistry? *ApJ*, 776:L38, October 2013. doi: 10.1088/2041-8205/776/2/L38.

S. Guilloteau, E. Di Folco, A. Dutrey, M. Simon, N. Grosso, and V. Piétu. A sensitive survey for ^{13}CO, CN, H_2CO, and SO in the disks of T Tauri and Herbig Ae stars. *A&A*, 549:A92, January 2013. doi: 10.1051/0004-6361/201220298.

M. Keppler, M. Benisty, A. Müller, T. Henning, R. van Boekel, F. Cantalloube, C. Ginski, R. G. van Holstein, A.-L. Maire, A. Pohl, M. Samland, H. Avenhaus, J.-L. Baudino, A. Boccaletti, J. de Boer, M. Bonnefoy, G. Chauvin, S. Desidera, M. Langlois, C. Lazzoni, G.-D. Marleau, C. Mordasini, N. Pawellek, T. Stolker, A. Vigan, A. Zurlo, T. Birnstiel, W. Brandner, M. Feldt, M. Flock, J. Girard, R. Gratton, J. Hagelberg, A. Isella, M. Janson, A. Juhasz, J. Kemmer, Q. Kral, A.-M. Lagrange, R. Launhardt, A. Matter, F. Ménard, J. Milli, P. Mollière, J. Olofsson, L. Pérez, P. Pinilla, C. Pinte, S. P. Quanz, T. Schmidt, S. Udry, Z. Wahhaj, J. P. Williams, E. Buenzli, M. Cudel, C. Dominik, R. Galicher, M. Kasper, J. Lannier, D. Mesa, D. Mouillet, S. Peretti, C. Perrot, G. Salter, E. Sissa, F. Wildi, L. Abe, J. Antichi, J.-C. Augereau, A. Baruffolo, P. Baudoz, A. Bazzon, J.-L. Beuzit, P. Blanchard, S. S. Brems, T. Buey, V. De Caprio, M. Carbillet, M. Carle, E. Cascone, A. Cheetham, R. Claudi, A. Costille, A. Delboulbé, K. Dohlen, D. Fantinel, P. Feautrier, T. Fusco, E. Giro, L. Gluck, C. Gry, N. Hubin, E. Hugot, M. Jaquet, D. Le Mignant, M. Llored, F. Madec, Y. Magnard, P. Martinez, D. Maurel, M. Meyer, O. Möller-Nilsson, T. Moulin, L. Mugnier, A. Origné, A. Pavlov, D. Perret, C. Petit,

J. Pragt, P. Puget, P. Rabou, J. Ramos, F. Rigal, S. Rochat, R. Roelfsema, G. Rousset, A. Roux, B. Salasnich, J.-F. Sauvage, A. Sevin, C. Soenke, E. Stadler, M. Suarez, M. Turatto, and L. Weber. Discovery of a planetary-mass companion within the gap of the transition disk around PDS 70. *A&A*, 617:A44, September 2018. doi: 10.1051/0004-6361/201832957.

E. J. Lee and E. Chiang. Breeding Super-Earths and Birthing Super-puffs in Transitional Disks. *ApJ*, 817:90, February 2016. doi: 10.3847/0004-637X/817/2/90.

F. Long, G. J. Herczeg, I. Pascucci, E. Drabek-Maunder, S. Mohanty, L. Testi, D. Apai, N. Hendler, T. Henning, C. F. Manara, and G. D. Mulders. An ALMA Survey of CO Isotopologue Emission from Protoplanetary Disks in Chamaeleon I. *ApJ*, 844:99, August 2017. doi: 10.3847/1538-4357/aa78fc.

E. E. Mamajek. Initial Conditions of Planet Formation: Lifetimes of Primordial Disks. In T. Usuda, M. Tamura, and M. Ishii, editors, *American Institute of Physics Conference Series*, volume 1158 of *American Institute of Physics Conference Series*, pages 3–10, August 2009. doi: 10.1063/1.3215910.

M. K. McClure, E. A. Bergin, L. I. Cleeves, E. F. van Dishoeck, G. A. Blake, N. J. Evans, II, J. D. Green, T. Henning, K. I. Öberg, K. M. Pontoppidan, and C. Salyk. Mass Measurements in Protoplanetary Disks from Hydrogen Deuteride. *ApJ*, 831:167, November 2016. doi: 10.3847/0004-637X/831/2/167.

J. P. McMullin, B. Waters, D. Schiebel, W. Young, and K. Golap. CASA Architecture and Applications. In R. A. Shaw, F. Hill, and D. J. Bell, editors, *Astronomical Data Analysis Software and Systems XVI*, volume 376 of *Astronomical Society of the Pacific Conference Series*, page 127, October 2007.

I. Pascucci, U. Gorti, D. Hollenbach, J. Najita, M. R. Meyer, J. M. Carpenter, L. A. Hillenbrand, G. J. Herczeg, D. L. Padgett, E. E. Mamajek, M. D. Silverstone, W. M. Schlingman, J. S. Kim, E. B. Stobie, J. Bouwman, S. Wolf, J. Rodmann, D. C. Hines, J. Lunine, and R. Malhotra. Formation and Evolution of Planetary Systems: Upper Limits to the Gas Mass in Disks around Sun-like Stars. *ApJ*, 651:1177–1193, November 2006. doi: 10.1086/507761.

M. J. Pecaut, E. E. Mamajek, and E. J. Bubar. A Revised Age for Upper Scorpius and the Star Formation History among the F-type Members of the Scorpius-Centaurus OB Association. *ApJ*, 746:154, February 2012. doi: 10.1088/0004-637X/746/2/154.

C. Pinte, D. J. Price, F. Ménard, G. Duchêne, W. R. F. Dent, T. Hill, I. de Gregorio-Monsalvo, A. Hales, and D. Mentiplay. Kinematic Evidence for an

Embedded Protoplanet in a Circumstellar Disk. *ApJ*, 860:L13, June 2018. doi: 10.3847/2041-8213/aac6dc.

J. B. Pollack, O. Hubickyj, P. Bodenheimer, J. J. Lissauer, M. Podolak, and Y. Greenzweig. Formation of the Giant Planets by Concurrent Accretion of Solids and Gas. *Icarus*, 124:62–85, November 1996. doi: 10.1006/icar.1996.0190.

T. Preibisch, A. G. A. Brown, T. Bridges, E. Guenther, and H. Zinnecker. Exploring the Full Stellar Population of the Upper Scorpius OB Association. *AJ*, 124:404–416, July 2002. doi: 10.1086/341174.

Chunhua Qi, Karin I. Öberg, Catherine C. Espaillat, Connor E. Robinson, Sean M. Andrews, David J. Wilner, Geoffrey A. Blake, Edwin A. Bergin, and L. Ilsedore Cleeves. Probing CO and N_2 Snow Surfaces in Protoplanetary Disks with N_2H^+ Emission. *ApJ*, 882(2):160, Sep 2019. doi: 10.3847/1538-4357/ab35d3.

R. Teague, J. Bae, E. A. Bergin, T. Birnstiel, and D. Foreman-Mackey. A Kinematical Detection of Two Embedded Jupiter-mass Planets in HD 163296. *ApJ*, 860:L12, June 2018. doi: 10.3847/2041-8213/aac6d7.

Richard Teague, Jaehan Bae, and Edwin A. Bergin. Meridional flows in the disk around a young star. *Nature*, 574(7778):378–381, Oct 2019. doi: 10.1038/s41586-019-1642-0.

M. L. R. van 't Hoff, C. Walsh, M. Kama, S. Facchini, and E. F. van Dishoeck. Robustness of N_2H^+ as tracer of the CO snowline. *A&A*, 599:A101, March 2017. doi: 10.1051/0004-6361/201629452.

H. Wang, B. P. Weiss, X.-N. Bai, B. G. Downey, J. Wang, J. Wang, C. Suavet, R. R. Fu, and M. E. Zucolotto. Lifetime of the solar nebula constrained by meteorite paleomagnetism. *Science*, 355:623–627, February 2017. doi: 10.1126/science.aaf5043.

C. D. Williams and S. Mukhopadhyay. Capture of nebular gases during Earth's accretion is preserved in deep-mantle neon. *Nature*, 565:78–81, January 2019. doi: 10.1038/s41586-018-0771-1.

Chapter 5

CARBON CARRIERS IN THE INNER REGIONS OF CO-DEPLETED PROTOPLANETARY DISKS

Dana E. Anderson[1], Geoffrey A. Blake[1], Edwin A. Bergin[2], Ke Zhang[2,3] & Kamber R. Schwarz[4,5]

[1]Division of Geological and Planetary Sciences, California Institute of Technology, 1200 E. California Blvd., Pasadena, CA 91125, USA

[2]Department of Astronomy, University of Michigan, 1085 S. University, Ann Arbor, MI 48109, USA

[3]Hubble Fellow

[4]Lunar and Planetary Laboratory, The University of Arizona, 1629 E. University Blvd., Tucson, AZ 85721, USA

[5]Sagan Fellow

Abstract CO is expected to be the dominant form of carbon in protoplanetary disks. Sub-mm observations, however, find significant depletion of CO relative to H_2 in the outer disk gas, even interior to the CO snowline. In contrast, infrared observations, which probe the innermost surface layers of the disk, reveal CO-rich gas. In the outer disk, depletion in CO/H_2 relative to interstellar levels may be caused by conversion of CO into less volatile species such as CO_2 and CH_3OH. Using chemical models, we explore the fate of these less volatile carbon carriers after being introduced to the hotter, denser inner regions of the disk. Carbon returns to CO in unshielded, transparent regions of the inner disk surface, consistent with infrared observations, but this is not representative of the carbon reservoirs closer to the disk midplane. Unique compositions, including the original carbon carriers from the outer disk, are preserved in these shielded regions based on a dynamically static chemical disk model. However, efficient vertical transport of materials may cause the entire column to reflect the photon-dominated surface. Overall, we expect that tracers of potential carbon carriers from the outer disk may be erased by photochemistry and difficult to observe with the upcoming *James Webb Space Telescope* (JWST).

5.1 Introduction

The chemical composition of protoplanetary disks influences the planet formation process and its potential outcomes. Carbon, because it is one of the most cosmically abundant elements after H and He, can play a significant role and is of particular interest due to its biological significance on Earth. A product of stellar nucleosynthesis, carbon is incorporated into solid dust grains around carbon-rich asymptotic giant branch (AGB) stars that have C/O > 1 in their photospheres. In this case, most of the oxygen is bound to carbon in the form of CO (Marty et al. 2013). Interstellar observations indicate that elemental carbon in the quiescent interstellar medium (ISM) is split roughly evenly between the refractory solid form and the volatile form, mainly CO (e.g., Savage and Sembach 1996; Mishra and Li 2015). Following survival or regeneration over 100s Myr in the ISM (Jones 2009), star formation via the gravitational collapse of a molecular cloud core sweeps up carbonaceous grains in addition to gas into a circumstellar disk around the developing star. This presents two initial reservoirs of carbon to the disk: a solid, non-volatile component of unknown molecular structure and a volatile component composed of mostly CO. Here we are concerned with the fate of the inherited volatile component.

Protoplanetary disk observations reveal that their carbon composition differs from the ISM. Constraints have been placed on the CO/H_2 ratio for a sample of disks with HD measurements from the *Herschel Space Observatory*. HD detections in three disks resulted in estimated CO/H_2 ratios up to 5–100$\times$ below the interstellar value of 10^{-4} (Bergin et al. 2013; Favre et al. 2013; McClure et al. 2016). This is not an uncommon problem. Earlier suggestions of CO depletion were made based on weak CO relative to mm continuum emission for disks BP Tau (Dutrey et al. 2003), CQ Tau, and MWC 758 (Chapillon et al. 2008). In addition, total gas mass estimates based on observed CO emission are found to be lower than those based on sub-mm/mm dust assuming a gas-to-dust mass ratio of 100 for numerous disks in recent surveys by the Atacama Large Millimeter/submillimeter Array (ALMA) (e.g., Miotello et al. 2017). In some cases, CO freezeout in cooler regions of the disk ($T \lesssim$ 20 K) and photodissociation of CO at the disk surface may contribute to such discrepancies. However, recent results show that CO remains depleted relative to interstellar values even interior to the CO snowline and near the midplane. These results are based on radial distributions of CO determined by spatially resolved observations of CO isotopologues in TW Hydra using

ALMA (Schwarz et al. 2016; Zhang et al. 2017). Chemical processes in the disk may result in the sequestration of CO over time into less volatile carbon species (Bergin et al. 2014; Furuya and Aikawa 2014; Reboussin et al. 2015; Yu et al. 2016; Eistrup et al. 2016). Schwarz et al. (2018) find that chemical reprocessing can account for up to an order of magnitude of CO depletion under the right disk conditions, but more severe depletion requires additional non-chemical processes such as mixing within the disk or incorporation of CO into large, km-sized, bodies forming in the disk (e.g., Krijt et al. 2018).

The main reservoirs of carbon following CO sequestration are expected to be CH_3OH and CO_2 and their subsequent surface products (Schwarz et al. 2018). If CO is sequestered into less volatile species such as CH_3OH and CO_2, this carbon would remain frozen on icy surfaces interior to the CO snowline. Our goal is to investigate the fate of these carbon carriers after they are introduced to the inner disk. Once dust grains grow large enough to decouple from the gas, they begin to drift radially inward as a result of the difference in velocity between the dust and pressure-supported gas moving at sub-Keplerian velocities. Radial drift supplies the inner disk gas with these carbon carriers as each species is released into the gas within its respective snowline or within the water snowline if it is trapped in a water ice matrix. Such inward drift is expected to influence inner disk chemical abundances as modeled by Bosman et al. (2018) for CO_2. The fate of the carbon carriers will depend on chemical pathways present in the inner disk. Here we explore the fate of carbon released from grain surfaces in the inner disk through chemical modeling. The results will inform future observations of the inner regions of protoplanetary disks by the *James Webb Space Telescope* (JWST).

5.2 Chemical Models

Using a dynamically static model of an azimuthally symmetric protoplanetary disk around a T-Tauri star, we explore three endmember scenarios featuring different carriers of the volatile carbon content of the disk. The chemical model includes the high-temperature gas-phase chemical reaction network of Harada et al. (2010) and the gas-grain network of Fogel et al. (2011), as described in Anderson et al. (2017). The physical disk model is similar to that of Cleeves et al. (2013, 2015). Dust consists of 80% astronomical silicates (Draine and Lee 1984), 16% aromatic carbon and 4% aliphatic carbon (Jones 2012) in two populations each described by an MRN size distribution. The large population

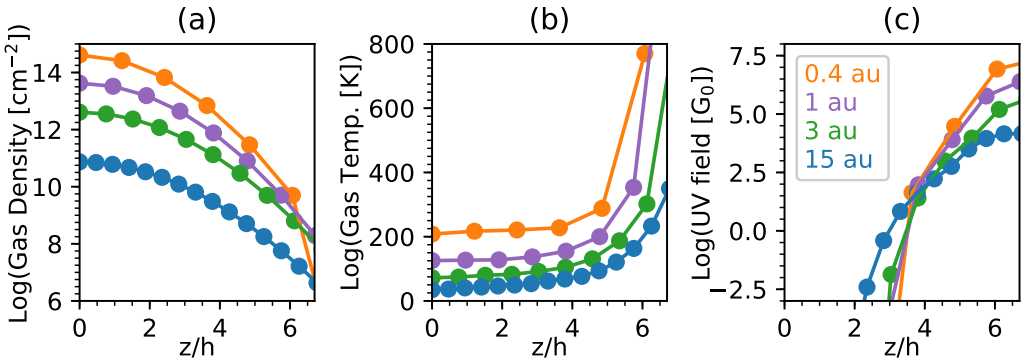

Figure 5.1: Gas density (a), gas temperature (b), and UV radiation (c) vs. height (z) at four representative disk radii in our models. Height is shown relative to the scale height (h) for each radius.

has a maximum size of 1 mm, contains 80% of the total dust mass, and has a scale height 20% of that of the small grain population to approximate grain settling. The remaining dust mass exists in a smaller population with a maximum size of 10 μm. The minimum dust size for both populations is 0.005 μm. A power law with an exponential cutoff, $\Sigma_{gas}(R)$= $\Sigma_c(R/R_c)^{-1}$exp[-(R/R_c)] where $\Sigma_c = 3.0$ g cm^{-2} and $R_c = 100$ au, describes the fixed radial dust distribution. The gas tracks the dust with a vertically integrated gas-to-dust mass ratio of 100. The disk is passively heated by a central K star and dust temperatures were calculated using TORUS (Harries et al. 2004). The Monte Carlo radiative transfer code of Bethell and Bergin (2011b,a) was used to compute the UV and X-ray radiation fields using the UV spectrum from TW Hya and a total luminosity of $10^{29.5}$ erg s^{-1} between 1–20 keV as inputs. Gas temperatures were estimated based on the thermochemical models of Bruderer (2013), as described in Cleeves et al. (2015).

The fate of carbon depends on disk density and therefore the structure of the inner disk region. The modeled disk structure used in this work is shown for four selected radii in Figure 5.1. The radii are selected to represent the hot, inner disk (0.4 au); the region near the H_2O and CH_3OH snowlines (1 au); the region near the CO_2 snowline (3 au); and the outer disk (15 au), which is within the CH_4 and CO snowlines in the chosen disk model. We simulate the scenario where carbon is locked up in less volatile species, such as CH_3OH and CO_2, and brought into the inner disk by radial drift. In each case, we alter the initial abundances of the model such that all of the available volatile carbon, $\sim 10^{-4}$ relative to total H, is in the form of a less volatile

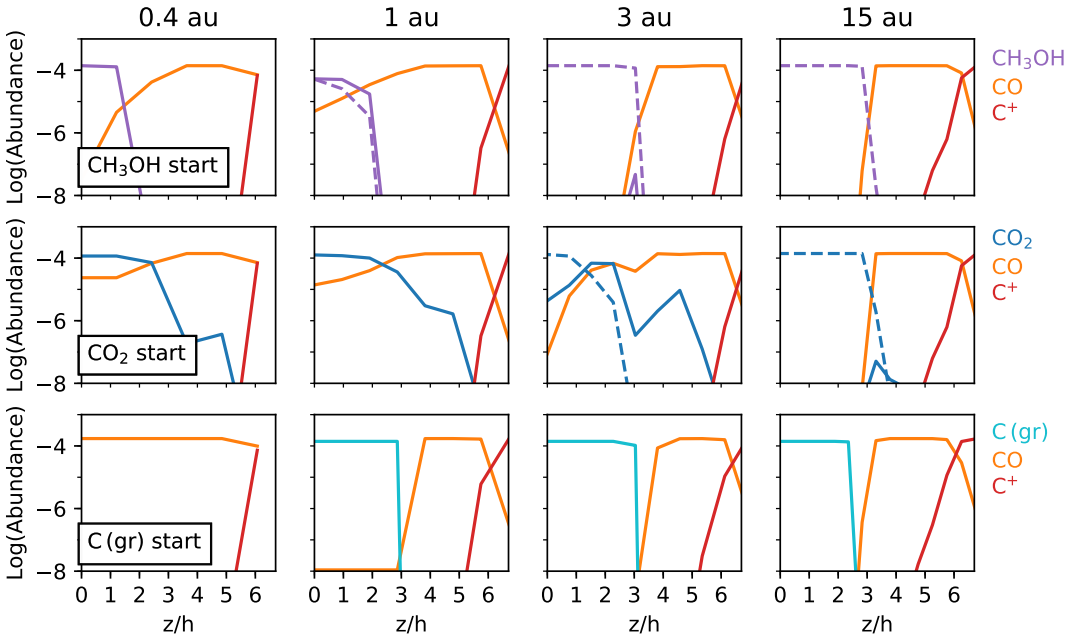

Figure 5.2: Abundance relative to total H of the initial carbon carrier (in purple for CH_3OH, blue for CO_2, or cyan for amorphous carbon grains), CO (in orange) and C^+ (in red) vs. height (z) relative to the vertical disk scale height (h) for four selected radii in our models: 0.4 au in the inner disk, 1 au near the H_2O and CH_3OH snowlines, 3 au near the CO_2 snowline, and 15 au in the outer disk. Each of the four radii is shown in a column including model results at 10^6 years for each initial carbon composition: CH_3OH ice (top row), CO_2 ice (middle row), and amorphous carbon grains (bottom row). Dashed lines indicate ice species.

carbon carrier rather than CO. Our first model assumes carbon is in the form of CH_3OH ice. In our second model, the carbon is initially in the form of CO_2 ice. To accommodate the extra oxygen we reduce the initial abundance of H_2O in this model by 10^{-4}. In our final model, we approximate larger carbon carriers, such as complex organics, as amorphous carbon grains with radii of 0.1 microns. Carbon is removed from these grains and reintroduced into the gas phase via oxidation and UV photolysis. These carbon grains and their destruction are modeled using the methods of Anderson et al. (2017).

5.3 The Fate of Carbon Carriers in the Inner Disk

Figure 5.2 shows the transition from the initial carbon carrier to the major surface products, CO and C^+, from the midplane to the ionized disk surface at the selected radii for each of the following endmember scenarios: all of the

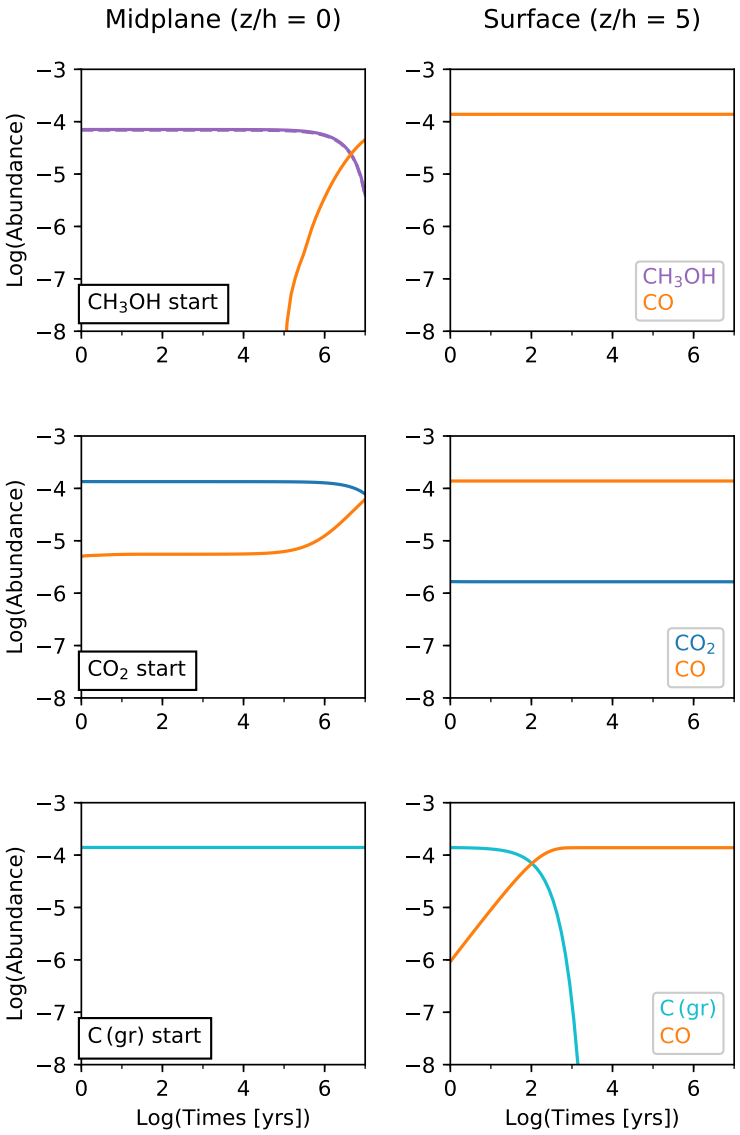

Figure 5.3: Abundance relative to total H of the initial carbon carrier (in purple for CH_3OH, blue for CO_2, or cyan for amorphous carbon grains) and CO (in orange) vs. time at a radius of 1 au in the disk midplane (left column) and surface layers at five scale heights (h) above the midplane (right column) in our models. Results are shown for three different models: all of the initial carbon starting in CH_3OH ice (top panels), in CO_2 ice (middle panels), and in amorphous carbon grains (bottom panels). Dashed lines indicate ice species. Conversion of CH_3OH and CO_2 from the ice to gas phase occurs within the first time step of 1 yr. Further conversion to CO also occurs at the disk surface within this time frame for the CH_3OH ice and CO_2 ice scenarios.

carbon initially stored in CH_3OH ice, CO_2 ice, and amorphous carbon grains. These abundances are computed in our dynamically static chemical model after 10^6 years. Carbon remains in its initial form for CH_3OH and CO_2 at the midplane, changing phase interior to their respective snowlines. At and above 2–3 scale heights from the midplane, all three initial carbon carriers are converted into CO transitioning to C^+ above 5–6 scale heights. In the case of carbon grains in the innermost disk radii, conversion to CO extends into denser regions in the midplane. While the dust optical depth depends on assumed opacity values, the τ=1 surface appears to lie $\gtrsim$4 scale heights above the midplane for wavelengths of 5–15μm these models. This limits the observability of the initial carbon carriers using infrared facilities.

The dominant form of carbon vs. height in the disk is mainly determined by the density structure and penetration of photons. Chemical changes in the disk surface occur within 1–10 years at 5 scale heights above the midplane at a distance of 1 au from the central star (Figure 5.3). Photodissociation rapidly converts CH_3OH and CO_2 to CO. UV photolysis releases CH_4 and larger hydrocarbons from amorphous carbon grain surfaces into the gas. Afterwards these species are also quickly converted to CO. Oxidation of these carbonaceous surfaces also produces CO, but at a temperature-dependent rate in a narrower region near the disk surface and in the innermost disk midplane where temperatures are above 200 K (Anderson et al. 2017). Regardless of the initial carbon carrier, nearly all of the available carbon is stored in CO at the disk surface when a form of oxygen is present in the gas (Figure 5.4). Additionally, in all of these scenarios CO_2, a species widely detected in inner disk surface gas by *Spitzer*, is present in the disk surface layers. At the location shown in Fig. 5.4, about 1% of the total carbon ends up in CO_2. In regions shielded from stellar photons, cosmic-ray ionization and ion chemistry control destruction of CH_3OH and CO_2. With the exception of the innermost disk, the midplane chemistry is much slower with little to no change in the dominant carbon carrier over a disk lifetime of 10^6 years (Fig. 5.3).

Midplane Compositions

Whereas the surface layers of the disk are dominated by CO in all three end-member scenarios, there are a distinct sets of carbon carriers found in the midplane (top three rows of Fig. 5.4). For the case where the initial carbon carrier is CO_2 ice, after 10^6 years carbon in the midplane at 1 au is distributed

between CO_2 and CO. For CH_3OH ice, a wider range of carbon species is found including CH_4, H_2CO, CH_3, and HCN. The exact set of products depends on the chosen chemical reaction network. For the carbon grain model, nearly all carbon in the midplane remains on grain surfaces beyond 1 au and in the form of CO in the innermost disk. When the model is allowed to run for 10^7 years, the percentage of CO increases from ∼10% to ∼45% for the CO_2 ice scenario. The percentages of CO and CH_4 also increase in the CH_3OH ice scenario, from ∼4% and ∼8% to ∼37% and ∼26%, respectively. Furthermore, additional hydrocarbons appear at the ∼1% level.

Midplane chemistry is largely dependent on the degree of ionization in these dense disk regions and therefore the cosmic-ray ionization rate. This parameter is not well constrained for most protoplanetary disks. The interstellar value is around 3×10^{-17} s^{-1}, but may be lower due to the stellar winds or magnetic fields of young, accreting T-Tauri stars. The cosmic-ray ionization rate has been estimated to be $\lesssim10^{-19}$ s^{-1} based on observations of ionized species for the disk of TW Hya (Cleeves et al. 2015). We tested the CH_3OH ice scenario at this lower ionization rate and found no carbon removed from the original carrier (CH_3OH) in the midplane at 1 au.

Altering Gas-phase C/O

The modeled scenarios described above suggest an accretion scenario in which solids from the outer disk dominate the composition of the inner disk upon entry. However, gas accretion may introduce outer-disk gas compositions into the inner regions as well. Originating from colder regions beyond the H_2O snowline, the outer-disk gas would be H_2O-poor as observed by (Hogerheijde et al. 2011; Du et al. 2017). Reducing the oxygen content of the gas will alter the chemical evolution and major carbon reservoirs (Du et al. 2015; Bergin et al. 2016). We test the scenario in which the carbon carriers that have radially drifted inward from the outer disk interact with H_2O-depleted gases also entering the inner disk regions. To model this, we reduce initial H_2O ice abundances from 10^{-4} to 10^{-9} relative to total H, preventing release of abundant H_2O from icy surfaces, therefore simulating H_2O-poor gas. It is assumed that the H_2O ice on the accreted grains will remain locked in solid form beyond the H_2O snowline and therefore can be ignored in this model scenario for radii >1 au.

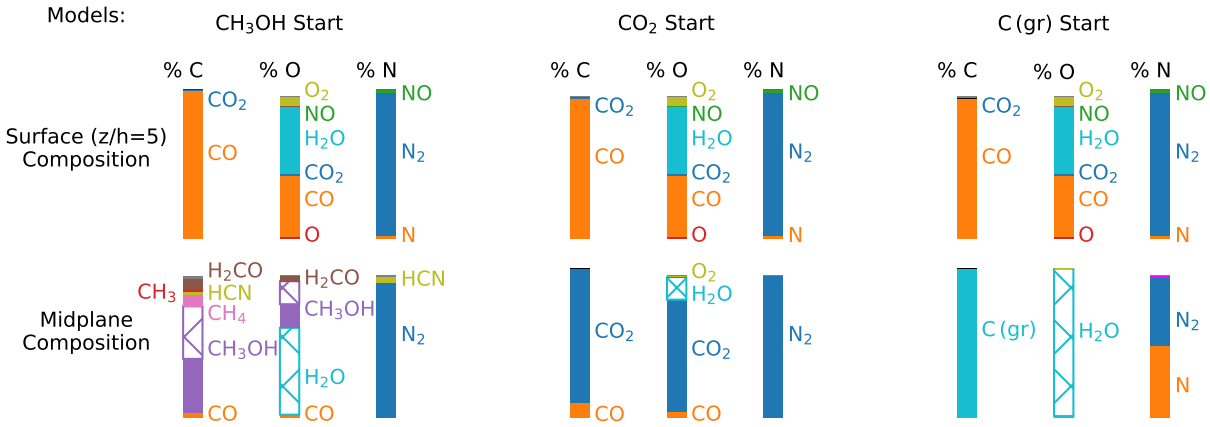

Figure 5.4: Major carbon, oxygen, and nitrogen species at five scale heights above the midplane in the disk surface layers (top row) and at the disk midplane (bottom row) at a radius of 1 au in our models. Results are shown at 10^6 years for three different models, from left to right: all of initial carbon starting in CH_3OH ice, CO_2 ice, and amorphous carbon grains. Bar colors indicate the distribution of each element by number of atoms across chemical species. All chemical species comprising more than 1% of the total budget for each element are labeled. Bars filled in solid colors represent species in the gas phase whereas hatch patterns represent ices.

Because of the oxygen content of CH_3OH and CO_2, the presence of H_2O-poor gas beyond the H_2O snowline has little effect on the main carbon products in the surface layers. For the amorphous carbon grain case however, the surface products change substantially (Fig. 5.5). The lack of H_2O in the gas limits the amount of oxygen available to produce CO. Instead, carbon is distributed over various nitrogen-bearing and hydrocarbon species, many containing large carbon chains.

5.4 Discussion

Observations of the potential carbon carriers in disks are crucial to test the modeled scenarios. The inner regions of protoplanetary disks are probed by space- and ground-based infrared telescopes. *Spitzer* detected CO_2, in addition to carbon-bearing species HCN and C_2H_2, in a number of protoplanetary disks (e.g., Pontoppidan et al. 2010; Salyk et al. 2011). Keck-NIRSPEC has provided CO observations for a comparable sample (Salyk et al. 2011). To date CH_4 has been observed via absorption in only one disk, GV Tau (Gibb and Horne 2013). While CH_3OH has not yet been observed in the inner disk regions, the sensitivity of ALMA has recently allowed for observations of CH_3OH in

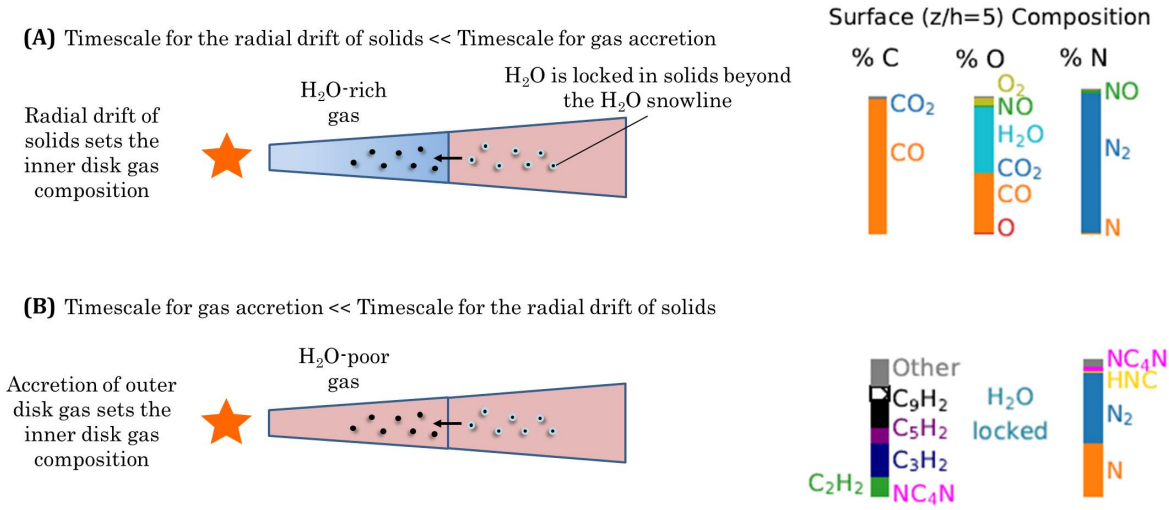

Figure 5.5: Comparions of major carbon, oxygen, and nitrogen species for distinct gas-phase C/O ratios. Plotted are two scenarios, first the initial model where carbon starts in the form of amorphous carbon grains and the inner disk gas composition is dominated by radial drift of solids and the subsequent vaporization of their volatile-rich icy surfaces (A) and then an additional carbon grain model that assumes that the inner disk gas composition is dominated by accretion of H_2O-poor gas from the cold outer disk where the bulk of the water is frozen on grain surfaces (B). Results are shown at 10^6 years for the disk surface at five scale heights above the midplane at a radius of 1 au. Bar colors indicate the distribution of each element by number of atoms across chemical species. All chemical species comprising more than 1% of the total budget for each element are labeled. The label "Other" represents C_6H_2, $C_{10}H_2$, HC_9N ice, NC_6N, C_8H_2, C_7H_2, HC_3N, C_4H_2, HC_5N, and HNC at levels of 1–4%. Bars filled in solid colors represent species in the gas phase whereas hatch patterns represent ices.

the the outer disk gas of TW Hya (Walsh et al. 2016). Further exploration of carbon species including CO, CO_2, CH_4, and CH_3OH in protoplanetary disks will be completed by JWST.

Our results suggest that abundant reservoirs that trace the original carbon carriers from the outer disk are only preserved up to 2–3 scale heights above the midplane. Further, chemical abundances in the higher surface layers appear very similar regardless of the initial carbon carrier because over short timescales the final compositions converge to the same dominant species. In these high layers, which are above the dust optical surface at mid-infrared wavelengths where key lines of these species will be observed, the original carriers are rapidly destroyed by photochemistry. Given the optical depth

limitations, we expect the observed compositions in the infrared to be largely uniform across many protoplanetary disks. If this is not the case, it may mean that photochemistry is much less efficient than modeled here or that dynamical processes are constantly resupplying material from the outer disk and/or midplane. Current observational constraints do not rule out disk compositions that are relatively uniform across different sources. Local thermal equilibrium (LTE) models fit to *Spitzer* and Keck-NIRSPEC survey data find that the best-fit column density ratios of CO_2, HCN, and C_2H_2 relative to H_2O range from 10^{-4}–10^{-2} within 1σ and the reported scatter in CO/H_2O is only a factor of $\sim$5–10 (Salyk et al. 2011).

Photochemistry may vary for different stellar environments. In fact, Herbig disks, which have stronger UV fields relative to T-Tauri sources, have been observed in CO but these same disks lack detections of HCN, C_2H_2, and CO_2 emission seen in many T-Tauri disks (Pontoppidan et al. 2010; Salyk et al. 2011). Sources with lower UV fluxes may reprocess carbon carriers more slowly, preserving the more diverse chemical compositions such as those seen closer to the midplane in our models. However, lower UV fluxes may also result in colder disks, where increased settling causes increased penetration of UV photons into the disk, moving the photoactive layer closer to the midplane. Fully understanding this process would require iterative modeling of the vertical disk structure and radiation environment, particularly for the dense inner disk regions.

The rate of vertical motion of material from the midplane to the observable surface layers depends on the means of angular momentum transport in the disk. Given the rapid photochemistry converting the initial carbon carriers into CO at the disk surface at timescales $<$1 yr, resupply from the midplane would need to be extremely efficient in order to maintain a diversity of carbon species in the photon-dominated surface layers. The diffusion timescale for a single scale height at 1 au is about 15 yrs based on the formula for the diffusion coefficient of gas from Dullemond and Dominik (2004) and turbulence characterized by a standard α value of 0.01. Uncertainty in the diffusion coefficient by orders of magnitude could largely vary this timescale estimate. If vertical mixing of materials occurs more slowly than the photochemistry, it would result in the surface composition spreading throughout the entire column.

Although infrared observations are limited to the disk surface due to the optically thick dust emission at these wavelengths, longer wavelength observations may probe deeper. Observatories such as the future Square Kilometer Array (SKA) with low frequencies of 50–350 MHz and mid-range frequencies of 350 MHz to 15.3 GHz, corresponding to cm to m wavelengths, may detect signatures from the midplane for low-frequency emitters including CH_3OH. This would provide crucial information about midplane CH_3OH abundances that could help distinguish the carbon carrier scenarios.

5.5 Conclusion

Here we modeled the carbon chemistry of the inner region of protoplanety disks assuming delivery of carbon from the outer disk where it has been chemically converted from CO into various less volatile carbon carriers. We simulate the entry of these carbon carriers into the inner disk using dynamically static chemical models and investigate the effects of the initial carbon carrier for three endmember scenarios: CH_3OH ice, CO_2 ice, and amorphous carbon grains. We have made the following conclusions based on these analyzes:

- Considering only chemical changes in a dynamically static disk, the surface layer composition in the inner disk is dominated by photochemistry which resets the initial chemical state towards one dominated by CO regardless of whether the initial carbon carrier is CH_3OH, CO_2, or amorphous carbon grains. Midplane compositions, however, are diverse and preserve product combinations unique to each carbon carrier.

- The degree of conversion of the original carbon carriers to new products that occurs in the midplane is largely driven by ion chemistry and therefore dependent on the cosmic-ray ionization rate.

- Mass transport will largely affect the inner disk composition. Efficient vertical transport of materials may result in the destruction of preserved midplane carbon species. In this case, observations of the surface layers would reflect the entire vertical column. In addition, the rate of resupply of carbon-coated and icy solids vs. H_2O-poor gases from the outer disk could vary the main carbon carriers from more oxidized species to hydrocarbons.

5.6 Acknowledgments

This material is based upon work supported by the National Science Foundation via the Graduate Research Fellowship Program under Grant No. DGE-1144469 and the Astronomy and Astrophysics Research Grants Program under Grant No. AST-1514918.

REFERENCES

D. E. Anderson, E. A. Bergin, G. A. Blake, F. J. Ciesla, R. Visser, and J.-E. Lee. Destruction of Refractory Carbon in Protoplanetary Disks. *ApJ*, 845: 13, August 2017. doi: 10.3847/1538-4357/aa7da1.

E. A. Bergin, L. I. Cleeves, U. Gorti, K. Zhang, G. A. Blake, J. D. Green, S. M. Andrews, N. J. Evans, II, T. Henning, K. Öberg, K. Pontoppidan, C. Qi, C. Salyk, and E. F. van Dishoeck. An old disk still capable of forming a planetary system. *Nature*, 493:644–646, January 2013. doi: 10.1038/nature11805.

E. A. Bergin, L. I. Cleeves, N. Crockett, and G. A. Blake. Exploring the Origins of Carbon in Terrestrial Worlds. *Faraday Discussions*, 168, February 2014. doi: 10.1039/C4FD00003J.

E. A. Bergin, F. Du, L. I. Cleeves, G. A. Blake, K. Schwarz, R. Visser, and K. Zhang. Hydrocarbon Emission Rings in Protoplanetary Disks Induced by Dust Evolution. *ApJ*, 831:101, November 2016. doi: 10.3847/0004-637X/831/1/101.

T. J. Bethell and E. A. Bergin. The Propagation of Lyα in Evolving Protoplanetary Disks. *ApJ*, 739:78, October 2011a. doi: 10.1088/0004-637X/739/2/78.

T. J. Bethell and E. A. Bergin. Photoelectric Cross-sections of Gas and Dust in Protoplanetary Disks. *ApJ*, 740:7, October 2011b. doi: 10.1088/0004-637X/740/1/7.

A. D. Bosman, A. G. G. M. Tielens, and E. F. van Dishoeck. Efficiency of radial transport of ices in protoplanetary disks probed with infrared observations: the case of CO_2. *A&A*, 611:A80, April 2018. doi: 10.1051/0004-6361/201732056.

S. Bruderer. Survival of molecular gas in cavities of transition disks. I. CO. *A&A*, 559:A46, November 2013. doi: 10.1051/0004-6361/201321171.

E. Chapillon, S. Guilloteau, A. Dutrey, and V. Piétu. Disks around CQ Tauri and MWC 758: dense PDR or gas dispersal? *A&A*, 488:565–578, September 2008. doi: 10.1051/0004-6361:200809523.

L. I. Cleeves, F. C. Adams, and E. A. Bergin. Exclusion of Cosmic Rays in Protoplanetary Disks: Stellar and Magnetic Effects. *ApJ*, 772:5, July 2013. doi: 10.1088/0004-637X/772/1/5.

L. I. Cleeves, E. A. Bergin, C. Qi, F. C. Adams, and K. I. Öberg. Constraining the X-Ray and Cosmic-Ray Ionization Chemistry of the TW Hya Protoplanetary Disk: Evidence for a Sub-interstellar Cosmic-Ray Rate. *ApJ*, 799:204, February 2015. doi: 10.1088/0004-637X/799/2/204.

B. T. Draine and H. M. Lee. Optical properties of interstellar graphite and silicate grains. *ApJ*, 285:89–108, October 1984. doi: 10.1086/162480.

F. Du, E. A. Bergin, and M. R. Hogerheijde. Volatile depletion in the TW Hydrae disk atmosphere. *ApJ*, 807:L32, July 2015. doi: 10.1088/2041-8205/807/2/L32.

F. Du, E. A. Bergin, M. Hogerheijde, E. F. van Dishoeck, G. Blake, S. Bruderer, I. Cleeves, C. Dominik, D. Fedele, D. C. Lis, G. Melnick, D. Neufeld, J. Pearson, and U. Yıldız. Survey of Cold Water Lines in Protoplanetary Disks: Indications of Systematic Volatile Depletion. *ApJ*, 842:98, June 2017. doi: 10.3847/1538-4357/aa70ee.

C. P. Dullemond and C. Dominik. The effect of dust settling on the appearance of protoplanetary disks. *A&A*, 421:1075–1086, July 2004. doi: 10.1051/0004-6361:20040284.

A. Dutrey, S. Guilloteau, and M. Simon. The BP Tau disk: A missing link between Class II and III objects? *A&A*, 402:1003–1011, May 2003. doi: 10.1051/0004-6361:20030317.

C. Eistrup, C. Walsh, and E. F. van Dishoeck. Setting the volatile composition of (exo)planet-building material. Does chemical evolution in disk midplanes matter? *A&A*, 595:A83, November 2016. doi: 10.1051/0004-6361/201628509.

C. Favre, L. I. Cleeves, E. A. Bergin, C. Qi, and G. A. Blake. A Significantly Low CO Abundance toward the TW Hya Protoplanetary Disk: A Path to Active Carbon Chemistry? *ApJ*, 776:L38, October 2013. doi: 10.1088/2041-8205/776/2/L38.

J. K. J. Fogel, T. J. Bethell, E. A. Bergin, N. Calvet, and D. Semenov. Chemistry of a Protoplanetary Disk with Grain Settling and Lyα Radiation. *ApJ*, 726:29, January 2011. doi: 10.1088/0004-637X/726/1/29.

K. Furuya and Y. Aikawa. Reprocessing of Ices in Turbulent Protoplanetary Disks: Carbon and Nitrogen Chemistry. *ApJ*, 790:97, August 2014. doi: 10.1088/0004-637X/790/2/97.

E. L. Gibb and D. Horne. Detection of CH_4 in the GV Tau N Protoplanetary Disk. *ApJ*, 776:L28, October 2013. doi: 10.1088/2041-8205/776/2/L28.

N. Harada, E. Herbst, and V. Wakelam. A New Network for Higher-temperature Gas-phase Chemistry. I. A Preliminary Study of Accretion Disks in Active Galactic Nuclei. *ApJ*, 721:1570, October 2010. doi: 10.1088/0004-637X/721/2/1570.

T. J. Harries, J. D. Monnier, N. H. Symington, and R. Kurosawa. Three-dimensional dust radiative-transfer models: the Pinwheel Nebula of WR 104. *MNRAS*, 350:565–574, May 2004. doi: 10.1111/j.1365-2966.2004.07668.x.

M. R. Hogerheijde, E. A. Bergin, C. Brinch, L. I. Cleeves, J. K. J. Fogel, G. A. Blake, C. Dominik, D. C. Lis, G. Melnick, D. Neufeld, O. Panić, J. C. Pearson, L. Kristensen, U. A. Yıldız, and E. F. van Dishoeck. Detection of the Water Reservoir in a Forming Planetary System. *Science*, 334:338, October 2011. doi: 10.1126/science.1208931.

A. P. Jones. The Cycle of Carbon Dust in the ISM. In T. Henning, E. Grün, and J. Steinacker, editors, *Cosmic Dust - Near and Far*, volume 414 of *Astronomical Society of the Pacific Conference Series*, page 473, December 2009.

A. P. Jones. Variations on a theme - the evolution of hydrocarbon solids. III. Size-dependent properties - the optEC$_s$(a) model. *A&A*, 542:A98, June 2012. doi: 10.1051/0004-6361/201118483.

S. Krijt, K. R. Schwarz, E. A. Bergin, and F. J. Ciesla. Transport of CO in Protoplanetary Disks: Consequences of Pebble Formation, Settling, and Radial Drift. *ApJ*, 864:78, September 2018. doi: 10.3847/1538-4357/aad69b.

B. Marty, C. M. O. Alexander, and S. N. Raymond. Primordial Origins of Earth's Carbon. *Reviews in Mineralogy and Geochemistry*, 75:149–181, January 2013. doi: 10.2138/rmg.2013.75.6.

M. K. McClure, E. A. Bergin, L. I. Cleeves, E. F. van Dishoeck, G. A. Blake, N. J. Evans, II, J. D. Green, T. Henning, K. I. Öberg, K. M. Pontoppidan, and C. Salyk. Mass Measurements in Protoplanetary Disks from Hydrogen Deuteride. *ApJ*, 831:167, November 2016. doi: 10.3847/0004-637X/831/2/167.

A. Miotello, E. F. van Dishoeck, J. P. Williams, M. Ansdell, G. Guidi, M. Hogerheijde, C. F. Manara, M. Tazzari, L. Testi, N. van der Marel, and S. van Terwisga. Lupus disks with faint CO isotopologues: low gas/dust or high carbon depletion? *A&A*, 599:A113, March 2017. doi: 10.1051/0004-6361/201629556.

Ajay Mishra and Aigen Li. PROBING THE ROLE OF CARBON IN THE INTERSTELLAR ULTRAVIOLET EXTINCTION. *The Astrophysical Journal*, 809(2):120, aug 2015. doi: 10.1088/0004-637x/809/2/120. URL `https://doi.org/10.1088%2F0004-637x%2F809%2F2%2F120`.

K. M. Pontoppidan, C. Salyk, G. A. Blake, R. Meijerink, J. S. Carr, and J. Najita. A Spitzer Survey of Mid-infrared Molecular Emission from Protoplanetary Disks. I. Detection Rates. *ApJ*, 720:887–903, September 2010. doi: 10.1088/0004-637X/720/1/887.

L. Reboussin, V. Wakelam, S. Guilloteau, F. Hersant, and A. Dutrey. Chemistry in protoplanetary disks: the gas-phase CO/H_2 ratio and the carbon reservoir. *A&A*, 579:A82, July 2015. doi: 10.1051/0004-6361/201525885.

C. Salyk, K. M. Pontoppidan, G. A. Blake, J. R. Najita, and J. S. Carr. A Spitzer Survey of Mid-infrared Molecular Emission from Protoplanetary Disks. II. Correlations and Local Thermal Equilibrium Models. *ApJ*, 731: 130, April 2011. doi: 10.1088/0004-637X/731/2/130.

B. D. Savage and K. R. Sembach. Interstellar Abundances from Absorption-Line Observations with the Hubble Space Telescope. *ARA&A*, 34:279–330, 1996. doi: 10.1146/annurev.astro.34.1.279.

K. R. Schwarz, E. A. Bergin, L. I. Cleeves, G. A. Blake, K. Zhang, K. I. Öberg, E. F. van Dishoeck, and C. Qi. The Radial Distribution of H_2 and CO in TW Hya as Revealed by Resolved ALMA Observations of CO Isotopologues. *ApJ*, 823:91, June 2016. doi: 10.3847/0004-637X/823/2/91.

K. R. Schwarz, E. A. Bergin, L. I. Cleeves, K. Zhang, K. I. Öberg, G. A. Blake, and D. Anderson. Unlocking CO Depletion in Protoplanetary Disks. I. The Warm Molecular Layer. *ApJ*, 856:85, March 2018. doi: 10.3847/1538-4357/aaae08.

C. Walsh, R. A. Loomis, K. I. Öberg, M. Kama, M. L. R. van 't Hoff, T. J. Millar, Y. Aikawa, E. Herbst, S. L. Widicus Weaver, and H. Nomura. First Detection of Gas-phase Methanol in a Protoplanetary Disk. *ApJ*, 823:L10, May 2016. doi: 10.3847/2041-8205/823/1/L10.

M. Yu, K. Willacy, S. E. Dodson-Robinson, N. J. Turner, and N. J. Evans, II. Probing Planet Forming Zones with Rare CO Isotopologues. *ApJ*, 822:53, May 2016. doi: 10.3847/0004-637X/822/1/53.

K. Zhang, E. A. Bergin, G. A. Blake, L. I. Cleeves, and K. R. Schwarz. Mass inventory of the giant-planet formation zone in a solar nebula analogue. *Nature Astronomy*, 1:0130, June 2017. doi: 10.1038/s41550-017-0130.

Chapter 6

CHARACTERIZATION OF LASER-INDUCED BREAKDOWN SPECTROSCOPY (LIBS) EMISSION LINES FOR THE IDENTIFICATION OF CHLORIDES, CARBONATES, AND SULFATES IN SALT/BASALT MIXTURES FOR THE APPLICATION TO MSL CHEMCAM DATA

D. E. Anderson[1], B. L. Ehlmann[1,2], O. Forni[3], S. M. Clegg[4], A. Cousin[3], N. H. Thomas[1], J. Lasue[3], D. M. Delapp[4], R. E. McInroy[4], O. Gasnault[3], M. D. Dyar[5], S. Schröder[6], S. Maurice[3], & R. C. Wiens[4]

[1]Division of Geological and Planetary Sciences, California Institute of Technology, Pasadena, California 91125, USA.

[2]Jet Propulsion Laboratory, California Institute of Technology, Pasadena, California 91109, USA.

[3]Institut de Recherche en Astrophysique et Planétologie (IRAP), 31400 Toulouse, France.

[4]Los Alamos National Laboratory, Los Alamos, New Mexico 87545, USA.

[5]Department of Astronomy, Mount Holyoke College, South Hadley, Massachusetts 01075, USA.

[6]German Aerospace Center (DLR), 12489 Berlin, Germany.

Abstract Ancient environmental conditions on Mars can be probed through the identification of minerals on its surface, including water-deposited salts and cements dispersed in the pore space of sedimentary rocks. Laser-induced breakdown spectroscopy (LIBS) analyses by the martian rover Curiosity's ChemCam instrument can indicate salts, and ChemCam surveys aid in identifying and selecting sites for further, detailed in situ analyses. We performed laboratory LIBS experiments under simulated Mars-conditions with a ChemCam-like instrument on a series of mixtures containing increasing concentrations of salt in a basaltic background to investigate the potential for identifying and quantifying chloride, carbonate, and sulfate salts found only in small amounts, dispersed in bulk rock with ChemCam, rather than concentrated in veins. Data indicate that the presence of emission lines from the

basalt matrix limited the number of Cl, C, and S emission lines found to be useful for quantitative analysis; nevertheless, several lines with intensities sensitive to salt concentration were identified. Detection limits for the elements based on individual emission lines ranged from ∼20 wt. % carbonate (2 wt. % C), ∼5–30 wt. % sulfate (1–8 wt. % S), and ∼5–10 wt. % chloride (3–6 wt. % Cl) depending on the basaltic matrix and/or salt cation. Absolute quantification of Cl, C, and S in the samples via univariate analysis depends on the cation-anion pairing in the salt but appears relatively independent of matrices tested, following normalization. These results are promising for tracking relative changes in the salt content of bulk rock on the martian surface with ChemCam.

6.1 Introduction

Salts act as a tracer of past environments. As ionic solids that precipitate from aqueous fluids, salts indicate the presence of liquid water and its geochemistry, which are relevant for evaluating habitability and organics preservation potential on planetary surfaces. Assessing past and present martian surface environments is the objective of in situ experiments performed by Curiosity, the Mars Science Laboratory rover, which is currently traversing the 155-km Gale impact crater that formed ∼3.8–3.6 billion years ago on the boundary between the southern highlands and northern lowlands [Thomson et al., 2011; Le Deit et al., 2013]. Within the crater are alluvial fan and lacustrine deposits and a 5-km-high central mound, Aeolis Mons, informally known as Mount Sharp. The sedimentary strata that constitute these features record the ancient geological and geochemical history of the region, including evidence of aqueous activity and a transition in minerology from clays to sulfates, potentially related to a global climate change on Mars [Anderson & Bell, 2010; Milliken et al., 2010]. Curiosity samples the chemical composition of Gale crater rocks and sediments using a suite of instruments including ChemCam, which performs laser-induced breakdown spectroscopy (LIBS) and remote micro-imaging (RMI) [Wiens et al., 2012; Maurice et al., 2012].

LIBS is an atomic emission spectroscopy technique initiated by laser ablation of the target surface resulting in the formation of a hot (electronically excited) plasma. As the plasma cools, continuum, ionic, and atomic emissions occur, revealing the elemental composition of the sample [Cremers & Radziemski, 2013]. At a late stage, when the plasma has sufficiently cooled, molecular

emissions can also be observed—not from molecules in the original sample, but due to recombination of atoms in the plasma [e.g., Gaft et al., 2014; Forni et al., 2015]. ChemCam acts as a survey tool, having collected more than 422,000 spectra to date. It targets rocks and soils at distances 1.5–7 m from the rover, analyzing spots of 350–500 µm diameter with multiple laser shots to remove dust from the surface and obtain chemical depth profiles, allowing the study of potential coatings [Lanza et al., 2015], [Wiens et al., 2012; Maurice et al., 2012]. The wealth of data collected by ChemCam aids in directing Curiosity towards intriguing science targets for further analyses with its instrument suite [e.g., Newsom et al., 2016; Frydenvang et al., 2016; Gasda et al., 2016] and provides a chemical record of samples throughout the entire rover traverse.

Chlorides, carbonates, and sulfates represent classes of potential evaporite minerals that have been previously detected on the martian surface; perchlorates and nitrates are also found in minor amounts [e.g., Ehlmann & Edwards, 2014; Gendrin et al., 2005; Hecht et al., 2009; Stern et al., 2015]. S and Cl are common bulk chemical components of Martian fine soils and rocks, as measured by APXS [e.g., Yen et al., 2005]. Sulfates have been detected within Mount Sharp strata from orbit [Milliken et al., 2010] and in situ by Curiosity in veins at multiple locations. Calcium sulfate, mostly bassanite, veins were first identified by ChemCam in Yellowknife Bay [Nachon et al., 2014; Rapin et al., 2016] and later confirmed through X-ray diffraction (XRD) with Curiosity's Chemistry and Mineralogy instrument (CheMin) [Vaniman et al., 2014]. Sulfates were also identified in the light-toned veins of Garden City [Nachon et al., 2017]. In addition, LIBS molecular emission lines of CaCl have been detected from some Gale crater rocks [Forni et al., 2015], potentially as a result of NaCl in the rock (Ca from the accompanying host rock mixes with the Cl in the plasma to produce the CaCl molecular line that is identified in the LIBS spectrum). At Gale Crater, carbonates have not yet been inferred from ChemCam data nor found at abundances >1–2 wt. % using CheMin [Leshin et al., 2013]. The ChemCam spot size of 350–500 µm allows the instrument to pinpoint and measure the composition of individual salt veins. However, an outstanding question is the ability of ChemCam to detect more dispersed salts that would appear at lower concentrations in the bulk rock, for example as detrital contributions, cementing agents, or diagenetic precipitates in the sedimentary rocks in Gale crater.

The presence of salts in bulk rocks has been inferred using ChemCam based on observed anti-correlations between the potential cation and other major elements [e.g., Clegg et al., 2013]; however, identification of salt anions can be a challenge. LIBS is more sensitive to elements that have low ionization energies (e.g., Na I, 5.1 eV) for which more atoms are excited in response to a particular energy input. It is less sensitive to elements with high ionization energies including chlorine (Cl I, 13.0 eV), carbon (C I, 11.3 eV), and sulfur (S I, 10.4 eV), which are crucial for identifying chloride, perchlorate, carbonate, and sulfate anions. These elements produce weak emission lines, making them more difficult to characterize than elements with prominent peaks such as alkalis, alkaline earth elements, and transition metals. The ChemCam team has therefore devoted particular attention to the measurement of Cl, C, and S in the laboratory. Cousin et al. [2011] developed a database of lines detectable by ChemCam under a martian atmosphere for 32 elements focusing on controlled samples composed of a single or a small number of elements to ensure proper line identification. They identified 27 lines for Cl, 33 for C, and 28 for S. Ollila et al. [2011] focused on carbon, identifying 18 C peaks and 21 C_2 Swan bandheads in graphite and all 18 C peaks and 4 of the C_2 Swan bandheads in one or more geologic samples. Lanza et al. [2010] found that different carbonates could be distinguished from igneous materials and from each other using multivariate techniques on LIBS spectra collected under martian conditions. Sulfur-bearing rock samples including sulfates and sulfides were used in the study by Dyar et al. [2011], which recommended implementing multivariate analysis of the spectral regions containing S lines around 540.08–550.10 and 559.18–567.10 nm instead of univariate analysis of the S emission lines for quantitative studies. Schröder et al. [2013] optimized multivariate techniques for distinguishing the spectra of eight chloride and sulfate salts and frozen salt-water solutions and selected 14 Cl and 10 S lines that were most relevant in their analysis. To complement this body of work, we conducted a systematic study of salts present at decreasing concentrations in prepared salt+basalt mixtures to address further questions regarding the influence of basaltic matrices and the detectability of salts present at low concentrations in the LIBS spectra.

Here we analyze LIBS spectra acquired for pressed pellets of salt+basalt mixtures measured in the laboratory under martian environmental conditions with a ChemCam-like instrument so as to ultimately aid in the study of chlorine,

carbon, and sulfur salt contents in martian rock and soil targets. We build upon prior work by (1) measuring LIBS spectra of controlled mixtures of Mars-relevant salts to investigate how effects due to the basaltic matrix—typical geochemistry for martian materials—influence the spectra and our ability to identify salt-related emission lines and (2) preparing the mixtures at several concentrations of salt relative to basalt to evaluate the potential for quantitative analysis of abundance and to establish detection thresholds. We present the spectral trends in continuum and line emission with salt concentration; identify Cl, S, and C detection thresholds; determine the best lines for use in anion detection and quantification; and then discuss how these results relate to the current literature and their applicability to the ChemCam dataset and future Mars LIBS investigations.

6.2 Materials and Methods

6.2.1 Sample Preparation & Analysis

The sample set represents a selection of chlorides, carbonates, sulfates, and basalts potentially relevant to martian surface science (Table 6.1–6.2). The set is designed to investigate the effects of two variables in sample composition on the anion lines in the LIBS spectra: the cation element in the salt and the rock matrix. To this end, at least two samples of a given salt anion were included, each with a different cation. All salts were mixed with K1919, a moderate-alkali (2.27±0.01 wt. % Na_2O and 0.52±0.01 wt. % K_2O) Hawaiian basalt. In addition, for a subset of salts, a suite of salt-basalt mixtures were produced with GBW07105, a higher-alkali basalt (3.32±0.01 wt. % Na_2O and 2.24±0.01 wt. % K_2O) from the Brammer Standard Company. Salt+basalt mixtures created at various concentrations allow for quantitative analysis of anion lines through production of calibration curves (Figure 6.1) and the determination of Cl, C, and S detection limits in these mixtures.

Mixture preparation was as follows. Salt and basalt powder endmembers were produced from reagent grade chemicals or natural rock and mineral samples (Table 6.2). Non-particulate samples were crushed with a jaw crusher to produce sub-mm particles. All endmember particulates were then run through a shatterbox for several minutes to produce powders with grain sizes less than the spot size of the laser ($\lesssim$350 µm; see Figure S1 in the supporting information for example size distributions of the grains prior to mixing). As a result of our preparation, 85–90% of the sample is <250 µm. While the existence

Table 6.1: Salt+Basalt Mixture Combinations.[a]

Basalts		Chlorides	Carbonates	Sulfates
K1919	+	$CaCl_2$	$CaCO_3$	$CaSO_4{\cdot}2H_2O$
	+	NaCl	$\underline{MgCO_3}$	$\underline{Fe_2(SO_4)_3}$
	+			$\underline{MgSO_4}$
	+			$\underline{Na_2SO_4}$
GBW07105	+	$\underline{NaCl}$		$\underline{CaSO_4{\cdot}2H_2O}$

[a]Each chloride, carbonate, or sulfate salt is paired with one of two basaltic backgrounds: the moderate-alkali K1919 (abbreviated here as KB) or high-alkali GBW07105 (GB). Underlined samples were measured in the second batch (see Methods).

of some clumps or grains larger than the spot size is not fully ideal, we do not observe sharp discontinuities in chemistry between laser shots or surface locations, which would occur if the measurements sampled only distinct individual grains. Thus, they appear well-mixed. Powders were physically mixed manually at concentrations of 5, 10, 30, 50, and 70 wt. % salt with a basaltic endmember for each combination listed in Table 6.1. Mixtures underlined in Table 6.1 were also prepared at a very low salt concentration of 0.5 wt. %. Elemental compositions of pure endmembers and a subset of the mixtures (the 10 and 50 wt. % salt mixtures of each salt+basalt series) were verified using flux-fusion inductively coupled plasma optical emission spectroscopy (ICP-OES) for major oxides, instrumental neutron activation analysis (INAA) for Cl, and combustion in a pure oxygen environment followed by gas-phase infrared spectroscopy (IR) for C and S (measured as CO2 and SO2, respectively) performed by Activation Laboratories Ltd. (Actlabs) (Table S1). Measured C, S, and Cl values match expected values (Figure S2).

Mixed sample powders were pressed into pellets, and LIBS analyses were performed using the ChemCam-analog instrument at Los Alamos National Laboratory [Clegg et al., 2017]. The instrument consists of the engineering model mast unit containing the laser, telescope, and RMI, placed inside an enclosure cooled to 14–19^{o}C, connected by a fiber to a body unit outside the enclosure containing the optical demultiplexer, spectrometers, and data processing unit. This setup generates a maximum ChemCam laser energy of 14 mJ/pulse. Samples were analyzed with 50 consecutive laser pulses on each of five different locations on the sample surface, producing 225 spectra per sample (after

Table 6.2: Endmembers and Their Sources Used in Mixtures.

Sample	Origin	Source
K1919	Kilauea, Hawaii	Caltech collection, near USGS BHVO-1 locality
GBW07105	NRCCRM, China	Brammer
$MgCO_3$		Ward's
$CaCO_3$	Minas, Nuevo Leon, Mexico	Ward's
$CaSO_4{\cdot}2H_2O$	Fremont County, Colorado	Ward's
$MgSO_4$	synthetic, reagent grade	Macron Chemicals
$Fe_2(SO_4)_3$	synthetic, reagent grade	Carolina Chemical
Na_2SO_4	synthetic, reagent grade	Carolina Chemical
NaCl	synthetic, reagent grade	Macron Chemicals
$CaCl_2$	synthetic, reagent grade	J.T. Baker
Fe_2O_3	Joan Monlevade, Minas Gerias, Brazil	Caltech Mineral Collection
SiO_2	NW end of Saline Valley, CA	Caltech Mineral Collection
$SiO_2{\cdot}nH_2O$	Colton, San Bernadino Co., CA	Caltech Mineral Collection

excluding the first five laser shots due to potential surface effects). The experiment was performed in a chamber containing 7 torr of CO2 to simulate a Mars-like atmosphere. Replicating the conditions under which the ChemCam dataset on Mars is collected is important for making relevant comparisons to data obtained by the mission [Cousin et al., 2011]. Emission was collected using three detectors over the following wavelength ranges: UV (240–340 nm), VIO (blue-violet, 380–470 nm) and VNIR (490–850 nm). The first batch of samples was measured in September-October 2013 at a laser-to-sample distance of 1.6 m and the second batch in August-September 2014 at a distance of 3 m. The change in distance was not an ideal difference between batches but was a consequence of the setup available at the time. Distance corrections were applied during data processing to account for the viewing geometry (see sections 6.2.2 and 6.4.2). Samples from the first batch of analyses with compositions measured by Actlabs were included in the database compiled by Clegg et al. [2017]. The identification labels for all samples are provided in Table S2 in the supporting information. A comparison of the total integrated LIBS emission per shot for each location on a sample surface showed similar behavior among, in most cases, all five and in a few anomalous cases, at least 3–4 of the spots. This suggests that the pellet material was reasonably homogeneous.

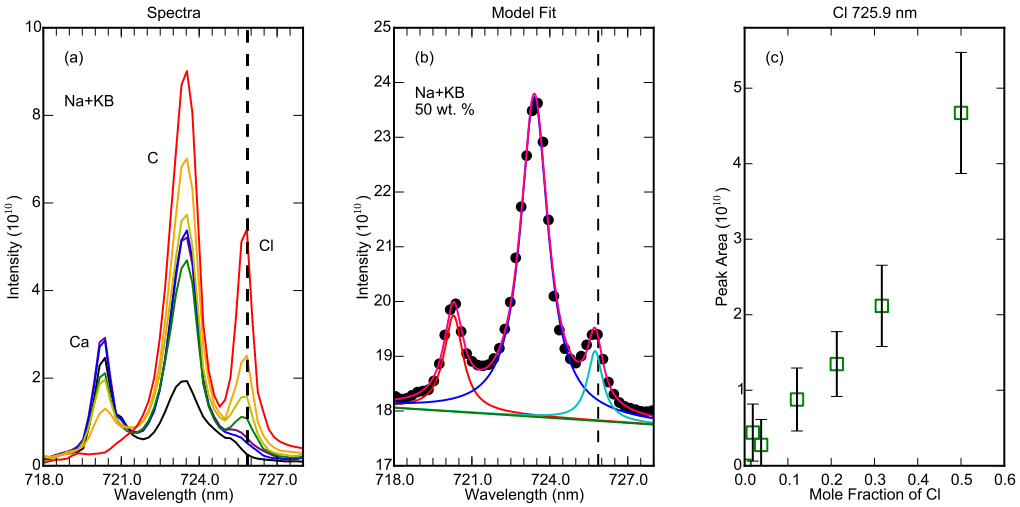

Figure 6.1: Example spectra, model fit, and resulting calibration curve for the Cl line at 725.9 nm in NaCl+K1919 mixtures (denoted by vertical dashed line). (a) Spectra for multiple salt concentrations are overlain after continuum removal. Colors in the spectra indicate different salt concentrations with pure basalt in black, pure salt in red, and mixtures containing salt mass fractions of 5 wt. % in purple, 10 wt. % in blue, 30 wt. % in green, 50 wt. % in yellow, and 70 wt. % in orange. Intensity is in units of photons/shot/mm^2/sr/nm. (b) An example model fit to the minimally-processed data (shown in black dots) of 50 wt. % NaCl in K1919. The final model (shown in magenta) is the sum of 3 Lorentzian peaks (shown in red, blue and cyan) with an underlying linear continuum (shown in green). (c) Peak area vs. mole fraction of Cl for the mixtures based on the model fits. Peak areas are in units of photons/shot/mm^2/sr.

6.2.2 Data Processing

Standard ChemCam data-processing techniques were applied to produce clean calibrated spectra (CCS) files used for analysis of ChemCam data [Wiens et al., 2013]. In addition, "minimally-processed" data products were produced to preserve characteristics of the raw spectra including the continuum emission. First, the "dark" background spectrum, the median of 50 spectra collected without the laser, was subtracted from each LIBS spectrum. This removes reflected light from the sample surface, any stray light in the instrument, and instrument noise, e.g., due to dark currents. A wavelength calibration was performed by applying an offset correction derived from the comparison between a Ti reference spectrum and the median spectrum of a Ti calibration target measured on the same day as the sample. The line wavelengths are calibrated to match those obtained in a vacuum to provide appropriate comparisons to reference databases. Each spectrum was then multiplied by a smoothed gain

function to correct for instrument response. Gaussian white noise was removed using the wavelet analysis method of Wiens et al. [2013]. The spectrum was decomposed into a series of consecutively lower resolution scales each described in terms of the wavelet basis and corresponding coefficients. A noise hard thresholding was defined at each scale by iteratively selecting wavelet coefficients less than three times the standard deviation from the average value. After ten iterations, wavelet coefficients less than the noise threshold were put to zero and the sum of the resulting wavelet scales became the de-noised spectrum. Finally, each spectrum is corrected for geometry, including the laser-to-sample distance, and the spectral resolution of each detector element. The spectrum is divided by the approximate area of the plasma (πr^2 where $r = 0.1$ mm), solid viewing angle ($\pi\ (h/d)^2$), where h is half the aperture of the telescope, 54.2 mm, and d is the distance to the target), and $\Delta\lambda$, obtained by fitting a second-order polynomial to the derivative of the wavelength vector. Following the processing steps outlined above, the units of the LIBS spectral data are spectral radiance, photons/shot/mm^2/sr/nm.

Continuum emission is typically removed from the spectrum during LIBS data processing to improve visibility of the spectral lines and prior to fitting peak areas for quantitative calculations. This is justified because unlike the spectral lines, continuum emission consists of Bremsstrahlung and recombination radiation from electron-ion interactions and does not provide direct information regarding elemental abundances [Cremers & Radziemski, 2013]. However, theoretically determining the exact shape of the continuum emission to be removed is challenging. Therefore, in typical ChemCam LIBS processing to produce CCS files, the intensity of the continuum is determined empirically by fitting the local minima or convex hulls after a wavelet decomposition, similar to that used in de-noising above [Wiens et al., 2013]. This continuum-removal algorithm is sensitive to large peaks and overall trends of the global spectrum. Because the existing algorithm is optimized to provide a global continuum removal, it can sometimes cause the weak anion lines of interest in this study to be over or under fit, altering the shape of the spectrum and the resulting peak areas. Only a few spectral regions display an observable difference in the spectra between the CCS and minimally-processed data. These include cases where two or more blended Cl lines appear at 507–510 nm (shown in Figure 6.2a,b) and 539–545 nm. However, to avoid altering our spectral regions prior to analysis, we elected to retain the continuum emission prior to peak fitting in

our minimally-processed spectra, and we only removed the continuum locally as part of peak area fitting for the anion lines. The sensitivity of the resulting calibration curves on this choice is discussed in section 6.2.4.

The spectra collected from individual laser shots were compared for different sample compositions to investigate changes in spectra due to depth into the sample or to random variation. Line intensity analyses were performed on the median spectra of shots 6-50 at the 5 sample locations. Median rather than mean spectra were selected to reduce the influence of outlier data. Two normalization techniques were tested: division of the area of individual channels (i.e., the intensity multiplied by $\Delta\lambda$) by the total integrated intensity of either (1) the entire spectrum resulting in a total normalized area equal to one (Norm 1) or (2) the spectral range of the detector to which the channel corresponds resulting in a total normalized area of three (Norm 3). The intensity totals were computed from the CCS files to include only the spectral lines and not the continuum. Work is ongoing to understand the applicability of normalization to atmospheric O and C lines for elements other than H. The effects of normalization on the results are described in sections 6.4.2–6.4.3.

6.2.3 Line Selection

To compare the spectral emission of different samples quantitatively, the integrated areas of emission lines of Cl, C, and S were measured. A selection of emission lines in the NIST Atomic Spectra Database [Kramida et al., 2015], representing elements relevant to the martian surface with ionization levels I-II, were considered and accessed via the ChemCam Quick Element Search Tool (C-QuEST, http://pds-geosciences.wustl.edu/workshops/ ChemCam_Workshop_Mar15.htm). For line identification, peak centers were allowed an uncertainty from the reference wavelength within $\pm 1.0\times$ the ChemCam spectrometer resolution ($\sim$0.2 nm for wavelengths $<$470 nm and $\sim$0.65 nm for wavelengths $>$470 nm). All emission lines in the C-QuEST database for the element of interest (C, S, Cl) were searched for in the LIBS data from a mixture suite by using an algorithm that checked for increasing line intensity with concentration as indicated by a positive slope between the intensity at the reference wavelength and the mole fraction of the element ($X_{element}$). Lines were ranked based on the value of this slope, with high values indicating a greater sensitivity, and the R^2 indicating a linear correlation. Line emission is expected to increase with the number of emitting atoms (mole fraction) in a

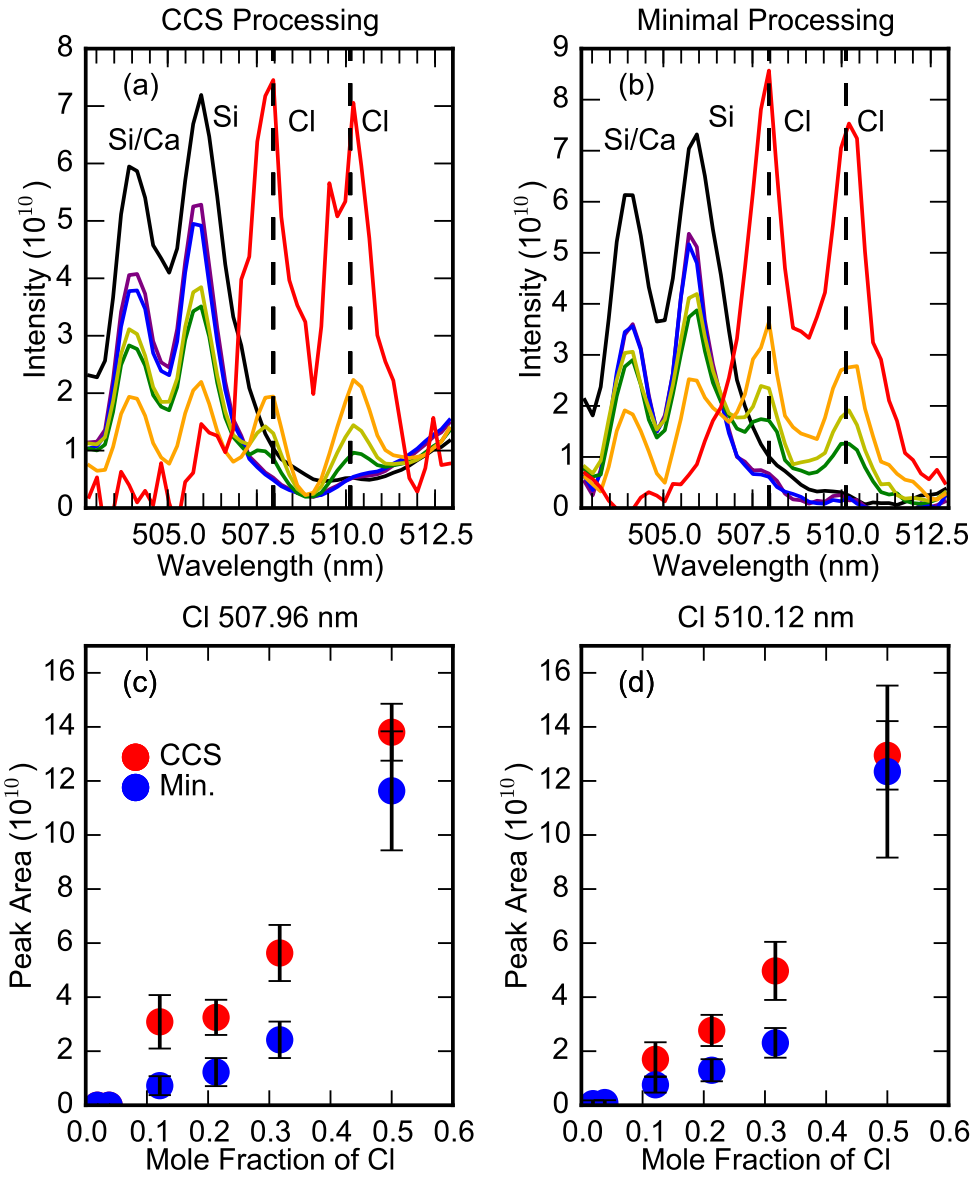

Figure 6.2: Comparison of spectra (a,b) and calibration curves (c,d) between CCS (a, red dots in c,d) and minimally-processed data (b, blue dots in c,d) for peaks at 507.9 and 510.1 nm in NaCl+K1919 mixtures. This example displays the uncommon case in which the resultant spectra are different, following the different data processing steps. Colors in the spectra indicate different salt concentrations with pure basalt in black, pure salt in red, and mixtures containing salt mass fractions of 5 wt. % in purple, 10 wt. % in blue, 30 wt. % in green, 50 wt. % in yellow, and 70 wt. % in orange. Intensity is in units of photons/shot/mm^2/sr/nm. Despite differences in the spectra, similar increasing trends are observed in the calibration curves. Peak areas are in units of photons/shot/mm^2/sr.

linear fashion when excluding complicating effects such as self-absorption at high abundances of the element or presence of the element in the blank (in our case, the pure basalt). Linear trends would provide the best ability to distinguish signals across a large range of concentrations improving quantification. However, emission lines were not excluded based on lack of linear trends since any monotonically increasing trend could be useful for some level of quantification. The increasing trends in the height of potential peaks with salt concentration in this subset of high-ranking lines were then visually verified by examination of the spectra.

Comparing a given spectral region among all salt+basalt mixtures, pure endmembers, and additional mixture sets including SiO_2+K1919, $SiO_2 \cdot nH_2O$+K1919, and Fe_2O_3+K1919 aided in identification of elemental lines. To avoid confusion with lines of other elements, the initial criteria for identification of anion lines that may be useful for univariate analysis in the mixture spectra were the following: (1) a visually detectable peak appeared above the level of the background emission at the location of the reference wavelength; (2) the peak was sufficiently free from interference such that it could be visually distinguished and fit separately from neighboring peaks; (3) the line strength generally increased with salt concentration, giving the calibration curve a positive slope; and (4) the line identity was supported by spectral comparison between mixtures, including those not containing the element in question. Stricter criteria to further select lines useful for future quantitative analyses based on our results were (5) a detection threshold of $\sim$50 wt. % salt or less regardless of mixture composition; (6) the line strength increased monotonically with salt concentration for high salt concentrations (with preference towards monotonically increasing trends starting at lower concentrations and with steeper slopes); and (7) reliable behavior independent of the chemistry of the matrix and host phase of the element of interest.

6.2.4 Fitting of Spectral Peaks

For lines identified according to the criteria outlined in section 6.2.3, the local spectral region was fit, using a Levenberg-Marquardt algorithm [Gill et al., 1981] as part of the LMFIT Python package [Newville et al., 2014] to model a spectrum composed of Lorentzian functions for all observable peaks and an underlying linear continuum. The local region to be fit was selected to include any nearby peaks of the same element, any peaks that interfered with or con-

tributed to the peak of interest, and a local region where the continuum could be reasonably approximated by including a linear function (Figure 6.1a,b). Simplified peak and continuum shapes were chosen to limit the use of excess free parameters. The number of peaks included in the model and their locations were determined based on those visibly present in the spectrum combined with knowledge provided in the C-QuEST data. Free parameters optimized with the Levenberg-Marquardt algorithm were: the continuum slope and its intercept as well as central wavelength, width, and height for each Lorentzian peak. Thus, each spectral region was fit with 3N+2 parameters, where N is the number of peaks. There were a minimum of 1.5 to a maximum of 9.4 spectral data points per parameter. Peak areas were computed with corresponding error estimates using the formula described by Fabre et al. [2014]: [(uncertainty in width/width) + (uncertainty in intensity/intensity)] × area. Uncertainties of one standard deviation on individual parameters were taken from the estimated covariance matrix.

Calibration curves were generated by plotting peak area vs. mole fraction of element (X). An example curve and the corresponding spectra are shown in Figure 6.1. We plot against mole fraction because fundamentally the strength of LIBS emission lines depends on the number of atoms producing emission rather than the mass of these atoms (or wt. %). The mole fraction is calculated from the theoretical chemical formula of the salt and the elemental composition of the basalt based on the ActLabs analysis (Table S1). This excludes the hydration state of the salt. Future work will focus on characterizing the hydration of these mixtures using the H peak [e.g., Thomas et al., 2015, 2016; Sobron et al., 2012; Rapin et al., 2016]. Peak area was selected rather than peak height because the total intensity of a single atomic emission line is typically spread over multiple spectral channels, and this method can better account for contributions to the line strength from interfering neighboring lines [Singh & Thakur, 2007]. A local continuum vs. global continuum fit affects the parameterization of the fit (curve shape and slope) but not the overall judgement as to the utility of the line (Figure 6.2c,d).

6.2.5 Calculation of Limits of Detection

For the analysis of unknown samples on the Martian surface, it is important to understand the lower limit of detectable salt concentrations. Three methods were used to determine the detection limits of Cl, C, and S in these mixtures

following the example of Wiens et al. [2013] and Lasue et al. [2012]. The first method (LOD1) defines the lowest measured concentration in the sample set where the line emission appears significantly above the noise. This threshold was determined by identifying the lowest salt concentration for which the height of emission at the elemental line locations is greater than three times the standard deviation of the noise in the data prior to de-noising. Peaks were only considered if they were centered on the same wavelength as the corresponding peak in the pure salt therefore excluding peaks due to matrix elements present near the line location at lower salt concentrations. The second method (LOD2) defines the concentration at which the signal is significantly above the blank [Cremers & Radziemski, 2013], in this case the spectrum of the basaltic composition endmember with no salt intermixed. LOD2 corresponds to the concentration where the signal of the anion line is two times the standard deviation of the blank above the signal in the blank. The signal from the blank can often be assumed to be close to zero; however, this is not the case for carbon, which is present in all measurements due to the atmosphere. Therefore, when above zero, the y-intercept of the calibration curve was taken as the signal in the blank. Due to difficulties in obtaining accurate statistics in the absence of an anion line signal, the standard deviation used for this calculation was that of the lowest measured salt concentration. The factor of two determines the probability of obtaining false positives, corresponding to a 95% confidence interval. The third and final method determines the limit of quantification (LOD3) taking into account the 95% confidence interval of the calibration curve [Massart et al. 1998, ch. 13]. This limit is included for consistency with previous ChemCam studies but is not as meaningful in this work because it assumes linear calibration curves, which was demonstrated to not be the case here (see section 6.4.3). Consequently, the limit increases with non-linearity.

6.3 Results

6.3.1 Whole Spectrum Trends with Salt Concentration: Systematic Change in Continuum

The emission lines present for a given mixture are the same between samples of given salt concentrations, as analyzed further below and as expected. However, comparison of the single-shot spectra revealed—in addition to random effects due to the composition of individual grains hit and fluctuations in the laser

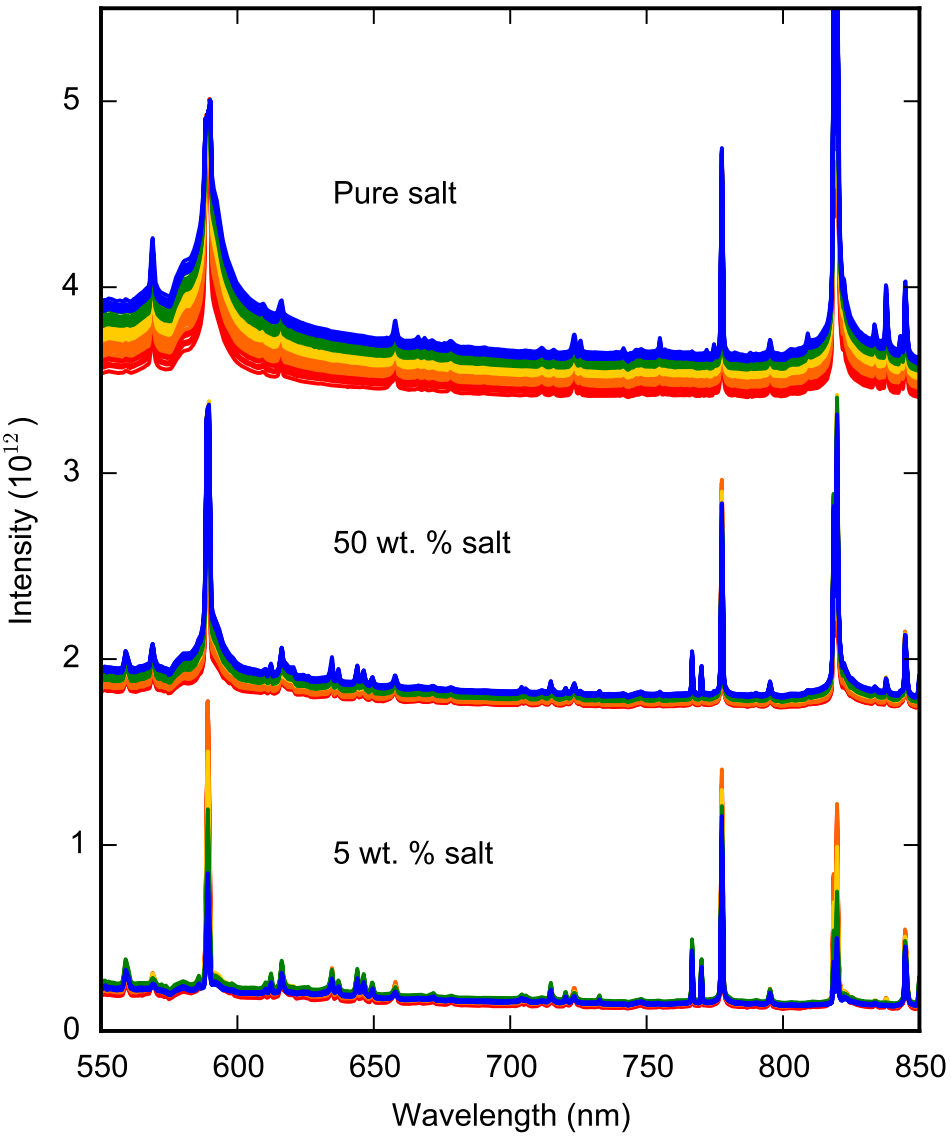

Figure 6.3: Processed LIBS spectra show an increase in intensity of continuum emission with shot number for NaCl+K1919 mixtures with increasing salt concentration over the wavelength range from 550–850 nm, a representative sample of the full spectrum. Colors correspond to shot numbers: red is shots 1–10, orange is 11–20, yellow is 21–30, green is 31–40, and blue is 41–50. Intensity is in units of photons/shot/mm^2/sr/nm. Absolute intensity for each salt concentration is offset by 1.6×10^{12} for the 50 wt. % salt and 3.2×10^{12} for the pure salt to aid visual comparison.

power or experimental environment between shots—systematic changes with shot number that appear to be correlated with salt content. Over consecutive laser shots at a particular location, in a sample with a set salt concentration, the continuum emission generally increases with shot number for salt-bearing samples. More interestingly, the amount by which the continuum emission increases over the 50 laser shots seems to depend on the salt content. As shown for NaCl+K1919, the continuum increase per shot is greater for mixtures with higher salt concentrations, creating a larger spread in intensity from the first to the final laser pulse. In contrast, the basalt samples show very little continuum increase with shot number (Figure 6.3). Following continuum removal, no consistent whole-spectrum trends with shot number are observed.

6.3.2 Spectral Line Analysis

6.3.2.1 Salt Anion Emission Lines Detected in Mixtures

Spectra averaged over many laser shots show the most sensitive anion lines in basaltic mixtures, particularly after removal of the local continuum. Table 6.3 lists the Cl, C, and S lines that met the initial four criteria for identification described in section 6.2.3 and for which peak areas were measured in the salt+basalt mixtures. The anion line intensities are 1–3 orders of magnitude lower than those of the strongest elemental lines. Therefore, emission line overlap prevents many anion lines from being detected. The identified lines are spread across the 240–850 nm detectable wavelength range although most fall within the spectral range of the VNIR detector (470–850 nm). Relative to the VNIR, the spectral ranges of the UV and VIO detectors are smaller and contain many strong lines from cation and basaltic matrix elements. Peak centers do not always coincide with the exact line location listed in the NIST database. However, the peak identity has been determined based on the criteria described in section 6.2.3.

6.3.2.1.1 Cl lines

Sixteen potential Cl lines are observed in the spectra of the chloride salt+basalt mixtures that met the initial criteria provided in section 6.2.3 (Table 6.3, Figure 6.4, 6.5, S3). Of the sixteen selected lines, one appears in the range of the VIO detector whereas the rest are in the VNIR. The nine lines at wavelengths shorter than 546 nm result from transitions of singly ionized Cl

whereas those above 725 nm are from neutral Cl.

The selected Cl lines are detectable despite some interference due to other elements in the sample. The outer tails of strong elemental lines can contribute emission to Cl peaks even a few nm away (e.g., an O peak at 777.6 nm affects the Cl peaks at 771.9 and 774.7 nm). Cl peaks are detected on the shoulder of some less intense lines (e.g., Cl at 725.9 nm appears on the outer tail of the C line at 723.8 nm) and blended with lines of comparable intensity (e.g., Cl at 507.9 and 510.1 nm; 544.5 and 545.9 nm). Weak emission features due to other elements appear within a few tenths of a nanometer of the Cl peak centers, but Cl emission appears to dominate the line location at high salt concentrations above LOD1 (Fig. 6.4). Most selected Cl peaks show a monotonic increase in peak area for concentrations above 5-10 wt. % salt (X_{Cl} = 0.019–0.041, Table 6.3).

The NaCl+GBW07105 composition series, including the pure salt, tends to have comparable or larger Cl peak areas than that of NaCl+K1919 in the un-normalized data with exceptions at 507.9, 510.1, and 521.9 nm. A few Cl lines differ in appearance (e.g., 741.6 and 809.1 nm) and peak area trends (e.g., 507.9, 510.1, 741.6, and 809.1 nm) between the $CaCl_2$- and NaCl-bearing mixtures. The distinct behavior of the line at 741.6 nm between different mixtures calls into question the usefulness of this line. Peak areas of the remaining Cl lines are comparable between the $CaCl_2$- and NaCl-bearing mixtures until concentrations reach X_{Cl} = 0.247–0.386 (50–70 wt. % $CaCl_2$) where the calibration curves diverge.

6.3.2.1.2 S lines

The two sulfur peaks identified are part of a series that appear between 540–565 nm. This is the same region recommended by Dyar et al. [2011] for identification of sulfur in geologic samples and used by Nachon et al. [2014] for the identification of calcium sulfate veins by ChemCam in Gale Crater. Peaks appear in this spectral region at high salt concentrations for all five of the sulfate+basalt mixtures investigated (Figure 6.5, 6.6). However, a large number of spectral lines populate this region, particularly Fe and a few Ca lines, complicating the determination of individual peak areas. Fe lines within range of the spectral resolution from both identified S peaks could not be definitively separated out. The influence of Fe emission on the peak shape and the con-

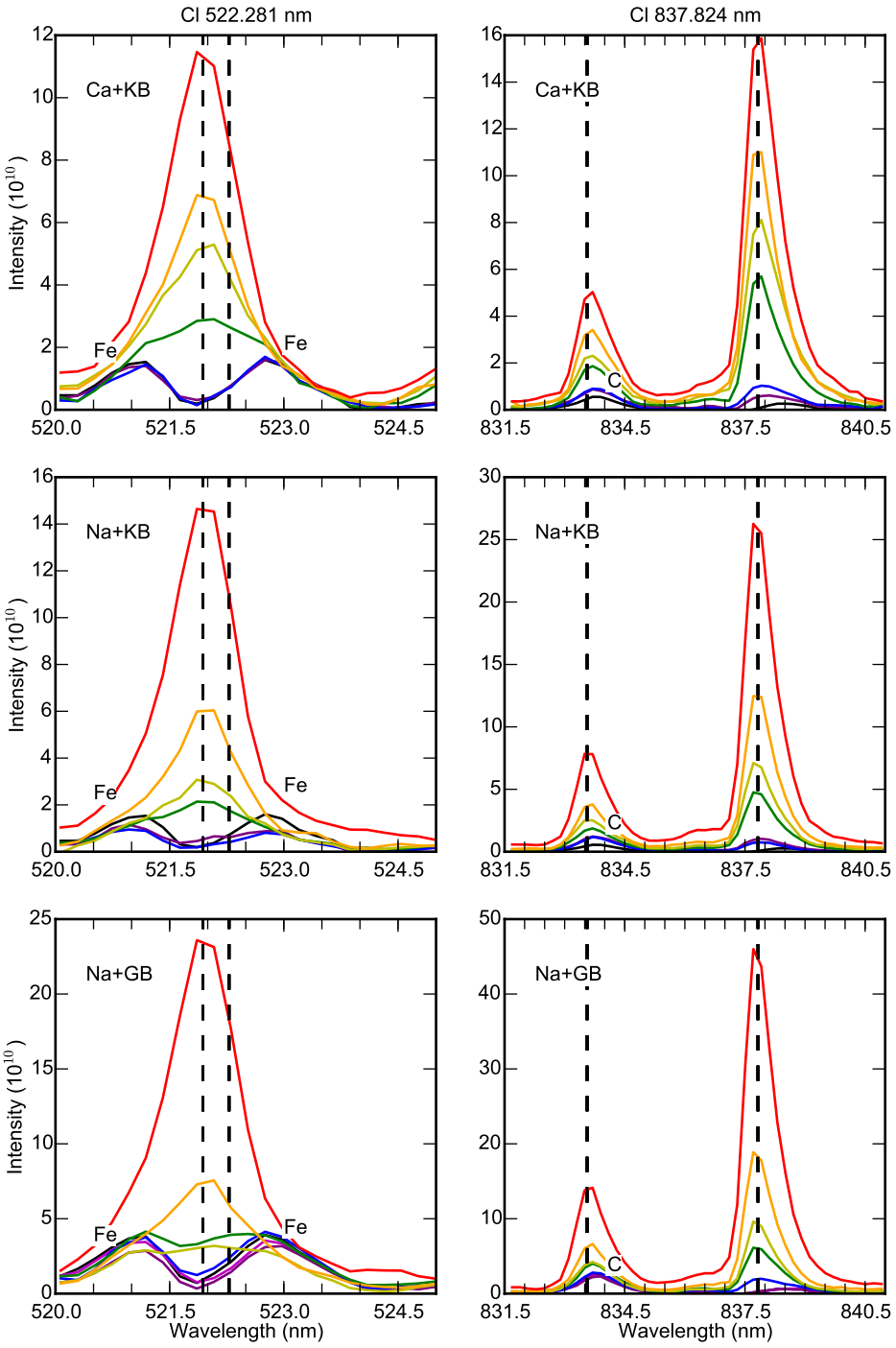

Figure 6.4: Spectra of Cl emission lines, denoted by vertical lines, at 521.9 nm (top row) and 837.8 nm (bottom row) in NaCl+K1919 (Na+KB), $CaCl_2$+K1919 (Ca+KB), and NaCl+GBW07105 (Na+GB) mixtures (columns). Colors in the overlain spectra indicate different salt concentrations with pure basalt in black, pure salt in red, and mixtures containing salt mass fractions of 0.05 wt. % (select mixtures only) in magenta, 5 wt. % in purple, 10 wt. % in blue, 30 wt. % in green, 50 wt. % in yellow, and 70 wt. % in orange. Intensity is in units of photons/shot/mm^2/sr/nm. Spectra for all Cl lines are provided in Figure S3 in the supplemental information.

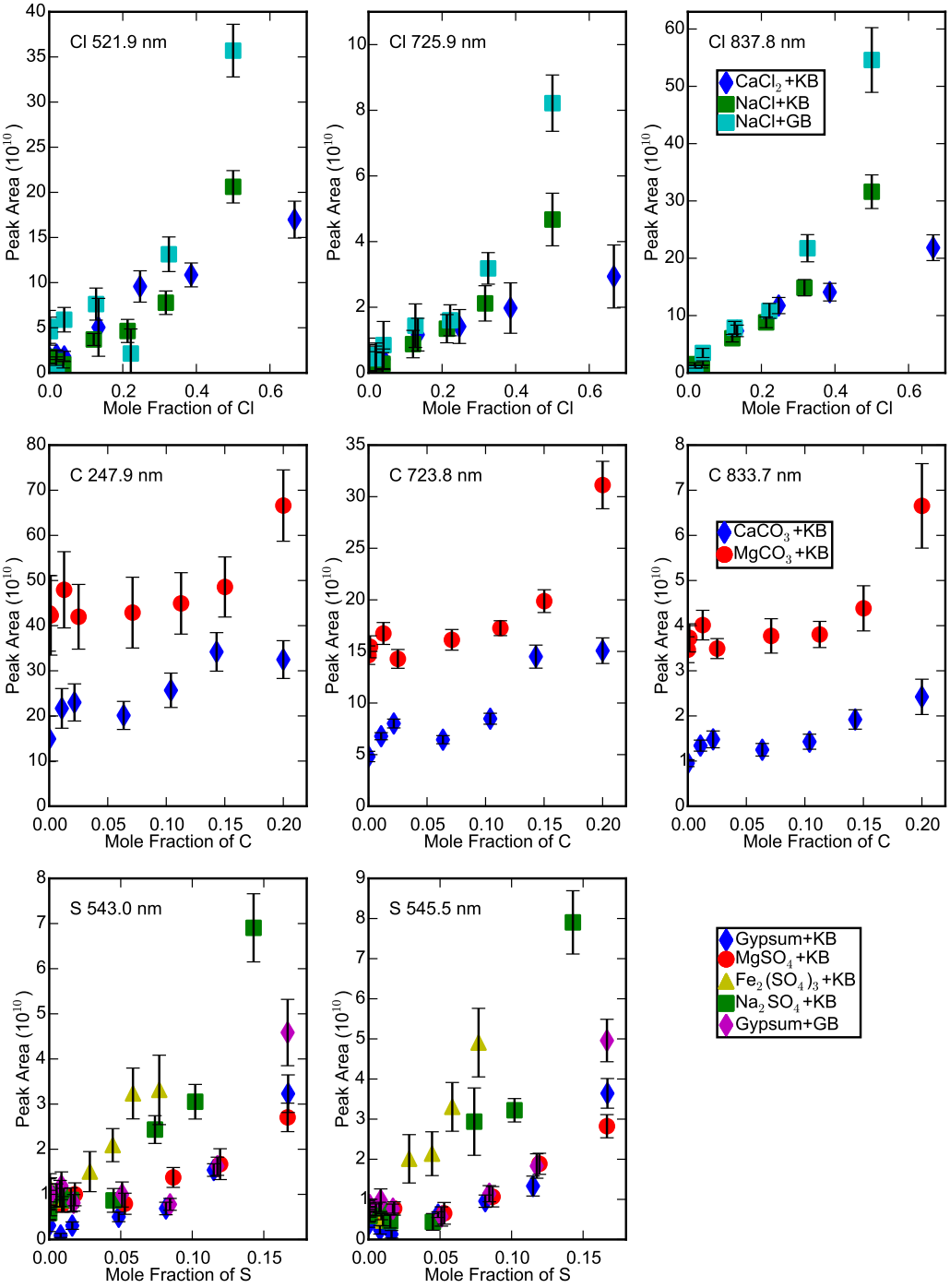

Figure 6.5: Calibration curves of peak area vs. mole fraction of element for a selection of Cl, C, and S peaks and each salt+basalt combination (provided in the legend for each row). Peak areas are in units of photons/shot/mm^2/sr. Calibration curves for remaining Cl and C lines are provided in Figures S3 and S4 in the supplemental information.

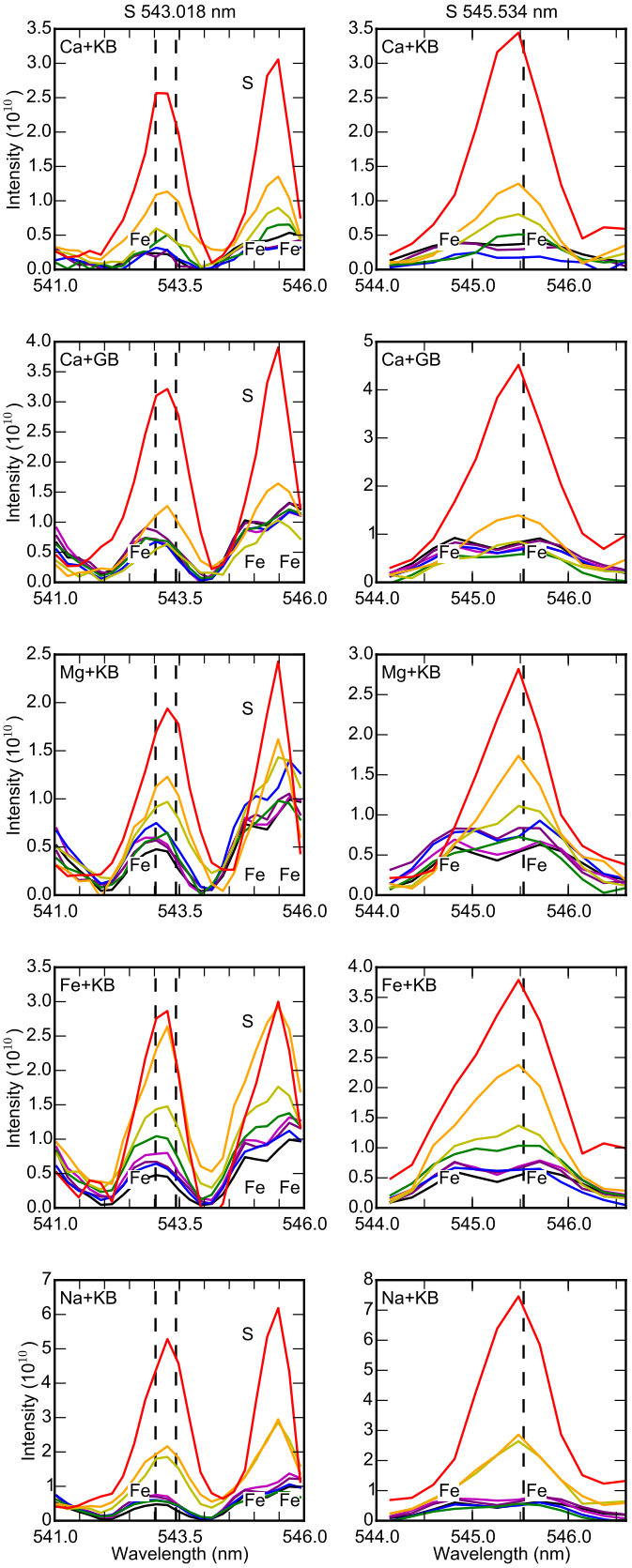

Figure 6.6: Spectra of S emission lines, denoted by vertical lines, at 543.0 nm (top row) and 545.5 nm (bottom row) in $CaSO_4 \cdot 2H_2O$+K1919 (Ca+KB) and GBW07105 (Ca+GB), $MgSO_4$+K1919 (Mg+KB), $Fe_2(SO_4)_3$+K1919 (Fe+KB), and Na_2SO_4+K1919 (Na+KB) mixtures (columns). Colors in the overlain spectra indicate different salt concentrations with pure basalt in black, pure salt in red, and mixtures containing salt mass fractions of 0.05 wt. % (select mixtures only) in magenta, 5 wt. % in purple, 10 wt. % in blue, 30 wt. % in green, 50 wt. % in yellow, and 70 wt. % in orange. Intensity is in units of photons/shot/mm^2/sr/nm.

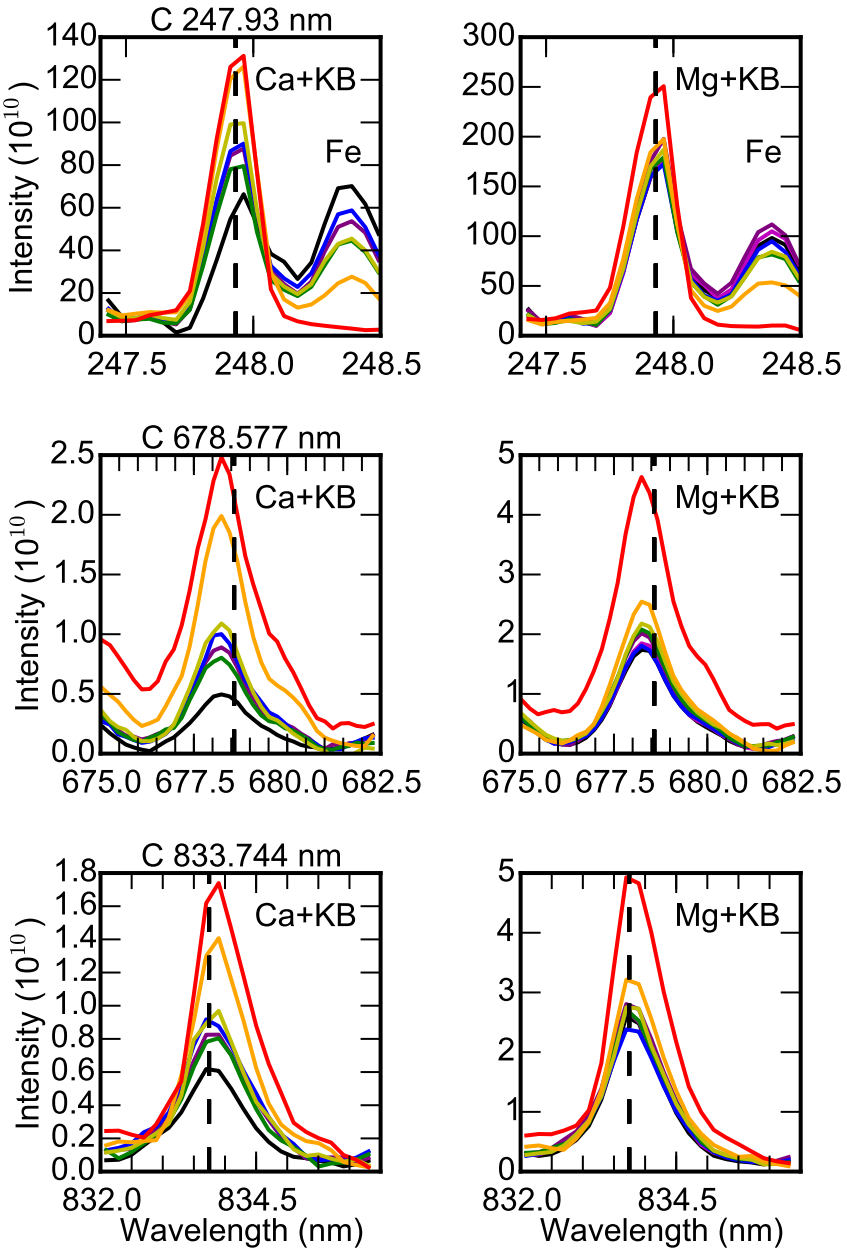

Figure 6.7: Spectra of C emission lines, denoted by vertical lines, at 247.9 nm (top row), 678.6 nm (middle row), and 833.7 nm (bottom row) in $CaCO_3$+K1919 (Ca+KB) and $MgCO_3$+K1919 (Mg+KB) mixtures (columns). Colors in the overlain spectra indicate different salt concentrations with pure basalt in black, pure salt in red, and mixtures containing salt mass fractions of 0.05 wt. % (select mixtures only) in magenta, 5 wt. % in purple, 10 wt. % in blue, 30 wt. % in green, 50 wt. % in yellow, and 70 wt. % in orange. Intensity is in units of photons/shot/mm^2/sr/nm. Spectra for all C lines are provided in Figure S3 in the supplemental information.

centration at which S begins to dominate, which can be seen for the 545.5 nm line in Fig. 6.6, depends on the sample composition.

Measured peak areas increase monotonically with salt concentration above 10–30 wt. % salt (X_S = 0.045–0.053) for all mixtures with the exception of gypsum+GBW07105 at 543.0–543.4 nm from 30–50 wt. % salt (X_S = 0.051–0.084). In the case of gypsum+K1919, the area of the peak at 543.0–543.4 nm increases monotonically for all concentrations. Gypsum- and $MgSO_4$-bearing mixtures have comparable peak areas at each salt concentration in the unnormalized data whereas the $Fe_2(SO_4)_3$- and $NaSO_4$-bearing mixtures have higher values. Peak areas differ for the pure salts, including the two gypsum measurements taken on different experimental setups (see section 6.2.1).

6.3.2.1.3 C lines

Detection of carbon is more complicated than that of Cl or S because the abundance of CO_2 in the Martian atmosphere can cause C lines to appear in the LIBS spectrum. The LIBS laser does not excite the ambient gas, but when a plasma is created by laser interaction on a solid target (soil, rock, or pressed pellets), the atmospheric constituents are also excited due to partial breakdown of the gas just over the sample surface. As such, the C peaks identified in the spectra of carbonate-bearing samples were also found in the spectra of other samples that did not contain appreciable carbon.

Seven potential C lines are identified in the carbonate+basalt mixtures that met the initial four criteria from section 6.2.3 (listed in Table 6.3). Two appear in the UV spectral window and five in the VNIR (Figure 6.5, 6.7, S4). The transitions are mainly from singly ionized C with 2–3 from neutral C. Some of the selected lines partially overlap with emission from other elements but this does not inhibit identification of the C line. The C lines at 247.9 and 283.8 nm experience interference due to Fe only in the presence of the basaltic matrix. The C line at 657.8 nm blends with the H line at 656.5 nm in the $MgCO_3$-bearing samples, but has little to no influence from the H line in $CaCO_3$-bearing samples. Although not clearly visible here, there may also be interference from Fe and Ti in this H/C line region [Schröder et al., 2015; Rapin et al., 2016]. Ca at 715.0 nm interferes with the C line at 711.8 nm in all $CaCO_3$- and $MgCO_3$-bearing samples.

Peaks areas monotonically increase for concentrations above 10–30 wt. % salt

(X_C = 0.025-0.064) with the exception of the lines at 247.9 and 283.8 nm in $CaCO_3$+K1919 (Fig. 6.7). The $MgCO_3$+K1919 composition series generally displays higher peak areas in the un-normalized data and different trends in the calibration curves compared to the $CaCO_3$+K1919. The change in sample-to-target distance between the mixture series likely contributed to these differences as described in section 6.4.2. Lines show weak sensitivity to concentration from 30–70 wt. % $MgCO_3$ (X_C = 0.071–0.150) and from 70 wt. % to pure $CaCO_3$ (X_C = 0.143–0.200) for some C peaks.

6.3.2.2 Limits of Detection for Salt Anion Elements

The detection limits depend on both the line selected and the mixture composition (Table 6.3). Based on LOD1, Cl is detectable via most lines at 30 wt. % salt, equal to a mole fraction of X_{Cl} = 0.12–0.14 or about 18–19 wt. % Cl. However, a few Cl lines can be detected down to 5–10 wt. % salt, equal to X_{Cl} = 0.02–0.04 or 3–6 wt. % Cl. LOD2 gives a comparable range of X_{Cl} = 0.02–0.17 with exceptions at 507.9, 510.1, 741.6, and 809.1 nm. The S line at 543.0-543.4 nm is detected (LOD1) at 0.5 wt. % salt (X_S = 0.001, 0.1 wt. % S) except in gypsum+K1919 where it is detected only above 10 wt. % (X_S = 0.016, 2 wt. % S). LOD2 produces higher values of X_S = 0.009–0.042 (∼5–25 wt. % salt, 1–6 wt. % S). The S line at 545.5 nm is detected (LOD1) at 30 wt. % salt (X_S = 0.034–0.053, 7–8 wt. % S) in all mixtures except $Fe_2(SO_4)_3$+K1919. LOD2 produces lower values ofX_S = 0.004–0.018 (∼3–10 wt. % salt, 0.7–3 wt. % S). For C, the limit of detection analysis is affected by carbon present in the CO_2 atmosphere. As a result, carbon emission is detected at all concentrations, even in the blank, and LOD1 does not provide any extra information (see note in Table 6.3). LOD2 is the meaningful limit in this case. C lines at 657.9, 678.6, 723.8, and 833.7 nm have detection limits X_C = 0.04–0.06 (∼20–25 wt. % salt, 2-4 wt. % C) in $MgCO_3$+K1919 with lower values in $CaCO_3$+K1919 (∼1–15 wt. % salt, 0.1–2 wt. % C). The remaining lines have higher detection limits, >35 wt. % salt, with the exception of 283.8 nm in $CaCO_3$+K1919 (∼15 wt. % salt, 2 wt. % C).

Table 6.3: Cl, C, and S lines that met the initial four criteria listed in section 6.2.3 for univariate analysis of salt+basalt mixtures in this work. The reference wavelength values in vacuum, ionization level, and corresponding ChemCam detector spectral window are also listed. The references are the Martian database of Cousin et al. [2011] and NIST spectral line database as described in the text. The remaining columns provide the results of this analysis: the detection limits determined based on the methods described in section 6.2.5, the concentration at which a monotonically increasing trend in peak area with salt concentration began (or an "x" if the peak area did not monotonically increase), and whether the peak area displayed unreliable behavior among the mixture compositions tested. Detection limits and concentrations are provided in mole fraction of element (X_X) for each cation+basalt mixture combination. Underlined values are above 50 wt. % salt. Mixtures in bold included an extra low concentration of 0.5 wt. % salt. A check mark in the final column indicates that the line met all seven criteria listed in section 6.2.3 for all mixture compositions tested and may among the most effective for quantitative analysis. Calculated LOD1 is the lowest concentration measured for all carbonate-bearing mixtures (a mole fraction of 0.011 for Ca+KB and 0.001 for Mg+KB), but this results from atmospheric CO_2 rather than sample carbon.

Reference Data					Quantitative Analysis					
λ (nm)	[1]	[2]	[3]		LOD1	LOD2	LOD3	[4]	[5]	[6]
Chlorine										
385.2	II	VIS	NIST	Na+KB	0.213	0.058	0.117	0.038		
				Ca+KB	0.386	0.14	0.185	0.134		
				Na+GB	0.325	0.123	0.204	0.222		
507.9	II	VNIR	Martian,		0.121	0.136	0.133	0.019		
			NIST		0.134	0.223	0.11	0.02		
					0.127	0.307	0.333	0.002		
510.1	II	VNIR	Martian,		0.121	0.145	0.152	0.019		
			NIST		0.134	0.117	0.11	0.02		
					0.041	0.224	0.328	0.002		
521.9	II	VNIR	Martian,		0.121	0.049	0.147	0.038		✓
			NIST		0.134	0.06	0.09	0.041		

				0.127	0.071	0.243	0.022		
539.4	II	VNIR	Martian,	0.121	0.065	0.182	0.121		✓
			NIST	0.134	0.144	0.135	0.02		
				0.127	0.164	0.16	0.022		
542.5	II	VNIR	Martian,	0.038	0.039	0.147	0.019		✓
			NIST	0.134	0.036	0.074	0.041		
				0.127	0.029	0.169	0.022		
544.5	II	VNIR	Martian,	0.019	0.049	0.155	0.019		✓
			NIST	0.134	0.049	0.1	0.02		
				0.127	0.052	0.217	0.222		
545.9	II	VNIR	Martian,	0.121	0.074	0.155	0.038		
			NIST	0.134	0.128	0.192	0.386		
				0.127	0.062	0.241	0.222		
725.9	I	VNIR	NIST	0.121	0.101	0.101	0.038		✓
				0.134	0.164	0.105	0.02		
				0.127	0.076	0.147	0.02		
741.6	I	VNIR	NIST	0.019	0.047	0.262	0.121	x	
				0.134	0.275	0.255	0.247		
				0.002	0.337	0.299	0.222		
754.9	I	VNIR	NIST	0.121	0.023	0.115	0.038		✓
				0.134	0.045	0.082	0.041		
				0.127	0.036	0.159	0.041		
771.9	I	VNIR	Martian,	0.121	0.161	0.224	0.019		
			NIST	0.134	0.035	0.125	0.02		
				0.325	0.134	0.35	0.002		
774.7	I	VNIR	NIST	0.121	0.053	0.132	0.038		✓
				0.134	0.034	0.083	0.02		
				0.127	0.166	0.229	0.002		
809.1	I	VNIR	NIST	0.019	0.027	0.095	0.019		✓
				0.02	0.003	0.137	0.041		
				0.041	0.103	0.191	0.002		
833.6	I	VNIR	NIST	0.121	0.02	0.102	0.038		✓
				0.134	0.037	0.053	0.041		
				0.127	0.036	0.151	0.02		
837.8	I	VNIR	Martian,	0.019	0.035	0.097	0.038		✓
			NIST	0.02	0.017	0.105	0.02		

					0.041	0.078	0.148	0.002	
Sulfur									
543.0,	II	VNIR	Martian,	Ca+KB	0.016	0.021	0.05	0.008	✓
543.4			NIST	Ca+GB	0.001	0.042	0.099	0.084	
				Mg+KB	0.001	0.031	0.042	0.053	
				Fe+KB	0.001	0.009	0.015	0.016	
				Na+KB	0.001	0.009	0.043	0.045	
545.5	II	VNIR	Martian,		0.049	0.011	0.056	0.016	✓
			NIST		0.051	0.011	0.078	0.051	
					0.053	0.018	0.046	0.053	
					0.016	0.004	0.014	0.016	
					0.045	0.005	0.044	0.045	
Carbon									
247.9	I	UV	Martian,	Ca+KB	a	0.083	0.076	x	
			NIST	Mg+KB		0.217	0.121	0.025	
283.8	II	UV	Martian,			0.035	0.067	x	
			NIST			0.117	0.079	0.025	
657.9	II	VNIR	Martian,			0.014	0.065	0.064	✓
			NIST			0.045	0.082	0.025	
678.6	II	VNIR	Martian,			0.031	0.06	0.064	✓
			NIST			0.046	0.099	0.025	
711.8	I/II	VNIR	Martian,			0.072	0.053	0.064	
			NIST			0.137	0.126	0.025	
723.8	II	VNIR	Martian,			0.009	0.065	0.064	✓
			NIST			0.043	0.09	0.025	
833.7	I	VNIR	NIST			0.002	0.07	0.064	✓
						0.06	0.11	0.025	

[1] Ionization level

[2] Spectral window

[3] Reference database

[4] Begins monotonic increase

[5] Unreliable behavior

[6] Met all criteria for all mixes

[a]Detected in atmosphere in all samples

6.4 Discussion

6.4.1 Detection of Salt Anions

Table 6.3 summarizes the results of the quantitative analysis. Ten Cl lines met our complete criteria for being useful for quantitative analysis of chloride+basalt mixtures. Chlorides were detectable at ∼5–10 wt. % in the basaltic background using select lines. The line at 837.8 nm appears to be the most promising for quantification with this univariate method based on its low detection limit, sensitivity to concentration, and reliable behavior in all mixture compositions. Of the detected Cl lines, this line also has the lowest upper state energy and a relatively high transition probability (Einstein A coefficient) based on values from the NIST database [Kramida et al., 2015].

Interference from Fe emission complicates the detection of S. Due to the broadness of the peak spanning Fe at 542.9 nm and individual S transitions at 543.0 and 543.4 nm; it is difficult to eliminate Fe interference by tracking changes in the peak center with salt concentration. Therefore, the LOD2 values seem more appropriate for this S peak. Given this consideration, sulfates are detected in the basaltic background at 5–30 wt. % salt (LOD1 at 545.5 nm) but could be detectable at as low as 3–10 wt. % based on LOD2. Even still, it will be difficult to distinguish Fe from S emission in the spectra. Quantification based on the S lines at 543.0/543.4 and 545.5 nm will require knowledge about the Fe content of the target due to almost direct overlap with Fe peaks in the spectral region. However, the Fe content can be measured relatively easily due to the multitude of strong Fe lines present throughout the ChemCam spectral range.

Carbonates are detectable in excess of the carbon emission due to the atmosphere at ∼20 wt. % in the basaltic background for either salt tested and potentially down to 1 wt. % salt for $CaCO_3$. The overall detection limit is similar to the value of 6 wt. % C determined by Ollila et al. [2013] for a set of geologic samples and 5 wt. % C by Beck et al. [2016] for $CaCO_3$+basalt mixtures, but appears lower for certain lines in $CaCO_3$+K1919. Precise quantification based on the lines selected here may be difficult because their areas lack sensitivity to changes in concentration from 30–70 or 70–100 wt. % salt depending on mixture composition.

Cl and S peaks are both present in the 540-548 nm range; however, these peaks can be distinguished by slight differences in the location of the peak

center in addition to peak shape. Cl peaks at 542.5, 544.5, and 545.9 nm, are visible in all three chloride salt+basalt mixtures and the 544.5 and 545.9 nm peak emission overlaps strongly creating a distinct shape compared to the two S peaks at 543.0/543.4 and 545.5 nm. Additionally, the fourth Cl peak at 539.4 nm can distinguish the presence of Cl. Another potential conflict in identification occurs between the Cl peak at 833.6 nm and the C peak at 833.7 nm. The Cl peak has a peak area 2–4 times larger than the C peak at high salt concentrations and has a lower detection limit. To eliminate confusion, the several of the stronger Cl lines including one nearby at 837.8 nm could indicate the presence of Cl.

6.4.2 Effects of Basaltic Matrix and Salt Cation on Anion Lines

The basaltic matrix and/or salt cations affect the appearance and behavior of some of the selected anion peaks. The detection limits also varied with mixture composition for these lines. For example, all selected C lines had higher LOD2 values in $MgCO_3$+K1919 than in $CaCO_3$+K1919. Several lines met all seven criteria from section 6.2.3 and were found useful for analysis regardless of sample composition (see Table 6.3). However, even for these lines, the intensities and the behavior of the calibration curves were not uniform for all mixtures.

Anion peak areas differed between some mixtures with identical salt content but different matrix compositions (moderate- vs. high-alkali basalt). However, the peak areas for the pure salts also differed between the two sets of measurements. This suggests that at least some, if not all, of the difference is due to factors unrelated to the composition of the matrix. Alteration to the experimental setup, in particular the laser-to-sample distance, between the first and second batches of measurements is observed in the comparison between distance-corrected, processed spectra of pure NaCl and K1919 samples measured in each batch (Figure 6.8). The spectra share the same emission lines but the data collected at a laser-to-sample distance of 3.0 m have larger intensities than those collected at 1.6 m. The differences in absolute line intensity therefore cannot be attributed to the composition of the matrix alone as the sample distance likely has a significant effect on this quantity, even after correcting for solely geometric effects.

Differences in total emission produced by the sample were accounted for through

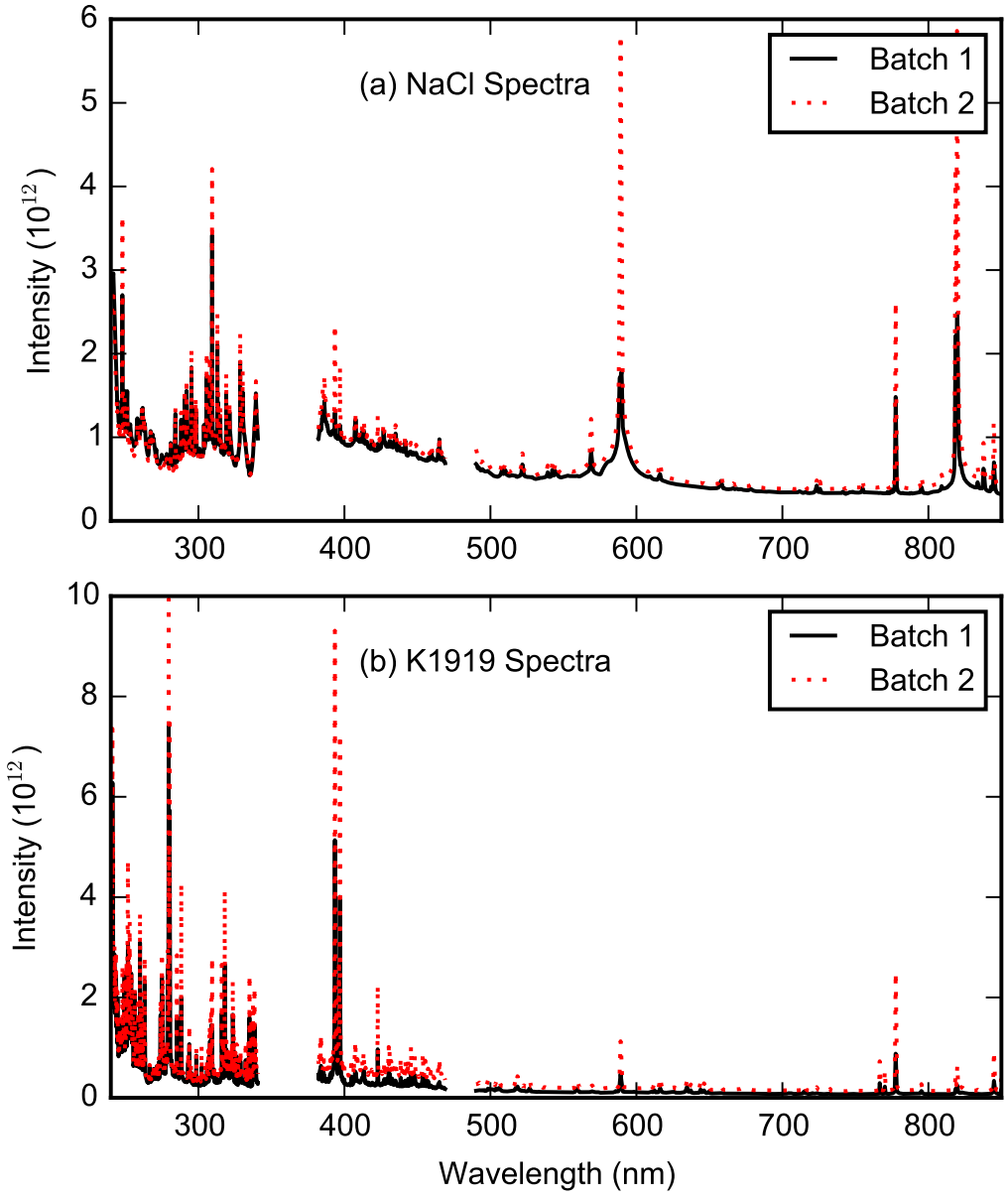

Figure 6.8: Comparison of (a) NaCl and (b) K1919 spectra collected in the first (solid black line) and second batches (dashed red line) of measurements at laser-to-sample distances of 1.6 and 3.0 m, respectively, after processing to correct for the geometric effects of distance.

normalization of key Cl and S lines (Figure 6.9b,c). Such normalization appears to reduce effects on the calibration curve caused by the composition of the matrix or experimental setup based on comparison between the two different NaCl and gypsum composition series. However, the calibration curves maintain some dependence on the identity of the salt cation despite normalization. Divergence of the calibration curves appears at high salt concentrations, above 50 wt. % chloride and above 30-50 wt. % sulfate. Therefore, the composition of the sample, at least the salt cation, will have an effect on quantification of the anion elements.

6.4.3 Univariate Analysis of Salt Anion Elements

The peak areas of select anion lines increased monotonically above the detection threshold of the line (see Table 6.3). Therefore, univariate analysis could be useful in tracking relative changes in salt content given a sufficient abundance of salt. However, absolute quantification of salts in unknown samples would be difficult with univariate analysis. Relating the line area to an absolute element or salt concentration relies on comparison with laboratory data collected on known standards under similar experimental conditions. The shape of the calibration curve for a given emission line as a function of mole fraction depends on the composition of the sample even after normalization of the peak areas (Figure 6.9b,c). This makes absolute measurements of elemental composition based on univariate analysis unreliable without prior knowledge of the sample composition, in particular the salt cation element. If trends were more similar as a function of weight percent, this might suggest a relationship with the mass of the atoms rather than total number of emitting atoms, e.g., due to the extra energy required to eject more massive elements from the sample surface and would result in a concentration of these elements at the surface. However, it is not clear that this is the case here (Figure 6.9d).

The primary goal of this work is to identify the most suitable anion lines for detection and quantification. A next step is to apply this knowledge to the Mars dataset. Developing quantitative calibration curves for the Mars data is beyond the scope of this work. It requires further investigation to correct for laser-to-target distance and laboratory-to-Mars instrument differences. In addition, there are challenges regarding univariate analysis itself. Finding the correct functional form to describe the calibration curves is also a question, even for the relatively well-behaved Cl line at 837.8 nm (Figure 6.10). For a

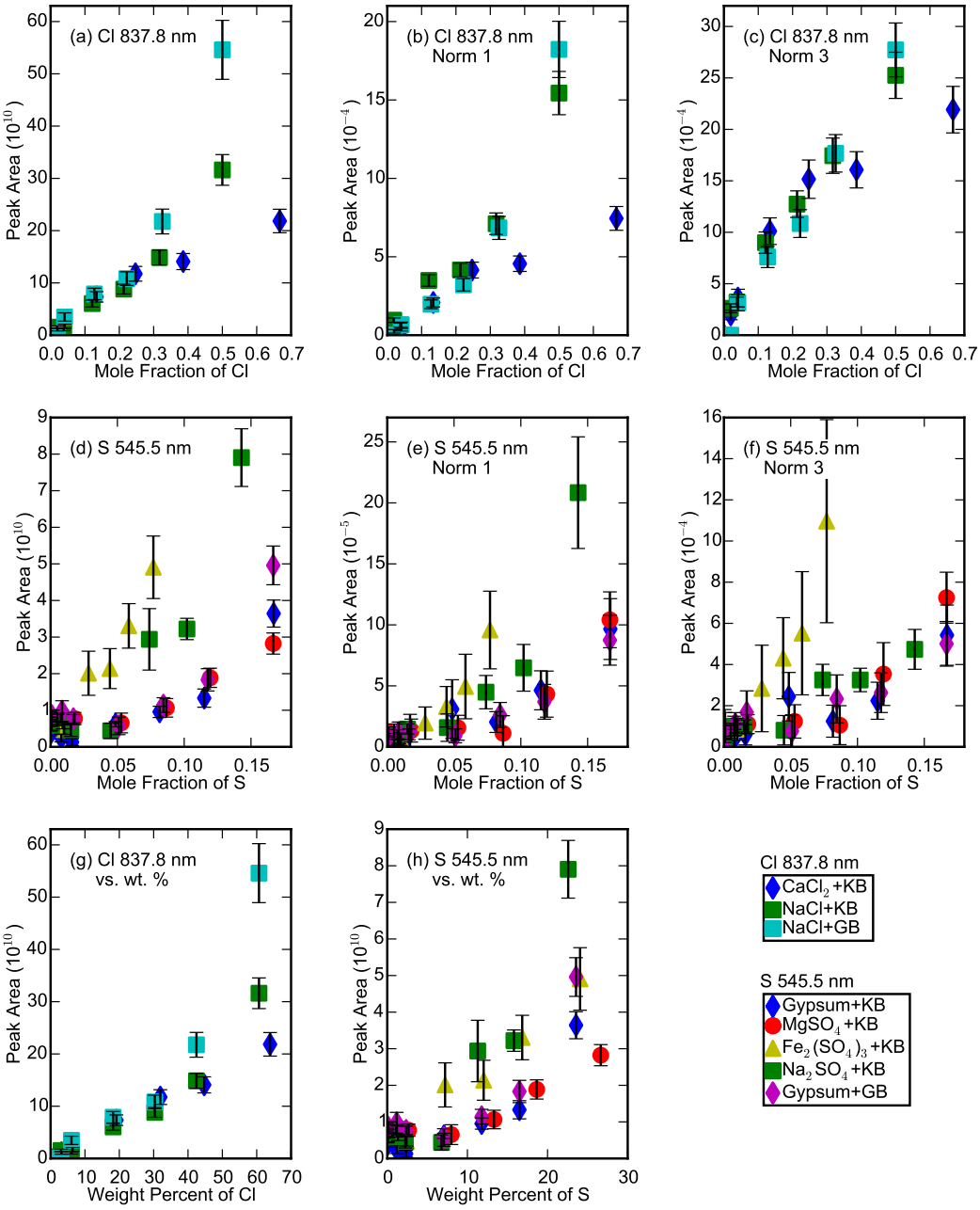

Figure 6.9: Calibration curves for Cl at 837.8 nm (a-c, g) in NaCl+K1919, $CaCl_2$+K1919, and NaCl+GBW07105 and S at 545.5 nm (d-f, h) in $Fe_2(SO_4)_3$+K1919, Na_2SO_4+K1919, $MgSO_4$+K1919, gypsum+K1919 and gypsum+GBW07105 plotting un-normalized peak area vs. mole fraction of element (a) and (d), peak area normalized by the total spectral emission across the entire spectral wavelength range (b) and (e), peak area normalized by the total spectral emission of the VNIR detector wavelength range (c) and (f), and un-normalized peak area vs. weight percent of element (g) and (h). Peak areas are in units of photons/shot/mm^2/sr.

given peak area of 7×10^{10} photons/shot/mm^2/sr, the estimate mole fraction of Cl can vary from 0.14–0.19 (∼19–25 wt. % Cl or 30–40 wt. % salt) for a single composition, depending on whether the fit is linear, exponential or power law (Figure 6.10). The uncertainty increases with increasing salt content and for a target with unknown composition. While normalization appears to increase linearity of some curves, it does not have the same effect on all lines or compositions (Fig. 6.10 panels b and f vs. d). We provide all of the data necessary to recreate the calibration curves in the supplementary material so that the interested reader may investigate further the application to ChemCam or other datasets.

6.4.4 Comparison to Prior Laboratory LIBS Studies of Cl, C, S: Most Effective Lines for Analysis

Previous studies focused on the identification of Cl, C, and S emission with ChemCam tested a range of samples from pure compounds to geologic materials (see Introduction). The salt+basalt mixture spectra evaluated here are complex, thus challenging observation of key emission lines. The large number of emission lines and additional matrix effects potentially including preferential recombination of elements of interest from the bulk basalt-containing mixture increase the likelihood of non-detection of lines due to interference. This causes fewer lines to be detected from anion elements in mixtures compared to those identified in the controlled laboratory compounds by Cousin et al. [2011]. Cousin et al. [2011] detected 27 transitions for Cl, 33 for C, and 28 for S of which only 9 Cl, 3 C, and 2 S lines met all our criteria for potential usefulness in analysis of the salt+basalt mixtures (not all of these were resolved as separate peaks). Unexpectedly, the C line at 883.7 nm and Cl lines at 725.9, 754.9, 774.7, 809.1, and 833.6 nm from the NIST database were detected and identified as useful in the salt+basalt mixtures but not previously by Cousin et al. [2011]. These differences in line detections may be due to the significantly improved spectrometers used for ChemCam.

The most effective lines for the analysis of unknown martian materials will likely be those that appear consistently in samples with various chemical compositions. Compared to the number of identified lines in pure elements and compounds, those found in the salt+basalt mixtures are more limited. However, there are emission lines of Cl, C, and S that appeared across multiple samples and may be promising for use in geologic targets. Tables 6.4–6.6 pro-

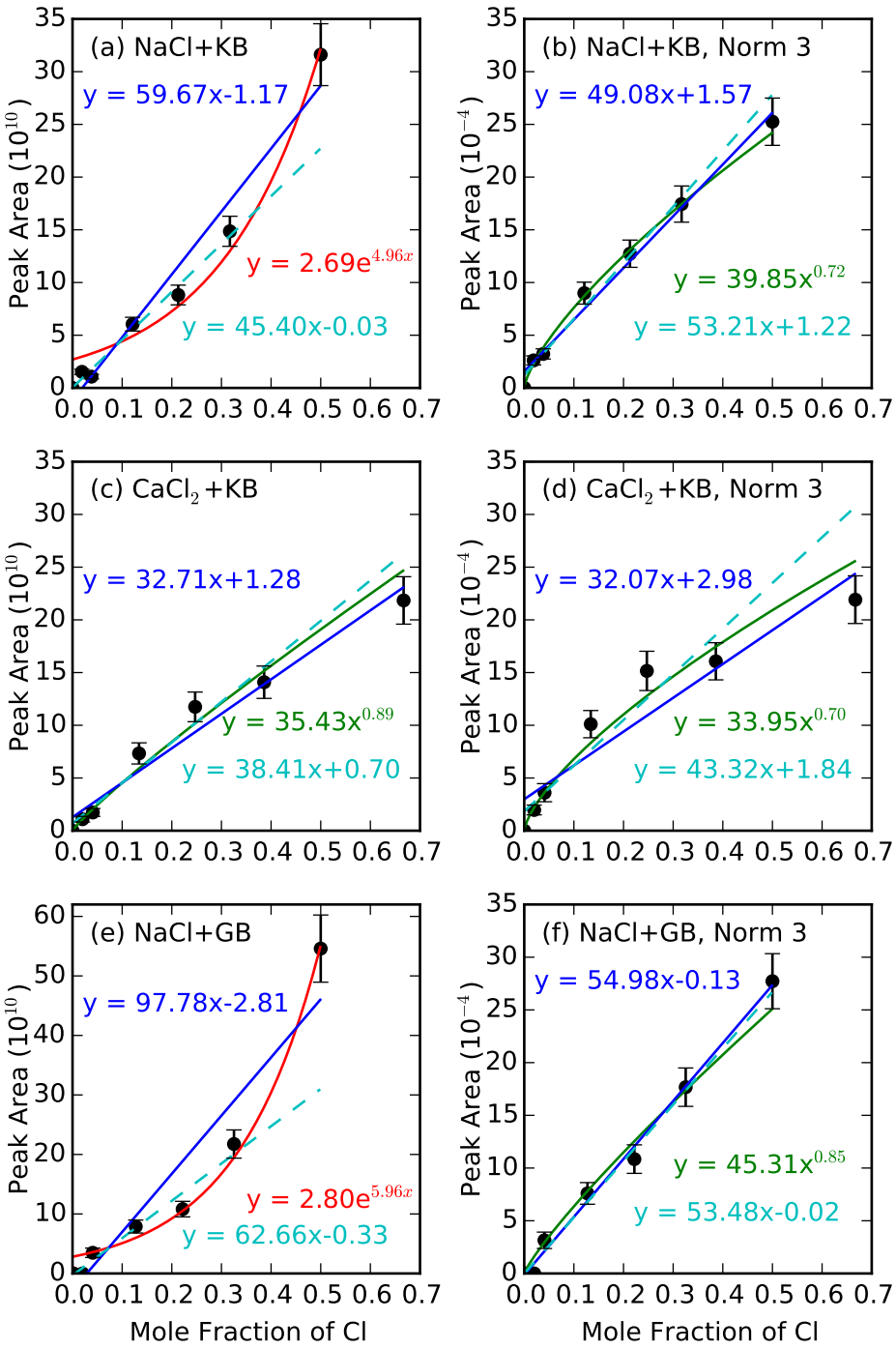

Figure 6.10: Potential fits to calibration curves for Cl at 837.8 nm in NaCl+K1919 (a,b), $CaCl_2$+K1919 (c,d), and NaCl+GBW07105 (e,f) un-normalized (a,c,e) and normalized by the total intensity of the VNIR spectral window (b,d,f). The blue line is a linear fit to all data points, the cyan line is a linear fit to all data points excluding the pure salt, the red curve is an exponential fit, and the green curve is a power law fit to all data points. Peak areas are in units of photons/shot/mm^2/sr.

vide a comparison of the lines selected in this study with those from the works of Cousin et al. [2011], Ollila et al. [2011], and Schröder et al. [2013]. The most reliable lines found in this work that may be useful for further analysis based on appearance in all tested samples here and in the literature are indicated in the final column of the table. For Cl, lines at 521.9, 539.4, 542.5, 544.5, and 837.8 nm have been identified in all sources listed here. All C lines selected here for the carbonate+basalt mixture sets were observed by Cousin et al. [2011] and Ollila et al. [2011] except for 833.7 nm. Our analysis of sulfate+basalt mixtures agrees with prior work by Dyar et al. [2011], Sobron et al. [2012] and Schröder et al. [2013] to focus on the 540–565 nm region for the identification of sulfur, in particular the 543.0, 543.4 (overlapping), and 545.5 lines while simultaneously evaluating the effects of contributing Fe lines at that location.

Table 6.4: Cl emission lines identified as being useful for identification of this element in salt+basalt mixtures according to the specific criteria applied in this work described in section 2.3 ("✓" for all seven criteria, "-" for only initial four criteria). To elucidate effects due to the matrix, lines selected in previous studies of pure elements or compounds by Cousin et al. [2011], Schröder et al. [2013], and Ollilia et al. [2011] are provided for comparison. A check mark in the final column indicates that the peak was selected as useful for analysis in all observed sources in this work and the literature.

Chlorine						
λ (nm)	NaCl (K1919)	$CaCl_2$ (K1919)	NaCl (GBW)	Cousin et al.	Schöder et al.	All sources?
299.8				✓		
310.5				✓		
385.2	-	-	-		✓	
386.1					✓	
413.4				✓		
422.8				✓		
426.6				✓		
460.9				✓		
479.6					✓	
481.1					✓	
482.0					✓	

489.8					✓		
507.9	✓	✓	-	✓			
510.1	✓	✓	-	✓			
521.9	✓	✓	✓	✓	✓	✓	
(2 lines)	✓	✓	✓	✓			
522.3				✓			
539.4	✓	✓	✓	✓	✓	✓	
542.5	✓	✓	✓	✓	✓	✓	
(2 lines)				✓			
544.5	✓	✓	✓	✓	✓	✓	
(2 lines)				✓			
545.9	-	✓	✓	✓	✓		
(2 lines)				✓			
611.6				✓			
614.2				✓			
684.2				✓			
693.5				✓			
725.9	✓	✓	✓				
741.6	-	-	-				
754.9	✓	✓	✓				
771.9	✓	✓	-	✓			
774.7	✓	✓	✓				
798.3				✓			
809.1	✓	✓	✓				
833.6	✓	✓	✓		✓		
837.8	✓	✓	✓	✓	✓	✓	
839.4				✓			
840.9				✓			
843.0					✓		

Table 6.5: For S lines, equivalent to Table 6.4.

Sulfur								
λ (nm)	$CaSO_4$ (K1919)	$CaSO_4$ (GBW)	$MgSO_4$ (K1919)	$Fe_2(SO_4)_3$ (K1919)	Na_2SO_4 (K1919)	[1]	[2]	All sources?
330.3						✓		
334.8						✓		
386.0						✓		
402.9						✓		
403.4						✓		
414.3						✓		
415.4						✓		
416.3						✓		
417.5						✓		
440.6						✓		
445.2						✓		
446.6						✓		
455.3						✓		
468.3						✓		
534.7						✓		
536.4						✓		
543.0	✓	✓	✓	✓	✓	✓	✓	✓
543.4	✓	✓	✓	✓	✓		✓	
545.5	✓	✓	✓	✓	✓	✓	✓	✓
547.5							✓	
547.9						✓		
551.1							✓	
553.8						✓		
556.7							✓	
560.7							✓	
564.1							✓	
564.7							✓	
566.1							✓	
566.6						✓		
605.4						✓		
614.1						✓		

631.4				✓	
638.7				✓	
639.7				✓	
639.9				✓	
(2 lines)				✓	

[1] Cousin et al.

[2] Schröder et al.

Table 6.6: For C lines, equivalent to Table 6.4.

Carbon					
λ (nm)	$CaCO_3$ (K1919)	$MgCO_3$ (K1919)	Cousin et al.	Ollila et al.	All sources?
247.9	-	-	✓	✓	
(2 lines)			✓		
250.9			✓	✓	
251.3			✓	✓	
274.2			✓		
274.7			✓		
283.8	-	-	✓	✓	
(2 lines)				✓	
298.3			✓		
299.3			✓	✓	
387.7				✓	
(3 lines)				✓	
				✓	
392.0				✓	
(2 lines)				✓	
406.9			✓		
407.0			✓		
407.1			✓		
407.6			✓	✓	
407.7			✓	✓	
426.8			✓	✓	
(2 lines)			✓	✓	
432.7			✓		

464.9			✓		
465.2			✓		
465.3			✓		
466.7			✓		
505.4			✓		
513.4			✓		
513.5			✓		
514.5				✓	
514.7			✓	✓	
564.8				✓	
566.2				✓	
569.4				✓	
569.8			✓		
589.1			✓		
(2 lines)			✓		
657.9	✓	✓	✓	✓	✓
658.5				✓	
658.9				✓	
678.6	✓	✓	✓	✓	✓
711.8	✓	-	✓	✓✓✓✓✓	
(5 lines)			✓		
723.3	✓	✓		✓	
723.8	✓	✓	✓	✓	✓
				✓	
833.7	✓	✓		✓	

6.4.5 Analysis of Salts with ChemCam in Gale Crater

Nachon et al. [2014] detected sulfur in calcium sulfate veins crossing sedimentary deposits in Yellowknife Bay. These detections were made through the presence of S lines at 543.3, 545.4, 547.4, and a doublet at 564.0 and 564.4 nm. The lines at 543.4 and 545.5 nm were selected for analysis in the salt+basalt mixtures. In contrast, the line at 547.5 nm only potentially appears in the Na_2SO_4+K1919 mixtures at high salt concentrations. Cousin et al. [2011] identified a line at 547.9 but not at 547.5 nm. The 547.5 nm region suffers interference from a small peak at 547.9 nm potentially due to Ti and large Ca peaks at 558–562 nm. The doublet at 564.0 and 564.4 nm did not

meet our criteria for selection given that it appeared in a noisy spectral region due to interference from multiple elements in the basaltic matrix. Cousin et al. [2011] did not identify this doublet either.

Forni et al. [2015] detected Cl in two Martian targets through molecular CaCl emission. Given the high abundance of Na detected in these Cl-bearing targets it was suggested that the Cl may have been present in the form of NaCl with the CaCl emission resulting from recombination of Cl in the plasma with Ca released from other phases. Chlorine was detected at levels as low as 0.6 wt. % in laboratory mixtures of $CaCO_3$ with $CaCl_2$ by Gaft et al., [2014] and 2.5 wt. % in synthetic chlorapatite+basalt mixtures by Meslin et al. [2016], well below the limit observed here for the atomic Cl lines. However, the ability to detect Cl through molecular lines relies on the presence of sufficient calcium in the sample [Vogt et al., 2017] whereas the atomic line emission can appear independently. Here we only observed the CaCl molecular lines in the $CaCl_2$+K1919 compositional series, not in the NaCl+basalt mixtures (see Figure S5). Work is ongoing to explore the detectability of perchlorates, which have been identified at Gale Crater by the Sample Analysis at Mars (SAM) instrument [Leshin et al., 2013; Ming et al., 2014] and previously at the Phoenix landing site [Hecht et al., 2009], in LIBS spectra [Schröder et al., 2017].

ChemCam analyses of carbon in the martian surface are underway and preliminary reports have suggested detections [Beck et al., 2016]. These results use the intensity of the C line at 723.7 nm relative to the O line at 777.6 nm. In addition, Rapin et al. [2016] use the C line at 247.9 nm for normalization of hydrogen emission therefore relying on the stability of its line strength assuming a relatively constant abundance of carbon in the martian CO_2 atmosphere. The 247.9 nm line was found to be rather insensitive to salt concentration with its peak area only significantly increased in the pure $MgCO_3$ sample, peak area decreasing from 70–100 wt.% $CaCO_3$, and a high detection limit. This suggests that the usage of this line for H normalization would only be affected by the composition of the rock target if the rock were majority carbonate.

6.4.6 Future Prospects for Salt Analysis on Mars with ChemCam & SuperCam

Applying these results to the study of the martian surface is the ultimate goal of this work. Multiple emission lines of Cl, C, and S were found in the LIBS spectra despite the interference from the basaltic background. Many of these lines displayed sensitivity to salt concentration and could provide at least some quantitative information about the sample composition. Clear detection of all three elements could be made in the spectra at ∼30 wt. % salt with some emission lines providing even lower detection limits. Therefore Cl, C, and S may be detectable in a porous sandstone mostly or completely filled with salt. Pore spaces can occupy 14–49% of the rock in sandstones [McWorter & Sunada, 1997]. This corresponds to rock compositions of about 11–43 wt. % NaCl or 15–52 wt. % $Fe_2(SO_4)_3$. Lower concentrations due to passing fluids coating grains or partially filling pore spaces may be detected for salts of certain compositions, which were found to have detection limits around 1–10 wt.% salt for select lines. Selected element lines were found to increase monotonically with salt concentration above a given threshold (Table 6.3), potentially allowing for relative changes in salt concentration to be observed. However, the dependence of calibration curve trends on the salt cation-anion pairing, at least for high salt concentrations, hinders the ability to obtain absolute quantification of Cl, C, and S through direct comparison between laboratory samples and martian targets of unknown composition. Differences between the moderate and high-alkali basalts were found to have little effect on the curves following normalization. Determination of the major element concentrations and identification of the salt cation may provide sufficient knowledge to make more accurate comparisons with the laboratory data. Although it is difficult due to their weak emission relative to that of the major elements, further work involving multivariate analysis of these elements or a multi-line approach may be warranted. Ultimately, even with only the ability to track relative changes in salt concentration assuming a single salt present, ChemCam will still be capable of distinguishing evaporite and siliciclastic layers throughout its traverse for follow-up with Curiosity's in-situ analysis instruments.

This work is likely to be useful for the Mars 2020 mission as well, for which LIBS will again be used, this time as part of the SuperCam instrument, which will have improved sensitivity and spectral resolution in the VNIR range. At the sulfur emission wavelengths (∼545 nm) SuperCam is expected to have a

factor of 2× better resolution (going from ∼0.65 nm on ChemCam to ∼0.30 nm full width half maximum on SuperCam). This will aid in separating the S emission lines from the interfering lines that complicate the ChemCam spectra. The spectral resolution will also be improved at longer wavelengths, e.g., for C and Cl emission lines. SuperCam will use a temporally gated intensifier for this spectral range, providing capabilities to boost the signal at times, so that minor peaks can be more clearly observed. The time gating can also be used to temporally distinguish between peaks. SuperCam will also have the ability to corroborate LIBS elemental identifications with mineral signatures from remote Raman and visible and infrared reflectance spectroscopy.

6.4.7 Potential Value of the Continuum Emission for Detecting Salts

As discussed in section 6.3.1, the continuum intensity displayed systematic trends over multiple consecutive laser shots that correlated with the salt content of the sample. Increasing continuum intensity has been noted in LIBS analysis of solid materials where consecutive laser pulses are targeted at the same location on a sample [Corsi et al., 2005]. These trends are not found when analyzing gases [e.g., Carranza & Hahn, 2002], suggesting that the cause is due to interaction with the solid surface. The cause may be confinement of the plasma within the ablation pit that develops following subsequent laser pulses on a single location. By enclosing the plasma, the interaction between its component electrons, ions, and atoms is intensified producing more emission. The strength of this emission will increase as the pit becomes deeper and is proportional to the ablated mass. However, there may be competing effects including cooling of the plasma due to interaction with the walls of the pit [Corsi et al., 2005].

The cause for the larger increase in continuum intensity over consecutive laser shots in the salts and salt-rich mixtures relative to the basalts is not clear. This distinction is unlikely to be caused directly by the elemental composition of the sample but may be related to or correlated with the physical properties of the sample surface. Relevant properties may include the hardness or strength of the material, which would affect the total ablated mass, or the laser-to-sample coupling due to differences in albedo or optical constants. However, correlations have been previously noted between the total integrated continuum intensity and the abundance of elements Fe and Na [Tucker et al., 2010]. This could be the result of more efficient ionization of these elements resulting

in higher electron densities in the plasma. Multiple hypotheses exist for the continuum behavior observed here, and future work is required to determine the cause. Such work may aid in devising additional methods for inferring the presence or tracking changes in abundance of salt in ChemCam targets with supporting elemental compositions. In conjunction with previous studies that have found the continuum to provide useful information or normalizations [e.g., Tucker et al., 2010; Schröder et al., 2015], this work suggests that the continuum emission warrants further consideration and may contribute diagnostic information particularly if included in multivariate LIBS analyses.

6.5 Conclusions

Weak anion lines of Cl, S, and C can be detected due to the presence of salt even among the large number of elemental lines and the matrix effects caused by a basaltic background. Of many more lines considered, a selection were evaluated using univariate analysis and 10 Cl, 4 C, and 2 S lines met all our criteria for potential usefulness in quantification. These results are promising for the detectability of diagenetic cements in basaltic sedimentary rocks on the surface of Mars. The selected lines are sensitive to salt concentration, providing a method for tracking relative changes in salt content above detection limits of about 5–10 wt. % salt for chlorides (3–6 wt. % Cl), ∼20 wt. % salt for carbonates (2 wt. % C), and 5–30 wt. % salt for sulfates (1–8 wt. % S). Absolute univariate quantification of the salt content of samples of unknown composition may be inaccurate for high salt concentrations due to differing trends in the calibration curves for different cation elements in salt+basalt mixtures. The basaltic matrix appeared to be less important in determining the calibration curves, following normalization by the total emission. The amount of increase in continuum emission following successive laser shots into the target may also track with salt content in the sample, providing an empirical method to identify potential samples with high salt, but requires further characterization to be developed into a useful method of analysis. These results suggest that as a survey tool, ChemCam should be able to track significant changes in the salt content of the bulk rock in the sedimentary units of Gale Crater by observation of selected emission lines of Cl, C, and S in the LIBS spectra. Distinguishing between the salts based on identification of specific Cl, C, and S lines would provide important implications regarding ancient environmental conditions of the region. These laboratory results will thus feed forward to in situ rover

investigations and analyses of LIBS data returned from Mars.

6.6 Acknowledgments

Thanks to Mike Baker for supplying the K1919 endmember and George Rossman for endmember acquisition advice. Thanks to the entire MSL ChemCam team for feedback throughout this project. Thanks to the anonymous reviewers for their valuable suggestions that have improved this document. This work was supported by a NASA MSL Participating Scientist Program grant to B. L. Ehlmann, a National Science Foundation Graduate Research Fellowship under grant no. DGE-11444469 to D. E. Anderson, and by contract from NASA's Mars Exploration Program to R.C. Wiens and S.M. Clegg.

Supplemental Information

Supporting information and data are available online:
https://doi.org/10.1002/2016JE005164

REFERENCES

Anderson, R. B. and J. F. Bell III (2010), Geologic mapping and characterization of Gale crater and implications for its potential as a Mars Science Laboratory landing site, Mars 5, 76-128, doi: 10.1555/mars.2010.0004.

Beck, P., O. Forni, J. Lasue, E. Lewin, A. Cousin, S. Maurice, P.-Y. Meslin, W. Rapin, O. Gasnault, R. C. Wiens, N. Mangold, V. Sautter, P. Coll, C. Szopa, T. Dequaire, and J. G. Blank (2016), Carbon Detection with ChemCam: Laboratory Studies and Mars Results, paper presented at 47th Lunar and Planetary Science Conference, The Woodlands, TX.

Carranza, J. E., and D. W. Hahn (2002), Sampling statistics and considerations for single-shot analysis using laser-induced breakdown spectroscopy, Spectrochim. Acta B, 57, 779, doi:10.1016/S0584-8547(02)00007-1.

Clegg, S. M., R. C. Wiens, R. B. Anderson, O. Forni, J. Frydenvang, J. Lasue, A. Cousin, V. Payre, T. Boucher, M. D. Dyar, S. M. McLennan, R. V. Morris, T. G. Graff, S. A. Mertzman, B. L. Ehlmann, I. Belgacem, H. Newsom, B. C. Clark, N. Melikechi, A. Mezzacappa, R. E. McInroy, R. Martinez, P. Gasda, O. Gasnault, and S. Maurice (2017), Recalibration of the Mars Science Laboratory ChemCam instrument with an expanded geochemical database, Spectrochim. Acta B, 129, 64-85, doi:10.1016/j.sab.2016.12.003.

Clegg, S. M., N. Mangold, S. Le Mouelic, 16 more authors and the MSL Science Team (2013), High Calcium Phase Observations at Rocknest with ChemCam, paper presented at 44th Lunar & Planetary Science Conference, The Woodlands, TX.

Corsi, M., G. Cristoforetti, M. Hidalgo, D. Iriarte, S. Legnaioli, V. Palleschi, A. Salvetti, and E. Tognoni (2005), Effect of Laser-Induced

Crater Depth in Laser-Induced Breakdown Spectroscopy Emission Features, Applied Spectroscopy, 59, 853-860, doi:10.1366/0003702054411607.

Cousin, A., O. Forni, S. Maurice, O. Gasnault, C. Fabre, V. Sautter, R.C. Wiens, and J. Mazoyer (2011), Laser induced breakdown spectroscopy library for the Martian environment, Spectrochim. Acta B, 66, 805-814, doi:10.1016/j.sab.2011.10.004.

Cremers, D. A., and L. J. Radziemski (2013), Handbook of Laser-Induced Breakdown Spectroscopy, Second Edition, John Wiley & Sons Ltd., Oxford, UK, doi: 10.1002/9781118567371.

Dyar, M. D., J. M. Tucker, S. Humphries, S. M. Clegg, R. C. Wiens, and M. D. Lane (2011), Strategies for Mars remote Laser-Induced Breakdown Spectroscopy analysis of sulfur in geological samples, Spectrochim. Acta B, 66, 39-56, doi:10.1016/j.sab.2010.11.016.

Ehlmann, B. L. and C. S. Edwards (2014), Mineralogy of the Martian Surface, Annual Reviews of Earth & Planetary Sciences, 42, 291-315, doi:10.1146/annurev-earth-060313-055024.

Fabre, C., A. Cousin, R. C. Wiens, A. Ollila, O. Gasnault, S. Maurice, V. Sautter, O. Forni, J. Lasue, R. Tokar, D. Vaniman, and N. Melikechi (2014), In situ calibration using univariate analyses based on the onboard ChemCam targets: first prediction of Martian rock and soil compositions, Spectrochim. Acta B, 99, 34-51, doi:10.1016/j.sab.2014.03.014.

Forni, O., M. Gaft, M. Toplis, S. M. Clegg, V. Sautter, and 14 more authors (2015), First detection of fluorine on Mars: Implications on Gale Crater's geochemistry, Geophys. Res. Lett., 42, 1020-1028, doi:10.1002/2014GL062742.

Frydenvang, J., P. J. Gasda, J. A. Hurowitz, J. P. Grotzinger, R. C. Wiens, H. E. Newsom, J. Bridges, O. Gasnault, S. Maurice, M. Fisk, B. Ehlmann, J. Watkins, N. Stein, O. Forni, N. Mangold, A. Cousin, S. M. Clegg, R. B. Anderson, V. Payré, W. Rapin, D. Vaniman, R. V. Morris, D. Blake, S. Gupta, V. Sautter, P.-Y. Meslin, P. Edwards, M. Rice, K. M. Kinch, R. Milliken, R. Gellert, L. Thompson, B. C. Clark, K. S. Edgett, D. Sumner, A. Fraeman, M. B. Madsen, I. Mitrofanov, I. Jun, F. Calef, and A. R. Vasavada (2016), Discovery of Silica-Rich Lacustrine and Eolian Sedimentary Rocks in Gale Crater, Mars, paper presented at 47th Lunar and Planetary Science Conference, The Woodlands, TX.

Gaft, M., L. Nagli, N. Eliezer, Y. Groisman, and O. Forni (2014), Elemental analysis of halogens using molecular emission by laser-induced breakdown spectroscopy in air, Spectrochim. Acta B, 98, 39-47, doi:10.1016/j.sab.2014.05.011.

Gasda, P. J., J. Frydenvang, R. C. Wiens, J. P. Grotzinger, J. A. Watkins, N. Stein, K. S. Edgett, H. Newsom, B. Clark, R. Anderson, N. Bridges, S. Clegg, S. Maurice, and the MSL Team (2016), Potential Link Between High-Silica

Diagenetic Features in Both Eolian and Lacustrine Rock Units Measured in Gale Crater with MSL, paper presented at 47th Lunar and Planetary Science Conference, The Woodlands, TX.

Gendrin, A., N. Mangold, J.-P., Bibring, Y. Langevin, B. Gondet, F. Poulet, G. Bonello, C. Quantin, J. Mustard, R. Arvidson, and S. LeMouélic (2005), Sulfates in Martian Layered Terrains: The OMEGA/Mars Express View, Science, 307, 1587-1591, doi:10.1126/science.1109087.

Gill, P. E., W. Murray, and M. H. Wright (1981), Practical Optimization, Academic Press, London, pp. 36-137.

Hecht, M. H., S. P. Kounaves, R. C. Quinn, S. J. West, S. M. M. Young, D. W. Ming, D. C. Catling, B. C. Clark, W. V. Boynton, J. Hoffman, L. P. DeFlores, K. Gospodinova, J. Kapit, and P. H. Smith (2009), Detection of perchlorate and the soluble chemistry of Martian soil at the Phoenix lander site, Science, 325, 64–67, doi:10.1126/science.1172466.

Kramida, A., Yu. Ralchenko, J. Reader, and NIST ASD Team (2015). NIST Atomic Spectra Database (version 5.3), [Online].
Available: http://physics.nist.gov/asd [2016]. National Institute of Standards and Technology, Gaithersburg, MD.

Lanza, N. L., A. M. Ollila, A. Cousin, R. C. Wiens, S. Clegg, N. Mangold, N. Bridges, D. Cooper, M. Schmidt, J. Berger, R. Arvidson, N. Melikechi, H. E. Newsom, R. Tokar, C. Hardgrove, A. Mezzacappa, R. S. Jackson, B. Clark, O. Forni, S. Maurice, M. Nachon, R. B. Anderson, J. Blank, M. Deans, D. Delapp, R. Léveillé, R. McInroy, R. Martinez, P.-Y. Meslin, and P. Pinet (2015), Understanding the signature of rock coatings in laser-induced breakdown spectroscopy data, Icarus, 249, 62-73, doi: 10.1016/j.icarus.2014.05.038.

Lanza, N. L., R. C. Wiens, S. M. Clegg, A. M. Ollila, S. D. Humphries, H. E. Newsom, and J. E. Barefield (2010), Calibrating the ChemCam laser-induced breakdown spectroscopy instrument for carbonate minerals on Mars, Applied Optics, 49, C211, doi:10.1364/AO.49.00C211.

Lasue, J., R. C. Wiens, S. M. Clegg, D. T. Vaniman, K. H. Joy, S. Humphries, A. Mezzacappa, N. Melikechi, R. E. McInroy, and S. Bender (2012), Remote laser-induced breakdown spectroscopy (LIBS) for lunar exploration, J. Geophys. Res. Planets, 117, E01002, doi:2011JE003898.

Le Deit, L., E. Hauber, F. Fueten, M. Pondrelli, A. P. Rossi, and R. Jaumann (2013), Sequence of infilling events in Gale Crater, Mars: Results from morphology, stratigraphy, and mineralogy, J. Geophys. Res. Planets, 118, 2439-2473, doi: 10.1002/2012JE004322.

Leshin, L. A., P. R. Mahaffy, C. R. Webster, M. Cabane, P. Coll, P. G. Conrad, P. D. Archer Jr., et al., (2013), Volatile, Isotope, and Organic Analysis of Martian Fines with the Mars Curiosity Rover, Science, 341, doi: 10.1126/science.1238937.

Massart, D. L., B. G. M. Vandeginste, L. M. C. Buydens, S. De Jong, P. J. Lewi, and J. Smeyers-Verbeke (Eds.) (1998), Handbook of Chemometrics and Qualimetrics: Part A, Elsevier, New York.

Maurice, S., R. C. Wiens, M. Saccoccio, B. Barraclough, O. Gasnault, and 65 more authors (2012), The ChemCam Instrument Suite on the Mars Science Laboratory (MSL) Rover: Science Objectives and Mast Unit Description, Space Science Review, 170, 95-166, doi: 10.1007/s11214-012-9912-2.

McWorter, D. B. and D. K. Sunada (1977) Ground-water Hydrology and Hydraulics, Water Resources Publications, LLC., Colorado, USA.

Meslin, P.-Y., L. Cicutto, O. Forni, C. Drouet, W. Rapin, M. Nachon, A. Cousin, J. G. Blank, F. M. McCubbin, O. Gasnault, H. Newsom, N. Mangold, S. Schröder, V. Sautter, S. Maurice, and R. C. Wiens (2016), Calibration of the Fluorine, Chlorine, and Hydrogen Content of Apatites with the ChemCam LIBS Instrument, paper presented at 47th Lunar and Planetary Science Conference, The Woodlands, TX.

Milliken, R. E., J. P. Grotzinger, and B. J. Thomson (2010), Paleoclimate of Mars as captured by the stratigraphic record in Gale Crater, Geophys. Res. Lett., 37, L04201, doi:10.1029/2009GL041870. Ming, D. W., P. D. Archer, D. P. Glavin, J. L. Eigenbrode, H. B. Franz, B. Sutter, A. E. Brunner, J. C. Stern, C. Freissinet, A. C. McAdam, and 438 coauthors (2014), Volatile and Organic Compositions of Sedimentary Rocks in Yellowknife Bay, Gale Crater, Mars, Science, 343, 1245267, doi:10.1126/science.1245267.

Nachon M., N. Mangold, O. Forni, L. C. Kah, A. Cousin, R. C. Wiens, R. Anderson, D. Blaney, J. G. Blank, F. Calef, S. M. Clegg, C. Fabre, M. R. Fisk, O. Gasnault, J. P. Grotzinger, R. Kronyak, N. L. Lanza, J. Lasue, L. Le Deit, S. Le Mouélic, S. Maurice, P.-Y. Meslin, D. Z. Oehler, V. Payré, W.

Rapin, S. Schröder, K. Stack, and D. Sumner (2017), Chemistry of diagenetic features analyzed by ChemCam at Pahrump Hills, Gale craters, Mars, Icarus, 281, 121-136, doi:10.1016/j.icarus.2016.08.026. Nachon, M., S. M. Clegg, N. Mangold, and 33 more authors (2014), Calcium sulfate veins characterized by ChemCam/Curiosity at Gale crater, Mars, J. Geophys. Res. Planets, 119, 1991-2016, doi:10.1002/2013JE004588.

Newsom, H. E., I. Belgacem, R. Jackson, B. Ha, Z. Vaci, R. C. Wiens, J. Frydenvang, P. Gasda, N. Lanza, S. Clegg, O. Gasnault, S. Maurice, A. Cousin, W. Rapin, O. Forni, S. Banham, S. Gupta, A. Williams, J. Grotzinger, D. Blaney, J. Schroeder, F. Calef, R. Francis, B. Ehlmann, A. Yen, N. Stein, D. Rubin, N. Bridges, J. Johnson, K. Lewis, V. Payré, N. Mangold, K. Edgett, D. Fey, M. Fisk, R. Gellert, L. Thompson, M. Schmidt, G. Perrett, L. Kah, R. Kronyak, R. Anderson, K. Herkenhoff, J. Bridges, J. Hurowitz, J. Schieber, E. Heydari, and J. Watkins (2016), The Materials at an Unconformity Between the Murray and Stimson Formations at Marias Pass, Gale Crater, Mars, paper presented at 47th Lunar and Planetary Science Conference, The Woodlands, TX. Newville, M., T. Stensitzki, D. B. Allen, and A. Ingargiola (2014), LMFIT: Non-Linear Least-Square Minimization and Curve-Fitting for Python, Zenodo. doi.org/10.5281/zenodo.11813.

Ollila, A. M., H. E. Newsom, R. C. Wiens, J. Lasue, S. M. Clegg, A. Cousin, O. Gasnault, O. Forni, S. Maurice, S. Schröder, P.-Y. Meslin, M. D. Dyar, J. G. Blank, B. Clark, B. Barraclough, and the MSL Team (2013), Early Results from Gale Crater on ChemCam Detections of Carbon, Lithium, and Rubidium, paper presented at 44th Lunar and Planetary Science Conference, The Woodlands, TX. Ollila, A. M., J. G. Blank, R. C. Wiens, J. Lasue, H. E. Newsom, S. M. Clegg, A. Cousin, and S. Maurice (2011), Preliminary Results on the Capabilities of the ChemCam Laser-Induced Breakdown Spectroscopy (LIBS) Instrument to Detect Carbon on Mars, paper presented at the 42nd Lunar and Planetary Science Conference, The Woodlands, TX.

Rapin, W., P.-Y. Meslin, S. Maurice, D. Vaniman, M. Nachon, N. Mangold, S. Schröder, O. Gasnault, O. Forni, R. C. Wiens, G. M. Martínez, A. Cousin, V. Sautter, J. Lasue, E. B. Rampe, and D. Archer (2016), Hydration of calcium sulfates in Gale Crater: identification of bassanite veins, Earth and Planetary Science Letters, 452, 197-205, doi: 10.1016/j.epsl.2016.07.045. Schröder, S., K. Rammelkamp, A. Cousin, D. Vogt, P.-Y. Meslin, S. Maurice, and H.-W.

Hübers (2017), LIBS Analysis of Perchlorates and Chlorides in Soil in Mars-like Conditions, paper presented at the 48th Lunar and Planetary Science Conference, The Woodlands, TX.

Schröder, S., P.-Y. Meslin, O. Gasnault, S. Maurice, A. Cousin, R. C. Wiens, W. Rapin, M. D. Dyar, N. Mangold, O. Forni, M. Nachon, S. Clegg, J. R. Johnson, J. Lasue, S. Le Mouélic, A. Ollila, P. Pinet, V. Sautter, and D. Vaniman (2015), Hydrogen detection with ChemCam at Gale crater, Icarus, 249, 43-61, doi:10.1016/j.icarus.2014.08.029.

Schröder, S., S. G. Pavlov, I. Rauschenbach, E.K. Jessberger, and H.-W. Hübers (2013) Detection and identification of salts and frozen salt solutions combining laser-induced breakdown spectroscopy and multivariate analysis methods: A study for future martian exploration, Icarus, 223, 61-73, doi:10.1016/j.icarus.2012.11.011.

Singh, J. P. and S. N. Thakur (2007), Laser-Induced Breakdown Spectroscopy, Elsevier Science, Oxford, UK.

Sobron, P., A. Wang, and F. Sobron (2012), Extraction of compositional and hydration information of sulfates from laser-induced plasma spectra recorded under Mars atmospheric conditions – Implications for ChemCam investigations on Curiosity rover, Spectrochim. Acta B, 68, 1-16, doi:10.1016/j.sab.2012.01.002.

Stern, J. C., B. Sutter, C. Freissinet, R. Navarro-González, C. P. McKay, P. D. Archer Jr., A. Buch, et al., (2015), Evidence for indigenous nitrogen in sedimentary and aeolian deposits from the Curiosity rover investigations at Gale crater, Mars, Proc. Natl. Acad. Sci., 112, 4245-4250, doi: 10.1073/pnas.1420932112.

Thomas, N. H., B. L. Ehlmann, S. M. Clegg, O. Forni, S. Schröder, D. E. Anderson, W. Rapin, A. Cousin, P.-Y. Meslin, J. Lasue, D. M. Delapp, R. E. McInroy, M. D. Dyar, G. R. Rossman, O. Gasnault, R. C. Wiens, and S. Maurice (2016), Characterization of Hydrogen in Basaltic Materials with Laser-Induced Breakdown Spectroscopy (LIBS), paper presented at 47th Lunar and Planetary Science Conference, The Woodlands, TX.

Thomas, N. H., B. L. Ehlmann, and D. E. Anderson (2015), Characterization of Hydrogen Abundance in LIBS Data, paper presented at 46th Lunar & Planetary Science Conference, The Woodlands, TX.

Thomson, B. J., N. T. Bridges, R. Milliken, A. Baldridge, S. J. Hook, J. K. Crowley, G. M. Marion, C. R. de Souza Filho, A. J. Brown, and C. M. Weitz (2011), Constraints on the origin and evolution of the layered mound in Gale Crater, Mars using Mars Reconnaissance Orbiter data, Icarus, 214, 413-432, doi: 10.1016/j.icarus.2011.05.002.

Tucker, J. M., M. D. Dyar, M. W. Schaefer, S. M. Clegg, and R. C. Wiens (2010), Optimization of the laser-induced breakdown spectroscopy for rapid geochemical analysis, Chemical Geology, 277, 137-148, doi:10.1016/j.chemgeo.2010.07.016.

Vaniman, D. T., D. L. Bish, D. W. Ming, T. F. Bristow, R. V. Morris, D. F. Blake, 30 more authors and the MSL Science Team (2014), Mineralogy of a Mudstone at Yellowknife Bay, Gale Crater, Mars, Science, 343, 1243480, doi:10.1126/science.1243480.

Vogt, D., K. Rammelkamp, S. Schröder, and H.-W. Hübers (2017), Suitability of Molecular Emission in Laser-Induced Breakdown Spectroscopy for the Quantification of Chlorine Under Martian Conditions, paper presented at 48th Lunar & Planetary Science Conference, The Woodlands, TX.

Wiens, R. C., S. Maurice, J. Lasue, O. Forni, R. B. Anderson and 19 more authors (2013), Pre-flight calibration and initial data processing for the ChemCam laser-induced breakdown spectroscopy instrument on the Mars Science Laboratory rover, Spectrochim. Acta B, 82, 1–27, doi:10.1016/j.sab.2013.02.003.

Wiens, R. C., S. Maurice, B. Barraclough, M. Saccoccio, W. Barkley, and 75 more of the ChemCam Team (2012), The ChemCam instrument suite on the Mars Science Laboratory (MSL) rover: Body unit and combined system tests, Space Science Review, 170, 167-227, doi:10.1007/s11214-012-9902-4.

Yen, A. S., R. Gellert, C. Schröder, R. V. Morris, J. F. Bell III, A. T. Knudson, B. C. Clark, D. W. Ming, et al., (2005), An integrated view of the chemistry and mineralogy of martian soils, Nature, 436, 49–54, doi:10.1038/nature03637.

Chapter 7

CONCLUSIONS & FUTURE DIRECTIONS

The work presented in this thesis has furthered our understanding of several key factors influencing the composition of planetary materials during their formation and evolution. Chemical processes in protoplanetary disk environments can largely alter inherited interstellar materials and may be able to recreate compositional trends seen in the carbon and nitrogen content of solar system bodies if certain environmental conditions are present. The processes studied in this work are not particularly fine-tuned to our solar system and could be widespread in extrasolar planet-forming disks. Future work will explore the applicability of the chemical processes studied in this work to a wider variety of planetary environments and characterize the occurrence rate of planetary outcomes similar to that of Earth.

7.1 LIBS Exploration of Planetary Surfaces

ChemCam is currently surveying the Martian surface and has collected hundreds of thousands of spectra to date. The analysis from Chapter 6 has been applied to the study of chlorides (Thomas et al. 2019) and sulfates (Rapin et al. 2019) in Gale Crater and the salt+basalt mixture samples have contributed to the spectral libraries of Clegg et al. (2017) and Anderson et al. (2017). LIBS will be further used in the upcoming Mars 2020 mission combined with Raman spectroscopy in the SuperCam instrument. As a quick remote analysis technique that is sensitive even to light elements, LIBS has many advantages for tracking volatile elements in future planetary missions (e.g., Lasue et al. 2012).

As more sophisticated analysis methods are pursued for the minor elements including C, S, and Cl, akin to the multivariate techniques used for the major elements (e.g., Anderson et al. 2017), the use of the continuum emission merits further study. An increase was seen in the LIBS continuum intensity for sample mixtures with higher salt concentrations (Chapter 6). Although continuum emission cannot be connected to specific elements with the precision of the spectral lines, it may relate to bulk compositions or material properties. In larger, whole spectrum analyses these factors may aid in the detection of

certain salts or other sample components.

7.2 Volatile Depletion

The observational characterization of volatile depletion in connection to disk masses for sources of different ages is crucial for both the study of disk evolution and planet formation. Direct measurements of the pure rotational transitions of H_2 will be feasible for select sources with JWST and the upcoming HIgh Resolution Mid-infrarEd Spectrometer (HIRMES) on the Stratospheric Observatory for Infrared Astronomy (SOFIA) will increase the number of HD detections. These studies will be essential to provide tests of current modeling predictions relating carbon- and nitrogen-bearing species to the total H_2 content of the gas. Understanding the level of depletion of the dominant volatiles in the disk will not only aid in disk mass determinations, but inform on the major reservoirs of life-enabling elements in planet-forming environments.

N_2H^+ may provide additional constraints regarding CO abundances and disk masses (Chapter 3 and 4). Recent ALMA and Submillimeter Array (SMA) follow-up observations have targeted N_2H^+, HCO^+, and CO isotopologue emission in a larger number of systems. ALMA Cycle 6 measurements explore a sample of three total Upper Sco disks with CO/dust flux ratios that vary over an order of magnitude (PI: Anderson, 2018.1.01623.S). SMA observations investigate younger sources in the Taurus region sampling distinct disk environments, sizes, and binary/multi systems (PI: Anderson, 2018B-S046). Finally, upcoming ALMA Cycle 7 observations will focus on the Lupus star-forming region where a wide range of CO/dust flux ratios, indicating either a range of gas-to-dust ratios or CO/H_2 abundances, have been observed (PI: Anderson, 2019.1.01135.S). Whether the Lupus disks have gas-to-dust mass ratios of $\sim$1–10 or are CO-depleted is an open question that is very relevant to planet formation timescales given their young age of 1–3 Myr (Miotello et al. 2017). Comparison of these datasets derived from disks of different ages and from distinct environments will provide a better understanding of N_2H^+ as a gas tracer and the carbon and nitrogen content of protoplanetary disks.

7.3 Refractory Carbon Abundances

Significant loss of carbon from solids is inhibited by grain growth for Class II disks where active accretion by the central star is less prominent and heating of disk materials is dominated by passive irradiation (Chapter 2). Distinct

environments present at earlier stages of the disk lifetime have the potential to greatly affect the growth and composition of protoplanetary materials and future rocky planets. In particular, two early-disk processes that could substantially alter refractory carbon reservoirs in young disks are accretion outbursts and early giant-planet formation.

Although observed in a small number of stars, FU Ori-like accretion outbursts are thought to be common processes and important for providing the bulk of mass from which young stars grow. Over ∼1–10 years the optical luminosity of the star increases by ∼5 mag and then decays over 10s–100s of years. As a result of the outburst, the bulk disk material will reach significantly higher temperatures than modeled in Chapter 2. Stars, including our early Sun, are thought to undergo multiple bursts with a frequency of $\sim 10^3$–10^4 years (Audard et al. 2014). Potential volatile loss and/or destruction of planetary building blocks caused by such outbursts is therefore highly relevant to the evolution and habitability of the resulting planetary systems.

Evidence of radial drift of solids in protoplanetary disks presents a challenge for maintaining carbon-poor solids in the inner disk. Continued disk evolution could draw carbon from outer regions of the disk inward, leading to replenishment over time. However, early giant-planet formation in the disk may be crucial to stopping this process, maintaining a refractory-carbon-poor inner disk. In fact, the timing of Jupiter formation has been used to explain trends in the chemical and isotopic compositions of asteroid classes (Kruijer et al. 2017). Gaps seen in the disk of 0.1 Myr-old HL Tau that may be caused by forming planets clearing surrounding material (ALMA Partnership et al. 2015) and recently detected proto-planets embedded in the disk of HD 163296 (Pinte et al. 2018; Teague et al. 2018) provide further evidence that planet formation starts early. If Jupiter formation during a specific time period is key to producing carbon-poor planetesimals in the inner disk and determining the Earth's carbon content, Earth-like planets may be limited in number to systems with gas-giant planets exterior to terrestrial planets. Including these early-disk phenomena in our models may provide a more realistic approximation of refractory carbon destruction throughout the lifetime of protoplanetary disks.

7.4 Connecting Protoplanetary Disk Models to Observational Constraints

High-resolution ALMA observations currently reveal depleted volatile abundances that likely depend on a combination of dynamical and chemical processes (Krijt et al. 2018). Considering these highly-coupled processes in isolation will no longer be sufficient to address the new questions derived from ALMA and future revelations from JWST regarding the planet-forming regions of disks. Mass transport is critical when estimating the extent of alteration experienced by both the bulk refractory (Chapter 2) and volatile (Chapter 5) carbon reservoirs. Further development of computationally-feasible methods for modeling chemistry and dynamics together is a crucial next step in understanding disk evolution and predicting planetary compositions.

A great deal of uncertainty remains regarding the physical conditions and mass transport in protoplanetary disks. How the solar nebula compares to observable protoplanetary disks and which disks may be the best analogs are also largely unknown. From a modeling perspective, exploring parameter space with grid-like approaches (as used Chapters 3 and 4) can provide the likelihood of producing certain outcomes, such as carbon-poor solids in the inner disk, for a given range of initial conditions and modeled processes. When combined with planet formation models, such efforts could help constrain the parameters required to form rocky planets with Earth-like compositions and the probability of these outcomes.

REFERENCES

ALMA Partnership, C. L. Brogan, L. M. Pérez, T. R. Hunter, W. R. F. Dent, A. S. Hales, R. E. Hills, S. Corder, E. B. Fomalont, C. Vlahakis, Y. Asaki, D. Barkats, A. Hirota, J. A. Hodge, C. M. V. Impellizzeri, R. Kneissl, E. Liuzzo, R. Lucas, N. Marcelino, S. Matsushita, K. Nakanishi, N. Phillips, A. M. S. Richards, I. Toledo, R. Aladro, D. Broguiere, J. R. Cortes, P. C. Cortes, D. Espada, F. Galarza, D. Garcia-Appadoo, L. Guzman-Ramirez, E. M. Humphreys, T. Jung, S. Kameno, R. A. Laing, S. Leon, G. Marconi, A. Mignano, B. Nikolic, L.-A. Nyman, M. Radiszcz, A. Remijan, J. A. Rodón, T. Sawada, S. Takahashi, R. P. J. Tilanus, B. Vila Vilaro, L. C. Watson, T. Wiklind, E. Akiyama, E. Chapillon, I. de Gregorio-Monsalvo, J. Di Francesco, F. Gueth, A. Kawamura, C.-F. Lee, Q. Nguyen Luong, J. Mangum, V. Pietu, P. Sanhueza, K. Saigo, S. Takakuwa, C. Ubach, T. van Kempen, A. Wootten, A. Castro-Carrizo, H. Francke, J. Gallardo, J. Garcia, S. Gonzalez, T. Hill, T. Kaminski, Y. Kurono, H.-Y. Liu, C. Lopez, F. Morales, K. Plarre, G. Schieven, L. Testi, L. Videla, E. Villard, P. Andreani, J. E. Hibbard, and K. Tatematsu. The 2014 ALMA Long Baseline Campaign: First Results from High Angular Resolution Observations toward the HL Tau Region. *ApJ*, 808:L3, July 2015. doi: 10.1088/2041-8205/808/1/L3.

R. B. Anderson, S. M. Clegg, J. Frydenvang, R. C. Wiens, S. McLennan, R. V. Morris, B. Ehlmann, and M. D. Dyar. Improved accuracy in quantitative laser-induced breakdown spectroscopy using sub-models. *Spectrochimica Acta*, 129:49–57, March 2017. doi: 10.1016/j.sab.2016.12.002.

M. Audard, P. Ábrahám, M. M. Dunham, J. D. Green, N. Grosso, K. Hamaguchi, J. H. Kastner, Á. Kóspál, G. Lodato, M. M. Romanova, S. L. Skinner, E. I. Vorobyov, and Z. Zhu. Episodic Accretion in Young Stars. *Protostars and Planets VI*, pages 387–410, 2014. doi: 10.2458/azu_uapress_9780816531240-ch017.

S. M. Clegg, R. C. Wiens, R. Anderson, O. Forni, J. Frydenvang, J. Lasue, A. Cousin, V. Payré, T. Boucher, M. D. Dyar, S. M. McLennan, R. V. Morris, T. G. Graff, S. A. Mertzman, B. L. Ehlmann, I. Belgacem, H. Newsom, B. C. Clark, N. Melikechi, A. Mezzacappa, R. E. McInroy, R. Martinez, P. Gasda, O. Gasnault, and S. Maurice. Recalibration of the Mars Science Laboratory ChemCam instrument with an expanded geochemical database. *Spectrochimica Acta*, 129:64–85, March 2017. doi: 10.1016/j.sab.2016.12.003.

S. Krijt, K. R. Schwarz, E. A. Bergin, and F. J. Ciesla. Transport of CO in Protoplanetary Disks: Consequences of Pebble Formation, Settling, and Radial Drift. *ApJ*, 864:78, September 2018. doi: 10.3847/1538-4357/aad69b.

T. S. Kruijer, C. Burkhardt, G. Budde, and T. Kleine. Age of Jupiter inferred from the distinct genetics and formation times of meteorites. *Proceedings of the National Academy of Science*, 114:6712–6716, June 2017. doi: 10.1073/pnas.1704461114.

J. Lasue, R. C. Wiens, S. M. Clegg, D. T. Vaniman, K. H. Joy, S. Humphries, A. Mezzacappa, N. Melikechi, R. E. McInroy, and S. Bender. Remote laser-induced breakdown spectroscopy (LIBS) for lunar exploration. *Journal of Geophysical Research (Planets)*, 117:E01002, January 2012. doi: 10.1029/2011JE003898.

A. Miotello, E. F. van Dishoeck, J. P. Williams, M. Ansdell, G. Guidi, M. Hogerheijde, C. F. Manara, M. Tazzari, L. Testi, N. van der Marel, and S. van Terwisga. Lupus disks with faint CO isotopologues: low gas/dust or high carbon depletion? *A&A*, 599:A113, March 2017. doi: 10.1051/0004-6361/201629556.

C. Pinte, D. J. Price, F. Ménard, G. Duchêne, W. R. F. Dent, T. Hill, I. de Gregorio-Monsalvo, A. Hales, and D. Mentiplay. Kinematic Evidence for an Embedded Protoplanet in a Circumstellar Disk. *ApJ*, 860:L13, June 2018. doi: 10.3847/2041-8213/aac6dc.

W. Rapin, B. L. Ehlmann, G. Dromart, J. Schieber, N. H. Thomas, W. W. Fischer, V. K. Fox, N. T. Stein, M. Nachon, B. C. Clark, L. C. Kah, L. Thompson, H. A. Meyer, T. S. J. Gabriel, C. Hardgrove, N. Mangold, F. Rivera-Hernandez, R. C. Wiens, and A. R. Vasavada. An interval of high salinity in ancient Gale crater lake on Mars. *Nature Geoscience*, 12:889–895, Oct 2019. doi: 10.1038/s41561-019-0458-8.

R. Teague, J. Bae, E. A. Bergin, T. Birnstiel, and D. Foreman-Mackey. A Kinematical Detection of Two Embedded Jupiter-mass Planets in HD 163296. *ApJ*, 860:L12, June 2018. doi: 10.3847/2041-8213/aac6d7.

N. H. Thomas, B. L. Ehlmann, P. Y. Meslin, W. Rapin, D. E. Anderson, F. Rivera-Hernández, O. Forni, S. Schröder, A. Cousin, N. Mangold, R. Gellert, O. Gasnault, and R. C. Wiens. Mars Science Laboratory Observations of Chloride Salts in Gale Crater, Mars. *Geophysical Research Letters*, 46(19):10,754–10,763, Oct 2019. doi: 10.1029/2019GL082764.